Design and manufacture of poly-ε-lysine hydrogels for corneal tissue engineering applications

Thesis submitted in accordance with the requirements of the
University of Liverpool for the degree of
Doctor in Philosophy

By

Georgia Lauren Duffy

October 2021

Abstract

The human cornea is the window to the eye, and acts to focus light onto the retina. It is composed of three main layers: a stratified epithelium, the stroma, and a monolayer of endothelial cells. Corneal opacities are the 4th leading cause of blindness worldwide, with the main current treatment being a tissue transplant from a cadaveric donor. This treatment method has several limitations, which has prompted researchers into finding suitable synthetic alternatives, with very few making it through to clinical trials thus far.

Cast hydrogels based on the natural polymer poly-ε-lysine have been investigated in our group for multiple ocular applications including antimicrobial contact lenses to treat keratitis, and an endothelial cell delivery device to treat damaged corneal endothelium. These studies found that hydrogels based on pεK were found to have tuneable mechanical properties, a high transparency and water content and supported the cell attachment and growth of several corneal cell types. However, the cast hydrogels do not demonstrate an interconnected porosity, a property which would expand the tissue engineering applications for which the hydrogels would be suitable.

This work investigated various manufacturing methods to produce a porous hydrogel construct based on poly-ε-lysine, including; fragmenting the hydrogels during polymerisation, the use of a porogen and 3D reactive inkjet printing. The various hydrogels were characterised for their optical, physical and mechanical properties and their compatibility with corneal cell types. Corneal cells were also seeded onto alternative peptide based hydrogels, including methacrylated gelatin (GelMA) and methacrylated poly-ε-lysine (pεKMA).

The results demonstrate that a poly-ε-lysine construct with interconnected porosity can be manufactured when the hydrogel is fragmented during polymerisation. These hydrogel variants demonstrate handleable mechanical properties, a high transparency and support the attachment of corneal epithelial and endothelial cells and the inward migration of corneal stromal cells. Hydrogel variants cast using a porogen demonstrated similar physical properties, however altering the chemistry of these hydrogels dramatically reduced the transparency, rendering them unsuitable for a corneal application. However, the porosity, high strength, water content and cyto-compatibility suggests they could be considered for alternative tissue engineering applications. Finally, this work has shown it is possible to print porous hydrogel constructs based on the polymers poly-ε-lysine and gellan gum using 3D reactive inkjet printing. These printed structures had a unique surface topography due to the instantaneous reaction between the polymers of opposing charges. This structure can be tailored to include pores throughout, and demonstrates a high resolution.

This work presents the versatility of manufacture of pεK hydrogels, and their potential as corneal tissue engineering constructs. They demonstrate comparable properties to alternative hydrogels used in tissue engineering applications, and are also comparable with native human tissue.

Contents

Acknowledgements

Firstly, I would like to thank my supervisors Professor Rachel Williams and Dr Kate Black for their support and guidance over the course of my PhD. Rachel, your knowledge and experience has been invaluable to me and Kate, I appreciate all your help and for encouraging me to work hard and be a better researcher. I would also like to thank Dr Don Wellings from SpheriTech Ltd for his help and expertise over the last three years.

A special thanks to all the students and staff in the Department of Eye of Vision Science and the School of Engineering for their help, support and friendship. In particular; Alys Davies, Liam Shaw, Danielle O'Loughlin and Stephnie Kennedy, I'm not sure how I would've got through it without you! I would also like to thank the technicians of the Materials Innovation Factory, in particular Dr Keith Arnold and Dr Alex Ciupa for their help with the SEM and the DSA.

I would also like to acknowledge two of my closest and oldest friends Katie and Ellie. You both kept me sane at times when I found it difficult, and listened to me vent about journal papers and experiment plans while we were on seemingly endless lockdown walks. I will forever be grateful for your support and friendship.

To my partner Sean and the O'Brien family. I can't thank you enough for being there for me when COVID lockdowns stopped me seeing my own family for months on end. I will always be grateful for your support during this time. Sean, you have been there for me through all of the highs and the lows over the last couple of years. Thank you for letting me chat your ear off about my work, listening to me complain when it got difficult, and for your continued love and support.

Most importantly, I would like to thank my family. To my Mum, thank you for always listening to me when I needed you, and for your love and encouragement. To my siblings, Ellena and Joe, for always being there for me when I need to talk, making me laugh and for pushing me to work hard. Finally, I'm not sure I would even be studying science without the encouragement and direction from my Dad from a young age. From helping me revise for my GCSEs and A levels to prepping me for PhD and job interviews, I couldn't have done it without you. Dad, you inspired me to pursue a career in scientific research and I hope I have made you proud.

List of Abbreviations and Symbols

2PP - Two-photon Polymerisation

AAPCM – Anterior acellular porcine corneal matrix

ANOVA – Analysis of Variance

APCS – Acellular porcine corneal stroma

Boston KPro I - Boston keratoprosthesis type 1

CAD – Computer Aided Design

CCK-8 - Cell counting kit-8

CIJ – Continuous Inkjet

CLET – Cultivated Limbal epithelial transplantation

COMET – Cultivated Oral mucosa epithelial transplantation

DALK - Deep Anterior Lamellar Keratoplasty

DAPI - 4',6-Diamidino-2-phenylindole

DMSO - Dimethyl sulfoxide

DMEK - Descemet's Membrane Endothelial Keratoplasty

DSEK - Descemet's Stripping Endothelial Keratoplasty

DOD – Drop-on-demand

ECM – Extracellular matrix

EDCI - 1-Ethyl-3-(3-dimethylaminopropyl) carbodiimide

EK – Endothelial Keratoplasty

FCS – Foetal Calf Serum

FDM – Fused Deposition modelling

FECD - Fuchs' Endothelial Corneal Dystrophy

GelMA – Gelatin methacrylate

GFP – Green fluorescent protein

GG – Gellan gum

hADSC - Human adipose derived stem cells

hAM – Human amniotic membrane

HAMA – Methacrylated hyaluronic acid

HCECs – Human corneal endothelial cells

HCE-T – Human corneal epithelial cell line

hCFs – Human corneal fibroblasts

hCSSC – Human corneal stromal stem cells

hLESC - Human limbal epithelial stem cells

IOFB – Intraocular Foreign Body

IOP – Intraocular pressure

IPN - Interpenetrating polymer network

KPro – Keratoprosthesis

LEC – Limbal epithelial cells

LSC – Limbal stem cells

LSCD – Limbal stem cell deficiency

NHS - N-Hydroxysuccinimide

NK – Natural Killer cells

NMM - N-Methylmorpholine

ODA – Octanedioic acid

Oh – Ohnersorge number

OOKP - Osteo-odonto-keratoprosthesis

PAA - Poly(acrylic acid)

PANI - Polyaniline

PBS – Phosphate Buffer Saline

PCL – Poly(ε-caprolactone)

PCEC - Primary porcine corneal endothelial cells

PEG - Poly(ethylene glycol)

PEGDA - Poly(ethylene glycol) diacrylate

pεK – Poly-ε-lysine

pεKMA – Methacrylated poly-ε-lysine

pHEMA – Poly(2-hydroxyethyl methacrylate)

PK – Penetrating Keratoplasty

PLGA - Poly(D,L-lactide-co-glycolide)

PMMA - Poly(methyl methacrylate)

PNIPAm - Poly(N-isopropylacrylamide)

PVA – Poly(vinyl alcohol)

RAFT - Real Architecture for 3D Tissues

RGD - Arginylglycylaspartic acid

RIJ – Reactive Inkjet

SC – Stem cell

SD - Standard deviation

SEM - Scanning electron microscope

SLA - Stereolithography

SOP - Standard operating procedure

TC - Tissue culture

TE – Tissue Engineering

TECE – Tissue Engineered Corneal Equivalent

TFLL - Tear Film lipid layer

List of Figures

List of Tables

Chapter 2

Chapter 3

Chapter 4

Publications

Published papers

- Lourenco E. A. J., Shaw L., Pratt H., Duffy G. L., Czanner G., et al. Application of SPF moisturisers is inferior to sunscreens in coverage of facial and eyelid regions. PLOS ONE. 2019 14(4): e0212548.
- Lace R., Duffy G. L., Gallagher A. G., et al. Characterization of Tunable Poly-ε-Lysine-Based Hydrogels for Corneal Tissue Engineering. Macromolecular Bioscience. 2021 May: e2100036.
- Duffy, G. L., Liang, H., Williams, R. L., Wellings, D. A., Black, K., 3D reactive inkjet printing of poly-ε-lysine/gellan gum hydrogels for potential corneal constructs, Materials Science and Engineering: C, 131, 2021, 112476

Published abstracts

- Duffy, G. L., Liang, H., Wellings, D., Black, K., Williams, R., 2020, Corneal regeneration using porous poly-ε-lysine hydrogels, In: 11th World Biomaterials Congress, 11-16th December. [Online]
- Duffy, G. L., Liang, H., Wellings, D., Black, K., Williams, R., 2021, 3D reactive inkjet printing of peptide based hydrogels for corneal tissue engineering. In: 31st Conference of the European Society of Biomaterials, 5th-9th September, Porto. [Online], pp. 184-185 [Accessed: 05 October 2021]

Chapter 1: Introduction

1.1.1 The Eye: Basic anatomy

The human eye is a sensory organ made up of multiple specialised structures and is maintained by specific physiological parameters. It is the primary organ that functions to facilitate vision, **Figure 1.1**. The structure of the eye can be broken down into three main layers, two overarching segments, and three intraocular fluids. The three layers are: the outer layer, the middle vascular layer and the inner nervous layer. The two segments of the eye are the anterior, all structures in front of and including the lens, and the posterior, which are all structures behind the lens. Finally, the three main intraocular fluids are aqueous humour, vitreous humour and blood [1].

The anterior segment refers to the front third of the tissues within the eye, and includes everything in front of the vitreous humour. The outer layer is made up of the cornea and the sclera [2]. The cornea is transparent and central on the eyeball, whereas the sclera is white and surrounds the cornea. The point at which these two layers meet is called the limbus. The sclera is covered by a thin, transparent mucous membrane called the conjunctiva, which becomes continuous with the epithelial layer of the cornea. The middle layer can be separated into the iris, the ciliary body and choroids. The iris is a thin disc which is perforated by the pupil. The pupil is contracted and dilated in response to light using muscles located in the iris. The ciliary body contains ciliary muscles which run either longitudinally or circumferentially through the eye [3]. At the back of the anterior chamber is the lens. This functions alongside the cornea to focus light onto the retina.

The posterior chamber of the eye is the remaining two thirds of the eyes tissue, which includes the vitreous humour and all optical structures behind it. The vitreous humour is a gel-like substance which takes up the bulk of the space within the eyeball. It functions to maintain the eye's shape, and sustains a high intraocular pressure (IOP) to keep ocular structures in places [4]. The inner layer consists of retinal tissue, and contains photoreceptors and neurons. This is known as the neurosensory layer. The function of the retina is to convert light into electrical

energy for transmission to the brain. The retina relies on photoreceptors, either rods or cones [5], to form visual images from light entering the eye.

Further important structures outside of the eyeball include the lacrimal gland and ducts, which act to continually release fluid, tears, to moisten and cleanse the eyes surface.

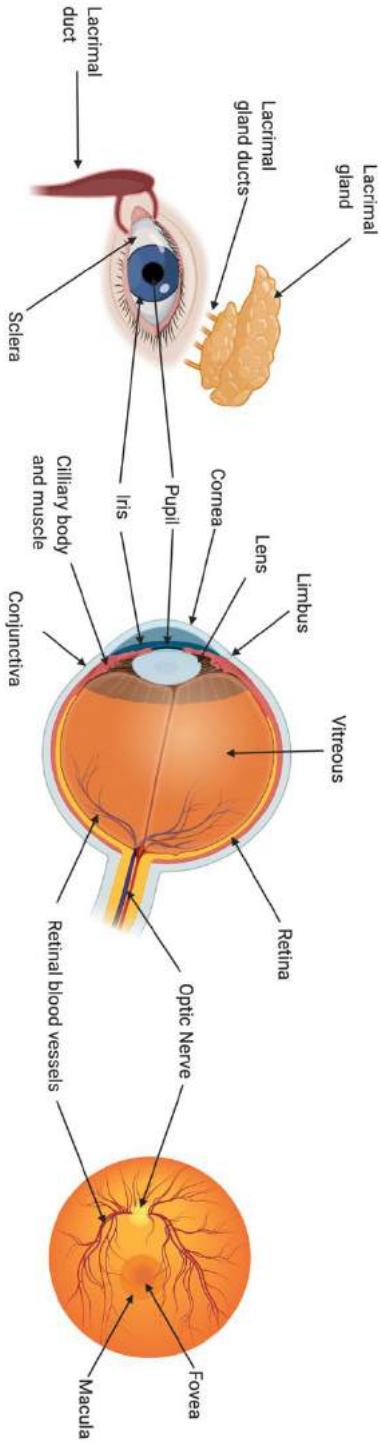

Figure 1.1: The main apparatus of the human eye. Created using BioRender.com

1.1.2 The Cornea: Structure and Function

This work focuses on the cornea, an avascular, transparent tissue on the outermost layer of the eyeball. The cornea is an integral part to the functioning of the eye, as it is the most important refractive layer of the eye, and acts to focus light onto the retina [6]. The cornea can be separated into five main layers; the epithelium, the Bowman's membrane, the stroma, the Descemet's membrane and finally the endothelium, **Figure 1.2**.

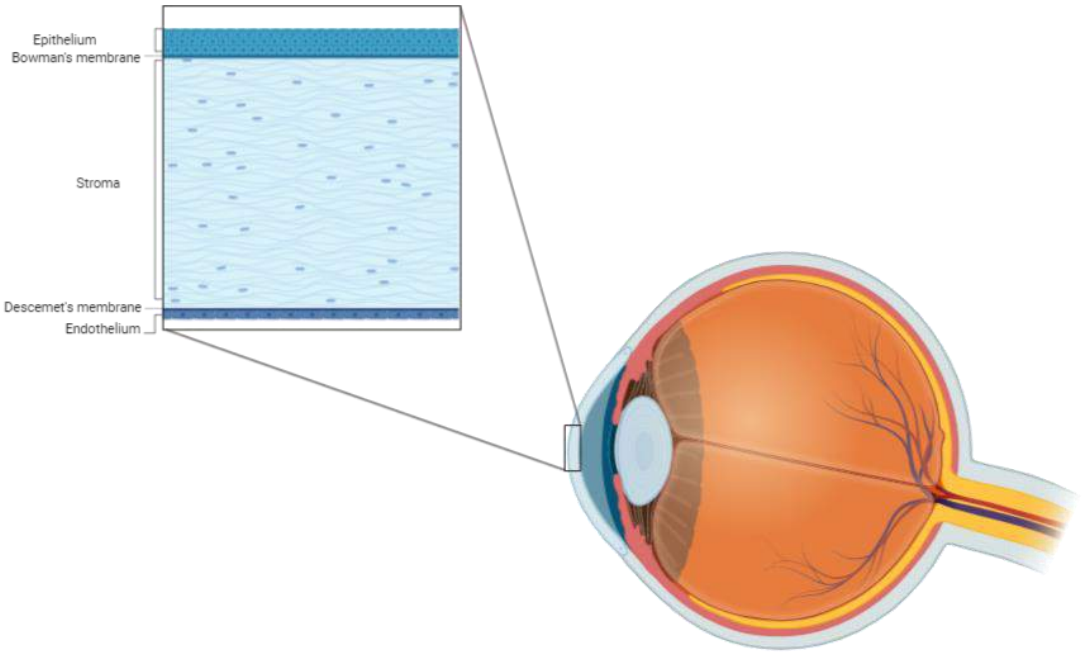

Figure 1.2: The five layers of the cornea, in the anterior segment of the eye. Created using BioRender.com

The epithelium is regenerative and acts as a protective barrier to the outer surface of the eye. The epithelial layer is an integral part of the tear film-cornea interface which is crucial to the refractive power of the eye. The epithelium contributes to transparency by having a smooth surface, tightly packed cells and no blood vessels, which all reduce light scattering when light enters the cornea. It is approximately 50 µm thick made up of 5-7 layers of cells, including a single layer of basal cells and several layers of squamous corneal epithelial cells, **Figure 1.3** [7]. Basal cells are present in the epithelium to anchor this layer to the Bowman's membrane using tight junctions, called hemidesmosomes [8]. The proliferation of these basal cells

further acts to maintain corneal transparency via the continuous renewal of the epithelial layer. The outer epithelial cells interact with and stabilise the tear film through microvilli projections. Tight junctions allow this interaction to act as an effective barrier protecting corneal structures beneath the epithelium.

The Bowman's membrane is a smooth, non-regenerating layer between the epithelium and the stroma. It contains collagen fibrils, of types I, III, V and VI, that are randomly orientated throughout its thickness. Further collagen type IV fibrils are present and act to anchor the Bowman's layer onto the above epithelium. The membrane is approximately 8-12 µm thick, but can thin as a result of age or corneal dystrophies. The functions of the Bowman's layer have not been confirmed, but it is suggested that it is involved in wound healing of the cornea by way of protection. For example, it can prevent the passing of viruses from the epithelium deeper into the cornea [9].

The stroma is composed of proteoglycans within collagen fibrils, mainly types I, V and VI. These fibrils make up approximately 250 layers of lamellae, which constitutes 90 % of the thickness of the cornea. Based on weight, the cornea is approximately made up of 78 % water, 15 % collagen and finally 7 % non-collagenous proteins, proteoglycans and salts [10]. The proteoglycans within this collagen matrix include: decorin, lumican, keratocan and mimecan, which are all rich in the amino acid leucine [11]. These proteoglycans contain both keratan sulphate and dermatan sulphate glycosaminoglycans (GAGs). Studies have shown these proteoglycans to be present in corneal collagen fibrils, which suggests their roles to involve corneal fibril assembly, matrix organization and, as a result, corneal transparency [10, 12]. Due to its unique organisation of the stromal fibres and the extracellular matrix (ECM), the stroma is the only collagenous structure in the body to be transparent. Furthermore, it contains mesenchymal cells, keratocytes, which lay quiescent in between the stromal fibres, but produce opaque scar tissue following trauma or injury [13]. These keratocytes are in very low numbers in the cornea, with a study finding approximately 10,000 cells in a 1 mm^2 area of a full thickness corneal stroma [14].

The Descemet's membrane is a basement membrane that resides between the stromal and endothelial layers. This membrane is laid down by squamous cells within the endothelial layer and is approximately 10 µm thick in adults [15]. The membrane can be separated into two parts, the anterior section, that is banded with type VIII collagen, and the posterior section, which is homogeneous and non-banded [5]. Descemet's membrane contains glycoproteins typical in basement membranes, including laminin and type IV collagen.

Finally, the endothelial layer is made up of a single layer of hexagonal shaped cells and is approximately 5 µm in thickness [16]. At birth, the human corneal endothelium contains approximately 500,000 cells in its monolayer, but this cell density reduces progressively over time [17]. These cells are joined together by focal tight junctions, but no junctions exist between this monolayer and the Descemet's membrane. Studies of the structure of corneal endothelial cells show a band of actin filaments around the circumference. This feature assists in cell migration and maintaining cell shape [18]. The endothelial layer is crucial for maintaining an optimal level of corneal thickness via a "pump-and-leak" mechanism. This mechanism also maintains stromal deturgescence by preventing fluid movement into the cornea, and using an Na^+/K^+/ATPase pump to move ions. It also draws water by osmosis into the aqueous humour from the stromal layer of the cornea [19, 20]. If this mechanism is disturbed, as it is in several corneal dystrophies, the loss of ion transport leads to oedema, which results in loss of corneal transparency.

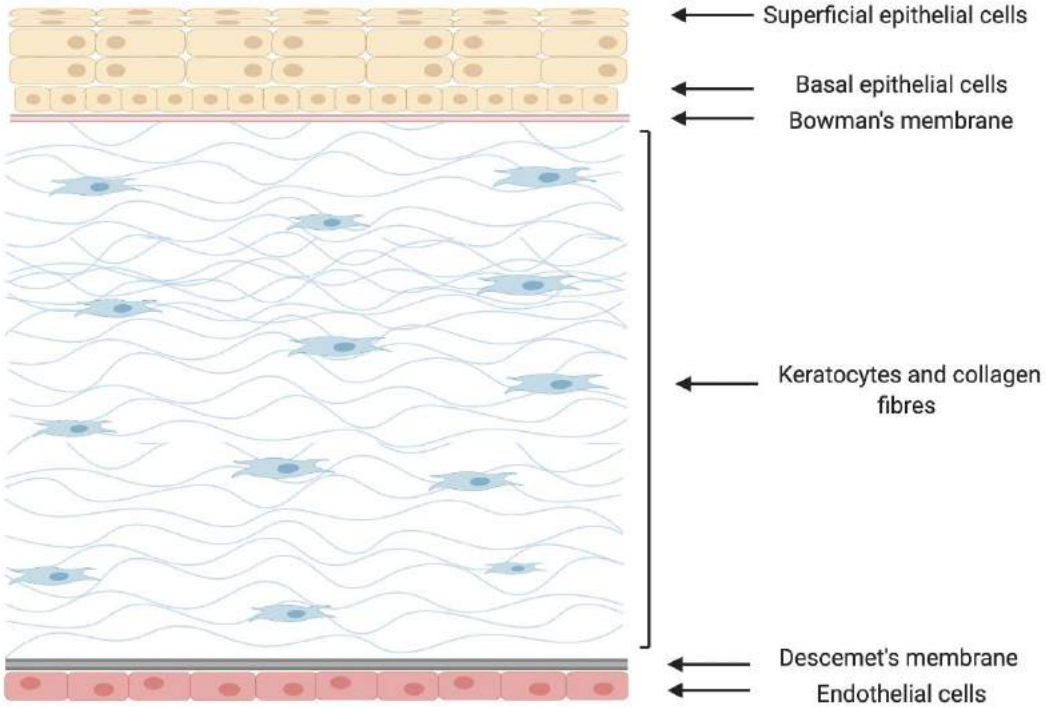

Figure 1.3: The cells of the cornea. Created using BioRender.com

The whole cornea including all of these layers is approximately 550 µm in thickness. It maintains a horizontally oval shape, with a horizontal diameter of 11-12 mm and a vertical diameter of 9-11 mm. The shape and curvature of the cornea is determined by the biomechanical structure and the environment, with an anterior curvature of 7.8mm and a posterior curvature of 6.5mm [7, 21].

The cornea has the overarching function of focusing light onto the retina, by the mechanism of refraction. The cornea contributes approximately 40-44 D of refractive power, which equates to around 70 % of total refraction [21]. The refractive power of the cornea is altered by its transparency, which is governed by the refractive index of the cells in each of the corneal layers. The combination of the tissue strength and the cell activity in the cornea facilitates the protection of ocular structures against disease and foreign organisms. Further protection of the cornea itself is provided by the tear film.

1.1.3 The Limbus

The limbus is located at the front of the eye, and is the border in between the transparent cornea and the opaque sclera [22]. It is often linked with the cornea, as

its stratified epithelium is continuous with the outer corneal epithelial layers. The limbus contains limbal epithelial stem cells (LESCs), which continually maintain the corneal epithelium, in turn facilitating clear vision. Depletion of the LESC population resulting in a deficiency can eventually cause blindness if left untreated. The LESCs are located within 'niches', which are specialised anatomical locations that influence stem cell function via interactions with extracellular matrix components and cell signalling factors [23]. Within the LESC niche, cells are contained withing radially oriented epithelial crypts made up of vascularised papillae, known as the palisades of Vogt [24]. LESCs communicate with their microenvironment via cell signalling pathways, which maintain stem cell renewal and control cell fate. These signalling pathways have been reported to show communication between LESCs and stromal limbal mesenchymal cells, which suggests the involvement of stromal cells in the maintenance of LESCs [25]. The presence of the limbal stem cell niche within the structure of the eye is widely accepted, however its exact 3D structure is disputed.

1.1.4 The Tear Film

The tear film lies directly on top of the cornea, and can be broken down into three distinct layers. The anterior layer contains fatty macromolecules, known as the tear film lipid layer (TFLL), the middle layer is predominantly water, and the posterior layer includes mucus molecules. Each layer provides a different function, with the overarching function of the film being to protect and moisten the surface of the cornea.

The TFLL acts to delay the evaporation of the tears from the ocular surface [26]. This layer is composed of polar lipids, phospholipids, which interact with the aqueous layer, and layers of non-polar lipids which form the outermost section interacting with the external environment [27]. The TFLL further acts to stabilise the tear film, and does this by reducing its surface tension to two-thirds that of water [28].

The aqueous layer makes up the majority of the volume of the tear film, and facilitates oxygen and nutrient delivery to the cornea and the removal of waste. It

contains various peptides, electrolytes and other small molecules, such as lipocalin and lysozyme, which facilitate these functions [29]. Some peptides are antimicrobial, such as defensins, which protect the eye by bursting the cell membranes of foreign microbial cells [26].

Finally, the innermost mucus layer stabilises the tear film and lubricates the cornea beneath it. Mucins present in this layer include both membrane-spanning mucins and secretory mucins [30], and are secreted into the tear film by corneal epithelial cells and goblet cells from the conjunctival epithelium. Membrane-spanning mucins binds with water to form a rigid gel [31], which prevents entry of foreign organisms including bacteria and viruses. Furthermore, some mucins exhibit anti-microbial properties, providing further protection of the cornea.

1.2 Corneal Diseases and Management

Diseases

There are numerous diseases that affect corneal opacity and function and therefore have the ability to disrupt normal vision. Different diseases affect the different layers of the cornea, for instance Fuchs' endothelial corneal dystrophy disrupts the endothelial layer, and limbal stem cell deficiency affects the corneal epithelial layer. The cornea can also be damaged by ocular trauma as a result of thermal and chemical burns.

1.2.1 Fuchs' Dystrophy

Fuchs' Endothelial Corneal Dystrophy (FECD) is a disease of the cornea that affects the endothelial layer. The disease is characterised by endothelial cell loss, focal outgrowths of extracellular matrix - termed guttae, and the thickening of the Descemet's membrane. These characteristics disrupt fluid pump function, reducing the ability of the endothelial layer to perform the 'pump-and-leak' mechanism where fluid is transported in and out of the cornea. This results in stromal oedema, an excess of water in the corneal stroma, which in severe cases can lead to loss of vision.

The disease can be classified as either early onset or late onset. Early onset of the disease is considered to be more severe and is often inherited genetically. This form

of the disease results in a much thicker Descemet's membrane and deeper corneal guttae. Whereas the late onset of the disease exhibits reduced thickening of the Descemet's membrane and more shallow and continuous guttae [32]. More often, FECD presents itself in the late onset form in the 5^{th} to 6^{th} decade of life [33], with early onset of the disease rarely recorded.

Symptoms of FECD at the early stages of the disease may include a decrease in visual acuity, photophobia and the presence of halos in a patient's vision. The oedema of the cornea gradually worsens and increases blurriness of vision over time. Increased oedema results in painful bullae in the epithelial and sub-epithelial layers, which, when untreated, result in subsequent corneal opacification. This process can be provoked by trauma, surgery and eye infections. Several factors have been seen to further encourage disease progression, these include extracellular matrix deposition, RNA toxicity, oxidative stress and apoptosis [34].

FECD can be diagnosed following identification of the markers: presence of guttae, fluid in the corneal stroma and an overall thickening of the cornea. Some methods used to identify these markers include: optical coherence tomography (OCT), slit-lamp bio-microscopy and newer techniques such as Brillouin microscopy [35]. The severity of these markers can then be used to determine the stage of the disease and the suitable course of action.

The epidemiology of FECD shows a large variability in the occurrence of the disease in patients across the world. Studies have shown an increased prevalence in Caucasian females, with higher incidences seen in Europe compared to other areas of the world. Furthermore, a global study performed in 2012 concluded that 39 % of all corneal transplants from 116 countries were used to treat FECD compared to other corneal dystrophies [36], and an American study in 2014 showed that FECD was the most common indication of keratoplasties 22 % [37], indicating a significant prevalence worldwide.

1.2.2 Limbal Stem Cell Deficiency (LSCD)

LSCD is a disorder that affects the corneal epithelium, characterised by the loss of limbal stem cells (LSCs). LSCs reside in the basal epithelial layer of the limbus, and are vital for re-population of the corneal epithelium [38]. When these cells are low in number, the barrier properties of the epithelium are compromised, resulting in an unstable ocular surface. The hallmark of LSCD is the replacement of corneal epithelium with conjunctival epithelial cells. Due to the permeability of the conjunctival epithelium compared to the corneal epithelium, this replacement leads to neovascularisation, epithelial defects, scarring and perforation of the cornea [39, 40]. These characteristics lead to corneal opacity and eventually blindness. LSCD occurs as a result of any process that reduces the number of LSCs, either by congenital LSCD or acquired LSCD. Congenital LSCD may be caused by genetic mutation, aniridia, keratitis, Turner syndrome and congenital epidermal dysplasia [38]. Acquired LSCD is as a result of external factors including ocular burns, contact lens wear and multiple surgeries in the limbal region [39]. Common symptoms of LSCD include eye pain, blurred vision, photophobia, tearing, inflammation, irritation and contact lens intolerance [40, 41]. Eye pain often occurs in recurrent episodes, which is likely due to the breakdown of the epithelial surface layer.

LSCD is a rare disease which has a variability in its occurrence worldwide, largely based on the cause of the deficiency. Chemical injury is the most common cause of LSCD in individual eyes, resulting in 66-75 % of LSCD cases worldwide [42]. In particular, LSCD caused by chemical injury is more prevalent in the developing world due to the poorer working conditions. In the UK, around 240 new cases of LSCD are estimated to be diagnosed each year [43]. LSCD can be treated using a variety of methods based on the stages of the disease. Early stage LSCD can be managed using eye drops, corneal scraping and bandage lenses, however advanced LSCD may need a surgical procedure to regain corneal transparency.

1.2.3 Keratoconus

Keratoconus is an ectatic disorder that causes corneal distending, thinning and fibrosis [44], and results in vision loss. These effects result in the corneal developing into a cone shape, which usually occurs in both eyes. In advanced disease, corneal

scarring can also contribute to further vision loss. This degenerative disorder typically presents itself in early adulthood, with a stable phase being reached after 10-20 years of progression. Without a known cause, keratoconus is likely due to a combination of genetic and environmental factors. However, several disorders have a common association with keratoconus such as myopia, atopy, Down syndrome, eczema and other connective tissue diseases [45].

Keratoconus has a highly variable nature in terms of how it affects the layers of the cornea. Irregularities within the epithelium have been observed in diseased corneas. Some studies report an extreme thinning on the central epithelium, however other contrasting reports have shown a thickening of the corneal epithelium during keratoconus [46, 47]. A large number of studies report that keratoconic corneas have a reduced stromal collagen content, but the distribution and type of collagen is seemingly unaffected [48]. The corneal stroma also experiences a reduction in the density of keratocytes, a corneal cell type which plays a key role in maintaining the transparency of the cornea and the production of collagen in the stroma. Finally, small folds have been observed in the Descemet's membrane but the endothelial layer is typically unaltered.

Similar microscopy techniques for diagnosing FECD can be employed to assess the progression of keratoconus. A system for classifying the various stages of keratoconus has been developed called the Modified Krumeich classification. This system separates the disease into four stages of severity based on corneal scarring, thickness, radii and refraction [49]. The treatment method for disease would vary based on the classification assigned.

The incidence of keratoconus varies across different geographical locations worldwide. It is reported that on average approximately 1 in 2,000 people develop keratoconus, with 7% of these patients having a family history of the disease [50]. Keratoconus can be treated by full or partial thickness corneal transplant surgeries. In the US, from 2008 keratoconus increased significantly as an indication for partial corneal transplantation, and now accounts for one third of lamellar keratoplasty procedures [37]. In the UK, a 2004 study has shown that the Asian population are more likely to develop keratoconus than white Caucasians [51]. The differences in

disease prevalence geographically are likely due to a combination of genetic and environmental factors.

1.2.4 Ocular Trauma

The most common cause of unilateral blindness in children in developing countries is ocular trauma [52]. Furthermore, monocular blindness is very often caused by ocular injuries making up 30-40% of these blindness cases. Ocular trauma can include accidental ocular injury and both thermal and chemical burns.

Full thickness injuries causing damage to the cornea and sclera by blunt trauma are classed as open globe injuries. The severity of the damage is based on the mechanism of injury, which can include: rupture, penetration, perforation and intraocular foreign body (IOFB) [53]. The location of the injury also has a bearing on the ability to regain visual acuity. Small injuries in outer edges of the eye could be treated with stitches, however more central full thickness injuries may require a corneal transplant.

Thermal burns, if severe and left untreated, can result in blindness. Contact between hot water and the eye can result in corneal epithelial cell death, and cause thermal necrosis within deeper corneal tissue layers. If not properly managed, this will lead to infection and inflammation within the cornea. When the inflammatory response is invoked, extracellular matrix fluid will accumulate in the cornea, and further reduce visual acuity [54]. Burns can further affect coagulating tissue proteins and induce ischemic vascular damage. Mild burns can be treated easily, however more severe burns will require a corneal transplant.

Chemical burns make up a larger proportion of ocular trauma as a result of burns, these most often occur in young males as a result of accidents in the workplace. The mechanism by which the corneal tissues are damaged are similar to thermal burns, however different chemicals induce injuries with varying severity. Acidic burns tend to be less severe, as the corneal epithelial layer induces protein coagulation in its responses, which prevents damage to any deeper tissues [55]. However, due to their lipophilic nature, basic chemicals can more easily penetrate deeper tissues in the eye, reaching even the lens and anterior chamber, and are

more likely to have more damaging results. In a similar mechanism, inflammatory cells populate the injury site and produce enzymes such as matrix metalloproteinases, which can cause further damage to ocular tissues. Scar tissue will then form during healing, along with ischemic lesions as a result of damage to vascular tissues [56]. Management of these types of burns again depends on the severity. This can range from taking drugs and eye drops to reduce inflammation in mild cases, to full corneal transplantation in severe cases.

Management

Due to varying pathologies of corneal dystrophies and injury, different management and surgical techniques can be used to regain transparency in the damaged cornea. Transplantation of the cornea, keratoplasty, is the most commonly performed transplant in the world, and has a high success rate [57]. Compared to other tissues, corneal tissue is easier to transport and store, often utilising eye banks to increase availability for transplantation. Keratoplasty procedures have evolved over the years and can now be much more precise in the layers of the cornea in which they target, based on which area of the cornea is damaged.

1.2.6 Penetrating keratoplasty (PK)

Penetrating keratoplasties involve the transplantation of a full-thickness cornea to a patient, which may be required following severe cases of ocular trauma or various different corneal dystrophies. The size of the section removed is dependent upon the area of damage due to varying pathologies, but is often around two thirds of the area of the cornea. During the procedure, all three layers of the patients cornea are removed using the appropriate size of trephine, and the donor cornea of the same size is secured in its place using sutures. Due to the size and thickness of the transplant tissue, graft failure is a common complication [58]. A contributing factor to graft failure is the onset of secondary glaucoma, where glaucoma is induced due to the increase in intraocular pressure (IOP) following the transplant procedure [59]. Due to these incidences of graft failure, a second PK surgery is often required several years after the initial transplant. Despite these disadvantages, PK still remains a largely successful procedure, however, over recent years PK procedures

to initially treat corneal defects have fallen, and have been replaced by partial-thickness transplants.

1.2.7 Deep Anterior Lamellar Keratoplasty (DALK)

DALK transplants are a new partial-thickness alternative to PK surgeries. During this procedure, the top layers of the patient's cornea are removed, leaving the native Descemet's membrane and endothelial layers in place. The stromal and epithelial layers are transplanted using donor tissue. DALK is often performed to repair opacity caused by corneal scarring and keratoconus, provided the endothelial layer is still intact. Tissue rejection of DALK transplants compared to PK is much less due to the reduced amount of foreign tissue being introduced. For this reason, steroids used to prevent rejection can be taken for a shorter amount of time, which reduces the likelihood of the side effects taking place. Due to the regenerative capabilities of the stromal and epithelial layers of the cornea, graft clarity is achieved following transplantation. As a result of these advantages, DALK has been seen in recent years to be increasingly used to treat diseases such as keratoconus in individual treatment centres [60, 61].

1.2.8 Endothelial keratoplasty (EK)

Endothelial keratoplasty is a commonly used partial corneal transplant technique where the endothelial layer of the cornea is replaced following damage as a result of diseases, such as FECD. This can be broken down into two different techniques named Descemet's Stripping Endothelial Keratoplasty (DSEK) and Descemet's Membrane Endothelial Keratoplasty (DMEK). In both cases, the damaged endothelium is removed and replaced with donor tissue. In DSEK, the endothelial layer, Descemet's membrane, and a small section of the stroma is transplanted, whereas in DMEK, only the endothelial layer and Descemet's membrane is transplanted. Finally, an air bubble is inserted into the anterior chamber to hold the implant in place [62]. EK procedures have several advantages over other keratoplasties. Due to the smaller amount of tissue being transplanted, a large surgical wound is avoided [63], which decreases both the healing time following surgery and reduces the likelihood of both tissue rejection and infection. However, complications still occur, including the dislocation of the graft following

transplantation. This would require a second surgery and a 're-bubbling', where another air bubble is inserted to try and re-position the endothelial layer. Furthermore, graft rejection can still occur, which is often due to the quality of the donor tissue or the experience of the surgeon [64]. Due to the high incidence of corneal endothelial diseases such as FECD, EK makes for around half of the corneal transplant procedures performed worldwide.

1.2.9 Cultivated Limbal Epithelial Transplantation (CLET) and Simple Limbal Epithelial Transplantation (SLET)

The ideal treatment of LSCD would restore the population of limbal stem cells in the affected cornea. Cultivated Limbal Epithelial transplantation (CLET) is a surgical intervention involving the external expansion of healthy LSCs, which are then transplanted into the affected eye using a substrate based on human amniotic membrane (hAM) [65]. CLET has an estimated success rate of 76 % [66], when compared to alternative treatment methods, however this is based on the stage of the patient's LSCD and the surgical approach. The LSCs used in CLET surgery can either be autologous or allogenic, with multiple clinical trials comparing the two approaches. Across the trials, no differences were seen in the visual improvement, however, the allogenic groups were shown to result in adverse effects including graft rejection, increased intraocular pressure (IOP) and corneal perforation [43, 67]. These results suggest that using autologous LSCs would be more suitable for the success of the implant, however, due to the relatively recent emergence of this procedure, there is little data showing long term graft survival and cure of LSCD.

Simple Limbal Epithelial Transplantation (SLET) is a similar, but simpler procedure, where a small section of the limbal epithelium is extracted from the patients healthy eye, and is transplanted into the eye affected by LSCD. An amniotic membrane is also used in this surgery to anchor the limbal epithelium. This procedure has shown a high success rate in clinical trials [68, 69] with improved visual acuity achieved in the majority of the patients.

1.2.10 Keratoprosthesis

Following several failed corneal transplants, a keratoprosthesis (artificial cornea), may be used. There are several products available on the market with varying

degrees of success. The most common keratoprosthesis is the Boston keratoprosthesis type 1 (Boston KPro I). The Boston KPro I uses a corneal graft sandwiched between two plates, one made of poly(methyl methacrylate) (PMMA) and back plate made of titanium. This implant is then sutured into the damaged eye similar to donor tissue in a standard PK procedure. The main complications associated with a Boston K-Pro I are infection, tissue necrosis, secondary glaucoma and inflammation [70]. Furthermore, this type of keratoprosthesis does not address the issue of the low availability of donor cornea tissue. Multiple other keratoprosthesis devices have been trialled clinically with limited success, including the AlphaCor, KeraKlear and the Legeais BioKPro-III. These devices resulted in complications such as stromal melts, intraocular deposits and implant extrusion [71-75]. Due to the limited outcomes of these devices, the Boston KPro remains to be the only synthetic artificial cornea that is clinically commissioned by the NHS. Studies have shown an improved visual acuity when this implant is used following failed PK surgery, when compared to a second PK procedure. However, it is rarely chosen as a first option to treat corneal blindness.

Despite being one of the most successful tissue transplant procedures worldwide, keratoplasties still have numerous complications that has pushed research into the development of a suitable alternative.

1.3 Previous Biomaterials for corneal replacement

A biomaterial is defined in the dictionary as a 'biological or a synthetic substance which can be introduced into body tissue as part of an implanted medical device or used to replace an organ or bodily function.' Biomaterials designed for artificial corneas, similarly to surgical replacement, can be separated into partial and full thickness replacements. Numerous materials have been utilised, both natural and synthetic, to attempt to mimic corneal tissue.

A tissue engineered cornea replacement has certain criteria that it must meet in order to be suitable for implantation. This is a complex list of requirements, some of which involves the mechanical properties, transparency, dimensions and curvature closely matching native corneal tissue. Furthermore, it must be

biocompatible, support integration with surrounding tissues, and not induce a chronic foreign body response. If all of these requirements are met, a corneal replacement has a greater chance of surviving implantation, and being used clinically as an alternative to tissue donation. However, due to the complexity of these requirements, few biomaterials can meet them all simultaneously. Therefore, a compromise of these criteria is required, with the potential success of the implant only being clear after long term testing.

1.3.1 Natural materials

Natural materials are classed as any material derived from a plant or animal source, and can be based on proteins, polysaccharides and de-cellularised tissues. Many different natural materials have been trialled for corneal regeneration applications, with some reaching clinical trials and others being used by the NHS clinically. The natural materials discussed in this section include: human amniotic membrane, fibrin, various sources of collagen, methacrylated gelatin (GelMA), silks and acellular tissue.

Amniotic membrane

The human amniotic membrane is used clinically in CLET surgery as mentioned in the previous section. The hAM is used as a carrier vehicle to transplant healthy LSCs into patients that suffer from LSCD. This procedure has a relatively high success rate, of 76 % [66], however, depending on the severity of the case of LSCD some complications do occur. The hAM has been reported to have a low transparency and weak mechanical properties [76-78], which leaves room for a material alternative to be superior over the hAM.

Further trials involving de-cellularised amniotic membrane has been performed both *in vitro* and *in vivo* for epithelial repair in various animal models with a significant success rate [79, 80]. Studies show that a thinner amniotic membrane has a better outcome in terms of maintaining transparency following transplantation and resembling the native corneal epithelium. However, issues arise with variability between donor tissues, which limits the use of amniotic membranes in a clinical setting.

Fibrin

Another example of a natural substrate used clinically is Holoclar, a stem cell (SC) treatment which utilises a fibrin membrane for cell delivery. This SC method has been used to treat patients that have developed LSCD as a result of corneal burns which have damaged the LSC niche reducing the production of limbal stem cells. The procedure involves a small 2x2 mm section of the healthy limbus being removed from the patient's other eye, from which LSCs are extracted, expanded and cultured on a fibrin hydrogel membrane for transplantation [81]. When the cells have become confluent on the membrane, approximately 300,000 – 1.2 million viable autologous corneal epithelial cells are implanted back into the damaged cornea [82]. Holoclar is an example of an advanced therapy known as a tissue engineered product, which has the aim of regaining corneal transparency and maintaining a reservoir of SCs to constantly regenerate the corneal epithelium post-surgery. This is a largely successful procedure, however a common side effect of Holoclar is blepharitis, inflammation of the patient's eyelid post-procedure.

Collagen

Collagen has been heavily investigated for corneal applications due to its biocompatibility, transparency and the high collagen content of the human cornea. Different collagen sources have been used to design both full thickness implants and partial thickness epithelial and endothelial cell delivery devices.

A biosynthetic construct based on collagen has been designed for a corneal stromal replacement. After multiple successful animal studies [83, 84], the biosynthetic construct underwent a phase 1 clinical trial. 10 patients with significant vision loss, primarily due to keratoconus, were treated with the construct. The implants were composed of recombinant human collagen type I cross-linked with 1-ethyl-3-(3-dimethylaminopropyl)carbodiimide (EDCI). These implants were around 500 um thick, similar to that of the native cornea. No cells were incorporated into the structure of the implant, to avoid immune rejection and to encourage the migration of the host cells. 6 months after implantation, visual acuity, ocular surface quality, and corneal sensitivity were seen to improve [85]. After 24 months, the implants became epithelialised, innervated, and populated with the patient's own cells from

all three main corneal cell types [86]. The implant also integrated into host tissue and did not induce an increase in IOP like that seen in donor cornea transplantation. Several of the biosynthetic corneas developed areas of haze and thinning. This could be compensated for by alternative suturing methods to allow for earlier epithelialisation, or implants with a higher tensile strength to reduce the likelihood of implants thinning. This trial was highly successful, but requires further trials with a larger cohort of patients before it can be used clinically.

An alternative collagen based material investigated for mimicking both corneal epithelial and endothelial tissue has been developed by the Daniels Group from University College London. The constructs are termed Real Architecture for 3D Tissues (RAFT) and are based on the plastic compression of type I collagen hydrogels [87]. These tissue equivalents (TE) have been developed to try and replace the use of partial thickness donor tissue replacements to combat corneal diseases such as LSCD and Fuchs Dystrophy. RAFT has been through multiple iterations to produce a construct that is robust for surgical handling and has a simple, fast and reproducible method of manufacture. RAFT TE has been reported to support the culture of human corneal endothelial and limbal epithelial cells *in vitro* [76, 88, 89].

Methacrylated gelatin (GelMA)

Gelatin has been heavily researched as a biomaterial due to its similarities with its parent protein collagen, its biocompatibility and biodegradability and its low cost [90]. Studies have shown that two-photon polymerisation (2PP) techniques can be used to manufacture high resolution GelMA scaffolds which mimic the limbal epithelial microniches [91]. Cell proliferation throughout the microniche was observed when human limbal epithelial stem cells (hLESCs) were seeded into the construct, with differentiated cells present in the base of the crypt and limbal progenitor cells at the edge. This study demonstrated that GelMA was a suitable material for mimicking the complex architecture of the limbal epithelium and that the constructs manufactured supported and controlled the growth of hLESCs.

For endothelial repair after diseases such as Fuchs dystrophy, a layer of endothelial cells would aid in restarting the ion exchange mechanism to regain corneal transparency. Several substrates have been trialled for an endothelial cell delivery device both *in vitro* and *in vivo*, including a substrate based on GelMA. This material was populated with a monolayer of human corneal endothelial cells (HCECs) and evaluated for its suitability for transplantation. Minimal damage to cells was seen when the substrate was implanted *in vivo* in rabbits, using a clinical corneal endothelial transplantation device [92]. This cell delivery method is well studied for endothelial and epithelial regeneration, and presents a viable potential alternative to partial donor cornea transplantation methods such as DMEK and DALK.

Silk

Biomaterials based on silk proteins have been widely researched for corneal tissue engineering due to their biocompatibility and desirable optical and mechanical properties. An *in vitro* study used human corneal fibroblasts (hCFs) and human corneal stromal stem cells (hCSSCs) to demonstrate the suitability of silk for a corneal stromal application [93]. The 3D substrates were seen to facilitate ECM production from hCSSCs compared to a 2D substrate, and a high cell viability was seen from both cell types over 9 weeks.

Further studies has shown that silk fibroin can be manufactured into membranes, which support the culture of corneal epithelial cells *in vitro* [94]. However, when cell viability was analysed, it was seen that fewer corneal epithelial cells adhered to the silk fibroin constructs when compared with the human amniotic membrane [95]. This suggests that silk fibroin based materials lack the appropriate number of cell binding sites, therefore may require additional modification to be suitable for corneal substrates.

Acellular tissues

Acellular porcine corneal tissue has also been trialled *in vitro* and *in vivo* for stromal regeneration. To achieve a porosity throughout the structure, acellular porcine corneal stroma (APCS) was freeze dried, and keratocytes seeded within the structure [96]. These maintained a high cell viability *in vitro*. Freeze-dried APCS

substrates were implanted *in vivo* in rabbits and demonstrated a transparency similar to that of the native cornea.

An *in vivo* study using de-cellularised porcine corneal matrix combined with human corneal cells demonstrated suitability for a full thickness corneal substitute [97]. Following de-cellularisation, the anterior acellular porcine corneal matrix (AAPCM) tissue constructs were re-populated with human keratocytes, epithelial cells, and hESC-derived CEC-like cells. Each of the cell types expressed proteins as they would in the native cornea, indicating normal cellular function. Keratocytes expressed vimentin, epithelial cells expressed cytokeratin-3 and endothelial cells formed a distinct layer which contained Na^+/ K^+/ATPase. A construct containing no cells induced no immune rejection when implanted, however the construct containing all three cell types initiated an immune response upon transplantation. This may be due to the genetic differences between the human cells and the rabbits used in the model. Despite this result, the behaviour of the human cells in the construct demonstrate its suitability for a 3D cell model of the cornea, but more investigation needs to be done in order for it to be suitable for transplantation.

Natural materials have numerous desirable properties that allow them to act as potential alternatives for corneal regeneration or replacement. Certain implants based on natural materials have made it through to the clinic, whereas others are still in early stage *in vitro* an *in vivo* testing. De-cellularised tissue implants perform well in pre-clinical trials due to their resemblance to native tissue, however face issues with rejection. Implants based on natural polymers have had similar success in ocular reconstruction due to their biocompatibility and transparency, but can be difficult to manufacture reproducibly due to their batch-to-batch variability. The limitations of current clinical techniques encourages researchers to continue to investigate alternative materials for corneal tissue engineering.

1.3.2 Synthetic materials

Synthetic materials include any materials not made from a natural source, and can be classed as metals, ceramics, polymers and composites. The use of synthetic polymers for corneal tissue engineering has been evaluated due to their tuneable mechanical properties and ease of manufacture. The materials discussed in the section include PLGA, PEG, PNIPAm and various synthetic composites including PAA, PEG, PVA and PCL.

PLGA

The use of synthetic polymers in epithelial cell sheet delivery began with those often used in contact lenses. However, these required additional surface treatments to encourage epithelial cell attachment and expansion. Poly(D,L-lactide-co-glycolide) (PLGA) is an example of a synthetic polymer investigated for the expansion of cells for corneal epithelial regeneration. This polymer can be manufactured into sheets using an electrospinning technique, which have shown handleable mechanical properties, suitable degradation properties, and cyto-compatibility with rabbit corneal epithelial cells *in vitro* [98]. Further studies showed that electrospun PLGA membranes supported the culture and expansion of limbal epithelial cells (LECs) in an *ex vivo* model [99, 100]. More recent clinical trials have shown the implantation of electrospun PLGA membranes into 5 patients to treat LSCD [101]. In all patients, the PLGA membranes has completely degraded after 8 weeks with no inflammation or infection. After 1 year, three in five patients showed a clear ocular surface with no epithelial defects. However, the surgeons remarked that the membranes were brittle and difficult to handle compared to human amniotic membrane. This finding suggests further research is required to optimise PLGA membranes for clinical use.

PEG

An alternative synthetic polymer, poly(ethylene glycol) (PEG), has been manufactured into hydrogel substrates and been trialled for tissue engineering applications based on its low toxicity and high water solubility. Furthermore PEG demonstrated hydrophilic properties, good biocompatibility, adjustable mechanical properties and is capable of photo-polymerisation [102]. A study based on corneal endothelial tissue engineering, showed that PEG hydrogels supported the growth of

a monolayer of sheep CECs *in vitro* and did not induce any toxicity when implanted *in vivo* [103]. Furthermore, polyethylene glycol diacrylate (PEGDA) has been used to manufacture structures to replicate the human corneal limbus using micro-stereolithography. When treated with fibronectin, the printed PEGDA structure was shown to support the attachment of rabbit limbal fibroblasts and rabbit limbal epithelial cells [104]. When used in an *ex vivo* model, cell outgrowth occurred on the PEGDA construct and resulted in the formation of a multi-layered epithelium. Studies have shown the suitability of PEG of ophthalmic applications, however they have not yet made it into clinical trials.

Thermo-responsive PNIPAm

An alternative synthetic polymer with desirable properties for an epithelial cell delivery device includes poly(N-isopropylacrylamide) (PNIPAm). PNIPAm is an example of a thermo-responsive polymer, which changes from water soluble and hydrophilic at low temperatures, to insoluble and hydrophobic at high temperatures. This property allows PNIPAm to retrieve cells when soluble, for them to then detach following a temperature change. Both *in vitro* and *ex vivo* studies have shown the suitability of this material for the expansion of corneal cells [105] and the transplantation of the device onto the corneal stroma [106]. The regeneration of damaged corneal endothelium utilises a similar cell delivery approach. Thermo-responsive polymer films can also be utilised for the expansion and delivery of corneal endothelial cells. An alternative study of PNIPAm demonstrated that poly(Nisopropylacrylamide-co-glycidylmethacrylate) (P(NIPAM-co-GMA)) was able to culture CECs and transfer them as an intact cell sheet [107]. PNIPAm demonstrates properties that would be ideal in a cell delivery device to treat corneal epithelial and endothelial disorders, however they are yet to reach pre-clinical studies in this application.

Composites

PEG and PAA

An alternative synthetic replacement based on an interpenetrating polymer network (IPN) of poly(ethylene glycol) (PEG) and poly(acrylic acid) (PAA) has been evaluated by multiple groups *in vivo.* The combination of these two polymers improves the mechanical properties compared to each polymer individually,

allowing the construct to mimic properties of the native cornea. When fabricated as a porous hydrogel, the PEG/PAA material, modified with ECM proteins, supported the adhesion and proliferation of corneal fibroblasts [108]. When analysed *in vivo* in a rabbit model, the PEG/PAA IPNs showed good biocompatibility over 6 months of implantation [109, 110].

PVA/PCL

Several alternatives to full thickness corneal replacements have been designed based on combinations of synthetic materials. Many artificial corneas have used a core-skirt structure to utilise different materials for different areas of the implant. The 'core' is the centre of the implant with the function of restoring transparency, and the 'skirt' surrounds the core and allows for better anchorage and tissue integration upon transplantation. *In vitro* studies have been carried out on various combinations of materials using this core-skirt design. A PVA hydrogel surrounded by PCL nano-fibres has been studied for its suitability for replacing a penetrating keratoplasty [111]. SEM analysis demonstrated the nanofibrous PCL structure contained pores that would facilitate bio-integration into the host tissue. The mechanical and optical properties of both the cornea and the skirt were similar to that of the native cornea. When cell studies were performed, plasma treated PCL fibres where shown to support limbal stem cell adhesion and proliferation. Further *in vitro* and *in vivo* studies would need to be performed on this device to more accurately determine its suitability.

Synthetic materials have been extensively reviewed for their use in corneal replacement, and have numerous advantages over natural materials. These include their versatility in manufacture, mechanical properties, and control over physical properties such as water content and degradation. The reproducibility of synthetic materials allows them to be suitable for multiple different manufacture methods, including casting, electrospinning and additive manufacturing techniques. This allows for the controlled manufacture of various different structures including fibres, mats, hydrogels and sponges. The mechanical properties of synthetic materials have also been shown to be more consistent than those of natural origin. Furthermore, the physical properties of synthetic materials can be fine-tuned to

meet specific criteria, such as adjusting the percentage cross-linking of synthetic hydrogels to tailor the water content of the substrate. Additionally, the molecular weight of synthetic polymers can be used to control the degradation and mechanical properties. Despite these advantages, synthetic materials often have fewer cell binding sites, and therefore a lower biocompatibility when compared with natural materials. For this reason, certain materials may need to undergo surface treatments in order to enhance their biocompatibility, which may compromise the materials inherent properties.

Biomaterials and tissue engineering research has developed many different devices with the aim of replacing traditional corneal transplantation methods. These have had varying success, with very few reaching stages of clinical trials. This gap in the field opens up opportunities for more research into suitable alternatives, based on both natural and synthetic materials. An ideal material would be a compromise between the properties of both natural and synthetic materials. For instance a material that is naturally based with a high biocompatibility, but able to be manufactured reproducibly with desirable mechanical properties.

1.4 Hydrogels as Biomaterials

1.4.1 Definition

A hydrogel is defined as a water-swollen network of cross-linked polymer chains. The polymers on which they are based can be either natural or synthetic, for example; collagen, alginate, polyethylene glycol (PEG) and poly(vinyl alcohol) (PVA).

Cross-linking of polymer chains stabilises the polymer and converts it from a liquid into a gel by restricting the movement of the chains [112]. Cross-linking polymer chains can alter the elasticity, viscosity and solubility of the polymer. Different cross-linking mechanisms are utilised in the production of hydrogels. Physical cross-linking is induced by ionic interaction, the formation of hydrogen bonds, crystallisation and stereo complex formation. Chemical cross-linking of hydrogels can be achieved by addition and condensation polymerisation and gamma and electron beam polymerisation, **Figure 1.4**. The polymerisation time of hydrogels can be modified depending on the application, for example hydrogels made in situ in the body may need to gel instantaneously. In these cases, stimuli-responsive

hydrogels can be utilised, where cross-linking occurs in response to a change in environment, such as temperature or pH.

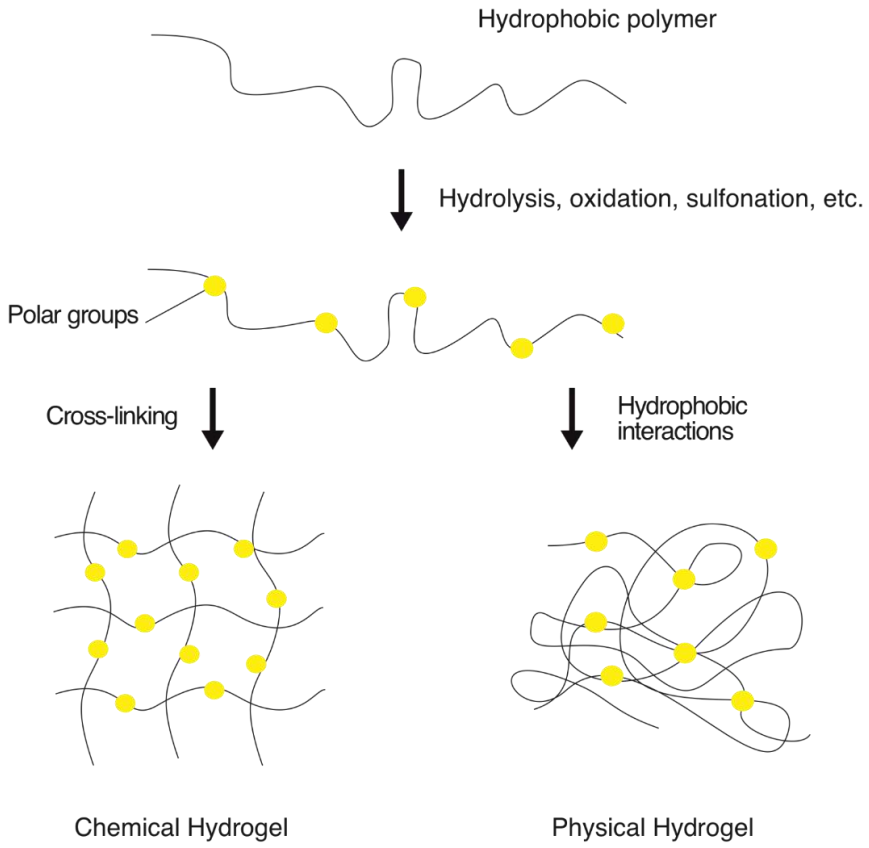

Figure 1.4: Different types of hydrogels depending on the cross-linking mechanism

Hydrogels can be made suitable for a wide range of biomaterial applications, due to the versatility of their properties [113]. The polymer network allows them to swell and absorb water, which mimics characteristics typical of soft tissue. Certain polymers can form highly transparent hydrogels which are suitable for ocular applications. A high strength in compression allows them to be able to withstand high load in cartilage applications. Free polymer side groups incorporated in the hydrogel network allows for the further addition of biomolecules, which can increase the biocompatibility of gels. Furthermore, hydrogels can be made to be injectable, which indicates a potential use as a carrier vehicle in drug delivery. This extensive versatility allows hydrogels to act as a large library of materials that can be individually tailored to suit specific applications.

1.4.2 Examples of hydrogels for various Biomaterial applications

Depending on their application, hydrogels can be based on different types of polymers. Soft tissues require weaker hydrogels that mimic ECM properties, whereas hard tissues, such as bone, require tougher hydrogels.

Alginate is a naturally occurring bio-polymer which has been extensively researched for biomaterial applications. It is a negatively charged polymer, and can form hydrogels by the addition of divalent cations, such as Ca^{2+} [114]. This forms a soft hydrogel which is capable of mimicking ECM in tissue engineering applications, such as wound dressings and scaffolds for cell delivery. The hydrophilic polymer network in alginate hydrogels allow it to absorb wound tissue fluid, which makes it suitable for wound healing applications. Both *in vitro* and *in vivo* studies have shown that hydrogels based on alginate, and other polysaccharide hydrogels, can improve wound healing [115]. An *in vivo* study with mice showed Capgel™ treated wounds had less wound contracture, a higher volume of granulation tissue and a higher degree of neovascularisation [116], all factors indicative of successful wound healing. Several wound dressings based on alginate are available commercially, including Algicell™ and AlgiSite M™ [114]. Alginate is also highly biocompatible and has versatile mechanical properties which can be adjusted to suit scaffolds for tissue regeneration in multiple locations in the body. Hydrogel scaffolds based on alginate cross-linked with cationic polymers have shown to enhance axon growth and cell adhesion, *in vitro*, when tested for a spinal cord application [117]. These scaffolds were also capable of delivering growth factors such as epidermal growth factor (EGF) and basic fibroblast growth factor (bFGF). Furthermore, alginate's injectability, long-term stability and stiffness has found an application in cartilage tissue engineering due to its ability to withstand load. When combined with hyaluronic acid, alginate composite hydrogels were found to sustain high compressive loads, even after immersion in cell culture media, and also supported the encapsulation of human MSCs [118].

Hydrogels based on synthetic polymers include poly(2-hydroxyethyl methacrylate), (pHEMA), which is classes as a methacrylate with hydrophilic substituent groups. pHEMA has been evaluated for use in biomedical applications such as contact

lenses, drug delivery and scaffolds for tissue engineering. Similar to other hydrogels, it has versatile mechanical properties, a high water content and is deemed biocompatible when tested *in vivo*. A study combining pHEMA with PCL produced composite hydrogels which were found to be suitable for scaffolds for cardiac tissue engineering. These hydrogels exhibited favourable mechanical properties and degradation times and showed no cytotoxicity towards fibroblasts in an MTT assay [119]. Further in vitro studies have found this versatile hydrogel to have advantageous properties for both bone [120] and ocular [121] tissue engineering. pHEMA hydrogels were selected for use in contact lenses due to their favourable mechanical and optical properties [122]. More recent studies have worked to optimise the anti-fouling surface properties of pHEMA to improve their functionality in a contact lens. It was shown that attaching positively charged amine and ammonium groups to the pHEMA surface reduced the amount of protein adsorption and bacterial deposition, but did not affect cytotoxicity of the product [123]. A disadvantage of pHEMA is its insufficient biodegradability, which limits its applications for scaffolds for tissue regeneration. This can be overcome by modification into a composite hydrogel to improve the degradation.

Both natural and synthetic hydrogels have their own advantages and disadvantages. Examples from both of these categories can be tailored to suit specific applications. Often, composite materials are made with both of these hydrogel types to benefit from the advantages of both. However, some polymers can behave in ways that mimic both natural and synthetic materials.

A final category of hydrogels includes those based on peptides, which have recently emerged into the field of tissue engineering. Peptide-based hydrogels have demonstrated desirable material properties, a high porosity, and versatility in their fabrication methods and can be manufactured to replicate the structure of the extracellular matrix (ECM) [124, 125]. Furthermore, additional peptides can be bound to these hydrogel chains due to the abundance of amine and carboxyl functional groups. This feature allows for peptide hydrogels to be suitable for biomedical applications, as they can be further tuned to enhance cell adhesion with the addition of arginylglycylaspartic acid (RGD) sequence and laminins [126].

Peptides act as molecular building blocks, which can be used to build up a biocompatible material which is easily synthesized.

1.4.3 Poly-ε-lysine hydrogels as biomaterials

Poly-ε-lysine (pεK) is a naturally occurring homo-poly-amide of L-lysine with water soluble, non-toxic, biodegradable and thermostable properties [127]. It is currently used as both an emulsifier and a preservative agent in food products, and has been classified as 'generally regarded as safe' by the FDA. The free amine groups on the backbone of pεK allow for the formation of amide bonds when combined with carboxyl groups. For example, a bis-carboxylic acid such as octanedioic acid can be used to cross-link pεK to form a stable hydrogel, **Figure 1.5**. This cross-linking mechanism is based on carbodiimide chemistry, and uses the activators N-hydroxysuccinimide (NHS) and 1-(3-Dimethylaminopropyl)-3-ethylcarbodiimide HCl (EDCI), **Figure 1.6**. Carbodiimide conjugation activates the carboxyl groups, on compounds such as carboxylic acids, for direct reaction with an amine group. EDCI is a water soluble, readily available carbodiimide for aqueous cross-linking, and can act alone or with NHS. NHS improves the efficiency of activating carboxyl groups by providing amine-reactive intermediates. This coupling mechanism has been widely used throughout polymer chemistry.

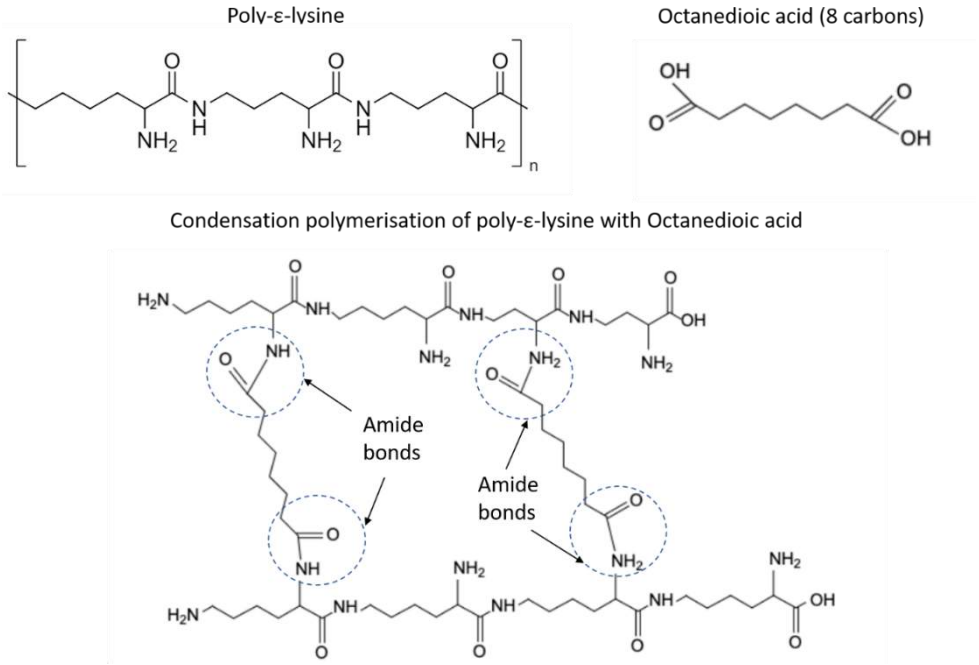

Figure 1.5: The structure of both poly-ε-lysine and octanedioic acid and the proposed polymerization mechanism

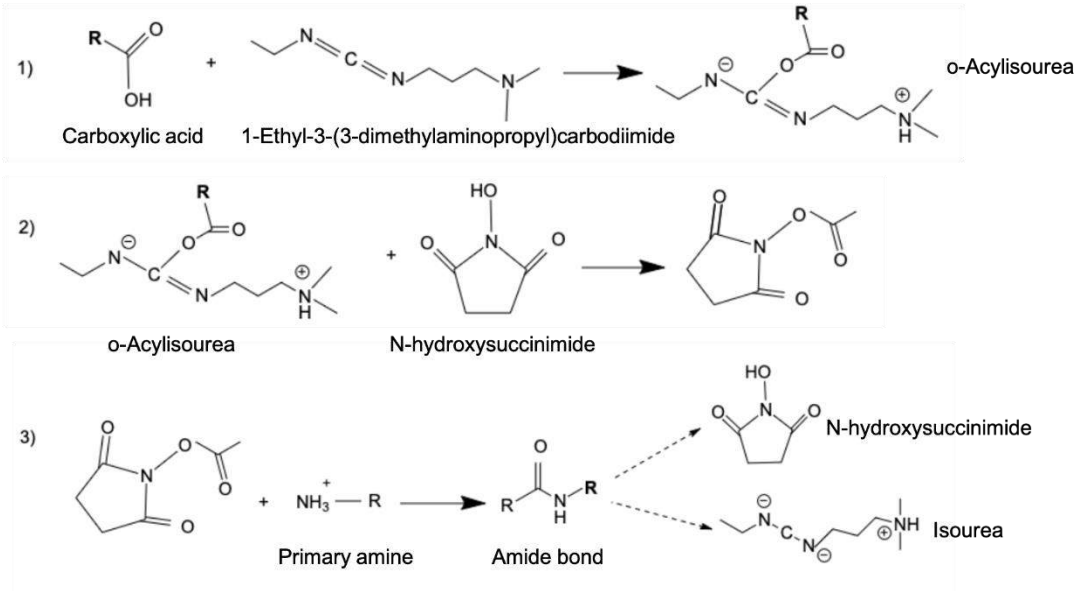

Figure 1.6: The proposed mechanism for the cross-linking of poly-ε-lysine with a carboxylic acid using NHS and EDCI as activators

The cross-linking of pεK with bis-carboxylic acids forms a stable hydrogel. The resulting gels have a high water content and transparency, tuneable mechanical properties and the polymer backbone can be utilised for the attachment of biomolecules. The mechanical and optical properties of the hydrogel can be altered by changing the density of the polymer, the percentage cross-linking, and the acid chain length. Due to the versatility of the optical and mechanical properties of these hydrogels, they have been evaluated by our group for various biomaterial applications.

Porous hydrogel scaffolds based on pεK can be manufactured and tailored to suit different tissue engineering needs. The pore structure, volume and dimensions can be tightly controlled, to fit different applications. These porous gels can be cast into various shapes, such as monoliths, tubes and sheets. For a kidney regeneration application, the porous hydrogel could act as a scaffold to regenerate kidney tissue *in vitro* using stem cells. When evaluated, the pεK hydrogel scaffold supported the attachment and proliferation of a human embryonic kidney cell line (HEK293Ts). The pεK scaffolds can be cast into tubes to assist in nerve regeneration following

injury. When Schwann cells were seeded onto the porous construct, an Alamar Blue assay indicated cell proliferation across several time points [128].

A synthetic corneal bandage was developed based on a hydrogel based on pεK, cross-linked with a bis-carboxylic acid, mediated by an N-hydroxysuccinimide (NHS)/1-(3-Dimethylaminopropyl)-3-ethylcarbodiimide HCl (EDCI) cross-linking technique. The natural antimicrobial properties of pεK hydrogels allow them to be a suitable material for use in treating fungal infections, such as fungal keratitis. When additional pendant pεK is bound using the free amine groups on the polymer chains, the antimicrobial activity and mechanical properties of the hydrogel can be further improved. Cyto-compatibility testing with a human corneal epithelial cell line (HCE-Ts) showed the hydrogel material did not induce any toxicity in the cells [129]. In both a cytotoxicity and a scratch assay, the hydrogels did not have any adverse effects on the cell line. Finally, the presence of the hydrogels interfered with the biofilm formation of *Staphylococcus aureus* bacteria, demonstrating its capability for antimicrobial bandage contact lenses [130].

Hydrogels manufactured using this same cross-linking mechanism with octanedioic acid have been evaluated for their potential use in corneal endothelial cell expansion for transplantation. In this application, the hydrogel acted as a carrier vehicle to allow for the attachment and expansion of both a human corneal endothelial cell line (HCEC-12) and primary porcine corneal endothelial cells (pCEC). This would be useful in increasing the number of recipients that could be treated by a single donor, as the current treatment option for corneal endothelial dystrophies is a 1:1 donor to patient ratio. The hydrogels evaluated were mechanically tough and easy to handle, ensuring their ability to withstand manipulation during DSAEK surgery. Cell evaluations showed that the HCEC-12s adhered and remained attached to the gels, and pre-adsorbing biomolecules to the hydrogels improved the adherence of pCECs [131].

pεK has alternative properties that allow for the formation of hydrogels using other cross-linking mechanisms. The amine groups on the pεK backbone are positively charged, which enables them to form ionic bonds with negatively charged polymers. This mechanism could form a physical hydrogel based on differences in

electrostatic charge. Negatively charged polymers that could be coupled with pεK to form a hydrogel include; alginate, gellan gum, pectin and carrageenan [132]. A suggested mechanism for the ionic cross-linking of pεK with gellan gum is shown in **Figure 1.7**. Ionic bonds will form between the positive NH_3^+ and the negative COO^- groups on the polymer chains. This reaction occurs immediately when the two polymers are combined.

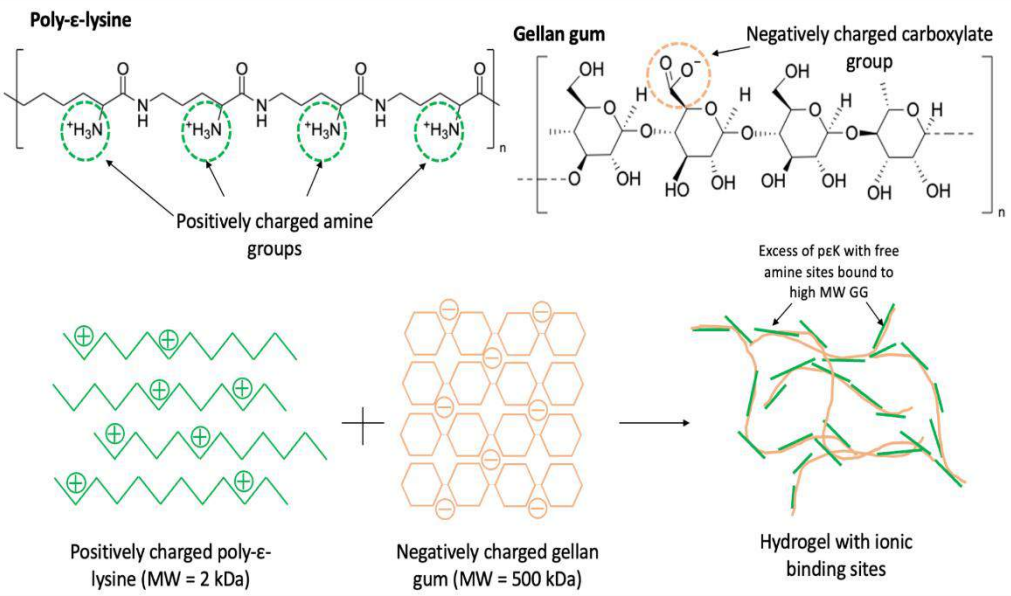

Figure 1.7: The proposed mechanism for the ionic cross-linking of poly-ε-lysine with gellan gum.

Gellan gum (GG) was selected to be paired up with pεK based on its negative charge, and therefore could be used to form a hydrogel based on ionic bonding. GG is a natural polysaccharide, and is often used as a plant based alternative to gelatin, boasting similar properties [133]. Furthermore, GG demonstrates a high melting point, transparency, biocompatibility and a strong gelling ability [133, 134] and has also been researched for tissue engineering applications, including wound dressings and cartilage repair [135-137]. Ionic bonds will form between the positive NH_3^+ on the pεK and the negative COO^- groups on the GG chains. The electrostatic interaction occurs immediately when the two polymers are combined. The combination of these two polymers for use in RIJ was investigated.

The increased speed of the reaction compared to using cross-linking with carbodiimide chemistry allows pεK to be suitable for a wider variety of manufacturing techniques. The hydrogels produced, even though a composite, would still maintain the desirable biocompatibility of pεK hydrogels. This increases the versatility of the polymer and its applications in biomaterials for tissue engineering.

1.5 Additive Manufacturing

Additive manufacturing (AM) is a branch of industrial techniques where 3D parts are constructed layer by layer. These techniques are commonly used in electronic, automotive and aeronautic industries. Due to the high resolution, low cost and ability to produce unique tailored parts, AM techniques have emerged into the field of manufacture of medical devices and tissue engineering.

1.5.1 Types of Additive Manufacturing

Extrusion printing

Extrusion 3D printing is a technique where material constructs are produced from extruding inks through a nozzle onto a substrate. The substrate is mounted on a stage which can move in the x,y and z directions to direct the flow of the extruded material. This is done continuously, building up a construct layer by layer, **Figure 1.8**. This is usually done using heat to melt the material, which then fuses each consecutive layer together upon solidification. This printing process can be achieved quickly and is much less wasteful of materials than other printing methods [138]. Extrusion printing can also be called fused deposition modelling (FDM). A resolution of 100-150 μm can be achieved using this method [139].

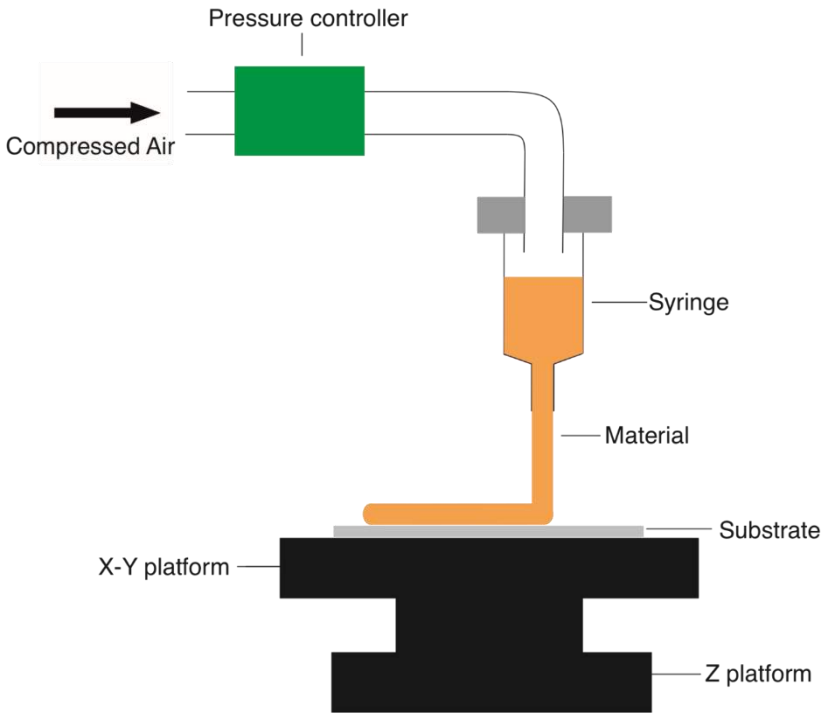

Figure 1.8: Schematic for a standard extrusion printer

This type of 3D printing is simple, and can be applied across various sectors including industry, aeronautics and medicine. Advantages of this technique include precise printing of constructs based on a computer aided design (CAD) model, scalability, ease of use and multiple solidification methods [140]. However, the resolution of the print is difficult to control and high detail parts will require lots of processing post-printing.

Stereolithography

Stereolithography (SLA) is a form of 3D printing where photo-sensitive liquid resin is converted into a solid polymer part by photo-polymerisation, **Figure 1.9**. This technique uses a laser to selectively solidify and cure the resin one layer at a time, and build up into a 3D part. The curing of the polymer occurs due to the decomposition of a photo-initiator into reactive species, either free radicals or a Bronsted or Lewis acid, when exposed to visible light sources. Acrylate or styrene based resins require free radical photo-initiators, and epoxy resins require cationic photo-initiators. SLA is the most accurate of the additive manufacturing techniques, and can achieve a resolution of up to 20 µm, compared to 50-200 µm resolution for other techniques [141].

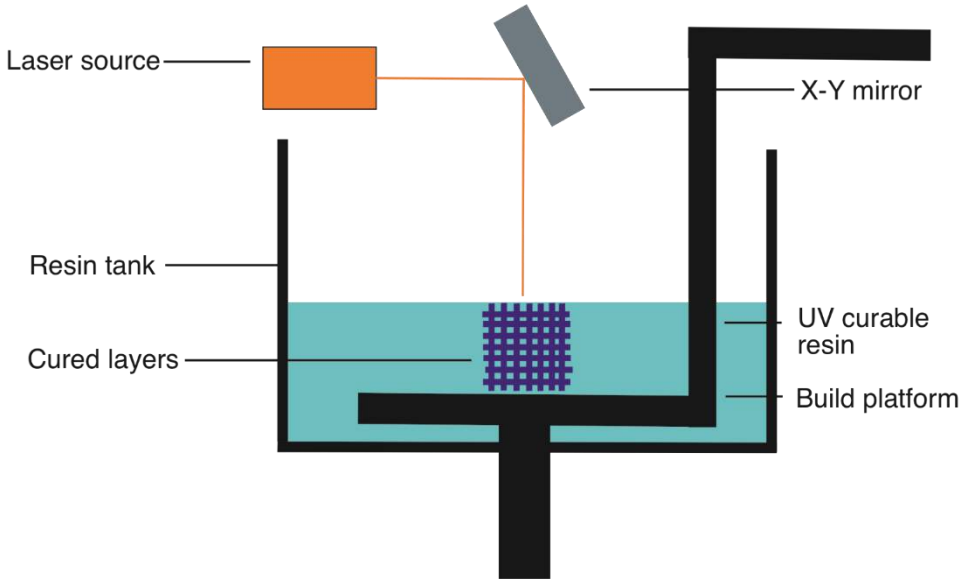

Figure 1.9: Schematic for the basis of stereolithography 3D printing

This is one of the most common forms of 3D printing used in various applications, for example medical models, prototypes for product design and computer hardware. SLA has numerous advantages; it is fast, and can precisely produce complex designs with a high quality and smooth finish [142]. However, the inks required for SLA printing must be photo-curable, which limits the variety of materials that can be used. A limitation of SLA for a biomedical application is that the environment required to print photo-active polymers requires the use of solvents, which can be toxic to cells. Furthermore, the UV light can damage the cells during the curing process, so cells are more often seeded into the structure after the construct is printed.

Inkjet printing

Inkjet 3D printing is an additive manufacturing technique where 3D structures can be built up by the precise dispensing of ink droplets onto a substrate, **Figure 1.10**. The structure produced is based on a computer model, which controls the speed of the print head, the space between droplets and the overall shape produced.

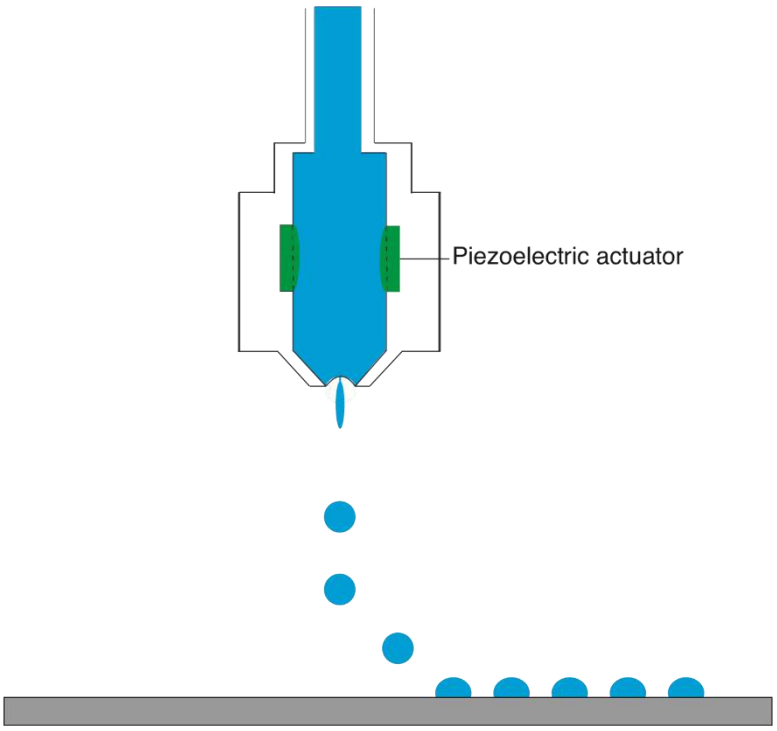

Figure 1.10: Schematic for the principles of operation of a piezoelectric DOD inkjet 3D printer

Inkjet printing can be separated into two groups; continuous inkjet (CIJ) and drop-on-demand inkjet (DOD) [143]. In CIJ, a pump directs ink from a reservoir through a microscopic nozzle, dispensing a continuous stream of droplets. DOD printers use either thermal or piezoelectric actuation to generate a pressure pulse in the fluid ink cavity, which dispenses a droplet. The dispensed droplets undergo solidification through either solvent evaporation, a temperature change, or through a chemical reaction [144]. Inkjet printing technologies have several advantages over other 3D printing methods, such as solution processability and a high accuracy and resolution in the micron range when depositing droplets [145].

The solidification of an inkjet printed deposit through chemical reaction can also be defined as reactive inkjet printing (RIJ). This usually requires at least two printer heads to dispense alternative inks, that when printed together, will react to form a solid. This process can be utilised in the 3D printing of hydrogels, but has the requirements that the gelation must be immediate, and ink droplets must maintain a stable 3D structure [146].

Each of these common types of 3D printing have their advantages and disadvantages. Extrusion printing has a lower resolution than other methods, stereolithography techniques can be expensive and inkjet printing has strict limits on the rheological properties of the inks it can use. Therefore the most suitable printing method should be determined based on the material being printed, and the application the printed deposit is for.

1.5.2 Additive Manufacturing for Tissue Engineering applications

Additive manufacturing techniques have been utilise to evaluate printed constructs for a variety of tissue engineering (TE) applications, such as; adipose, bone, nerve and cartilage tissue engineering.

Extrusion based printers have been thoroughly evaluated in the development of biomaterials for TE applications. Extruded materials for TE applications should have several key properties, such as; biocompatibility, minimal batch-to-batch variation and scalability and must form self-supporting scaffolds [147]. Based on these criteria, a wide variety of materials can be extruded, with thermoplastics being popular across multiple applications. A study found extrusion printing was suitable for producing electroactive scaffolds based on poly(caprolactone) and polyaniline (PCL/PANI) composites for bone TE [148]. In this method, conductive PANI was ball milled into a suitable size, and melt-blended with PCL. The constructs produced supported the growth and proliferation of human adipose derived stem cells (hADSCs). AM technologies suit applications in bone tissue engineering due to the ability to base printed constructs on a CAD model, and the capability of including growth factors and cells [149]. Another study used FDM to print TE constructs for bone regeneration based on poly(vinyl alcohol)/ β-tricalcium phosphate. The scaffolds produced had an interconnected porosity, suitable load bearing capabilities and did not induce cytotoxicity on a fibroblast cell line [150].

The detailed structures produced by SLA printing methods make them suitable for the production of intricate porous scaffolds for TE applications. Biocompatible polymers can be modified to include photo-polymerisable functional group through

chemical conjugations. These need to be carefully selected to ensure the toxicity of the constructs is not compromised. A photo-cross-linkable material GelMA, has been extensively studied for its use in the SLA printing of TE constructs. Physically cross-linked GelMA is stabilised by free radical initiated photo-crosslinking, which allows it to withstand human body temperature [151]. A study by Elomaa *et al* found when GelMA is combined with methacrylated PCL (PCL-MA) it can be printed using SLA techniques. This ink produced high detailed constructs which were suitable for small intestine scaffolds [152], and supported the growth and differentiation of micro-villi containing epithelial cells. An alternative study focused on SLA printing of GelMA for a nerve guidance conduit application, where a multichannel conduit was printed and a PC-12 cell line was seeded thereafter [153]. This study demonstrated the speed and scalability of SLA printing for biomaterial applications, and showed that the construct supported the attachment of a rat neural embryonic cell line, and induced neuronal stem cells to differentiate into neurons.

Inkjet printing may be a useful tool for the manufacture of biomaterials due to its high resolution and the capability of jetting cells into 3D constructs [154]. However, the mechanism of inkjet printing restricts the inks that can be used, as the rheological properties have to meet certain criteria. These criteria include a low viscosity, a suitable ink surface tension and a high contact angle when on the substrate [155]. Despite these restrictions, several materials have been printed using this technology and evaluated for their use in TE.

Silk fibroin is a natural polymer which has been manufactured into biomaterials via various routes. Inkjet printing has been evaluated for producing membranes of silk fibroin for dental barrier membranes [156]. This study used RIJ methods to produce films of regenerated silk fibroin (RSF) using methanol to convert it from a solution to a water insoluble structure. Further components could be added into the ink to improve its bioactivity for example nano-hydroxyapatite. The mechanism of inkjet printing has also been utilised for cell patterning, either by printing cells into the construct, or the inclusion of bioactive molecules in the inks. Cell patterning of hADSCs was achieved on an inkjet printed construct based on PLGA [157]. In this

study, hADSCs were seeded post-printing, and cells were found to adhere well to PLGA patterns on top of a polystyrene substrate. This finding shows the potential for inkjet printing as a technique to direct the growth and adherence of cells in tissue engineering constructs.

3D bio-printing is an example of multidisciplinary bio-fabrication, in which cells, bioactive molecules, biomaterials or cell-aggregates are printed to produce a construct [158]. This approach has been introduced following limitations in cell viability when these are printed into constructs using more traditional additive manufacturing methods. Bioprinting is not a single method, but involves a combination of techniques to transfer biologically important materials onto a substrate [159]. The same layer-by-layer process is used to build up a 3D construct using a cell suspension in the ink, carried out in sterile conditions.

1.5.3 Additive Manufacturing of Hydrogels

The versatile nature of hydrogels has allowed them to be manipulated for manufacture using a variety of additive manufacturing techniques.

Extrusion printing methods can be used to print structures based on a hydrogel material. For extrusion printing, it is desirable for the hydrogel ink to have a low viscosity at a high shear rate, to allow the ink to pass through the nozzle, then a high viscosity at a low shear rate, to ensure the gel maintains its shape once printed [160]. Often, substances that increase viscosity are included in ink solutions to ensure a successful print. A study used extrusion printing methods to produce a composite ink based on PEG and alginate [161], which produced tough hydrogels suitable for cartilage replacement. This ink required the inclusion of nanoclay to both increase the viscosity and improve its shear thinning capabilities. Once a porous structure was printed, human embryonic kidney (HEK) cells were encapsulated in collagen and gelled throughout the pores. The extrusion printing of soft hydrogels has been evaluated and can be achieved by printing into a support fluid gel. This gel behaves as a viscoelastic fluid which self-heals to provide support, and can be removed following printing to leave the printed part [162]. This

technique allows for the manufacture of complex structures made of soft hydrogels that would otherwise collapse under their own weight during printing.

In order to be suitable for SLA, hydrogels must be modified to contain photo-polymerizable groups such as methacrylates. Methacrylated hyaluronic acid (HAMA) and GelMA were found to be capable of producing TE constructs via SLA printing [163], which contained chondrocytes encapsulated in the structure. When these cells were analysed post-printing, HAMA was seen to increase cell viability, and cells within GelMA constructs underwent enhanced chondrogenesis. Synthetic hydrogels can also be printed using SLA technology, for example PEGDA. An additional study showed that both PEGDA and GelMA could be used to print a variety of 3D structures, using lithium phenyl-2,4,6-trimethyl benzoyl phosphinate (LAP) as the photo-initiator [164]. This setup required a laser radiation of 404 nm to initiate the photo-cross-linking of the polymers used. Both of these polymers can be 3D printed for multiple applications, including biomaterials and scaffolds for tissue engineering.

Inkjet printing of polymerised hydrogels is difficult due to the rheological properties, the viscosity of these inks would be too high to expel through the printer head. For this reason, reactive inkjet printing has been explored where more than one inkjet head will be used to expel different solutions that react together to form a hydrogel. The DOD technique can also be utilised for the control of cells and growth factors within a printed hydrogel structure. The droplets from different print heads can also be finely tuned to use different volumes of polymer compared to crosslinker, to ensure there is not an excess of fluid whilst printing. Alginate is a polymer that can become a cross-linked hydrogel when combined with a positively charged solution, such as calcium chloride (CaCl). Reactive inkjet printing of sodium alginate and CaCl produced stable hydrogel structures [165]. These could be further modified to include cells of a fibroblast cell line encapsulated within the structure. The inkjet setup in this study was angled so that the ink droplets would meet and react in air before reaching the substrate. Alginate can also be inkjet printed using an alternative setup, where the reactant is printed onto a positively charged

substrate, inducing a reaction. This setup can produce hydrogels both with and without cells throughout the structure [146], but requires lots of optimisation.

As described, additive manufacturing can be utilised across a variety of applications and using different types of materials. In order to additively manufacture hydrogels, specifically for tissue engineering applications, the inks used must meet certain criteria, including appropriate rheological properties. Once these criteria are met, the printing process will still need optimisation, but can inevitably be used to print a wide range of hydrogel structures.

1.6 Hypothesis/Aims

It was hypothesised that a porous hydrogel could be manufactured based on poly-ε-lysine. The production of this hydrogel could utilize various polymer cross-linking mechanisms and additive manufacturing techniques. The resulting gel would have mechanical, physical and optical properties similar to those of the human cornea.

The aims were:

- To investigate various additive manufacturing techniques to produce a hydrogel with an interconnected porous network.
- To vary polymer chemistries and cross-linking mechanisms to produce the hydrogel with the optimum mechanical and physical properties.
- To demonstrate cyto-compatibility of the hydrogels with both a corneal epithelial and endothelial cell line and primary human stromal cells.

Chapter 2: Materials and Methods

2.1: Hydrogel manufacture

Codes for hydrogel composition

As various different hydrogel compositions were used, a code was developed to abbreviate their composition into a shorter name by which they can be easily compared.

Gel key:

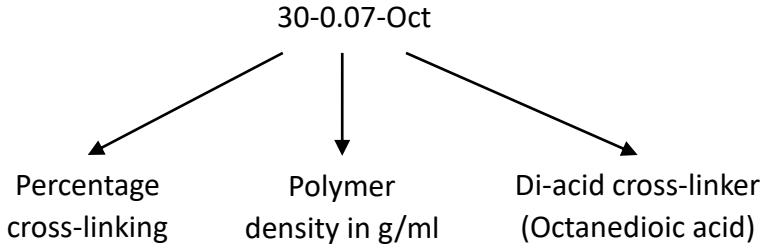

Chemicals

The following raw chemicals were used to produce the hydrogels:

Poly-ε-lysine (pεK) (Zhengzhou Bainafo Bioengineering Co., Ltd., Zhengzhou City, China). **Gelzan™ CM** G1910, **Heptanedioic acid** P45001, **Hexanedioic acid** A26357**, Hydrochloric acid (HCL)** 320331, **Sodium Chloride (NaOH)** S9888, **Octanedioic acid** (ODA) S5200, **N-Methylmorpholine** (NMM) M56557, **N-Hydroxysuccinimide** (NHS) 130672 (Sigma-Aldrich, St Louis, MO, USA). **1-Ethyl-3-(3-dimethylaminopropyl) carbodiimide** (EDCI) FD05800 (Carbosynth Ltd., Compton, England). **Tween 80 28830** (VWR International Ltd., Lutterworth, England). **Phosphate Buffered Saline** (PBS) BR0014 (Oxoid Ltd., Hampshire, England).

Hydrogel manufacture

2.1.1 Porous poly-ε-lysine in stirrer device

A method for producing a gel with a porous structure involved stirring the hydrogel during polymerisation, using a device shown in **Figure 2.1**. The device was composed of a motor connected to a rotary spinner, which had a grater shaped paddle attached to the end. Each component was weighed out according to Table

2.1 to produce 20 ml of hydrogel solution. The four reagents were added together in a 60 ml beaker inside the spinner device and the paddle was submerged in the solution. This was set running at 78 rpm in the lab and took around 20 minutes to form fragments. Once these fragments had formed, they were removed from the stirrer and placed in between two glass plates and left to set for 4-5 hours. In this time the hydrogel fragments fused together leaving gaps throughout the structure.

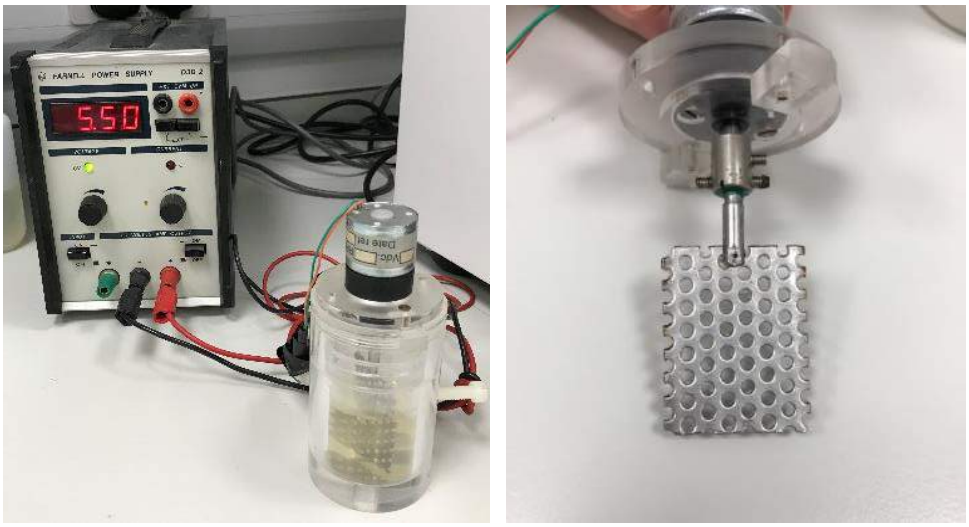

Figure 2.1: Stirrer device used to fragment gels

Table 2.1: 20 ml of poly-ε-lysine/octanedioic acid hydrogel compositions

Gel composition	pεK (g)	ODA (g)	NMM (ml)	NHS (g)	EDCI (g)
30-0.07-Oct	1.696	0.258	1.082	0.567	1.417
30-0.08-Oct	1.978	0.300	1.262	0.662	1.653
30-0.1-Oct	2.374	0.361	1.515	0.794	1.984

2.1.2 Fragmented hydrogel washing and sterilisation

The reaction of pεK with ODA produces by-products such as isourea and NHS, which can remain associated with the amine functional groups of the hydrogel. This may reduce cellular attachment to the hydrogel, and also hinder any further biomolecule addition. For this reason, several washing steps were put in place following the production of a sheet of gel, to remove these by-products and any further unreacted pεK or ODA from the structure.

The hydrogel sheets were washed using the following steps:

1. 5 x 5 minute washes in 10 ml 10 % NMM

2. 5 x 5 minute washes in 10 ml DI H_2O

If the gels were being used for cell culture, prior to cell seeding, the gels were sterilised using the protocol below:

1. Gels were punched using a trephine and placed into the wells of a 24 well plate.

2. Each well filled with 1-2 ml of 70 % ethanol and left for 1 hour.

3. Gels washed 3 times in PBS, each wash for 5 minutes.

4. Gels left in PBS overnight at 37 °C in the incubator.

5. Cells seeded the following morning.

2.1.3 Macroporous hydrogel manufacture

The porous hydrogels were manufactured via static casting. A stock solution of the di-acid with the porogen (Reagent X – commercially sensitive to SpheriTech Ltd) was made up to a 500 mM concentration based on the amounts in **Table 2.2**. 20 ml of hydrogel solution was made up based on the amounts in **Table 2.3**. pεK, NHS and EDCI were dissolved separately in DI water and added together with the di-acid stock solution and inverted multiple times before being cast into a petri dish. The hydrogel was left to set for 4-5 hours.

Table 2.2: Amounts for stock solutions of varying di-acid with porogen X – 500 mM concentration, 200 ml stock.

Di-acid stock solution	Di-acid (g)	Reagent X (g)	NaOH (g)	DI Water (g)
Hexanedioic	14.6	96.62	8.4	200
Heptanedioic	16	96.62	8.4	200
Octanedioic	17.42	96.62	8.4	200

Table 2.3: Amounts for 20 ml of porous hydrogel solution with varying di-acid and percentage cross-linking

Hydrogel composition	pεK (g)	Di-acid stock (ml)	NHS (g)	EDCI (g)
30-0.07-Hex	1.746	3.045	0.584	1.46
60-0.07-Hex	1.563	5.451	0.523	2.612
30-0.07-Hept	1.721	3	0.576	1.438
60-0.07-Hept	1.522	5.31	0.509	2.544
30-0.07-Oct	1.696	2.962	0.567	1.417
60-0.07-Oct	1.483	5.17	0.496	2.48

2.1.4 Macroporous Hydrogel washing

Several washing steps were put in place following the production of a sheet of gel, to remove any by-products and any further unreacted pεK or di-acid from the structure.

The gel sheets were washed using the following steps:

1. 1 x 5 minute washes in 10 ml DI H_2O

2. 3 x 5 minute washes in 10 ml 0.1 M NaOH

3. 3 x 5 minute washes in 10 ml DI H_2O

4. 3 x 5 minute washes in 10 ml 0.1 M HCL

5. 3 x 5 minute washes in 10 ml DI H_2O

2.2 Physical hydrogel characterisation

2.2.1 Percentage light transmittance

Percentage light transmittance is indicative of the transparency of the hydrogels, and was performed to compare different hydrogel variants. The percentage light

transmittance of each gel sample was measured using a spectrophotometer which recorded the absorbance at wavelengths of 300-700 nm. The light transmittance was calculated at 486 nm, a wavelength within the visible light spectrum. The hydrogels were prepared using a 6 mm diameter trephine, producing 4 x 0.36 cm^2 discs from which an average was taken. These discs were placed in a 96 well plate each with 100 µl of water. The 96-well plate was placed into a FLUOstar Omega microplate reader (BMG LABTECH GmbH, Ortenberg, Germany) and read at 486 nm with an emission filter of 520 nm. The resulting table of absorbance values were exported into an excel document, and the following equation used to convert from absorbance into percentage light transmittance:

$$\textbf{Transmittance}\ (\%) = \mathbf{10}^{(-\textbf{Absorbance})} * \mathbf{100}$$

For each measurement, 4 sections were punched from the same hydrogel sheet and an average light transmittance taken. This was repeated 3 times, with 3 separate hydrogels made.

2.2.2 Refractive Index

Refractive index measurements were taken using an AR200 digital refractometer (Reichert Technologies, New York, NY, USA). The refractometer was initially calibrated using DI water. A 0.5 cm^2 sample of each hydrogel was punched and excess surface water was removed using filter paper. The sample was then placed onto the glass prism of the refractometer and a measurement taken. Narafilcon A was included as a positive hydrogel control.

2.2.3 Percentage Water Content

The percentage water content of the hydrogel is indicative of porosity within a hydrogel structure. A section of gel was punched using a 6 mm diameter trephine, which was blotted dry using filter paper. This section was then weighed, and the mass of the wet hydrogel was recorded. The hydrogel was then placed in a desiccator and left for 24 hours to dry out. Following this, the dry material was weighed and the mass recorded. The percentage water content can be calculated using the following equation:

$$\textbf{Water Content}\ (\%) = \frac{\textbf{Wet weight} - \textbf{dry weight}}{\textbf{Wet weight}}\ \textbf{X 100}$$

For each measurement, 3 pieces were punched from the same hydrogel and an average percentage water content calculated. This was repeated 3 times, using 3 separate hydrogel sheets.

2.2.4 Porosity and degree of swelling measurements

In order to calculate an average porosity, sheets of hydrogel were freeze dried and punched using a 6 mm diameter trephine and each gel sample weighed (M_1). The hydrogel pieces were then soaked in ethanol overnight and the wet samples weighed again the following day (M_2). The following equation was used to determine the percentage porosity:

$$\textbf{Porosity}\ (\%) = \frac{\mathbf{M_2} - \mathbf{M_1}}{\boldsymbol{\rho}\mathbf{V}}$$

The same values were used to calculate the degree of swelling (S):

$$\textbf{Degree of swelling}\ (\mathbf{S}) = \frac{\mathbf{M_2}}{\mathbf{M_1}}$$

2.2.5 Swelling Behaviour and Degradation of Hydrogels

The swelling behaviour of the hydrogels was further evaluated based on the change in diameter of the hydrogels over time. The hydrogels were punched from a sheet using an 11.5 mm diameter trephine, and left in either PBS or dH_2O for 8 weeks. The diameter of each of the hydrogel variants was measured using a micrometre at 1, 4 and 8 week time points and recorded.

The degradation of the hydrogels was evaluated by measuring the weight loss of hydrogels over time. Similarly, the hydrogels were punched and the original weight recorded before being left in either PBS, NaOH or Trypsin for 8 weeks. At 1, 4 and 8

weeks, the hydrogels were removed from the solution, blotted dry using filter paper and weighed.

2.2.6 Scanning electron microscopy (SEM) imaging

Scanning electron microscopy produced images of hydrogel samples by scanning the surface with a focused beam of electrons. The images produced can provide information about the topography of the sample as well as the hydrogel porosity. SEM imaging was performed on both a Table-top SEM and a field emission SEM.

Table-top SEM:

All samples were freeze dried for at least two hours before they were imaged. The dried samples were cut and placed onto a carbon strip on the SEM mount with both the top surface and the cross section visible. Images were taken on a SEM TM3030 (Hitachi High-Technologies Europe GmbH, Berkshire, England) according to the manufacturer's protocol. Samples were not sputter coated prior to imaging. For each hydrogel variant, at least 3 different images were taken for both the top surface and the cross section, and representative images were used. An average pore size was established using ImageJ software, using 3 different SEM images of each gel cross section.

Figure 2.2: Tabletop SEM TM3030 and lyophilized hydrogel top and cross-section visible on SEM stump

Field emission SEM:

Printed hydrogel samples were left to dry out in a desiccator and mounted onto carbon strips on SEM stubs. These were chromium sputter coated using a Q150T ES coater (Quorum, Sussex, UK) prior to imaging. SEM images were taken using a S4800 SEM (Hitachi, Tokyo, Japan). Images were taken at a voltage of 5.0 kV and a 45 ° angle to visualise the surface topography.

Rheological characterisation

Rheology measurements were performed to characterise the viscoelastic properties of the hydrogel variants. To prepare the hydrogels for rheological characterisation, 10 ml of gel solution was cast into a 12 cm diameter petri dish, to keep the gel thickness consistent. A punch with a diameter of 5 cm was used to prepare individual pieces of hydrogel for the rheometer. Prior to loading the sample, the hydrogels were blotted to remove excess water using filter paper. For all of the hydrogel characterisation an Anton Paar MCR 302 Rheometer (Anton-Paar, Graz, Austria) was used with a sandblasted parallel plate 50 mm diameter configuration. In each case, during sample loading the parallel plate height was set to 60 mm then lowered to the 1.1mm to run the sample. All measurements were performed at 20 °C and repeated 3 times using 3 different hydrogel sections.

Figure 2.3: Anton Paar MCR 302 Rheometer

2.2.7 Amplitude Sweep

The sample was loaded onto the stage and the plate height was lowered to 1.1 mm. The amplitude sweep ran from 0.1 % - 1000 % and recorded a graph of storage and loss modulus over strain. Once the measurement was complete, the data were exported to excel and the modulus crossover point was identified.

Complex modulus (G*) was calculated using the following equation:

$$\mathbf{G}^* = \sqrt{\mathbf{G'^2 + G''^2}}$$

Where G‘ = storage modulus and G‘‘ = loss modulus at 0.1 % strain taken from the amplitude sweep.

2.2.8 Frequency Sweep

The sample was loaded onto the stage and the plate height was lowered to 1.1 mm. The frequency sweep measurement was then set running from 1 - 100 rad/s and recorded a graph of storage and loss modulus over frequency. Once the measurement was complete, the data was exported to excel and the storage and loss modulus at 10 rad/s was recorded.

Mechanical Testing

2.2.9 Compression Measurements

Compression measurements were performed to establish the mechanical properties of the fragmented and cast hydrogel variants. The measurements were taken using the CellScale UniVert mechanical test system (CellScale Biomaterials Testing, Ontario, Canada).

Hydrogel samples were pre-prepared prior to using the compression tester. To keep the thickness consistent, 10 ml of hydrogel solution was cast into a 12 cm diameter petri dish. 5 samples were punches from the same sheet of hydrogel using a 12.5 mm diameter trephine, which was repeated using sheets made at three different times.

To prepare the equipment, the top and bottom platens were screwed into position. The CellScale software was loaded on the computer and the load cell calibration steps were performed. The top platen was lowered gradually using the actuator controls until it reached the top of the specimen. When a positive force is exhibited by the platen touching the sample, the test was executed, and the sample was compressed at a strain rate of 0.01 s^{-1}, until it reached breaking point. When the sample had broken, the test was terminated, and the top platen jogged upwards to remove the sample. The data were exported to excel for analysis. All measurements were performed with either a 10 or 50 N load cell.

Figure 2.4: CellScale Univert mechanical test system with compression platen set up

2.3 Hydrogels as printable ink preparation and characterisation

Ink preparation

The cross-linking of poly-ε-lysine to form a stable hydrogel was analysed by various mechanisms. Various polymer chemistries were also trialled to establish its suitability for different additive manufacturing methods.

2.3.1 Poly-ε-lysine with ODA

Poly-ε-lysine cross-linked with octanedioic acid was analysed in varying polymer chemistries to establish its printability for either extrusion or inkjet printing. The gel compositions characterised for printing were 60-0.07-Oct and 60-0.1-Oct. The amounts of reagents were weighed out according to **Table 2.4**.

Table 2.4: 40 ml of poly-ε-lysine/octanedioic acid hydrogel compositions

Gel composition	pεK (g)	ODA (g)	NMM (ml)	NHS (g)	EDCI (g)
60-0.07-Oct	2.967	0.901	1.893	0.992	4.959
60-0.1-Oct	4.154	1.262	2.651	1.389	6.943

The four reagents were dissolved separately and made up to 10 ml in DI water to be characterised as separate inks. NMM is added to facilitate the dissolution of ODA in water. For reactive inkjet printing, these reagents were combined to form inks 1 and 2 which were characterised alongside the four separate reagents. Where: Ink 1 = pεK + ODA dissolved in water and Ink 2 = NHS + EDCI dissolved in water. For extrusion printing, the four reagents were added together and the rheological properties during polymerisation were characterised.

2.3.2 Poly-ε-lysine with Gellan gum

Hydrogels made by ionic cross-linking between poly-ε-lysine and gellan gum were evaluated with various polymer concentrations. Poly-ε-lysine was made up to 10 and 20 wt % in DI water and left on a roller until fully dissolved. Gellan gum was made up to 0.35, 0.5 and 0.75 wt % in DI water, this was left to dissolve for three hours at 60 °C under constant stirring.

Rheological Evaluations

Equipment:

Anton Paar MCR 302 Rheometer (Anton-Paar, Graz, Austria), using 6cm 1° angle cone configuration, **Figure 2.3**. Rheocompass software used to produce data.

Rheological evaluations were performed to establish the viscosity of the inks separately and during polymerisation, in various temperature and shear rate conditions. The viscosity of the different inks were compared for their printability.

Prior to the rheological measurements, the inks were prepared as outlined in table 2.4. When assessing Inks 1 and 2, these were left for several minutes to fully dissolve before being loaded onto the rheometer.

For all measurements performed, the cone height was set to 60.0 mm while 1-2 ml of the sample was placed onto the plate using a Pasteur pipette, and then lowered to 0.118 mm to run the sample.

2.3.3 Shear Rate Ramp

The shear rate was set to record points from 1-100 s^{-1}, which plotted 21 time points on a graph of viscosity over shear rate. The software also recorded the corresponding values for shear stress at each time point. Once the measurement was complete, a final viscosity value was recorded, and the data exported to excel to be plotted. The measurement was performed at a constant temperature of 20 °C and repeated three times.

2.3.4 Temperature Ramp

Once the sample was loaded onto the rheometer and the cone lowered, it was trimmed to remove any excess, and the solvent trap added to prevent any evaporation with the increasing temperature. The software plots the viscosity over temperature graph whilst the measurement is running. Once the measurement was complete, a table of values was exported to excel for the data to be plotted. The measurement was performed at a constant shear rate of 50 s^{-1} and repeated three times.

2.3.5 Viscosity over time during polymerisation

To establish the changes in viscosity over time during polymerisation, all four reagents were added together immediately prior to sample loading onto the rheometer. A program was developed to record the viscosity changes over a time of 20 minutes, and different hydrogel variants were compared. The measurement was performed at a constant shear rate of 50 s^{-1}, a temperature of 20 °C and was repeated three times.

2.3.6 Storage and Loss modulus over time during polymerisation

To further characterise the properties of the inks during polymerisation, a time sweep was performed to establish the storage and loss modulus of different hydrogel variants over time. Again, the four reagents were added together and allowed to mix before loading onto the rheometer. The measurement was

performed at a constant frequency of 10 rad/s and an amplitude of 0.5 %. The temperature was kept constant at 20 °C and the measurement was repeated three times.

Ink stability

Equipment:

Kruss DSA 100 (KRÜSS GmbH, Hamburg, Germany)

Figure 2.5: Kruss DSA 100 equipment

2.3.7 Surface tension

Surface tension is the tendency of the surface of a fluid to resist an external force, based on the cohesive nature of its molecules. Surface tension measurements were used to determine if the inks used for the inkjet printing of poly-ε-lysine would form a stable droplet. Furthermore surface tension helps us to understand the behaviour of an ink when it is deposited onto a substrate.

The surface tension of the inks were measured using a DSA 100 and Advance software. The program used to perform the measurement was 'Surface tension – pendant drop'. Prior to loading the inks, a water control was performed with a known surface tension of 72 dynes/cm. The inks were then loaded into a syringe and manually dosed until a large droplet was released. This droplet was captured by

the camera and the measurement performed. An average of 5 measurements were taken for each ink.

2.3.8 Contact angle

A materials contact angle demonstrates the wettability of a substrate by a fluid and is also dependent on the surface tension of the liquid. Contact angle measurements were performed to establish how the ink would behave when printed onto a glass substrate.

Again, a Kruss DSA 100 was used for contact angle measurements. For these measurements, a glass slide was placed on the stage as the substrate. A micropipette was used to dispense the inks onto the slide in 5 µl droplets. Once dispensed, the software was set to capture an image of the droplet and measure both the left and right hand side contact angle. From these two values an average was taken and this process was repeated at least 5 times.

2.3.9 Density measurements

Fluid density is measured as the mass of the fluid per unit volume and can have an influence on the printability of inks for inkjet printing.

The density of the inks was established using a DMA 35N density meter (Anton Paar, Graz, Austria) in order to input into the Z number equation for printability. The ink was manually drawn up into the density meter using the button, and the density automatically calculated. This measurement was taken at least three times and an average taken.

2.3.10 Printability of hydrogel inks

Multiple dimensionless numbers can be used to determine the printability of inks for inkjet printing by using the rheological properties. These numbers are the Reynolds number (Re), Weber number (We), the Ohnesorge number (Oh) and the Z number (Z).

The Reynolds number represents the relationship between viscous and inertial forces of a moving fluid:

$$\mathbf{Re} = \frac{\boldsymbol{\rho VL}}{\boldsymbol{\mu}}$$

Where ρ is the density of the liquid, V is the fluid velocity, L represents the drop diameter and μ is the dynamic viscosity. The Weber number relates the ratio between inertia and an inks surface tension:

$$\mathbf{We} = \frac{\boldsymbol{\rho V^2 L}}{\boldsymbol{\sigma}}$$

Where σ is the surface tension of the measured ink. The Ohnesorge (Oh) number relates viscous forces of liquids to their inertial forces and surface tension, and also takes into account the size of the ink droplet:

$$\mathbf{Oh} = \frac{\sqrt{\mathbf{We}}}{\mathbf{Re}} = \frac{\boldsymbol{\mu}}{\sqrt{\boldsymbol{\rho\sigma L}}}$$

The Z number is the inverse of the Oh number and describes the printability of inks:

$$\mathbf{Z} = \frac{\mathbf{1}}{\mathbf{Oh}}$$

A Z number which falls between 1-10 is deemed as printable [144, 155], and can be investigated for inkjet printing.

2.4 Inkjet Printing

2.4.1 MicroFab setup

For all inkjet printing, a MicroFab Jetlab 4 printer was used, **Figure 2.6**. This is a DOD inkjet printer that works using a piezoelectric head. In order to expel the ink from the printer head, a voltage is applied which is based on a waveform. Waveforms can be optimised to control when the voltage is applied to the printer head, and for how long. This voltage induces a pressure pulse to be generated inside the fluid cavity, which causes droplets of ink to be ejected from the printer head nozzle.

Figure 2.6: MicroFab Jetlab4 inkjet printer

2.4.2 Ink waveforms

The waveforms can be optimised based on the inks rheological properties, to ensure a variety of inks can be jetted. For instance, a more viscous ink might require a higher voltage that is applied for a longer period of time, than a less viscous ink. **Table 2.5** shows the different waveforms used to jet poly-ε-lysine and gellan gum to produce a hydrogel.

Table 2.5: Waveforms of 20 wt % pεK and 0.35 wt % GG for inkjet printing

	20 wt % Poly-ε-lysine	**0.35 wt % Gellan gum**
Rise Time 1	25 µs	20 µs
Dwell Time	20 µs	20 µs
Fall Time	15 µs	10 µs
Echo Time	25 µs	50 µs
Rise Time 2	50 µs	5 µs
Idle Voltage	5 V	5 V
Dwell Voltage	50 V	60 V
Echo Voltage	-50 V	- 60 V
Frequency	300 Hz	500 Hz

2.4.3 Track optimisation

The speed at which the printer head travels and the spaces left between ink droplets can be further optimised to produce continuous lines of each ink. For poly-ε-lysine, speeds of 10, 15, 20, 25 30 mm/s were trialled, and step spacings of 0.05, 0.1 0.15, 0.2 mm. For gellan gum, speeds of 10, 15, 20, 25 30 mm/s and step spacings of 0.025, 0.05, 0.1 mm were trialled. The tracks produced at each of these different settings were analysed by optical microscopy to establish their uniformity.

2.4.4 Printing

After establishing the optimal speeds and step spacings for each of the two inks, and the suitable temperature of the printhead and the base plate, hydrogels were printed via reactive inkjet printing. The prints were varied based on scripts, which altered the number of passes of each ink. In all prints, a layer of gellan gum was printed first, followed by a layer of poly-ε-lysine on top, schematic **Figure 2.7.** To introduce pores into the structure, bitmaps were included in the jetlab scripts, **Figure 2.8**.

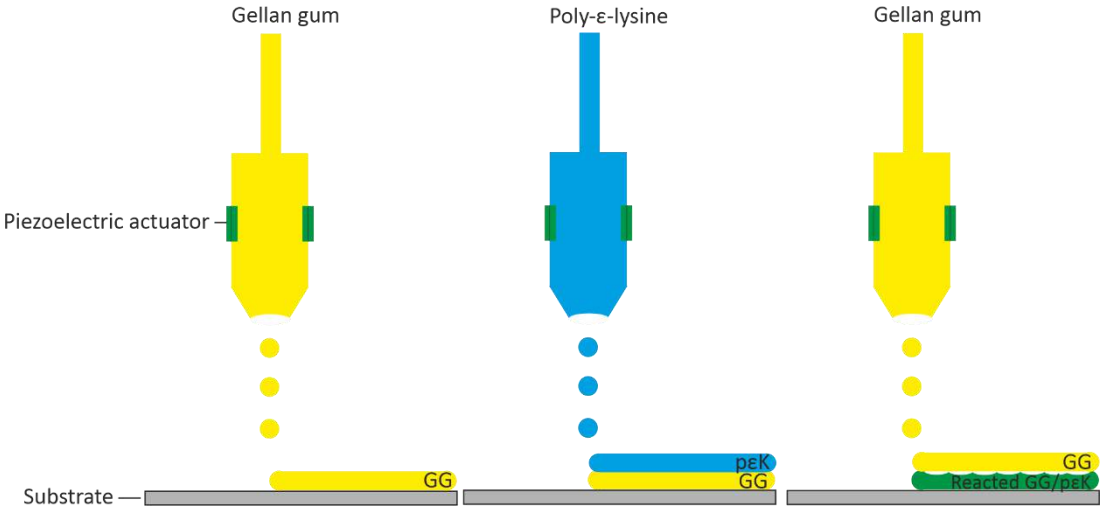

Figure 2.7: Schematic showing the DOD reactive inkjet process of poly-ε-lysine and gellan gum to form a hydrogel

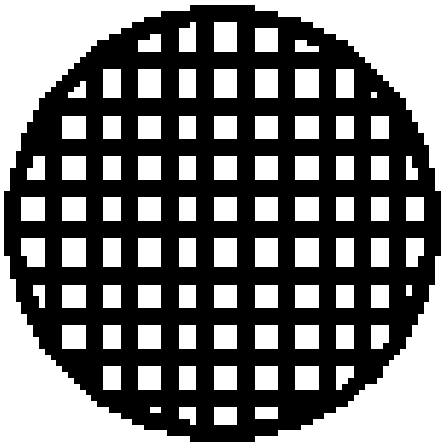

Figure 2.8: Example of bitmap included in jetlab scripts to print a hydrogel including pores

2.4.5 Brightfield microscopy

Once the hydrogels had been printed, they were taken to a Nikon Ti-E fluorescent microscope to be imaged. Samples were visualised at 4 and 10 X magnification on a brightfield channel and images taken using Nikon software.

2.4.6 Image Analysis

All images taken were exported to ImageJ software for analysis. This was done to establish the optimal speed and step spacing, based on the thickness and the uniformity of the tracks produced. All images were exported from the microscope software with a scale bar, which was used to calibrate the ImageJ software. The thicknesses of the tracks were measured using the 'Measure' plugin, and an average thickness from three repeats was calculated.

2.5 General Cell culture

The following materials were used for cell culture:

CCK-8 cell viability kit (Dojindo Laboratories, Kumamoto, Japan), **Na+/K+-ATPase α** sc-58628 (**Insight Biotechnology Limited, Middlesex, UK)**, **PBS** BR0014 (Oxoid Ltd., Hampshire, England), **Amphotericin B** A2942, **Bovine serum albumin (BSA)**, **Dimethyl sulfoxide (DMSO)** D2650, **Dulbecco's Modified Eagle's Medium/Ham's F12 (DMEM/F12)** D8062, **Fetal calf serum (FCS)** F7524, **Goat serum** G9023, **L-Ascorbic acid 2-phosphate sesquimagnesium salt hydrate** A8960, **Penicillin-streptomycin** P4333, **Triton X-100, Trypsin-EDTA** T3924, and **Tween 20** P9416

(Sigma Aldrich, St Louis, USA), **4',6-diamidino-2-phenylindole (DAPI)** D1306, **Alexa Fluor™ 488 Phalloidin** A12379, **Alexa Fluor™ 647 Phalloidin** A22287, , **Dulbecco's Modified Eagle's Medium no phenol red** 31053028, **Dulbecco's Modified Eagle's Medium with GlutaMAX™ Supplement** 61965240, **Goat anti-Mouse IgG (H+L) Highly Cross-Adsorbed Secondary Antibody Alexa Fluor 594** A-32742, **Goat anti-Rabbit IgG (H+L) Highly Cross-Adsorbed Secondary Antibody Alexa Fluor 488** A-32731, **Goat anti-Rabbit IgG (H+L) Cross-Adsorbed Secondary Antibody Alexa Fluor 647** A-21244, **Ham's F-12 Nutrient Mix** 11765054, **Medium 199** 11150059, **Mr Frosty™, ZO-1 Polyclonal Antibody** 61-7300, (Thermo Fisher Scientific, Waltham, MA, USA), **Anti-Collagen I antibody** ab34710, **Anti-Collagen VI antibody** ab6588 (Abcam, Cambridge, UK).

The corneal cells used in this thesis were a human corneal epithelial transformed cell line (HCE-T), a human corneal endothelial cell line (HCEC-12) and primary human corneal fibroblasts (hCF).

The materials used for cytocompatibility testing in this thesis were: fragmented 30-0.07-Oct, macroporous 30-0.07-Oct, cast and inkjet printed pεK/GG hydrogels, cast and printed pεKMA hydrogels (provided by He Liang from the University of Liverpool) and 3D printed GelMA hydrogels (provided by Jonathan Wojciechowski from Imperial College London).

2.5.1 Cell recovery

A cryovial containing the cells was retrieved from liquid nitrogen and transported to the tissue culture lab. The cryovial was placed in the water bath until a small amount of frozen suspension remained, minimising the effects of DMSO on the cells during defrosting. A centrifuge tube of appropriate media was prepared, and the contents of the cryovial was added. This was then placed in the centrifuge for 5 minutes at 185 x g. The supernatant was then discarded, and the pellet resuspended in 2 ml of fresh media using a pipette. The cell suspension was added to a T75 flask with 8 ml of cell culture media and left to grow. The following day the

cells were fed, and any dead cells were removed. The flask was incubated at 37 °C with 5% CO2 prior to any cell culture experiments.

2.5.2 Feeding cells

HCE-T, HCEC-12 and hCF cell culture media was prepared according to **Table 2.6**. When feeding the cells, the appropriate media was placed in the water bath at 37 °C 20 minutes prior. The cells were removed from the incubator and placed into the class II cabinet. Using a pipette, 7 ml of spent media was removed from the flask and discarded in virkon. This was replaced with 7 ml of fresh media. The remaining media was left in the flask so that any growth factors present were not lost from the environment. The cells were then observed under a light microscope to visually check for their confluency, following this, they were returned to the incubator. This process was carried out once a week.

Table 2.6: Components of cell culture media for HCE-Ts, HCEC-12s and hCFs

Standard HCE-T media	Standard HCEC-12 media	Standard hCF media	Supplemented hCF media
Dulbecco's Modified Eagle's Medium/Nutrient Mixture F-12 Ham media	Medium 199, Hams F12 Nutrient mix 1:1	Dulbecco's Modified Eagle's Medium GlutaMAX™	Dulbecco's Modified Eagle's Medium GlutaMAX™
10 % fetal calf serum	5 % fetal calf serum	10 % fetal calf serum	10 % fetal calf serum
1% Amphotericin B	1% Amphotericin B	1% Amphotericin B	1% Amphotericin B
1% Penicillin-Streptomycin	1% Penicillin-Streptomycin	1% Penicillin-Streptomycin	1% Penicillin-Streptomycin
			1% Ascorbic acid

2.5.3 Passaging cells

When the cells reached 80 % confluency they were passaged. This is established by viewing the T75 flask under a light microscope and visually inspecting the amount of coverage. PBS, cell culture media and 10 v/v% trypsin were all placed in the water bath at 37 °C 20 minutes before the passage to ensure they were warmed through. The cells were removed from the incubator and taken to a class II cabinet where the old media was removed. 5 ml of PBS was then added to remove any loose cells and wash the remaining cells, before being discarded. Immediately after, 5 ml of trypsin was added to the T75, which was then transferred into the incubator for 5 minutes. After this time, the flask was placed under the light microscope to establish if the cells had detached from the tissue culture plastic. When this had occurred, the flask was returned to the cabinet where 5 ml of media was added to the flask to counteract the action of trypsin. This solution was then pipetted into a centrifuge tube which was placed in a Heraeus Multifuge X1 centrifuge (Thermo Fisher Scientific, Waltham, MA, USA) at 185 x g for 5 min. Following this, the supernatant was discarded in virkon using a pipette to ensure the pellet was undisturbed. The pellet was then re-suspended in 10 ml of fresh media, ensuring thorough mixing with a pipette. 10 µl of the solution was micro-pipetted onto a haemocytometer to count the cells, this was then multiplied to estimate the number of cells in the total solution. Using this value, 1 ml of cell solution was transferred into a new T75 flask with 9 ml of fresh media. This process was done once a week.

2.5.4 Cryopreserving cells

When the cells were frozen, the same method was followed as when they were passaged (section 2.5.3) until the point at which the cells were removed from the centrifuge. Here, the pellet was re-suspended in a solution of DMSO and cell culture media in a ratio of 1:10. The solution was mixed with a pipette to ensure the pellet had been broken up. 1 ml was pipetted into each cryovial being frozen down. The cryovials were transferred into a Mr Frosty^{TM} container with isopropanol, and taken to the -80 °C freezer. The container allows the temperature of the cells to be

brought down gradually by -1 °C min^{-1}. After at least 4 hours, the samples are then transferred into liquid Nitrogen where the cells are kept at -196 °C.

2.5.5 Seeding cells

The method for seeding the cells was the same as passaging the cells (section 2.5.3) until the pellet was re-suspended. For seeding, the pellet was suspended in a lower amount of media, typically 4-5 ml. 10 µl of this suspension was transferred to a haemocytometer, and the number of cells was averaged. This was then multiplied up to calculate the amount of media containing the number of cells to be seeded. This amount was then pipetted carefully on top of the gels, ensuring the majority remains on the gel and does not transfer to the surrounding well. The plate was then transferred back to the incubator for a couple of hours, to allow the cells to attach, before 1-2 ml of media was added. This was done so that the cells would remain on the gel and not be washed off onto the surrounding tissue culture plastic.

Cell viability methods

2.5.6 Immunostaining cells

Each of the cell lines were seeded separately onto the hydrogel material for testing and left to culture with the appropriate media. Prior to immunostaining, the media was removed from around the gel, and the cells washed 3 times with PBS. Then, formaldehyde was added to each well plate so that the cells were completely covered. The plate was then left for 10 minutes in the fume hood to fix the cells. Following this, the cells were again washed 3 times in PBS. To permeablise the cells, 1 % Triton X was added to each well plate, covering the cells, and was left for 10 minutes. Again the cells were washed in PBS 3 times. After washing, the cells were blocked with 10 % goat serum at 37 °C. After 30 minutes, the goat serum was removed and another PBS wash performed. A chosen primary antibody (concentrations in **Table 2.7**) was added to each well and left overnight at 4°C. The following day the antibody was removed and 3 x PBST washes were performed

before adding a chosen secondary antibody (usually at 1:500 dilution). This was left for an hour at 37 °C wrapped in foil, then removed. Then a 1:30,000 solution of DAPI was added to completely cover the cells, and the plate was wrapped in aluminium foil to keep the cells from the light. This was left for 30 minutes. Following this, the cells were washed in PBS 3 times and were stored at 4°C until they were imaged.

Table 2.7: Typical concentrations of primary antibodies used for immunostaining

Antibody	Concentration	Supplier	CAS Number
DAPI	0.1 µg/ml	Thermo Fisher	D1306
488 Phalloidin	10 µg/ml	Thermo Fisher	A12379
647 Phalloidin	25 µg/ml	Thermo Fisher	A22287
ZO-1	10 µg/ml	Thermo Fisher	61-7300
Na^+/K^+/ATPase	10 µg/ml	Insight Biotechnology	sc-58628
COL-1	10 µg/ml	Abcam	ab34710
COL-6	2 µg/ml	Abcam	Ab6588

2.5.7 CCK-8 Assay

Prior to a CCK-8 assay, several sections of 30-0.07-Oct fragmented hydrogel were soaked in the appropriate culture media for three days. This test was performed to establish the cytotoxicity of the leachables from the hydrogel for several time points over 7 days. 50,000 HCE-T/HCEC-12 cells were seeded into each well of a 48 well plate and 300 µl of gel-soaked or regular media was added to each well. On each time point, 30 µl of CCK-8 solution was added to each well. The plate was then returned to the incubator and left for two hours. 100 µl aliquots of solution from each well was transferred to a 96 well plate. This was inserted into a FLUOstar Optima plate reader (BMG Labtech, Ortenberg, Germany) with the absorbance read at 485 nm and a background reading at 600 nm and the results were recorded.

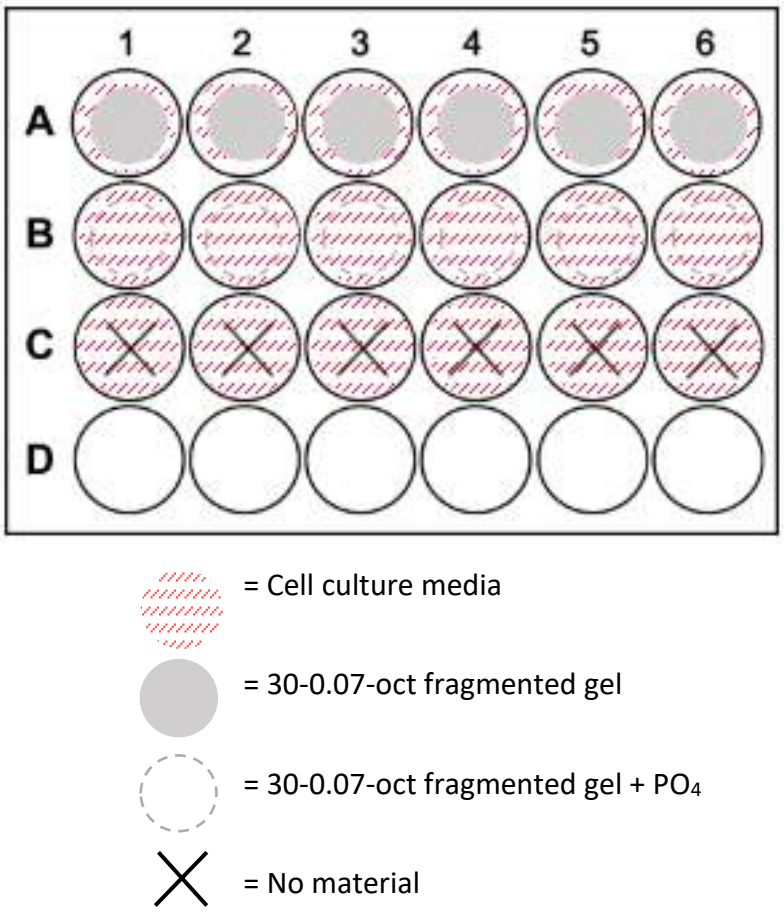

Figure 2.9: Diagram for CCK-8 assay

2.5.8 Live-Dead Assay

For this assay a live/dead kit for mammalian cells was used (Thermo Fischer Scientific), containing calcein AM and ethidium homodimer (EthD-1). Calcein AM distinguishes any live cells in a fluorescent green colour and EthD-1 enters cells with damaged membranes and highlights these dead cells in a red colour when viewed under a fluorescence microscope. The kit was stored in the freezer at -20 °C, and the two vials were warmed up to room temperature prior to the assay. The reagents ethidium homodimer and calcein AM were added in 1:200 and a 1:500 ratios to pre-warmed PBS solution. The cells were first washed in regular PBS solution which was then discarded in virkon. 150 µl was pipetted into each well containing cells, the plate was then wrapped in aluminium foil and was taken to be

imaged on a live cell fluorescence microscope (Nikon Ti-E). The Nikon software was used to take the images, and had pre-set values for excitation wavelengths for both reagents. The images were analysed on Image-J software, where the number of live and dead cells were counted, and a percentage cell viability was calculated.

Primary human Stromal fibroblast (hCF) Cell Culture

hCF cells were cultured as described in Section 2.5, and were seeded either as regular hCFs or were transduced with GFP and seeded as a culture of green hCFs.

2.5.9 Green fluorescent protein (GFP) Transduction

eGFP expression was established through the use lentiviral particles gifted by Kevin Hamill (DEVS, ILCAMS, University of Liverpool). To transduce the cells with GFP the cells were seeded at a density of 2.5 x 10^5 cells in each well of a 6 well plate. The following day, the transduction was performed using 10 µg/ ml polybrene (Sigma Aldrich, UK). Then, adenovirus was added to each well in varying amounts: 0 µl, 2 µl, 4 µl, 6 µl, 10 µl, 15 µl and the plate was returned to the incubator. After 24 hours, the media was replaced with fresh stromal cell media and the plate was imaged to check for green cells. After 48 hours, the antibiotic puromycin, was added. This was in a 5 µg/ml concentration made up with culture media. The plate was returned to the incubator and left for several days, to allow time for the antibiotic to kill the cells that had not taken up the virus. After 4-5 days, the dose of puromycin was increased to 10 µg/ml and the cells were returned to the incubator for a few more days. Once all of the cells that had not taken up the virus were killed, the GFP fibroblasts were transferred into a T75 flask to expand. At the next passage, they were further expanded into a T175 flask and allowed to reach confluency before being frozen down.

2.5.10 Movement of GFP hCFs into porous hydrogel

An initial experiment was performed using the GFP hCFs to establish if they migrated into the porous hydrogel structure, and further experiments using regular hCF cells were designed based on these results. Cells were seeded onto the 30-0.07-Oct fragmented gels in varying densities, from 1 x 10^4 - 5 x 10^4 to establish if the stromal fibroblasts would travel into the porous structure of the hydrogel. The

densities in which they were seeded were taken from the literature. Live cell images were taken every week until 5 weeks after seeding when they were fixed. A volume plot was generated at 3 weeks to show the distribution of cells throughout the construct.

2.5.11 Compression and Transparency Assay

Regular hCF cells were seeded at a density of 5 x 10^4 cells/well on top of 30-0.07-Oct fragmented gels. Phenol red free culture media with and without the addition of 1 % ascorbic acid was added to the wells, and control wells containing fragmented gels with no cells were included. These plates were incubated for 6 weeks in total with compression and transparency measurements performed at 24 hours, 2 weeks, 4 weeks and 6 weeks.

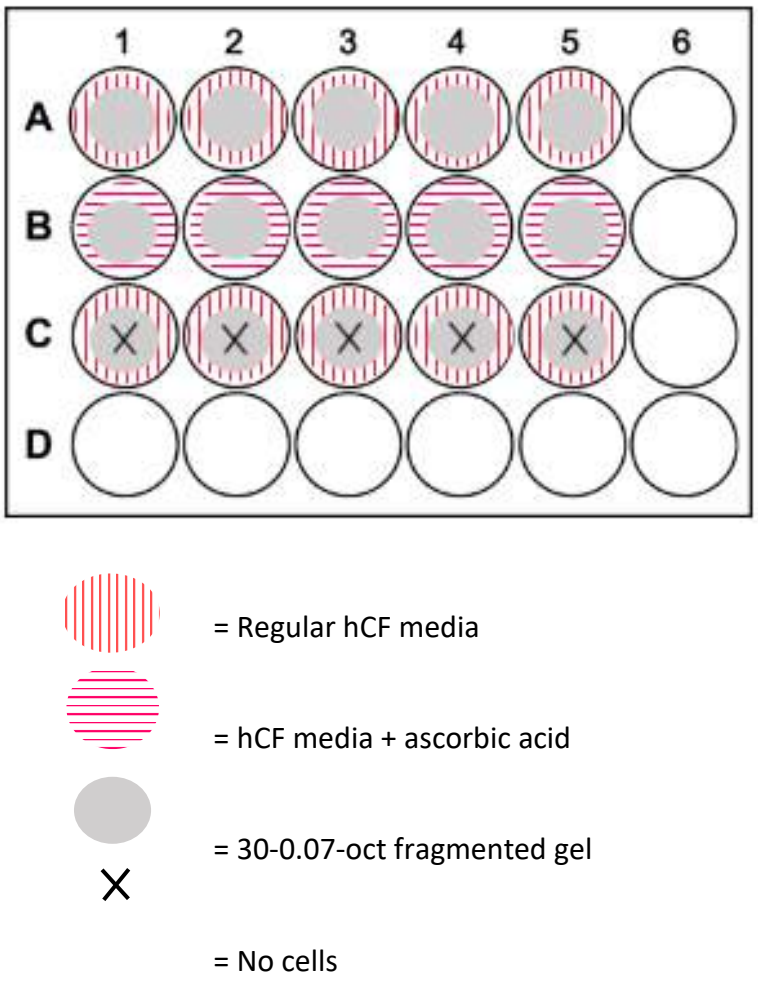

Figure 2.10: Diagram for Compression/Transparency Assay

2.6 Statistical Analysis

The graphs presented in this thesis were plotted using Excel 16.56 (Microsoft, Washington, US), and statistical analysis was performed using SPSS Statistic 25 (IBM, New York, US) software. All materials characterisation was performed with 3 technical repeats, with each repeat containing 3-5 individual samples per run, based on availability of material. The statistical tests used were a one-way ANOVA with a Tukey post-hoc, except for Figure 4.22 where an independent T-test was used as only two separate groups were compared.

Chapter 3: Porous poly-ε-lysine hydrogels using alternative casting methods

3.1 Introduction

Due to the limitations surrounding corneal transplantation from donor tissue, synthetic alternatives have been investigated for their potential to replace traditional surgical practice. Very few biomaterials for corneal tissue engineering applications have made it through to clinical trials, which leaves the floor open to researchers to propose alternative materials as potential replacements. As corneal transplantation is currently the 'gold-standard' for regaining transparency following corneal opacity, an alternative implant must meet several requirements in order to be suitable to replace this. The criteria are based around the properties of the native human corneal tissue, its transparency, mechanical and physical properties, and the material must be bio-compatible and not induce rejection or infection.

The transparency of a corneal replacement is arguably the most important feature which needs to be met in order for the implant to be successful. The cornea is a complex structure, which due to its unique organisation of the stromal fibres and the extracellular matrix, is the only collagenous structure in the body to be transparent. The cornea has a percentage light transmittance of 90 % [166, 167], so any implant that is designed for the cornea should meet this requirement. The optical properties of the cornea are also affected by its shape and refractive index. The curvature of the cornea is vital for its refractive properties, as it contributes 40-44 D of refractive power and 70 % of the total refraction of the eye [21]. Therefore, the shape and dimensions of the human cornea must be replicated for an artificial replacement to be successful. The full thickness of the cornea equates to around 550 µm, and has a horizontal diameter of 11-12 mm and vertical diameter of 9-11 mm. The curvature further impacts the refractive properties of the cornea, with a measured anterior curvature averaging around 7.8mm and a posterior curvature of approximately 6.5mm [7, 21]. Literature places the value for the refractive index of the human cornea in-between 1.373- 1.432 nD [168, 169], which again must be closely matched to ensure the success of mimicking human corneal tissue.

Stable mechanical properties of an artificial cornea are vital for ensuring the surgical handling of the construct during implantation and the ability of the implant to withstand the normal pressures of the eye. To ensure an implant with appropriate mechanical properties, the design can be based upon the mechanical properties of human corneal tissue. Literature has recorded the mechanical properties of the human cornea, which demonstrates a tensile strength of 3.8 MPa and an elastic modulus within the range of 3-13 MPa [170]. A further physical property of the artificial cornea to ensure comfort for the patient would be a high water content. The water content of the cornea is approximately 78 % [171], which should be closely matched in order to mimic the native human cornea.

Finally, to ensure the survival of the implant, the artificial cornea must be compatible for implantation in humans. Therefore, it must be biocompatible, support integration with surrounding tissues, and not induce a foreign body response. Furthermore, it should feature an interconnected porous network, to allow for cell migration and facilitation of exchange of metabolic waste.

The hypothesis for this chapter was that porous poly-ε-lysine hydrogels could be manufactured via alternative casting techniques. Two methods were investigated; one which fragments the hydrogel to produce pores upon polymerisation, and another includes the use of a porogen to develop pores throughout the construct. A further hypothesis was that the poly-ε-lysine hydrogels produced could demonstrate suitability for corneal tissue engineering substrates, when compared with other substrates in literature and native human corneal tissue.
The objectives to test these hypotheses were:

1. Optimise manufacture methods that produce hydrogels with an interconnected porosity throughout.
2. Characterise the hydrogels for their optical and mechanical properties.
3. Compare the hydrogels produced with alternative materials for corneal tissue engineering and with the properties of native corneal tissue from literature.

The work in this section included the manufacture of porous poly-ε-lysine hydrogels via different casting techniques, outlined in method section 2.1, and the characterisation of their physical and mechanical properties, detailed in method section 2.2. This chapter concludes with a discussion of how these hydrogels compare to one another, and to others investigated for corneal tissue engineering in the literature.

3.2 Fragmented hydrogel physical characterisation results

3.2.1 Optical properties of fragmented and cast pεK hydrogels

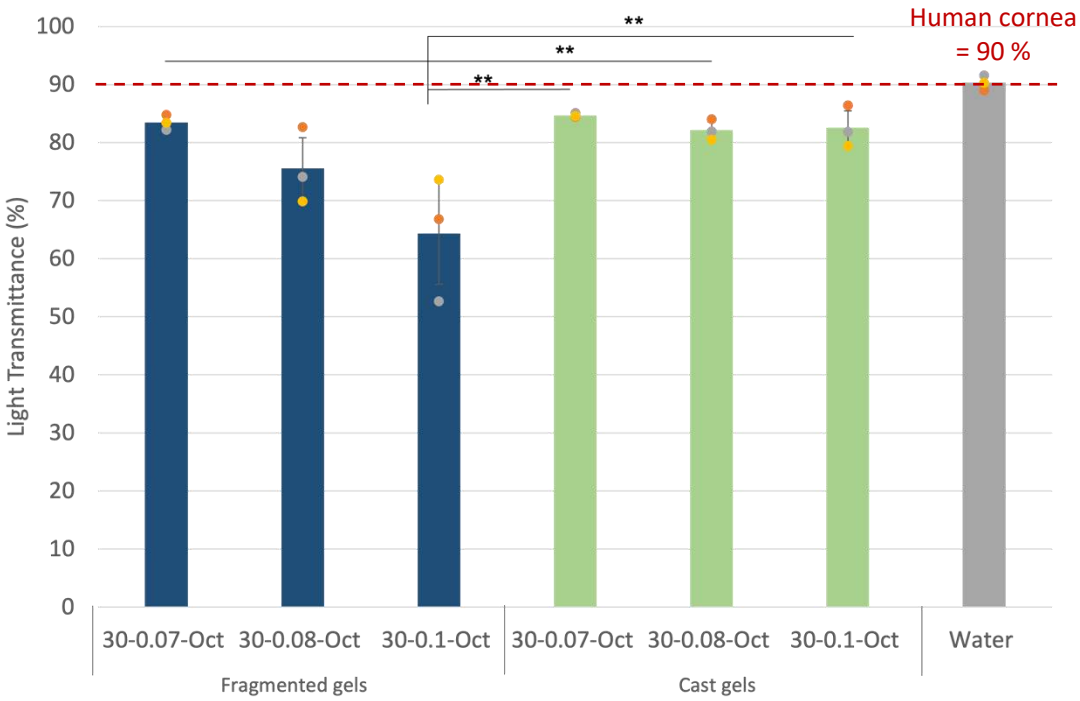

Figure 3.1: Percentage light transmittance of fragmented vs cast poly-ε-lysine hydrogel variants. 5 samples/run (n=3) (** = $p < 0.01$) Graph plots mean ± SD and individual data points. **Key:** Blue bars = fragmented hydrogel variants, Green bars = cast hydrogel variants, Grey bar = water control. Percentage light transmittance of the human cornea taken from literature is highlighted on the graph

Producing hydrogels with a fragmented structure and increasing the polymer density influenced their transparency (**Figure 3.1**). It can be seen that the lowest polymer density of 0.07 g/ml has the highest percentage light transmittance in both fragmented and cast hydrogel varieties. This is followed by the next lowest polymer density, 0.08 g/ml, and finally the highest density of 0.1 g/ml. The fragmented

hydrogel with 0.1 g/ml density had a significantly lower percentage light transmittance compared to every other gel type apart from the fragmented 0.08 g/ml gel, all p values < 0.01. The data shows that fragmenting the hydrogels and introducing pores into the microstructure does not significantly alter the percentage light transmittance and therefore the transparency of the hydrogels, for polymer densities of less than 0.1 g/ml. The polymer density has a larger influence than the fragmenting process on the percentage light transmittance of the hydrogels. As the 30-0.1-Oct hydrogel had a significantly lower transparency, and out of a suitable range for a cornea application, it was not taken forward and characterised using other methods.

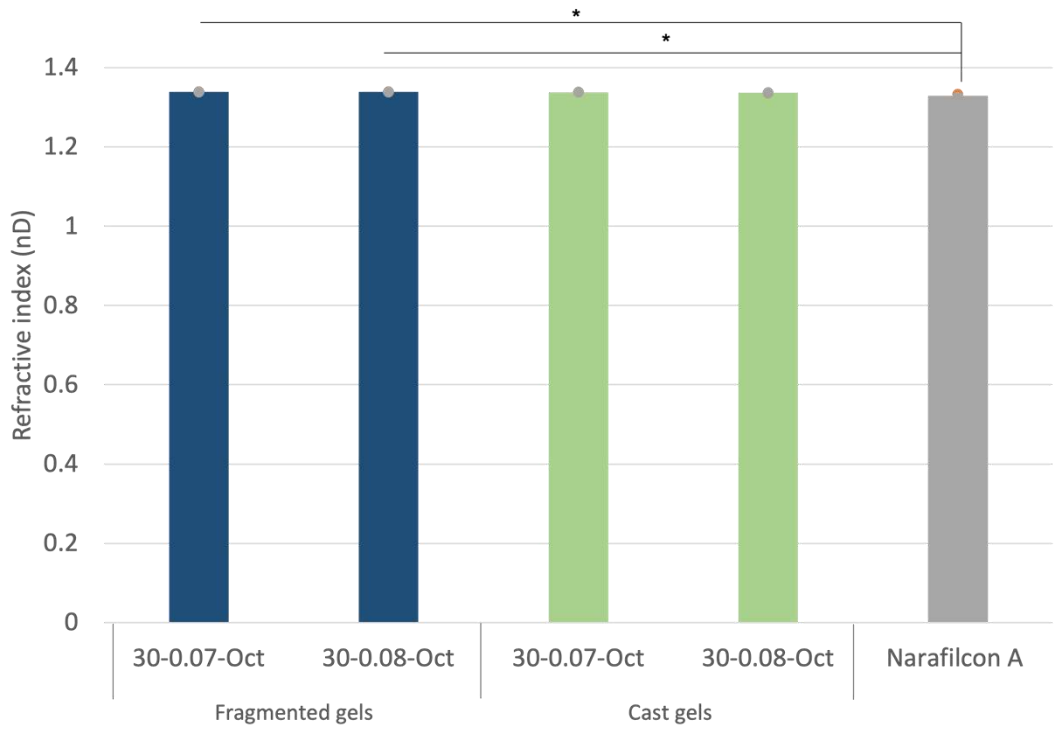

Figure 3.2: Refractive index of fragmented vs cast poly-ε-lysine hydrogel variants . 5 samples/run (n=2) (* = p < 0.05) **Key:** Blue bars = fragmented hydrogel variants, Green bars = cast hydrogel variants, Grey bar = Narafilcon A contact lens control

Fragmenting the hydrogels was shown to have little influence on the refractive index of the hydrogels when compared with cast hydrogels of the same chemistry (**Figure 3.2**). These measured values were compared with a Narafilcon A hydrogel contact lens which is sold commercially. All of the poly- ε-lysine hydrogel variants had comparable refractive index measurements (1.336-1.339) with no significant

differences seen. Narafilcon A had a slightly lower refractive index measurement of 1.329 nD compared to the poly-ε-lysine variants. This was significant when compared with the two fragmented hydrogel variants, 30-0.07-Oct and 30-0.08-Oct, with p values of 0.043 and 0.037.

3.2.2 Percentage Water content of fragmented and cast pεK hydrogels

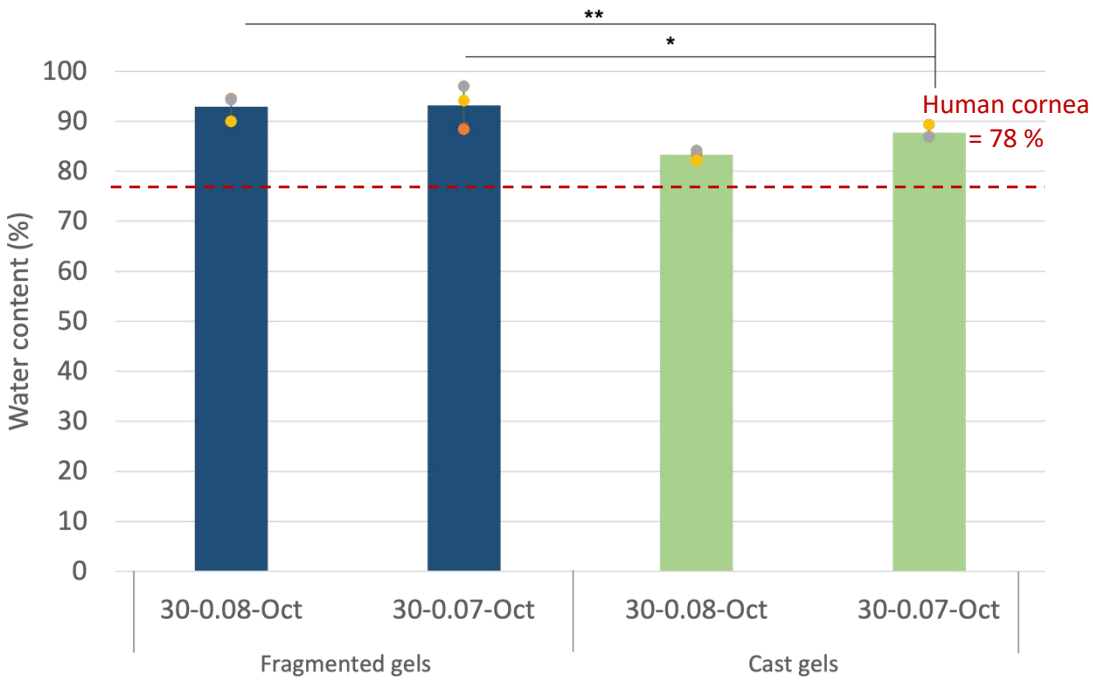

Figure 3.3: Percentage water content of fragmented vs cast poly-ε-lysine hydrogel variants. 3 samples/run (n=3) (** = $p < 0.01$). Graph plots mean ± SD and individual data points. **Key:** Blue bars = fragmented hydrogel variants, Green bars = cast hydrogel variants. Percentage water content of the human cornea taken from literature is highlighted on the graph

Hydrogels produced by a fragmentation were seen to have a higher percentage water content than cast hydrogels with the same chemistry (**Figure 3.3**). It can also be seen that the lower polymer density variants have a higher percentage water content than the higher polymer density variants. Both fragmented variants had a statistically significant higher water content than the 30-0.08-oct cast variant. Fragmented 30-0.07-oct and 30-0.08-oct demonstrated p values of 0.008 and 0.01 respectively. These results suggest that there is more water retained in the structure and therefore a higher porosity throughout the fragmented gels and the lower polymer density hydrogels.

3.2.3 SEM Micrographs of freeze-dried of fragmented and cast pεK hydrogels

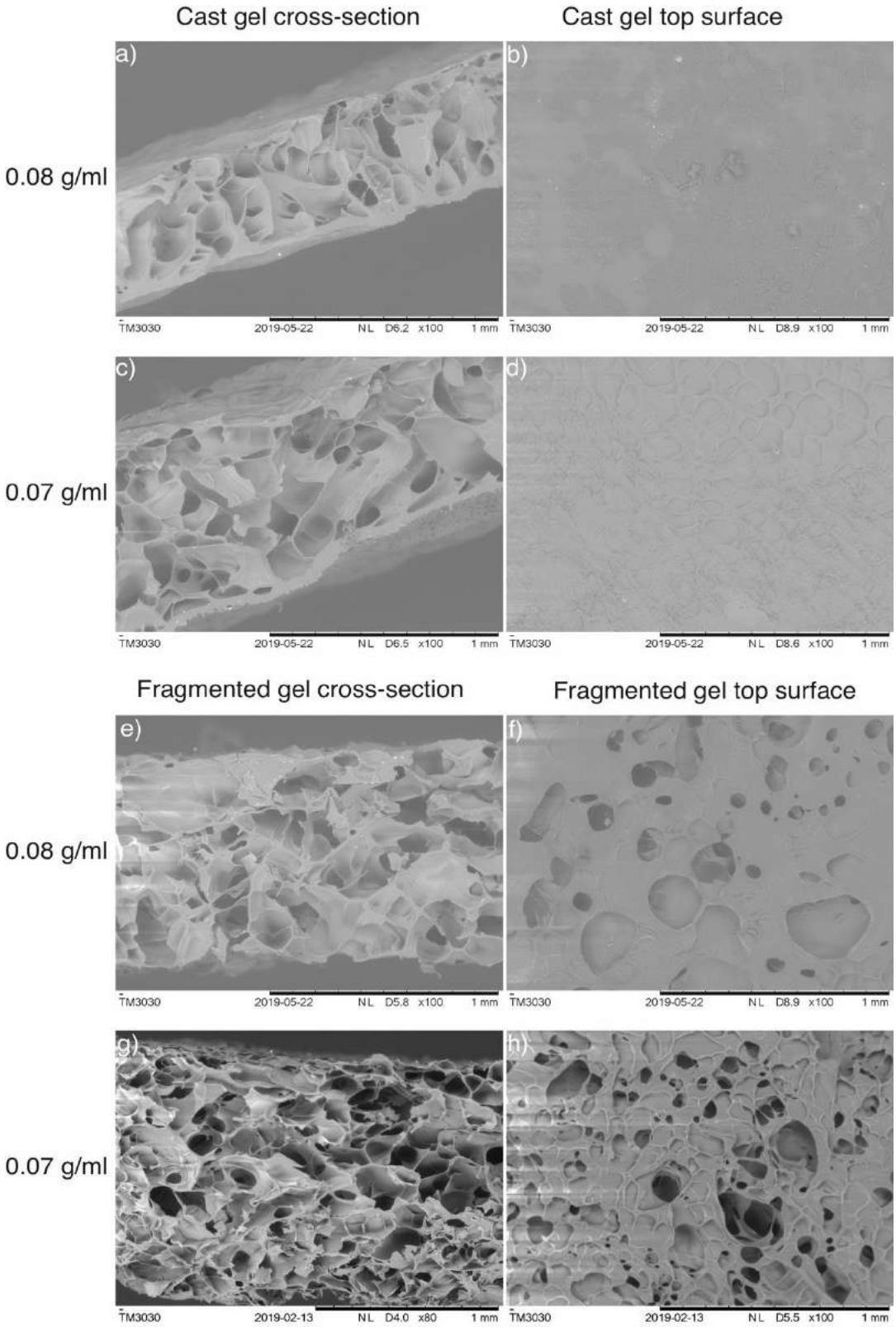

Figure 3.4: Representative SEM micrographs of fragmented vs cast poly-ε-lysine hydrogel variants. Images a,b,e and f) are 30-0.08-Oct and c,d,g and h) are 30-0.07-Oct. Top images are cast hydrogels and bottom images are fragmented hydrogels.

The effect of fragmenting the hydrogels and increasing the polymer density on the percentage porosity and overall pore size was analysed (**Figure 3.4**). The fragmented hydrogel micrographs demonstrate an interconnected porosity throughout both the cross-section and the hydrogel surface. The cast hydrogel variants had porosity throughout their cross-sections, but had no pores on their surface. For the fragmented variants, increasing the polymer density seemed to reduce the porosity slightly of the hydrogels on the surface and throughout the cross-section. Whereas for the two cast hydrogels, altering the polymer density did not seem to affect the porosity in the cross-section. These micrographs support the trend for hydrogel porosity inferred from the percentage water content data represented in Figure 3.2.

3.2.4 Porosity and swelling behaviour of freeze-dried of fragmented and cast pεK hydrogels

Table 3.1: Pore size and percentage porosity of poly-ε-lysine hydrogel variants. F= fragmented C= cast (n=3)

Gel chemistry	Pore size (µm)
30-0.07-Oct F	117.075 ± 5.5
30-0.08-Oct F	99.6 ± 17.4
30-0.07-Oct C	105.5 ± 7.3
30-0.08-Oct C	76.4 ±7.15

The average pore sizes of the fragmented and cast hydrogel variants, calculated using ImageJ to measure the pores seen in the SEM micrographs (**Table 3.1**), demonstrated the hydrogels made with the polymer density of 0.07 g/ml had a higher average pore size compared to the higher density of 0.08 g/ml. Also, the fragmented hydrogel variants had a higher average pore size than the cast hydrogel with the same chemistry.

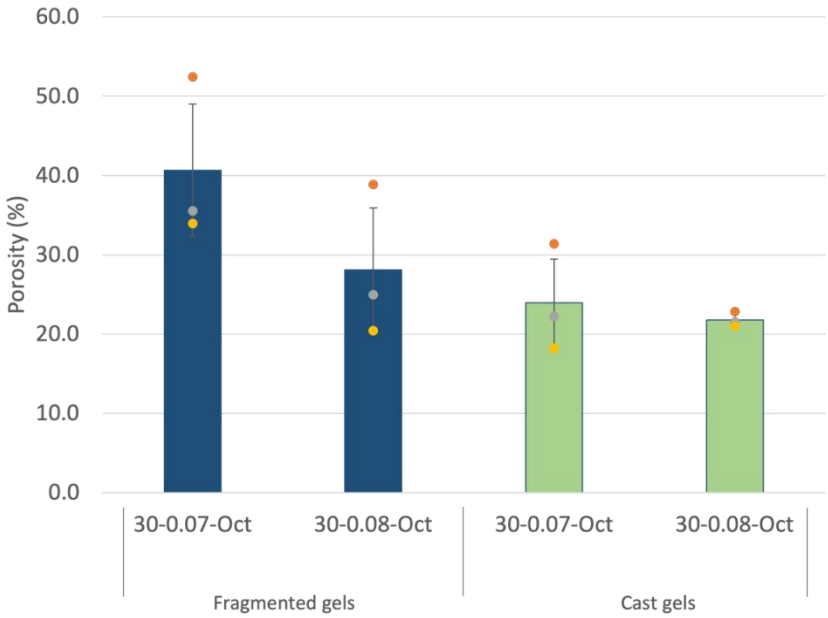

Figure 3.5: Percentage porosity of fragmented vs cast poly-ε-lysine hydrogel variants. 3 samples/run (n=3) Graph plots mean ± SD and individual data points. **Key:** Blue bars = fragmented hydrogel variants, Green bars = cast hydrogel variants

Hydrogels manufactured by a fragmentation method were shown to have a higher porosity than cast hydrogels (**Figure 3.5**)**.** The porosity was calculated based on weight displacement measurements with ethanol as a solvent. It can be seen that the percentage porosity is higher in the two fragmented hydrogel variants compared to the two cast hydrogel variants with the same polymer chemistry. Similar to the trends for percentage water content and average pore size, the 0.07 g/ml polymer density variants have a higher porosity than the 0.08 g/ml, however, there are no significant differences between the variants.

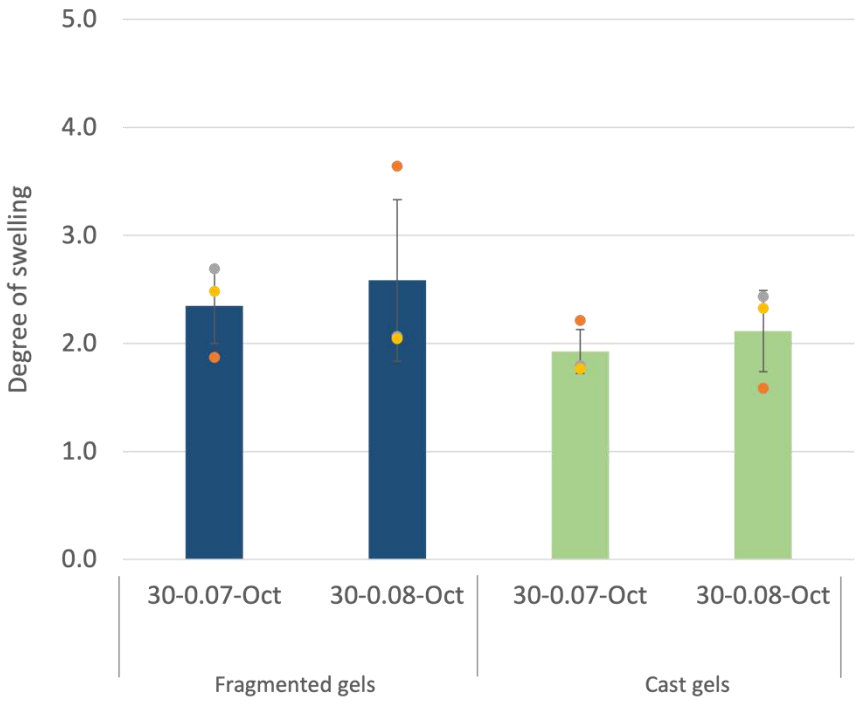

Figure 3.6: Degree of swelling of fragmented vs cast poly-ε-lysine hydrogel variants. 3 samples/run (n=3) Graph plots mean ± SD and individual data points. **Key:** Blue bars = fragmented hydrogel variants, Green bars = cast hydrogel variants

Fragmented hydrogel variants have a higher swelling ratio compared to the cast variants (**Figure 3.6**). The degree of swelling of a hydrogel varies based on the strength of the cross-linking throughout the hydrogels structure. The swelling ratio has units of grams per gram and indicates the weight of solvent that it can absorb per grams of its own weight. The 0.08 g/ml density variants have a higher degree of swelling compared to the 0.07 g/ml variants, however this is minimal and with no significant difference shown.

Table 3.2: Swelling behaviour of fragmented and cast hydrogel variants based on change in diameter over time in PBS and dH_2O. Value is the mean ± the standard deviation with the percentage of the original diameter. F= fragmented C= cast (n=3)

	Sample	Original Diameter (mm)	1 week	4 weeks	8 weeks
PBS	30-0.07-Oct F	11.50 ± 0	11.12 (97%) ± 0.5	11.14 (97%) ± 0.1	11.3 (98%) ± 0.2
	30-0.08-Oct F	11.50 ± 0	10.65 (92%) ± 0.1	10.46 (91%) ± 0.1	10.2 (88%) ± 0.3
	30-0.07-Oct C	11.50 ± 0	11.47 (99%) ± 0.3	11.45 (99%) ± 0.2	11.4 (98%) ± 0.2
	30-0.08-Oct C	11.50 ± 0	11.38 (99%) ± 0.2	11.54 (100%) ± 0.1	11.5 (100%) ± 0.2
dH_2O	30-0.07-Oct F	11.50 ± 0	11.77 (102%) ± 0.1	11.57 (100%) ± 0.1	11.7 (101%) ± 0.2
	30-0.08-Oct F	11.50 ± 0	10.64 (93%) ± 0.4	10.38 (90%) ± 0.2	10.8 (94%) ± 0.3
	30-0.07-Oct C	11.50 ± 0	11.87 (103%) ± 0.1	11.7 (101%) ± 0.1	11.8 (102%) ± 0.03
	30-0.08-Oct C	11.50 ± 0	11.67 (101%) ± 0.2	11.58 (101%) ± 0.2	11.9 (103%) ± 0.05

The swelling behaviour of the fragmented and cast hydrogel variants, characterised by measuring the change in diameter of a punched hydrogel section over the space of 8 weeks (**Table 3.2**), showed there was a negligible effect on the hydrogel diameter for all hydrogel variants. All of the hydrogels had the same original diameter of 11.5 mm as the same punch was used. The percentage change above 100% shows that swelling has taken place, and below 100% that the hydrogel sample has contracted. The highest difference seen was with the fragmented 30-0.08-Oct variant, which contracted to 88-93% of its original diameter in both PBS and dH_2O. These data suggest that the fragmented and cast hydrogels are stable in both PBS and dH_2O for up to 8 weeks at room temperature.

3.2.5 Degradation of fragmented and cast pεK hydrogels

Table 3.3: Degradation behaviour of fragmented and cast hydrogel variants based on weight loss over time in PBS, NaOH and Trypsin. Value is the mean ± the standard deviation with the percentage of the original weight. F= fragmented C= cast (n=3)

	Sample	Original Weight (g)	1 week	4 weeks	8 weeks
PBS	30-0.07-Oct F	0.23 ± 0.06	0.18 (78%) ± 0.06	0.16 (71%) ± 0.05	0.16 (70%) ± 0.04
	30-0.08-Oct F	0.32 ± 0.04	0.28 (86%) ± 0.04	0.27 (84%) ± 0.03	0.24 (75%) ± 0.03
	30-0.07-Oct C	0.08 ± 0.03	0.09 (116%) ± 0.04	0.07 (89%) ± 0.02	0.07 (85%) ± 0.02
	30-0.08-Oct C	0.09 ± 0.01	0.11 (119%) ± 0.01	0.1 (110%) ± 0.01	0.09 (100%) ± 0.1
NaOH	30-0.07-Oct F	0.26 ± 0.05	0.25 (99%) ± 0.03	0.24 (94%) ± 0.03	0.25 (98%) ± 0.05
	30-0.08-Oct F	0.31 ± 0.05	0.28 (90%) ± 0.03	0.27 (86%) ± 0.03	0.26 (83%) ± 0.05
	30-0.07-Oct C	0.12 ± 0.02	0.13 (106%) ± 0.01	0.1 (83%) ± 0.02	0.1 (81%) ± 0.04
	30-0.08-Oct C	0.12 ± 0.01	0.14 (113%) ± 0.01	0.12 (96%) ± 0.01	0.12 (96%) ± 0.02
Trypsin	30-0.07-Oct F	0.29 ± 0.05	0.18 (63%) ± 0.05	0.18 (64%) ± 0.03	
	30-0.08-Oct F	0.34 ± 0.03	0.28 (83%) ± 0.03	0.27 (80%) ± 0.02	
	30-0.07-Oct C	0.14 ± 0.01	0.09 (63%) ± 0.02	0.08 (56%) ± 0.01	
	30-0.08-Oct C	0.13 ± 0.01	0.1 (78%) ± 0.01	0.09 (70%) ± 0.01	

Over an 8 week period it was demonstrated the fragmented hydrogels degraded more than the cast hydrogel equivalents as evaluated by weight loss measurements (**Table 3.3**). The percentage of the hydrogels original weight was calculated, to establish the extent of degradation that had occurred. The hydrogels incubated in PBS show a percentage weight loss after 8 weeks. For fragmented hydrogels, the percentage weight loss was 25-30 % and cast hydrogel variants had a maximum weight loss of 15 %. The hydrogels left in NaOH also demonstrated a weight loss over 8 weeks, which ranged between 2-19 % of weight loss, however there was no

trend seen between the hydrogels that were either fragmented or cast. After 4 weeks, the use of trypsin was discontinued as this needed to be replenished every day, and there wasn't a significant change between the weight of the hydrogels after 1 week and 4 weeks. However, these hydrogel variants demonstrated the most weight lost after 4 weeks, compared to hydrogels left in PBS and NaOH. Fragmented variants lost between 20-36 % of their original weight and cast hydrogel variants lost 30-44 %. There were no differences seen between the degradation of fragmented hydrogels compared to cast hydrogels with the same chemistry, however the lower polymer chemistry variants demonstrated a higher percentage weight loss over this time.

Rheological characterisation of fragmented and cast pεK hydrogels

3.2.6 Amplitude sweep

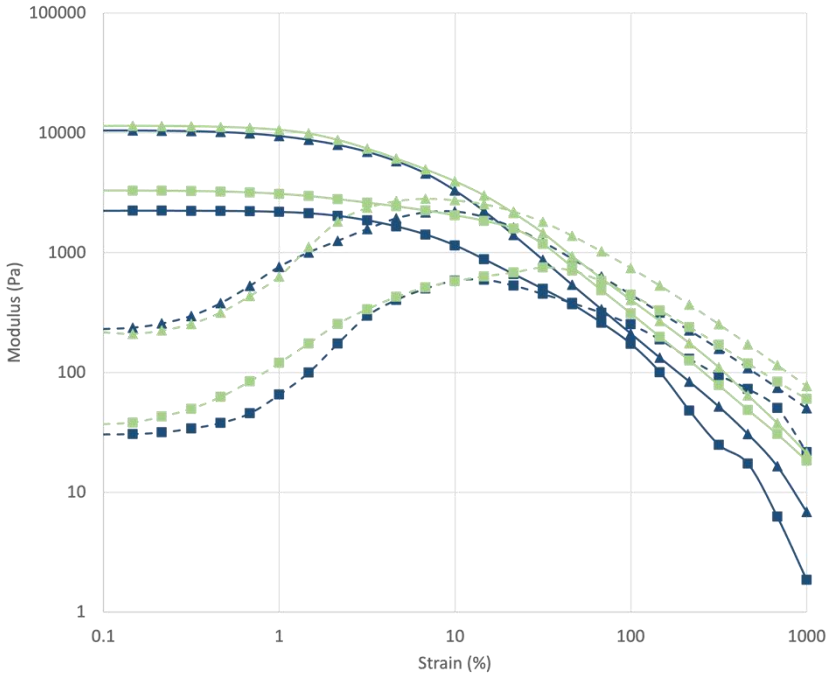

Figure 3.7: Amplitude sweep of fragmented vs cast poly-ε-lysine hydrogel variants. (n=3) **Key:** Navy blue lines = fragmented gels, Green lines = cast gels, Squares = 0.07 g/ml polymer density, Triangles = 0.08 g/ml polymer density, Dashed lines = Storage modulus (G'), Solid lines = Loss modulus (G'')

Fragmenting the hydrogels during polymerisation and increasing the polymer density was shown to have an influence on the viscoelastic properties (**Figure 3.7**). The amplitude dependence of modulus was plotted and the modulus at which the storage modulus (G') and (G'') crossed over in the amplitude sweep was recorded.

In both cases for the different polymer densities, the cast hydrogel had a higher crossover modulus compared to the fragmented hydrogel with the same chemistry. The hydrogels with the higher polymer density of 0.08 g/ml had a higher crossover modulus in both the fragmented and the cast hydrogels. Significance was seen when comparing the crossover moduli of 30-0.08-Oct cast with 30-0.07-Oct cast and fragmented variants, with p=0.008 and p=0.003 respectively, and 30-0.08-Oct fragmented was significantly higher than 30-0.07-Oct fragmented, p=0.038.

This data was included to show that the fragmented and cast pεK variants demonstrate rheological behaviour typical of hydrogels, where a yield point is reached, and after this point, the storage and loss modulus decrease. The amplitude sweep data was used to calculate the complex modulus for comparison between different hydrogel variants.

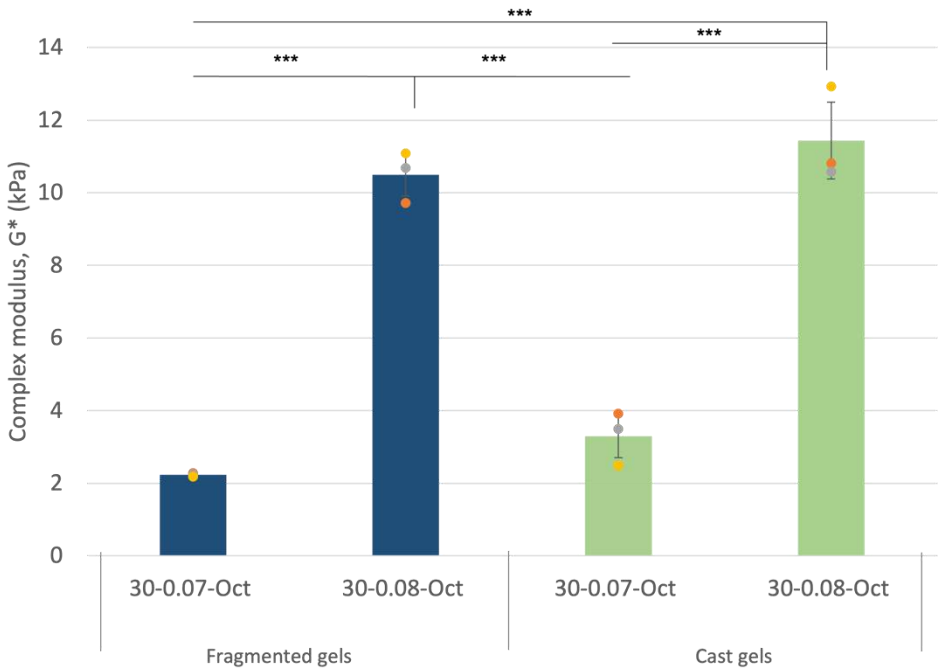

Figure 3.8: Complex modulus of fragmented vs cast poly-ε-lysine hydrogel variants (n=3) (*** = p < 0.001) Graph plots mean ± SD and individual data points. **Key:** Blue bars = fragmented hydrogel variants, Green bars = cast hydrogel variants

Fragmenting the hydrogels during polymerisation and reducing the polymer density was seen to reduce the complex moduli (**Figure 3.8**). The complex moduli were calculated for the different hydrogel variants to determine the resistance of the hydrogel to deformation. This was taken from the amplitude sweep data at a strain

value equal to 0.1 %. This value was chosen as it is in the linear viscoelastic region (LVER) before the yield point of the hydrogel. It can be seen that increasing the polymer density has the biggest influence on the complex modulus, with the both the fragmented and cast 0.08 g/ml variants being significantly higher than the lower 0.07 g/ml variants, all p values < 0.001. Fragmenting the hydrogels reduced the complex modulus of the hydrogels when compared with cast variants, however this had less of an influence.

3.2.7 Frequency Sweep

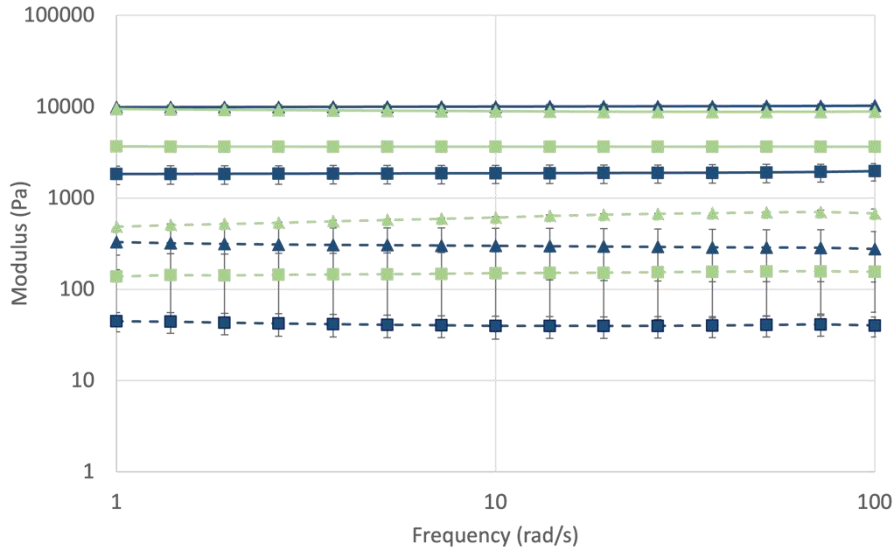

Figure 3.9: Frequency sweep of fragmented vs cast poly-ε-lysine hydrogel variants. (n=3) **Key:** Navy blue lines = fragmented gels, Green lines = cast gels, Squares = 0.07 g/ml polymer density, Triangles = 0.08 g/ml polymer density, Dashed lines = Storage modulus (G'), Solid lines = Loss modulus (G'')

Manufacturing the hydrogels via fragmentation and varying the polymer density was shown to have an effect on the frequency dependence of modulus (**Figure 3.9**). This frequency data were included to further corroborate the hydrogels exhibiting typical rheological behaviour, in that all of the hydrogel variants show parallel G' and G'' throughout the frequency sweep, and all exhibited a storage modulus that was consistently higher than the loss modulus. The results show that increasing the polymer density increases the modulus, and fragmenting the hydrogels reduces the modulus. The differences were significant in the storage moduli at 10 rad/s, between 30-0.08-Oct cast with 30-0.07-Oct cast, p=0.002 and 30-0.07-Oct fragmented, p=0.001, and between 30-0.08-Oct fragmented with 30-0.07-Oct cast and 30-0.07-Oct fragmented, with p=0.001 and p=0.0003 respectively. There were

no significant differences observed in the loss moduli of the fragmented and cast hydrogel variants. It can be seen that varying the polymer density has a larger influence on the modulus than fragmenting the hydrogels does, as the fragmented hydrogels are only slightly weaker than the cast variants with the same polymer chemistry.

Mechanical characterisation of fragmented and cast pεK hydrogels

3.2.8 Compressive Measurements

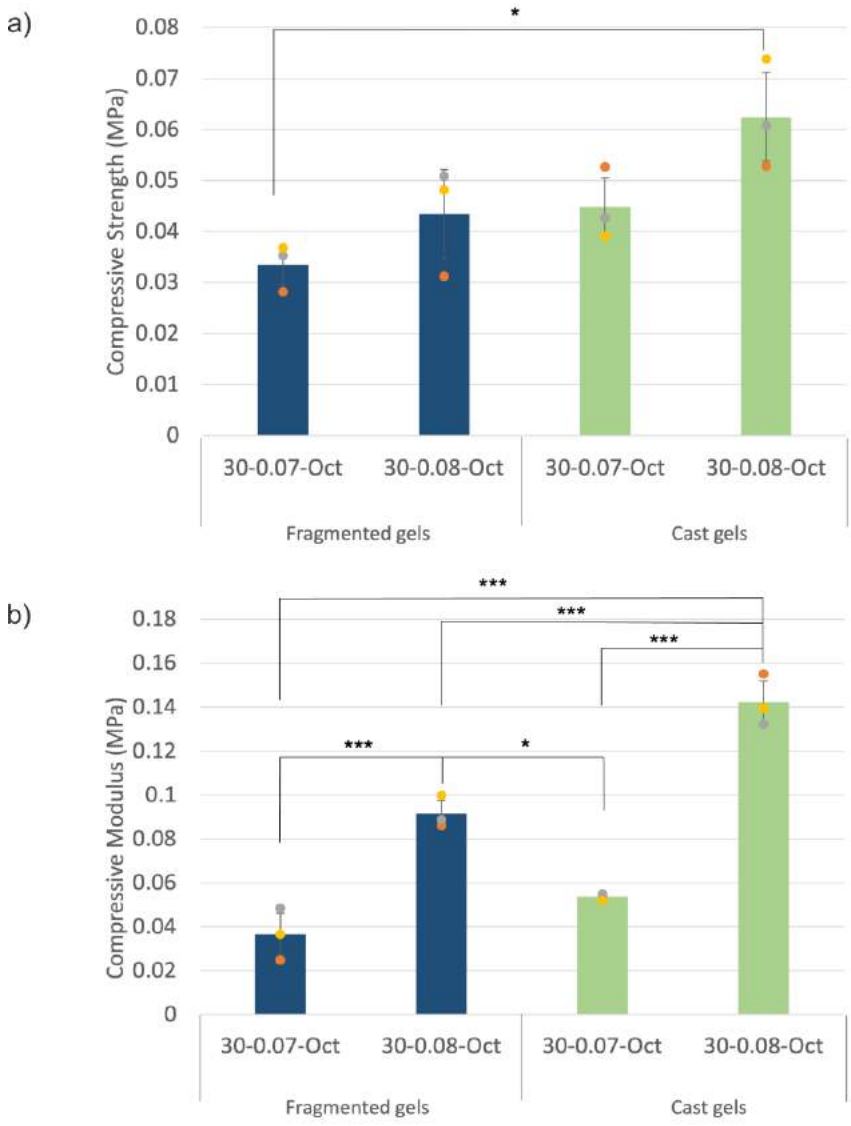

Figure 3.10: a) Ultimate compressive strength of fragmented vs cast poly-ε-lysine hydrogel variants b) Compressive modulus of poly-ε-lysine hydrogel variants. 5 samples/run (n=3) (* = $p < 0.05$, ** = $p < 0.01$, *** = $p < 0.001$) Graph plots mean ± SD and individual data points. **Key:** Blue bars = fragmented hydrogel variants, Green bars = cast hydrogel variants

Increasing the polymer density and fragmentation of the hydrogels was shown to have an effect on the mechanical properties (**Figure 3.10**). It can be seen that fragmenting the hydrogels reduces the compressive strength compared to cast hydrogels with the same chemistry and that increasing the polymer density increases the compressive strength. The only significant differences in the compressive strength are between the fragmented low density variant and the cast high density variant, $p = 0.029$. A similar trend is shown when comparing the compressive moduli of the fragmented and cast hydrogel variants. However in this instance, varying the polymer density has a much bigger influence on the compressive properties. Fragmented 30-0.08-Oct has a significantly higher modulus than fragmented 30-0.07-Oct, $p < 0.001$, and cast 30-0.07-Oct, $p = 0.004$. Cast 30-0.07-Oct has a significantly higher modulus than all three other variants, with all p values < 0.001. The mechanical data show that the introduction of pores into the structure via fragmentation reduces the mechanical properties of the hydrogel.

3.3 Macroporous hydrogel physical characterisation results:

3.3.1 Optical properties of macroporous hydrogel variants

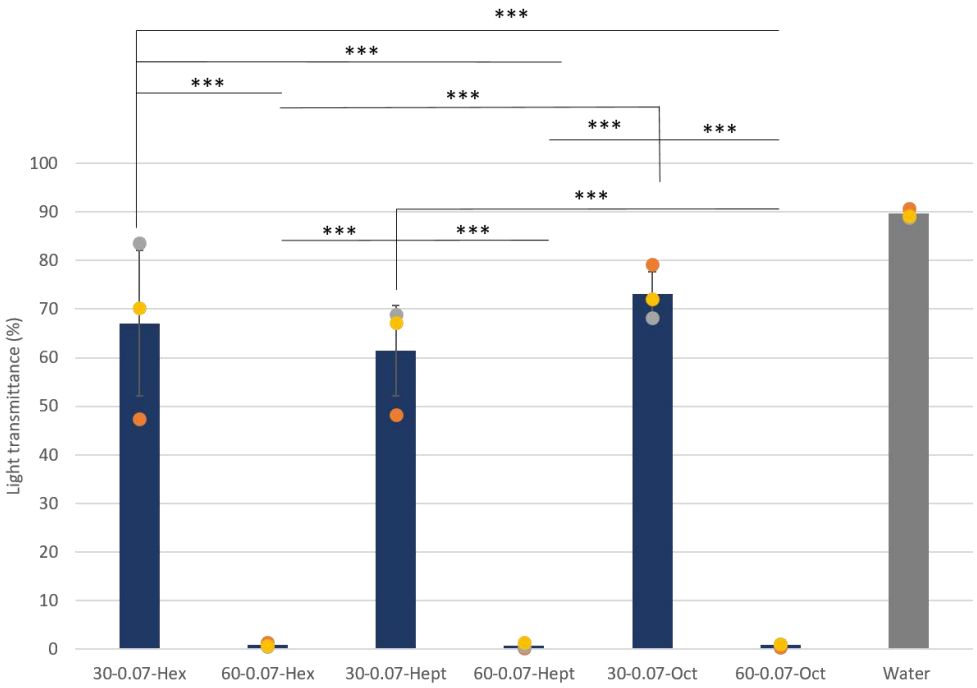

Figure 3.11: Percentage light transmittance of macroporous poly-ε-lysine variants. 5 samples/run (n=3) (*** = $p < 0.001$) Graph plots mean ± SD and individual data points. **Key:** Blue bars = macroporous hydrogel variants, Grey bar = water control

Altering the di-acid cross-linker and increasing the percentage cross-linking was shown to influence the percentage light transmittance (**Figure 3.11**). It can be seen that the three hydrogel variants with 30 % cross-linking had significantly higher light transmittance than the three variants with 60 % cross-linking. Out of the 30 % cross-linked hydrogels, the variant with the highest percentage light transmittance was 30-0.07-Oct (77%), followed by 30-0.07-Hex (63%) and finally 30-0.07-Hept (61%), however there was no significant differences between these three variants. All three 30 % cross-linked variants had significantly higher light transmittance than all three 60 % cross-linked variants, with all p values < 0.001.

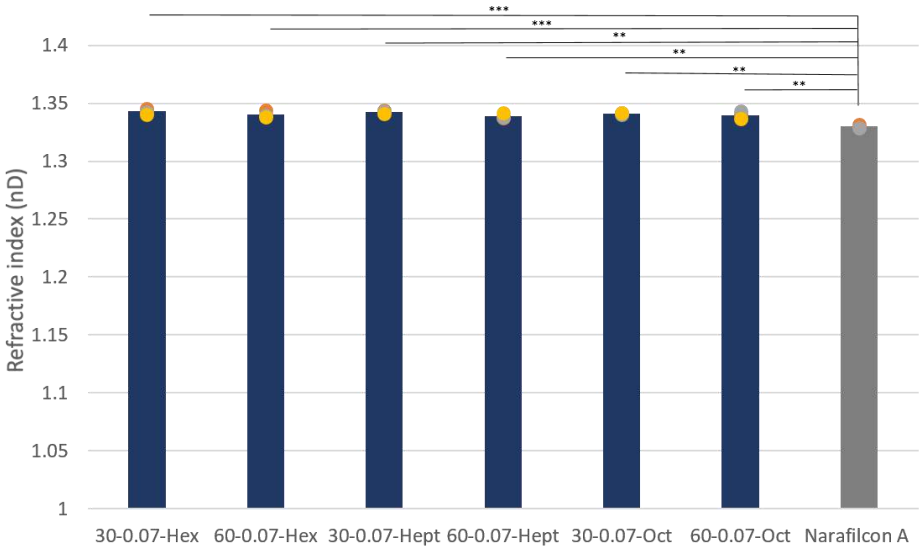

Figure 3.12: Refractive index of macroporous poly-ε-lysine variants. 3 samples/run (n=3) (** = p < 0.01 and *** = p < 0.001) Graph plots mean ± SD and individual data points. **Key:** Blue bars = macroporous hydrogel variants, Grey bar = Contact lens control

Varying the di-acid cross-linker and increasing the percentage cross-linker had little effect on the refractive index (**Figure 3.12**)**.** The refractive index of all the macroporous hydrogels were very similar, despite the contrast in percentage light transmittance results. All of the hydrogel variants had a refractive index in the range 1.339-1.343 nD. The contact lens control had a slightly lower refractive index of 1.329 nD. There were no significant differences in between the hydrogel variants, but all of the hydrogels were seen to be significantly higher than the contact lens control, all p values < 0.05.

3.3.2 Percentage Water Content of macroporous hydrogel variants

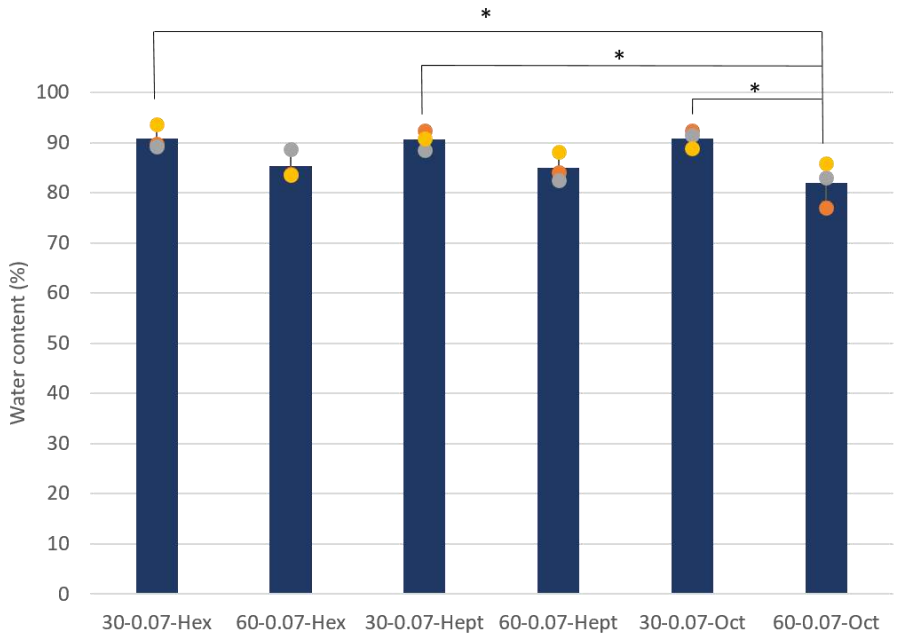

Figure 3.13: Percentage water content of macroporous poly-ε-lysine variants. 3 samples/run (n=3) (* = $p < 0.05$) Graph plots mean ± SD and individual data points.

Increasing the percentage cross-linking was shown to have more of an effect on the percentage water content than altering the di-acid cross-linker (**Figure 3.13**)**.** These data show that the three 30 % cross-linked hydrogel variants have a higher percentage water content than the higher percentage cross-linking hydrogel variants at 60 %. The 30 % cross-linked hydrogels all have water contents of 90 %, whereas the 60 % are slightly lower at between 81-85 %. There are little differences seen between the different di-acid cross-linker and the percentage water content. There were significant differences seen between the 60-0.07-Oct variant and all three 30 % cross-linked variants. 30-0.07-Hex, 30-0.07-Hept and 30-0.07-Oct had significantly higher water contents than 60-0.07-Oct with p values of 0.024, 0.03 and 0.024 respectively.

3.3.3 SEM Micrographs of macroporous hydrogel variants

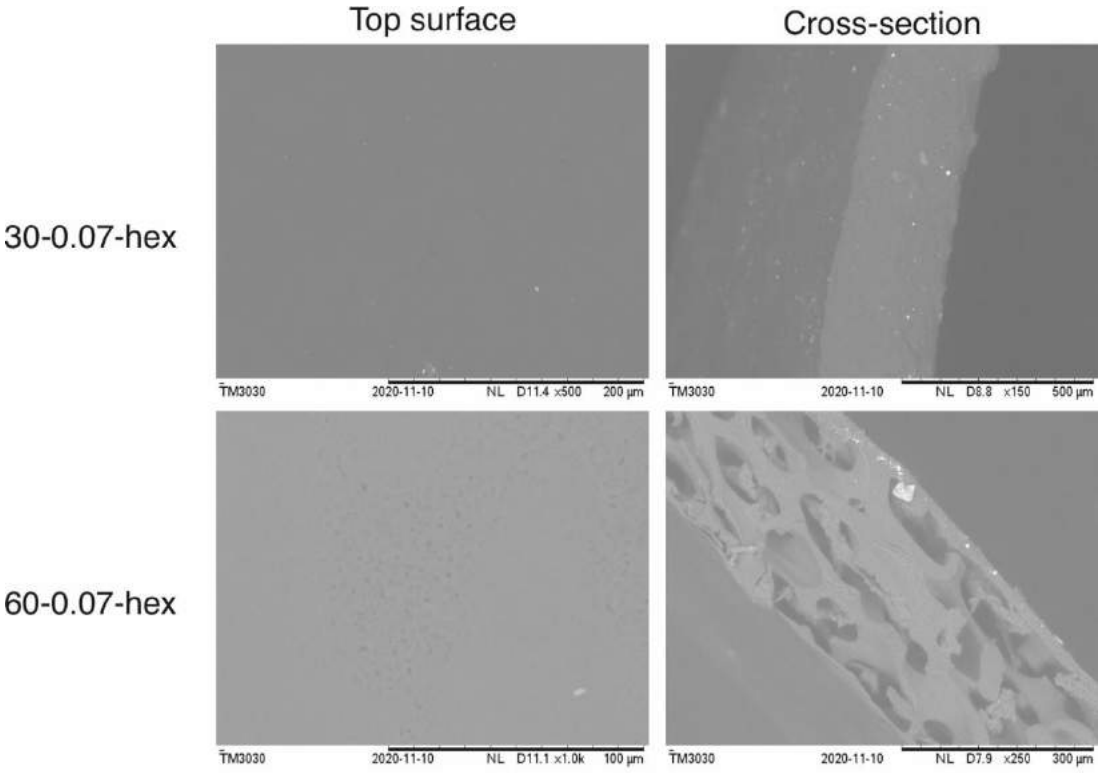

Figure 3.14: SEM micrographs of hexanedioic macroporous poly-ε-lysine variants

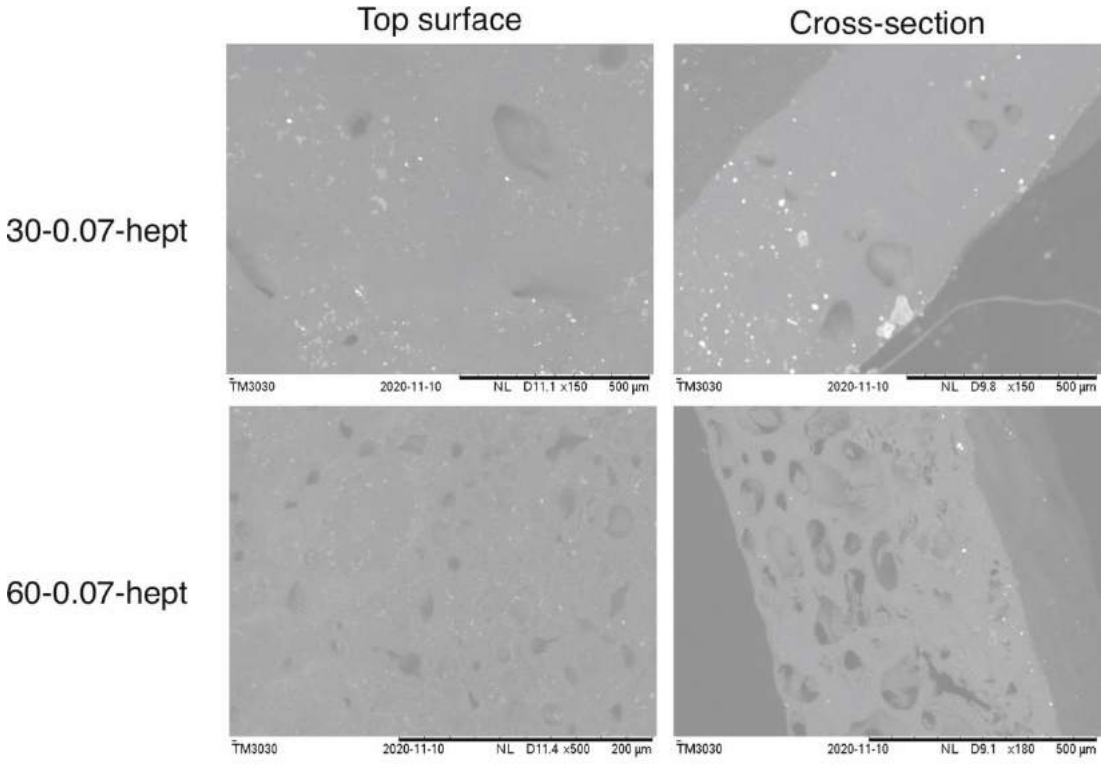

Figure 3.15: SEM micrographs of heptanedioic macroporous poly-ε-lysine variants

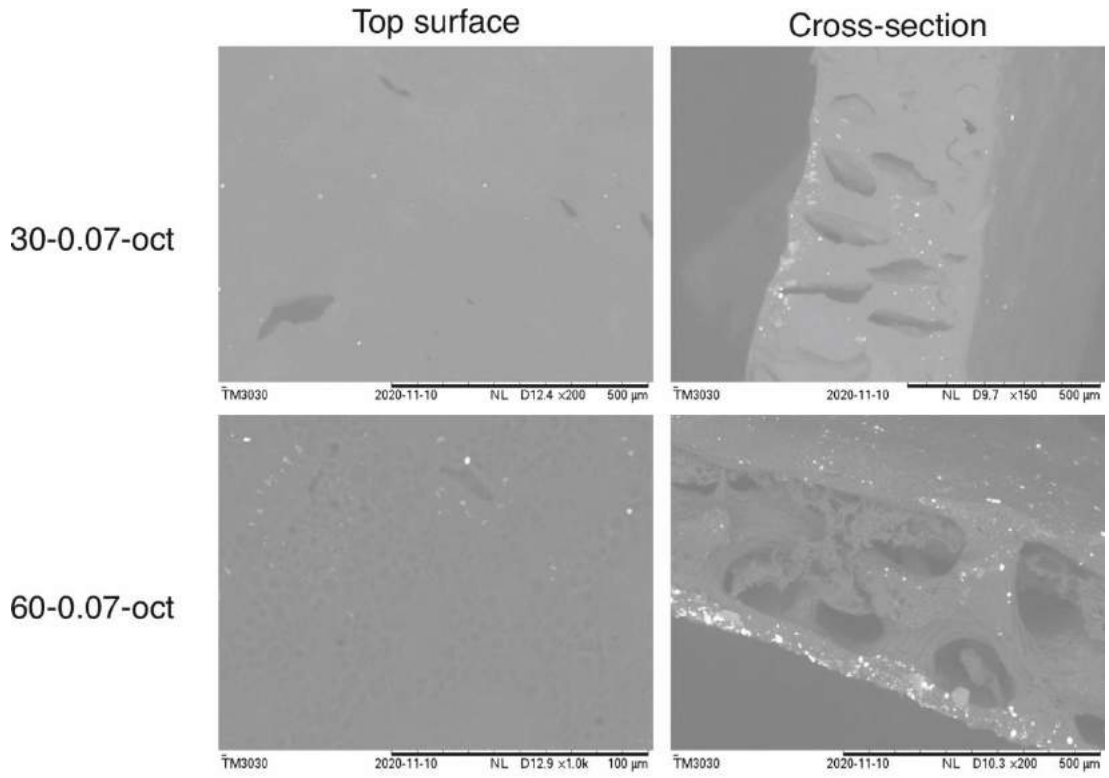

Figure 3.16: SEM micrographs of octanedioic macroporous poly-ε-lysine variants

The microstructure of the surface and the cross-sections of the macroporous hydrogel variants (**Figures 3.14-3.16**) demonstrated there were few pores on the top surface, whereas pores were visible throughout the cross-sections. Increasing the percentage cross-linking was shown to increase the porosity throughout the cross-sections in all hydrogel variants. Increasing the di-acid chain length was shown to increase the porosity in the lower percentage cross-linking variants. Due to the lack of pores in all of the measured hydrogel variants, the average pore size was unable to be calculated.

3.3.4 Swelling Behaviour of macroporous hydrogel variants

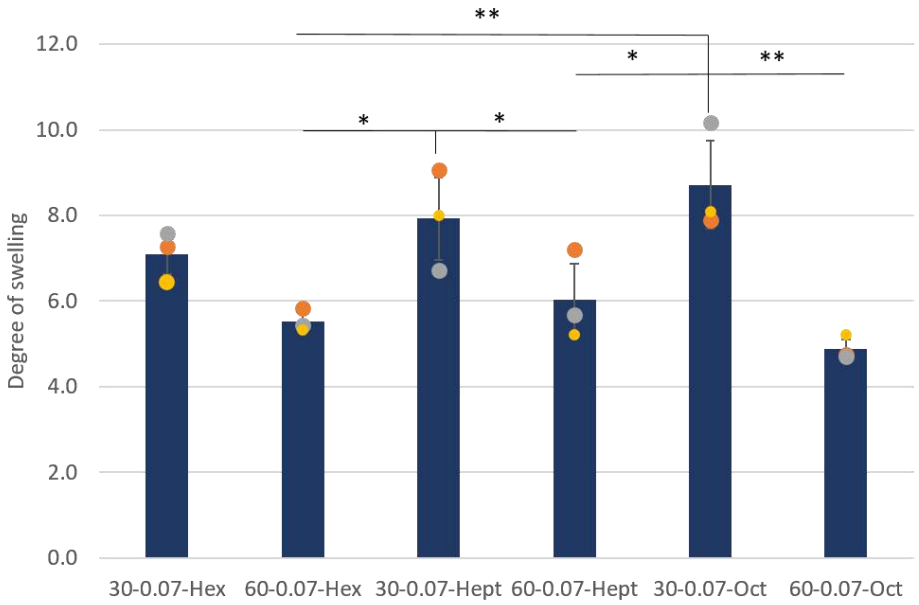

Figure 3.17: Degree of swelling of macroporous poly-ε-lysine variants. 3 samples/run (n=3) (* = $p < 0.05$, *** = $p < 0.001$) Graph plots mean ± SD and individual data points.

Increasing the percentage cross-linking and the chain length of the di-acid cross-linker was shown to influence the degree of swelling (**Figure 3.17**). It can be seen that increasing the percentage cross-linking of the hydrogel variant decreases the degree of swelling, as there is less water retained in the structure. Additionally it can be seen that increasing the chain length of the di-acid cross-linker from C6 to C8 increases the degree of swelling for 30 % cross-linked variants. This is likely due to the increasing space within the structure of the hydrogel due to the longer chain length. The 60 % cross-linked variants follow a similar trend, however at a di-acid length of C8, the degree of swelling decreases again. Significant differences were seen throughout these results. 30-0.07-Hept was significantly higher than 60-0.07-Hex and 60-0.07-Oct with p values of 0.049 and 0.012 respectively. 30-0.07-Oct was significantly higher than 60-0.07-Hex, 60-0.07-Hept and 60-0.07-Oct with p values of 0.008, 0.026 and 0.002 respectively.

Table 3.4: Swelling behaviour of macroporous and cast hydrogel variants based on change in diameter over time in PBS and dH_2O. Value is the mean ± the standard deviation with the percentage of the original diameter. M = macroporous C = cast (n=3)

	Sample	Original Diameter (mm)	1 week	4 weeks	8 weeks
PBS	30-0.07-Oct M	11.50 ± 0	13 (113%) ± 0.5	12.9 (112%) ± 0.5	13 (113%) ± 0.3
	60-0.07-Oct M	11.50 ± 0	12.1 (105%) ± 0.05	12 (104%) ± 0.04	11.9 (104%) ± 0.1
	30-0.07-Oct C	11.50 ± 0	11.45 (99%) ± 0.2	11.4 (99%) ± 0.2	11.6 (101%) ± 0.1
	60-0.07-Oct C	11.50 ± 0	11.8 (102%) ± 0.01	11.7 (102%) ± 0.02	11.45 (100%) ± 0.2
dH_2O	30-0.07-Oct M	11.50 ± 0	16 (139%) ± 0.15	15.8 (137%) ± 0.2	15.9 (138%) ± 0.3
	60-0.07-Oct M	11.50 ± 0	13.3 (115%) ± 0.6	13.2 (115%) ± 0.6	14.4 (125%) ± 0.2
	30-0.07-Oct C	11.50 ± 0	11.8 (103%) ± 0.1	11.7 (102%) ± 0.1	12 (104%) ± 0.3
	60-0.07-Oct C	11.50 ± 0	11.5 (100%) ± 0.3	11.4 (99%) ± 0.3	11.2 (97%) ± 0.1

Increasing the percentage cross-linking and the chain length of the di-acid cross-linker was shown to influence the degree of swelling (**Table 3.4**). Overall, it is shown that the macroporous variants swell in both PBS and dH_2O compared to cast hydrogels with the same chemistry. The macroporous variants swell more in dH_2O than those left in PBS, and the 30 % cross-linked variants swell more than the 60 % cross-linked. The highest increase in diameter occurred in the first week, and after this time the diameter was maintained. After 8 weeks, the macroporous hydrogels remained swollen, whereas the cast hydrogels were more stable with a similar diameter to the original. Macroporous variants in PBS had a swelling of 104-113 % after 8 weeks, whereas when left in dH_2O this swelling was seen to be higher at 125-138%. The cast hydrogel variants were shown to behave similarly in PBS and dH_2O, maintaining a diameter within ± 4 % of the original punched diameter of 11.5 mm.

3.3.5 Degradation of macroporous hydrogel variants

Table 3.5: Degradation behaviour of macroporous and cast hydrogel variants based on weight loss in PBS, NaOH and Trypsin. Value is the mean ± the standard deviation and percentage of the original weight. M = macroporous C = cast (n=3)

	Sample	Original Weight (g)	1 week	4 weeks	8 weeks
PBS	30-0.07-Oct M	0.19 ± 0.01	0.14 (76%) ± 0.02	0.14 (72%) ± 0.02	0.13 (70%) ± 0.02
	60-0.07-Oct M	0.13 ± 0.02	0.12 (95%) ± 0.01	0.11 (89%)± 0.01	0.1 (82%) ± 0.01
	30-0.07-Oct C	0.13 ± 0.02	0.11 (89%) ± 0.1	0.097 (77%) ± 0.02	0.1 (79%) ± 0.02
	60-0.07-Oct C	0.076 ± 0.02	0.08 (107%) ± 0.01	0.07 (94%) ± 0.01	0.06 (82%) ± 0.01
NaOH-	30-0.07-Oct M	0.17 ± 0.01	0.11 (63%) ± 0.003	0.09 (54%) ± 0.003	0.08 (48%) ± 0.005
	60-0.07-Oct M	0.13 ± 0.001	0.12 (90%) ± 0.01	0.1 (78%) ± 0.004	0.087 (67%) ± 0.003
	30-0.07-Oct C	0.11 ± 0.01	0.10 (94%) ± 0.01	0.08 (77%) ± 0.02	0.077 (72%) ± 0.003
	60-0.07-Oct C	0.09 ± 0.01	0.084 (97%) ± 0.01	0.08 (92%) ± 0.01	0.07 (79%) ± 0.003
Trypsin	30-0.07-Oct M	0.2 ± 0.01	0.12 (61%) ± 0.01	0.11 (57%) ± 0.002	
	60-0.07-Oct M	0.13 ± 0.01	0.12 (96%) ± 0.002	0.11 (90%) ± 0.004	
	30-0.07-Oct C	0.11 ± 0.02	0.1 (89%) ± 0.01	0.09 (82%) ± 0.01	
	60-0.07-Oct C	0.09 ± 0.01	0.08 (93%) ± 0.01	0.086 (99%) ± 0.003	

The degradation of the macroporous and cast hydrogels over an 8 week period was evaluated by weight loss measurements (**Table 3.5**). Again, the hydrogel variants were left in either PBS, NaOH or trypsin. After 8 weeks in PBS, the macroporous variants showed similar degradation behaviour to the cast variants with the same polymer chemistry. Macroporous variants showed a weight loss of 18-30 % when left in PBS for 8 weeks whereas cast variants lost 18-21 %. After 8 weeks in NaOH, the macroporous variants showed a more significant degradation, compared to cast hydrogels with the same chemistry. In particular, the 30 % cross-linked macroporous hydrogel had lost over half of its weight when compared to the

original. Whereas, the 60-0.07-Oct macroporous variant lost 33 % of its original weight, and cast variants between 21-28 % when left in NaOH. Again, the use of trypsin in this study was discontinued after 4 weeks because of the high frequency of changing the solution. After 4 weeks, it was shown that there was more degradation in the fragmented hydrogels compared to cast hydrogels with the same chemistry. Macroporous variants showed a weight loss of 10-43 % when left in PBS for 4 weeks, whereas cast variants lost 1-18% of their original weight. Additionally, there was more degradation in the 30 % cross-linked variants compared to the 60 % cross-linked.

Rheological Characterisation of macroporous hydrogel variants

3.3.6 Amplitude Sweep

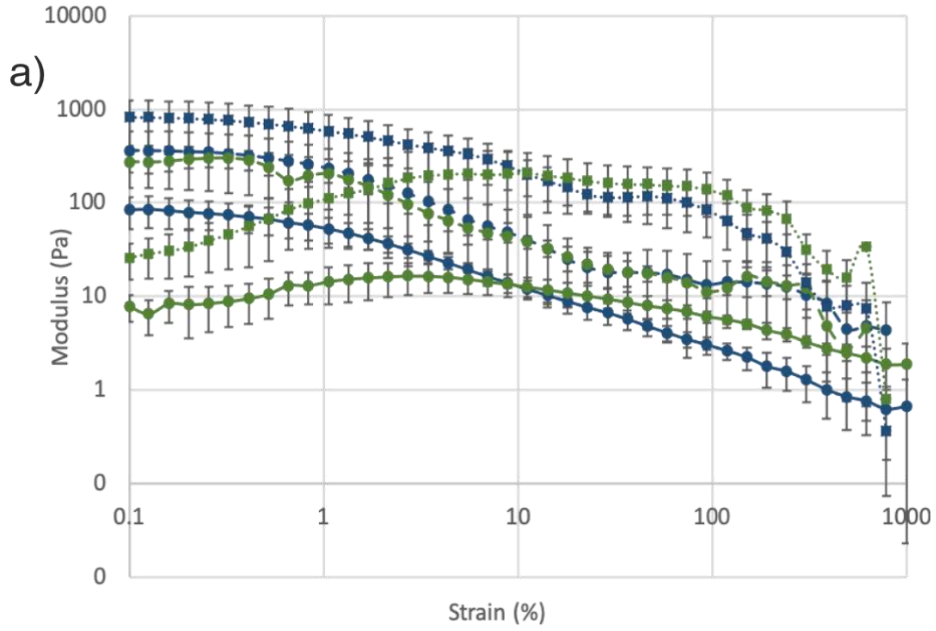

Figure 3.18 a: Amplitude sweep of 30 % cross-linked macroporous poly-ε-lysine hydrogel variants. (n=3) **Key:** Navy blue lines = Storage modulus (G'), Green lines = Loss modulus (G''), Solid lines and circles = Hexanedioic acid, Dashed lines and circles = Heptanedioic acid, Dashed lines and squares = Octanedioic acid.

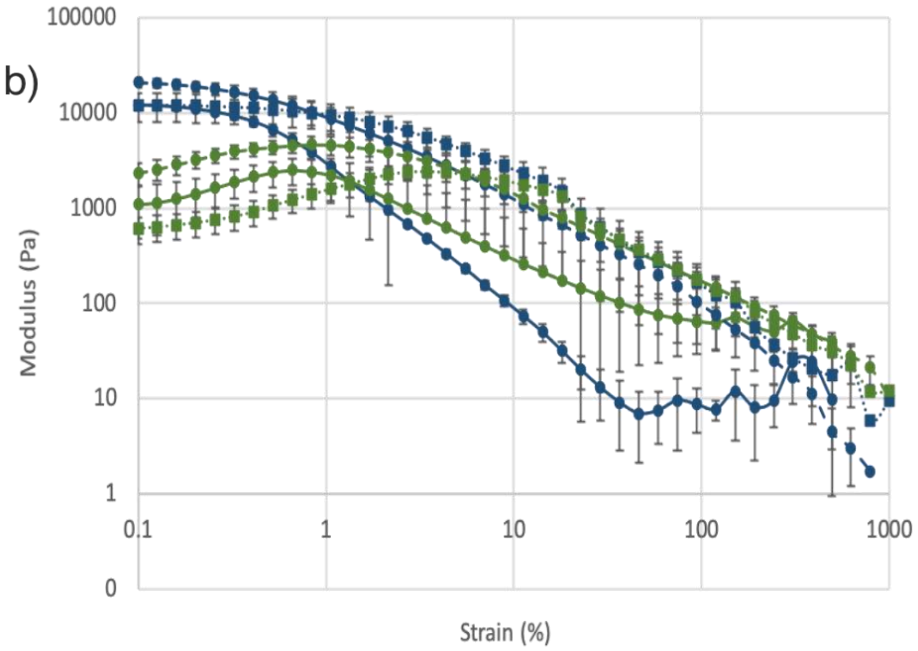

Figure 3.18 b: Amplitude sweep of 60 % cross-linked macroporous poly-ε-lysine hydrogel variants. (n=3) **Key:** Navy blue lines = Storage modulus (G'), Green lines = Loss modulus (G''), Solid lines and circles = Hexanedioic acid, Dashed lines and circles = Heptanedioic acid, Dashed lines and squares = Octanedioic acid.

Increasing the percentage cross-linking and the chain length of the di-acid cross-linker was shown to influence their viscoelastic properties (**Figure 3.18**). All of the macroporous hydrogels follow in the same trend where they display a linear viscoelastic region, reach a yield point, and following which, all decrease in modulus. The crossover modulus varies between hydrogel variants. Increasing the percentage cross-linking from 30 to 60 % increases the cross-over modulus at which the hydrogels begin to deteriorate. For the 30 % cross-linked variants, increasing the di-acid chain length from C6 to C8 increases the crossover modulus, suggesting the stiffness increases with the chain length. However, for the 60 % cross-linked variants, the crossover modulus increases from C6 to C7, but then the 60-0.07-oct hydrogel variant has a lower crossover modulus. These amplitude data were used to establish a complex modulus which further characterises the stiffness of the hydrogels.

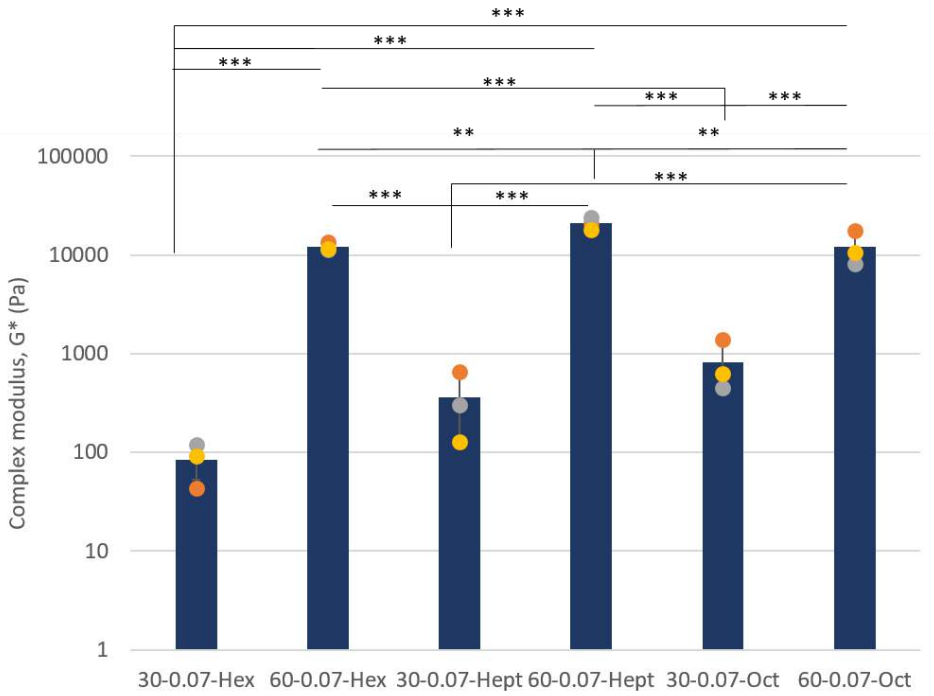

Figure 3.19: Complex modulus of macroporous poly-ε-lysine variants (n=3) (** = $p < 0.01$, *** = $p < 0.001$) Graph plots mean ± SD and individual data points.

Increasing the percentage cross-linking was shown to have more of an effect on the complex moduli than altering the di-acid cross-linker (**Figure 3.19**). A pattern is shown in that increasing the percentage cross-linking from 30 % to 60% increases the complex modulus. A similar trend is seen for increasing the chain length of the di-acid cross-linker, whereby increasing the length, increases the complex modulus. The 60-0.07-Oct variant slightly falls out of this trend, which may suggest there is a limit on how much the increasing di-acid chain length affects the stiffness of the hydrogels. Statistical significance was seen between the hydrogel variants. The complex modulus for all of the 30 % cross-linked hydrogels were significantly lower than the 60 % cross-linked variants, all p values < 0.001. Furthermore, the complex modulus of the 60-0.07-Hept hydrogel variant was significantly higher than the 60-0.07-Hex and the 60-0.07-Oct variants, with both p values equal to 0.001.

3.3.7 Frequency Sweep

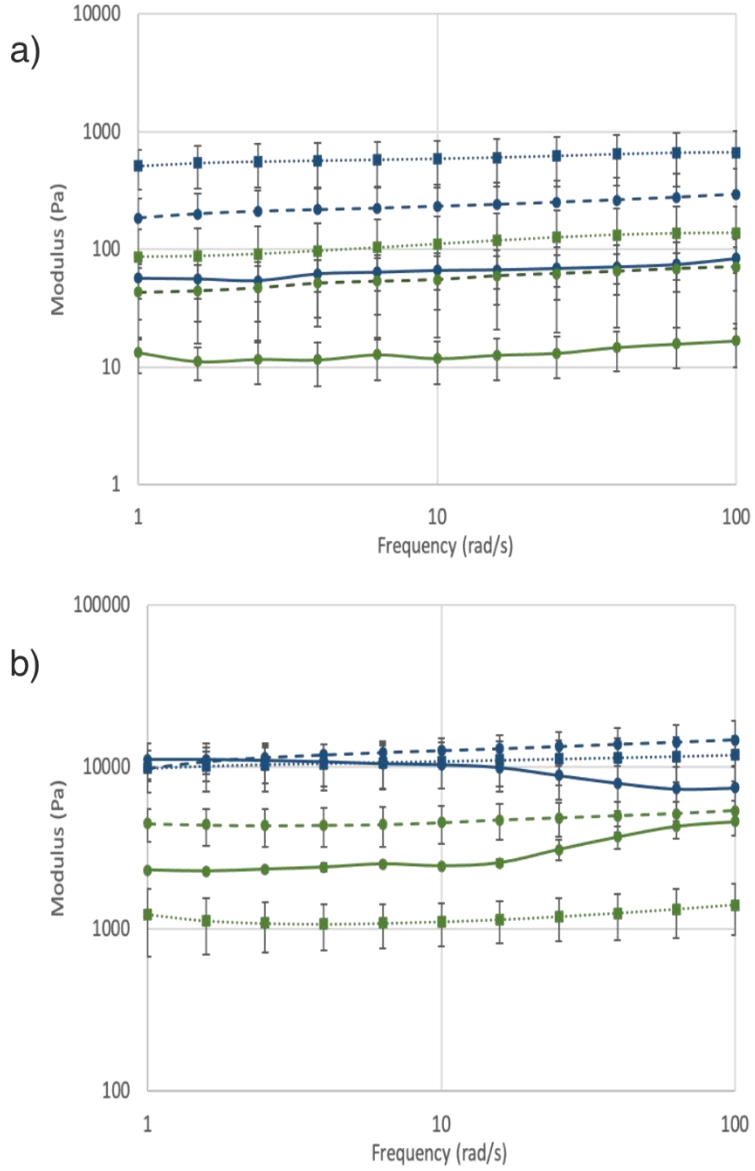

Figure 3.20: Frequency sweep of macroporous poly-ε-lysine hydrogel variants. (n=3) **a)** 30% cross-linked variants **b)** 60 % cross-linked variants **Key:** Navy blue lines = Storage modulus (G'), Green lines = Loss modulus (G''), Solid lines and circles = Hexanedioic acid, Dashed lines and circles = Heptanedioic acid, Dashed lines and squares = Octanedioic acid

Increasing the percentage cross-linking and the chain length of the di-acid cross-linker was shown to influence the frequency dependence of modulus (**Figure 3.20**). This data show that all of the hydrogel variants show parallel G' and G'' throughout the frequency sweep, and all exhibited a storage modulus that was consistently higher than the loss modulus. This is typical rheological behaviour of a hydrogel material. The results show that increasing the percentage cross-linking from 30 to

60 % increases the modulus by a factor of 10-100. This has a larger influence on the modulus than the di-acid chain length. Increasing the di-acid chain length from C6 to C8 also increases the modulus, for 30 % cross-linked variants. Similar to the amplitude data, the 60-0.07-Oct variant lays outside of this trend as the modulus is slightly lower than that of the 60-0.07-Hept variant. However, this difference is minimal suggesting that the two variants display a similar stiffness.

Mechanical Characterisation of macroporous hydrogel variants

3.3.8 Compressive Measurements

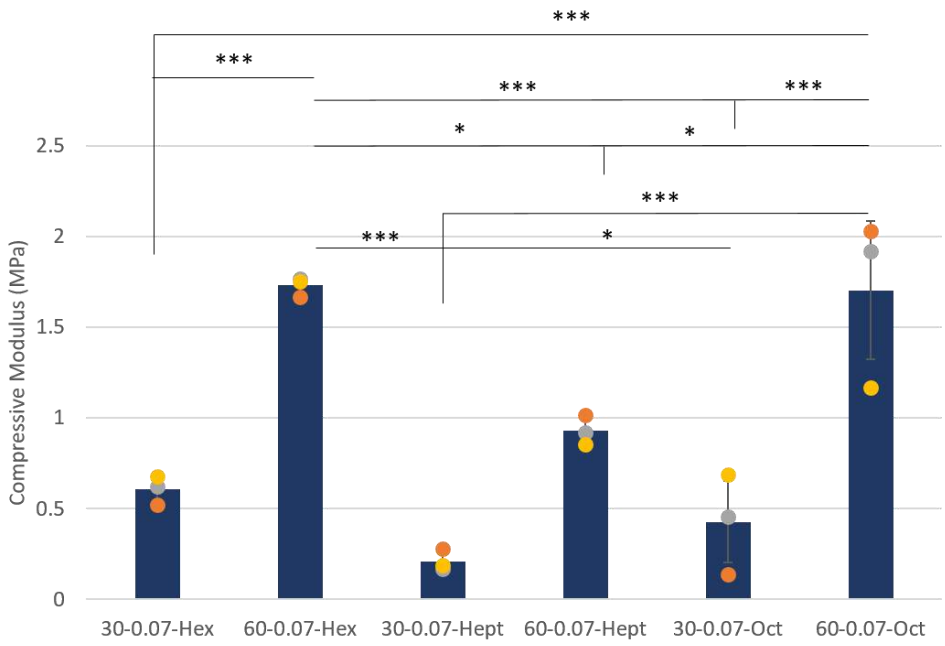

Figure 3.21: Compressive modulus of macroporous poly-ε-lysine variants. 5 samples/run (n=3) (* = $p < 0.05$, *** = $p < 0.001$) Graph plots mean ± SD and individual data points.

Increasing the percentage cross-linking and the chain length of the di-acid cross-linker was shown to influence the mechanical properties of macroporous variants (**Figure 3.21**). The compressive strength of the hydrogel variants could not be included, as the 60 % cross-linked variants did not reach failure when using a 50 N load cell. Increasing the percentage cross-linking across all three different di-acids increased the compressive modulus of the hydrogel variant. However, varying the di-acid had little effect on the compressive modulus. The highest compressive modulus of the higher percentage cross-linking variants, and therefore the stiffest

hydrogel was 60-0.07-Hex, followed by 60-0.07-Oct and finally 60-0.07-Hept. The 30 % cross-linked variants followed this same pattern, with the heptanedioic acid variant being the weakest in compression. Statistical significance was seen when comparing these data. All three of the 30 % cross-linked variants had a significantly lower compressive modulus than the 60-0.07-Hex and 60-0.07-Oct variants, with p values < 0.001. Additionally, the 60-0.07-Hept variant was significantly lower than the 60-0.07-Hept and 60-0.07-Oct variants with p values of < 0.05.

3.4 Discussion

This work has shown that it is possible to introduce interconnecting pores into the structure of a pεK based hydrogel by fragmenting the hydrogel during polymerisation. The optical and physical properties of the hydrogels are approaching those of the native human cornea [166, 167, 171] and the mechanical properties are comparable to other hydrogels used for tissue engineering applications [172-174]. Additionally, macroporous hydrogels manufactured using a porogen, which, when altering the material chemistry, can produce a library of materials with a range of properties. These can be tailored for various applications in tissue engineering the ocular surface and elsewhere in biomaterials research.

This section discusses poly-ε-lysine hydrogels made using two different casting methods and compares their optical, physical and mechanical properties with native corneal tissue and with other materials investigated for the same application.

3.4.1 Fragmented hydrogel manufacture

The fragmentation technique was designed based on a method reported by the Farres *et al* [175, 176]. This method utilises a pin-stirrer device to produce fluid gels based on alginate, **Figure 3.22**. The separate injection points of alginate and $CaCl_2$ allows for the formation of alginate particles with a diameter of < 10 µm.

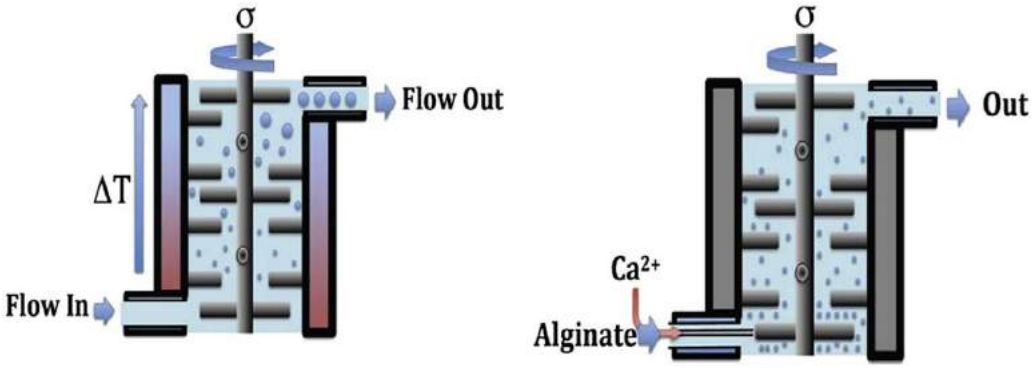

Figure 3.22: Schematic published by Fernandez Farres *et al* for the pin-stirrer device to manufacture alginate fluid gels [7]

A stirrer device was developed in our group which would utilise a similar process to break the hydrogel up whilst it's gelling, as opposed to casting the hydrogel in a petri dish. We hypothesised that this would allow for the formation of small particles, which could be cross-linked together to form porous hydrogel sheets.

In order to produce porous pεK hydrogels reproducibly using the stirrer device, several steps were taken to optimise the process. The stirrer speed, the duration of stirring, the temperature and the hydrogel chemistry were altered to achieve a final hydrogel with optical and mechanical properties that closely mimicked the native human cornea. Out of all of the parameters, the speed at which the stirrer was set had little effect on the fragmentation of the gels. In order to change the speed of the stirrer, the voltage on the motor is altered, increasing the voltage increases the speed. All of the fragmented hydrogel samples were produced at a voltage of 5.5 V, which ran the stirrer at a speed of 78 rpm.

Figure 3.23: Photograph of hydrogel fragments produced when the stirrer device left to run for 1-2 hours. Fragments not stuck together as a sheet and appear opaque. Hydrogel imaged in a 6 cm diameter petri dish. Hydrogel chemistry: 60-0.07-Oct

The duration of stirring was altered from between 10 minutes to up to several hours. When the hydrogels are cast, they take up to a couple of hours to fully polymerise, however, gelling begins to occur after around 15-20 minutes. To begin with, the hydrogel components were added to the device, and left to stir for 1-2 hours. However, this duration produced small gel fragments which were opaque due to their small size (**Figure 3.23**), which were also fully polymerised and therefore difficult to additionally cross-link to form a porous sheet. As a result, the duration of stirring was reduced so that the fragments were removed after around 20 minutes, when polymerisation had just began to occur. This allowed small fragments to form, but did not allow enough time to fully disrupt cross-linking. This allowed the fragments to polymerise together to form a porous sheet. Removing the fragments at a time less than 20 minutes was not investigated as polymerisation would not have occurred before this time. Therefore, fragments would not have formed and the porosity would likely have been unaffected.

The temperature at which the polymerisation took place would affect the time taken for the hydrogel to gel and form fragments. Trials were performed where the stirrer device would be set up either on the lab bench at room temperature, in the cold room (4 °C) or in the warm room (37 °C). Increasing the temperature increased the rate of reaction and the hydrogels would polymerise faster than at room

temperature. Following the same trend, leaving the stirrer in the cold room reduced the rate of reaction, and for certain polymer chemistries, (30-0.07-Oct), the hydrogel did not polymerise even when left for several hours. Based on these findings, and on the ease and location of other equipment, the stirrer device was operated at room temperature (~20 °C) for all hydrogel variants tested.

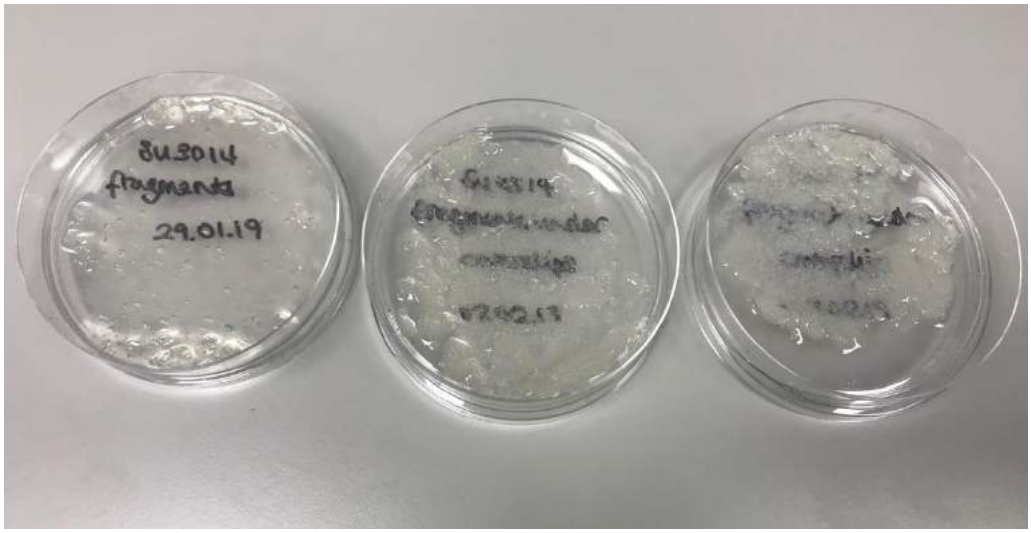

Figure 3.24: Photograph of fragmented gels with varying hydrogel chemistry. Left to right: 30 % cross-linking, 45 % cross-linking, 60 % cross-linking. All hydrogel variants have a 0.07 g/ml polymer density. Transparency visibly reduces as the percentage cross-linking increases. Hydrogel imaged in a 10 cm diameter petri dish.

The ideal hydrogel chemistry was later identified after specific physical and mechanical characterisation, however a preliminary assessment was done to obtain a suitable percentage cross-linking. A higher percentage cross-linking resulted in a more opaque fragmented hydrogel sheet (**Figure 3.24**). This is the same trend seen as when the hydrogels are produced by static polymerisation (casting) however, the fragmenting step further reduces the transparency. For this reason, the percentage cross-linking was chosen to be 30 %, to produce a sheet with a transparency closely resembling the cornea. The effect of the polymer density on the transparency of the hydrogel is further discussed in section 3.4.3.

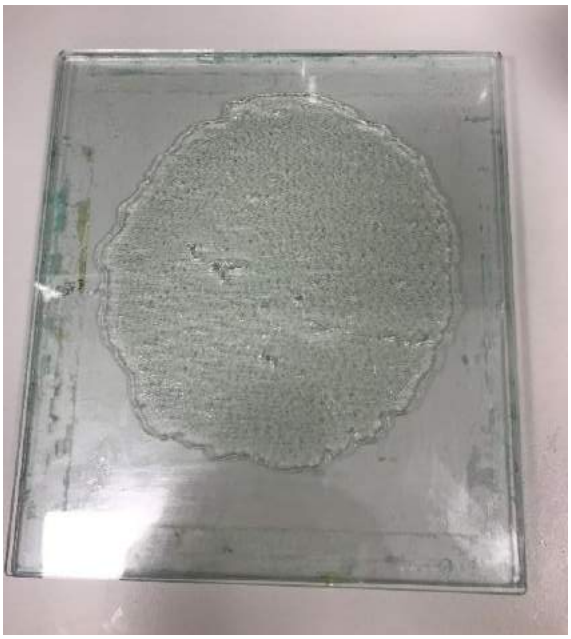

Figure 3.25: Photograph of hydrogel fragments pressed between glass plates and left for 2+ hours to fully polymerise. Gel chemistry: 30-0.07-Oct

Finally, to achieve a desired thickness of close to 500 um, roughly the thickness of the cornea [177], the fragments were left to polymerise pressed between two glass plates (**Figure 3.25**). A ruler was used when pressing the plates down to achieve the desired thickness, and a weight left on top of the plates to ensure the desired height was maintained.

3.4.2 Macroporous hydrogel manufacture

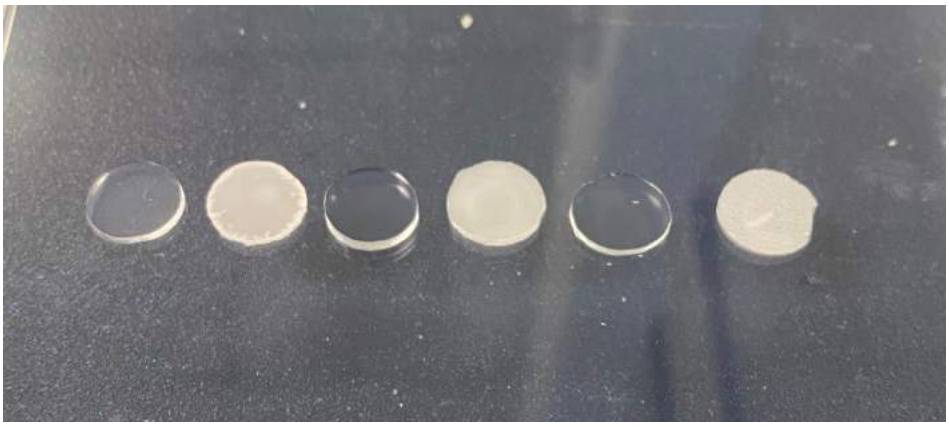

Figure 3.26: Image of macroporous hydrogels from L to R: 30-0.07-Hex, 60-0.07-Hex, 30-0.07-Hept, 60-0.07-Hept, 30-0.07-Oct, 60-0.07-Oct

Macroporous hydrogels based on poly-ε-lysine (SpheriGen^{TM}) have been investigated for use in kidney and nerve regeneration and wound management

[128]. However, the chemistry used to make these hydrogels renders them opaque. As the application was chosen to be corneal tissue engineering, the transparency of the hydrogels was essential. Therefore, the chemistry of the macroporous hydrogels was modified in order to create a library of materials that have tailorable properties suitable for ocular surface tissue engineering (**Figure 3.26**). The cross-linking was altered between 30 % and 60 %, and the di-acid cross-linkers used were hexanedioic, heptanedioic and octanedioic. Modifications to the hydrogel chemistry had a direct effect on the optical, physical and mechanical properties which are discussed further.

In this project, the two manufacture methods were compared based on how they affected the optical, physical and mechanical properties of the hydrogels produced.

3.4.3 Optical properties:

The transparency of the hydrogel variants was analysed by measuring the percentage light transmission. The aim of this measurement was to identify a hydrogel variant which achieved as high a transparency as possible, approaching that of the human cornea at 90 % [166, 177]. The percentage light transmittance of the porous sheets produced by the two different casting methods were compared, as these techniques affected the transparency in different ways.

Increasing the polymer density reduced the light transmittance of the fragmented variants, which ranged from 64 % ± 8 – 84 % ± 1. The only significance seen between the fragmented and the cast variants was for the highest polymer density of 0.1 g/ml. This hydrogel variant was subsequently removed from further testing as the transparency would be too low for a corneal application. Studies have shown that increasing the polymer concentration of poly(vinyl alcohol) (PVA) reduces the transparency of hydrogels, due to the increasing crystallite size inducing opacity [178, 179]. The reduction in hydrogel transparency with increasing poly-ε-lysine density may be caused by the same phenomenon, as the higher concentration of pεK restricts the transmission of light through the hydrogel. The cast hydrogels with the same polymer chemistry had similar values for light transmittance to each other, ranging from 82 % ± 1 – 84 % ± 0.2; increasing the polymer density has no significant effect on the transparency for these hydrogel variants. This result

demonstrates that fragmenting the hydrogels during manufacture combined with the increasing polymer density has a more significant effect on the transparency than the polymer density alone. The fragmented hydrogels used for cell seeding were 30-0.07-Oct, which had a percentage light transmittance approaching that of the native human cornea. A high transparency is a requirement for a corneal application to ensure the restoration of normal vision following implantation, however, in certain applications such as CLET surgery which utilises opaque amniotic membrane, transparency of the eye can be restored if the opaque substrate degrades quickly.

The percentage light transmittance data for the macroporous hydrogel variants showed differences between hydrogels with different percentage cross-linking. The 30 % cross-linked hydrogels ranged from 63 % ± 9 – 77 % ± 4 and all three variants showed were significantly more transparent than the 60 % cross-linked variants. The variant with the highest transparency was the 30-0.07-oct hydrogel, which was taken forward for cell culture work with corneal epithelial cells. The 60 % cross-linked hydrogels had percentage light transmittance values between 0.88 % ± 0.36 – 1.07 % ± 0.56, showing opacity which renders them unsuitable for a corneal tissue engineering application. Alternatively, these hydrogels could be used elsewhere on the ocular surface, for example the regeneration of the conjunctiva, where transparency is not a vital requirement.

Research into suitable replacements for donor corneal transplantation is ongoing, with the amniotic membrane and RAFT collagen hydrogels being extensively investigated. One of the drawbacks of these two alternatives is their variable transparency [180, 181] (**Table 3.6**). The limitations in terms of transparency of these materials encourages the investigation into an optimal corneal replacement, which would demonstrate a high optical clarity whilst maintaining desirable physical and mechanical properties. PCL is a synthetic alternative, which has been extensively investigated for various biomaterials applications due to its desirable mechanical properties, low cost and tuneable porosity [182]. However, its transparency must be significantly improved to more closely mimic the properties of the human cornea, and allow it to be suitable for a corneal tissue engineering

application. When compared with these other potential biomaterials taken from literature, hydrogels based on poly-ε-lysine have shown a higher and less variable transparency and therefore may overcome some of the current issues in terms of transparency.

Table 3.6: Percentage light transmittance values of other common biomaterials for corneal tissue engineering taken from literature

Material	Light Transmittance	Reference
Human Cornea	90 %	[166]
Gelatin	62 %	[172]
RAFT collagen	13 – 81 %	[76, 183]
Silk fibroin	95 – 99 %	[184]
Human amniotic membrane	70-80 %	[76-78]
Poly-caprolactone	11-28 %	[185]
Poly(ethylene glycol)	98 %	[186, 187]
Gelatin : Collagen	80 %	[172]
Electrospun GelMA: poly(HEMA)	74 %	[188]
Poly-caprolactone: Silk fibroin (50:50)	80 %	[189]

The fragmented and the macroporous hydrogel variants taken forward for cell culture both had the same chemistry of 30-0.07-Oct. They showed comparable transparency, both approaching that of the human cornea. This comparison shows that despite the method of manufacture, poly-ε-lysine based hydrogels with this formulation produce transparent substrates, which has the potential in terms of transparency to be investigated further for corneal tissue engineering applications.

Further optical characterisation of the hydrogel variants was performed using refractive index measurements. These measurements would confirm whether the inclusion of pores throughout the hydrogel construct would alter the refraction of light through the material when compared to a cast hydrogel. The hydrogels were compared with a contact lens control, Narafilcon A.

When comparing the fragmented and cast hydrogel variants, it was demonstrated that the different methods of casting has no significant effect on the optical

properties. All of the poly-ε-lysine variants measured had comparable refractive index values between 1.336-1.339 nD, with no significant differences seen between the hydrogels. These values were also comparable with the contact lens control. Similarly, despite the contrasting differences in the percentage light transmittance of the macroporous hydrogel variants, they all demonstrated refractive index values in the range 1.339-1.343 nD. Similar to the fragmented and cast variants, there was no significance seen between the hydrogels.

Literature places the value for the refractive index of the human cornea somewhere between 1.373- 1.432 nD [168, 169]. This varies based on the region of the cornea where the measurement is taken, and based on the method used to obtain the reading. The data for both the fragmented and the macroporous hydrogel variants show that although they are out of this range found in literature, they are approaching the ideal refractive index of the human cornea.

3.4.4 Physical properties:

The percentage water content of the hydrogel variants were analysed from the differences in the wet and dry weight. The water content of a hydrogel is somewhat indicative of its porosity, as a higher water content will result from a higher intermolecular spacing within the hydrogel.

The fragmented hydrogels had a higher water content in comparison to their cast pεK equivalents, with significance observed between the two fragmented variants and the lower density cast variant. Fragmenting the hydrogels during polymerisation introduces pores into the microstructure, which would allow more space for water to be retained. These results suggest that the fragmented hydrogels have a higher porosity throughout.

The macroporous hydrogel variants showed a higher water content when cross-linked at 30 % than at 60 %. The 30 % cross-linked hydrogels have a higher intermolecular spacing throughout the structure due to the presence of fewer links between chains of poly-ε-lysine. This allows them to retain more water in the structure.

The water content of the cornea is approximately 78 % [171], a value which all of the fragmented and macroporous hydrogel variants exceed. A high water content is beneficial for cell culture as a low interfacial tension allows hydrogels to adsorb proteins and growth factors from cell culture media [190]. Following implantation, a high water content is important for oxygen permeability and transport to the tissues below, which in turn will prevent corneal oedema [191]. Patients with a hostile corneal environment, for instance as a result of Steven Johnson's syndrome, trachoma or ocular burns, are unable to receive a traditional keratoprothesis [192]. Therefore, research has focused on improving upon the properties of these commonly used implants, such as the Boston KPro. An implant with a high water content may further encourage host cell integration and anchor the implant into this environment [81], and allow for epithelial cell growth and overall corneal health, which would in turn reduce the likelihood of implant extrusion and rejection [193]. The percentage water content also affects the resulting mechanical properties of the hydrogel, so the polymer chemistry used would be a compromise between a high water content and the mechanical integrity of the hydrogel.

The porosity of the hydrogels was analysed via scanning electron microscopy. SEM micrographs demonstrate the porosity throughout the different fragmented, cast and macroporous hydrogels.

The fragmented hydrogels display an interconnected porosity throughout its entire structure, whereas the cast hydrogels seem to have a surface layer with no pores. Increasing the polymer density visibly reduced the porosity of the fragmented hydrogel variants, whereas it had little effect on the porosity of the two cast variants. The percentage porosity showed that reducing the polymer density increased the porosity, and fragmenting the hydrogels during polymerisation increased the porosity. The increased percentage porosity of the fragmented hydrogels, combined with the SEM images, gives confidence of the presence of an interconnected porosity throughout the hydrogel network. Due to the swelling behaviour of the macroporous hydrogels, the porosity was unable to be calculated using this method.

The macroporous hydrogels demonstrated distinct porosity throughout the cross-sections of the 60 % cross-linked variants, however, the 30 % cross-linked hydrogels showed very few pores and in the 30-0.07-Hex variant, no pores. All of the hydrogels showed few, if any, pores across the material surface, likening them to the cast hydrogels with no porogen. The 30 % cross-linked macroporous hydrogels that were seen to be more suitable for a corneal application based on their transparency, are let down by their lack of an interconnected porous structure.

An interconnected porosity is ideal for a tissue engineering scaffold to allow for the infiltration and migration of cells into the construct. Pores act as anchorage points for integrating cells and can also provide gateways for the passage of blood vessels [192]. The average pore size throughout the construct also has a direct effect on the material properties and biocompatibility. Pores that are too small will not be able to accommodate cell migration whereas too large pores will reduce the surface area of the construct and result in poor cell binding. A pore size of 20 µm at minimum would facilitate the integration of corneal stromal cells and allow for an adequate surface area for cell adhesion [108]. Additionally, porosity throughout a construct allows for gas and ion exchange which influences cell proliferation [194, 195]. However, increasing the porosity of the construct will have an influence on the mechanical properties, therefore a compromise is introduced between prioritising mechanical strength or cell attachment.

Swelling behaviour is typical of hydrogels due to their water filled structure, however the degree of swelling is influenced by the amount of cross-linking and the intrinsic properties of the main polymer chemistry. An increased hydrogel swelling usually results in a decrease in mechanical integrity of the gel [196], however this feature would increase the adsorption of nutrients from cell culture media, and therefore could be beneficial for the incorporation of cells into the construct. It is important to characterise the swelling behaviour of the hydrogel variants in order to understand how the material will respond to different environments, and can help to determine the most suitable method for storage. The hydrogel variants manufactured using different casting methods were compared, as the swelling ratio was affected in different ways. For instance, the high porosity of the freeze-dried

fragmented hydrogels had an abundance of space which could be filled with water, resulting in swelling. Whereas the inclusion of the porogen into the hydrogel network increased the mesh size, allowing the polymer chains to stretch further, which in turn, allowed these hydrogel variants to take on more water.

Fragmenting the hydrogels during polymerisation was seen to increase the swelling ratio compared to the cast variants with the same chemistry. Increasing the polymer density was seen to slightly increase the swelling ratio. This is likely due to the higher monomer density increasing the mesh size of the hydrogel, which allows the structure to take on more water [197]. The swelling behaviour of the hydrogels was further characterised by measuring the diameter of pεK hydrogel variants over 8 weeks that were left in either PBS or dH_2O. It was shown that both the fragmented and cast hydrogels were stable in both of these solutions for at least 8 weeks, as little changes were seen in the diameter of the hydrogels in this time.

For the macroporous hydrogel variants, increasing the percentage cross-linking reduces the swelling ratio of the hydrogels. When the swelling behaviour was analysed by change in diameter over 8 weeks, it was shown that the macroporous hydrogel variants increased in diameter much more than the cast hydrogel variants. In particular, the 30 % cross-linked variants showed up to a 139 % increase in diameter compared to its original size when left in dH_2O. A similar trend is shown in that the 30 % cross-linked macroporous variants had a higher increase in diameter compared to the 60 % cross-linked variants. This may be explained by the increased cross-linking reducing the mobility of the polymer chain. This would allow for less movement in the 60 % cross-linked hydrogel structure, hence, it would be able to take on less water than the 30 % cross-linked variants.

The macroporous variants had a much higher swelling ratio than the fragmented and cast variants, and increased in diameter considerably in comparison when left for 8 weeks in PBS and dH_2O. This suggests that the inclusion of the porogen allows the polymer chains to stretch more than they do in the original pεK hydrogel chemistry. This property may be to their detriment in an artificial cornea application, however in some tissue engineering applications, a high swelling ratio is favoured. The high swelling ratio of the 30 % cross-linked macroporous hydrogels,

as well as its natural antimicrobial properties suggests suitability for a wound healing bandage. This application requires a material with suitable viscosity and mechanical properties [198], which additionally is capable of absorbing large amounts of fluid.

The final physical property of the hydrogel variants that was characterised was degradation. The degradation properties of the pεK hydrogel variants were assessed by mass loss measurements, with hydrogels left to soak in PBS, NaOH and trypsin. The degradation studies were set up for 8 weeks, to evaluate long term outcomes of the hydrogels subject to different conditions.

After 8 weeks in PBS, fragmented variants had a degradation of up to 30 % of their original mass, where cast hydrogels had up to 15 %. In NaOH, fragmented variants had degradation up to 17% of their original mass, and cast variants had up to 19 %. After 4 weeks in trypsin, fragmented variants had lost 20 - 36 % of their original mass, and cast variants 30 – 44%. These result show that there were little differences seen between the behaviour of fragmented and cast hydrogel variants.

The macroporous variants showed similar behaviour. In PBS, macroporous variants lost a maximum of 30 % of their original weight. In NaOH, more degradation occurred, with macroporous variants losing up to 52 % of their original weight. Finally, after 4 weeks in trypsin, the macroporous variants lost between 10 – 43 % of their original weight. These results showed a higher degradation of macroporous variants, in particular in NaOH, when compared with cast hydrogel variants with the same chemistry. Additionally, it was shown that 30 % variants, both macroporous and cast, were more susceptible to degradation than the 60 % cross-linked variants. This increased degradation is likely due to the higher intermolecular spacing in the 30 % cross-linked variants, allowing the solutions to more easily disrupt the cross-links.

Understanding the degradation properties of a biomaterial is important for translating it into a potential implant. Currently, the gold standard of corneal surgery is the replacement of a damaged cornea with tissue from a cadaveric donor during either a partial or full thickness keratoplasty. The lifespan of a corneal

transplant has been reported to be up to 30 years, with a low probability of survival after this time [199]. This intervention, for some patients, restores corneal transparency which lasts the remainder of their life. However, younger patients may need more than one transplant throughout their lifetime to maintain corneal transparency.

Different artificial corneas have been designed to mimic this feature of corneal transplantation, where the material does not degrade, with the aim of surviving the patient's lifetime [200-202]. Additionally, low levels of degradation would reduce the likelihood of implant extrusion, which is a common contraindication of keratoprotheses. The osteo-odonto-keratoprosthesis (OOKP) was designed to regain corneal transparency for patients unable to receive a penetrating keratoplasty. The implant is based on using biological material taken from a patients tooth to develop a corneal skirt, on which a transparent PMMA cylinder is anchored [203]. The degradation behaviour of dental material in physiological conditions ensures its suitability for a permanent implant, however, harsh pH conditions in the eye following diseases such as Steven Johnson's syndrome can accelerate the degradation of implants [204]. This may result in loosening of the corneal skirt and ultimately the failure and removal of the implant. The limitations with this method have encouraged research into investigating materials that are more chemically stable and less likely to degrade.

An alternative approach to an artificial cornea is based on materials which will be populated with epithelial, endothelial and stromal cells. This method will encourage re-epithelialisation and establish a functional corneal endothelial monolayer, in turn regaining the transparency of the cornea. This approach is suitable for patients that have suffered from Limbal stem cell deficiency (LSCD), as they would need to repopulate the corneal tissue with limbal epithelial stem cells. Constructs based on a fibrin-agarose scaffold with human corneal fibroblasts implanted within the gel, and donor corneal limbal epithelial cells seeded on top have reached clinical trials [205, 206]. This trial showed positive results after a two year follow up, with complete healing in 5 patients, with no signs of infection or rejection [207]. Furthermore, several cell-based studies have shown that primary corneal stromal

cells can be influenced to lay down their own extracellular matrix, which in turn, support the growth of epithelial and endothelial cells [208, 209]. This ECM material combined with a slowly degrading artificial corneal implant could provide a suitable alternative to a lifelong implant, as when implanted into the body, it is likely that the biomaterial will eventually be slowly broken down by cellular enzyme activity. This degradation behaviour could be advantageous for supporting corneal cells as they gradually re-build the corneal matrix.

The success of each of these approaches is dependent upon the degradation behaviour of the materials being investigated, therefore it is important to understand this behaviour before progressing to *in vivo* or clinical trials.

The absence of significant weight loss under the varying conditions demonstrates a stability of the porous pεK hydrogel variants, in particular the fragmented variants. This stability may vary when subject to enzymatic activity, which would likely increase the rate of degradation. Due to the strong cross-linking of poly-ε-lysine, it would likely take several months to break down. If an implant was designed based on pεK, cells could be included throughout the construct which can lay down collagen and ECM material to build up a structure similar to that of the native cornea. The degradation profile of pεK may increase its suitability for this type of implantation over the human amniotic membrane, which has a rapid rate of biodegradation [210, 211].

The success of any style of corneal implant is dependent on the patient's age and their condition which has resulted in blindness, as an implant that may be suitable for a cornea affected by physical trauma, may not be able to withstand harsher conditions of a diseased cornea. The variation in corneal environment allows for flexibility with approaches based on different degradation behaviours. Further degradation studies could include more closely mimicking physiological conditions, for example by incubating the hydrogel samples at 37 °C, altering the pH and using alternative enzymes, such as lysozyme and amylase found in human tears.

3.4.5 Rheological properties:

The viscoelastic properties of poly-ε-lysine hydrogel variants, both fragmented and macroporous, were characterised using rheological measurements.

The amplitude dependence of modulus was measured and all hydrogel variants follow a trend whereby the storage modulus (G') and loss modulus (G'') crossed over in the amplitude sweep. This is indicative of the yield point of the hydrogel as the crossover modulus demonstrates where the gel switches from 'solid-like' to 'liquid-like' behaviour [212]. Cast hydrogel variants demonstrated higher crossover moduli when compared with fragmented hydrogel variants. The higher polymer density hydrogels, 30-0.08-Oct, had higher crossover moduli in both fragmented and cast variants. The complex modulus (G*) is taken from the amplitude data and combines the elastic and viscous contributions and therefore describes the hydrogels entire viscoelastic behaviour, characterising its resistance to deformation [213]. The fragmented hydrogel variants had complex moduli between 2.2 – 3.3 kPa, whereas the cast hydrogels had complex moduli between 10.5 – 11.4 kPa. The frequency dependence of modulus further characterises the stiffness of a material. A higher storage modulus indicates a more 'solid-like' behaviour, resulting in a stiffer hydrogel with a higher resistance to deformation [214]. In the frequency sweeps, the fragmented and the cast gels performed similarly. The cast gels showed similar or higher storage moduli at 10 rad/s, demonstrating a higher resistance to deformation compared to the fragmented variants. There were no significant differences observed in the loss moduli of the fragmented and cast hydrogel variants. Overall, the results showed that cast pεK variants were stiffer, which may be due to the increased number of fracture points introduced in the fragmented gels during their manufacture, and their higher water content.

The macroporous pεK hydrogels demonstrated similar trends in the rheological characterisation. The results demonstrate that the higher percentage cross-linked hydrogels were much stiffer than the 30 % cross-linked. The 30 % cross-linked hydrogels also had a lower complex modulus than the 60 % cross-linked hydrogels. These results further demonstrate that increasing the percentage cross-linking of the hydrogels, from 30 to 60 %, increases the stiffness. Similar to the fragmented

hydrogel results, the frequency data showed that all of the hydrogel variants displayed typical strong gel characteristics, in that the storage modulus was higher than the loss modulus throughout the sweep.

Based on the rheological analysis, the 30 % cross-linked macroporous hydrogels had comparable stiffness to the fragmented hydrogel variants. This is likely due to the similar chemistry used in both of these hydrogel types. Despite this same polymer chemistry, the cast hydrogel variants demonstrated a higher stiffness than the macroporous and the fragmented variants. This finding suggests that the pores introduced into the hydrogel structures reduced the stiffness and handleability. The 60 % cross-linked macroporous hydrogels have the highest stiffness of the variants measured, which shows a direct link between percentage cross-linking in the polymer chemistry and the stiffness of the material produced.

When compared to alginate and gelatin hydrogels for tissue engineering applications, the rheological properties were very similar. Several frequency sweep studies of different concentrations of alginate hydrogels yielded G' values of between 2-50 kPa [173, 174], and gelatin hydrogels have a lower storage modulus of 2 kPa. Rheological analysis of porcine corneal tissue demonstrated that the stroma exhibits viscoelastic properties in shear, with shear storage moduli values ranging from 2-8 kPa. [215] This shows that poly-ε-lysine had similar elastic properties to two alternative common hydrogels for tissue engineering, and porcine corneal stromal tissue, with all G' values for fragmented variants in the range of 1.9-10 kPa, and the macroporous variants with G' values between 0.06 – 12 kPa.

3.4.6 Mechanical properties:

The compressive strength and modulus of a hydrogel gives an idea of its mechanical properties and handleability. This is an important characterisation for a biomaterial, as it needs to be able to withstand force during implantation, and the normal pressure placed on the tissue in situ.

Fragmenting the hydrogels to introduce pores into the structure reduced the compressive modulus. The reduced compressive modulus of the fragmented hydrogels may be due to a higher number of fracture points throughout its

microstructure. The increased porosity would allow for cracks to more easily propagate through the structure of the hydrogel and result in failure [195]. Increasing the percentage cross-linking of the macroporous pεK variants was shown to significantly increase the hydrogels compressive modulus. The increased stiffness of the higher cross-linked variants is likely due to the energy required to break the additional bonds when the material is reaching failure.

Table 3.7: Mechanical properties of other common materials investigated for corneal tissue engineering

Material	Young's Modulus	Yield Stress	Reference
Fragmented pεK	0.04 MPa	0.03 MPa	This work
Human Cornea	0.1-57 MPa	3.8 MPa	[216-219]
Gelatin	3.92 kPa	4 kPa	[172]
RAFT collagen	20-80 kPa	0.35 – 0.7 MPa	[76, 183]
Silk fibroin films	800 – 1200 MPa	14 – 35 MPa	[184]
Silk fibroin fibres	15-17 GPa	610-690 MPa	[220]
Human amniotic membrane	2.3 -3.6 MPa	0.5 – 0.9 MPa	[76, 77]
Poly-caprolactone	0.06 MPa	1.74 MPa	[185]
Poly(ethylene glycol)	1.02 MPa	0.6 MPa	[186, 187]
Gelatin : Collagen	6.28 kPa	16 kPa	[172]
Electrospun GelMA: poly(HEMA)	7 kPa	518 kPa	[188]
Poly-caprolactone: Silk fibroin (50:50)	2.62 MPa	5 MPa	[189]

Alternatives to native corneal tissue have been investigated, and their mechanical properties have been evaluated to assess for their suitability for surgical handling. These materials have been sourced from natural and synthetic origin and additionally have been combined together to form composite materials, **Table 3.7**. Amniotic membrane has been researched as an alternative to native tissue corneal replacements, however it demonstrates weak mechanical properties and handleability [181, 221]. An alternative naturally based material for an artificial cornea application is silk-based biomaterials. Silk fibroin can be used to make a variety of types of material, including hydrogels, sponges, films, mats and fibres [220]. Silk-based materials have shown a versatility in their properties; they can be

made into porous structures, demonstrate a high water content and finally they have shown mechanical properties significantly stronger than other materials for tissue engineering (**Table 3.7**) However, silk based materials have demonstrated few cell binding motifs and may require materials modification to encourage cell attachment [95, 222]. Synthetic based materials such as poly(ethylene glycol) (PEG) and poly-caprolactone (PCL) have shown less variable mechanical properties when compared to natural materials. PEG and PCL have demonstrated a higher Young's modulus and yield stress when compared to natural materials such as gelatin and RAFT collagen. Furthermore, the synthetic materials demonstrate comparable mechanical properties with the human amniotic membrane. However, although they are more suitable for surgical handling, in particular PCL has a much lower transparency than natural materials, which reduces its capability for corneal regeneration. Furthermore, PCL often has to be modified to reduce its hydrophobicity, which in turn increases cell attachment [182]. This is an additional step which is not necessary with other materials, such as collagen, that are inherently bio-compatible.

Table 3.8: Summary of hydrogel properties with 30-0.07-Oct chemistry based on different manufacture techniques

	Cast	Fragmented	Macroporous
Light transmittance (%)	84.7	83.5	77
Water content (%)	87.7	93.2	91
Porosity (%)	24	40	-
Degree of Swelling	1.9	2.3	8.7
Complex Modulus (kPa)	3.3	2.2	0.8
Compressive Modulus (MPa)	0.054	0.037	0.43

The limitations with previously reported materials allows for the introduction of other materials with improved properties. These include enhanced mechanical properties, high water content and porosity, high transparency and biocompatibility. A summary of the material properties of fragmented, cast and macroporous hydrogels introduced in this chapter are outlined in Table 3.8. The mechanical properties of the cornea vary dependent on the tests performed, with literature placing the modulus somewhere between 0.1-57 MPa [216-218].

Although slightly outside of this range, the fragmented porous pεK variants are similar to other polymer hydrogels for corneal tissue engineering and are approaching the mechanical properties of the cornea [223]. The macroporous pεK variants have moduli that fall into the lower end of this range, however they lack other vital requirements for a corneal replacement, such as transparency.

3.5 Conclusions

Based on the strict requirements that come with mimicking the properties of the cornea, it transpires that the fragmented pεK variants meet more of the physical criteria for a corneal replacement than the macroporous pεK variants. Although the fragmented variants demonstrate slightly inferior mechanical properties to the macroporous hydrogels, they show a higher and less variable transparency, a more distinct interconnected porosity and are more stable in storage for at least 8 weeks in PBS/dH_2O. Additionally, the two variants have a similar water content, both of which are comparable to that of human corneal tissue. A further feature of interest of these porous hydrogels is the simple casting methods, which are easy to replicate and can be scaled up for mass production at a low cost. Although the macroporous hydrogels demonstrated properties that render them less suitable for a corneal application, they show promise for alternative tissue engineering applications. Their opacity does not rule them out of ocular tissue engineering, as their desirable mechanical properties and high water content demonstrate potential for a substrate in conjunctival tissue engineering. Also, their swelling ability allows them to be suitable for a wound healing application, which requires a high propensity for fluid absorption.

Furthermore, altering the polymer chemistry of both the fragmented and the macroporous hydrogels resulted in distinct changes in the transparency and the mechanical properties. This finding allows for the development of a library of porous hydrogels, which can be tailored towards different biomaterial applications.

In the next chapter, I will discuss the potential for poly-ε-lysine to be used as a printable ink to generate hydrogel constructs via additive manufacturing. This work includes trials for the pεK chemistry discussed in this chapter, and an alternative chemistry where pεK is cross-linked via electrostatic interaction.

Chapter 4: Poly-ε-lysine as a printable ink

4.1 Introduction

Additive manufacturing has been shown to be a useful tool for the manufacture of biomaterials for complex tissue engineering applications. In particular, corneal tissue engineering has been investigated for manufacture using AM methods due to the complexity of its structure. Several groups have investigated different AM methods for manufacturing an artificial cornea substitute. A study by Kim *et al* has demonstrated the manufacture of a bioengineered cornea based on shear stress during extrusion 3D printing of a decellularized extra-cellular matrix (dECM) bioink [224]. The induced shear stress during extrusion allows for the formation of aligned collagen fibres, replicating the natural structure of the human cornea. The printed dECM constructs demonstrated a high transparency, comparable to human corneal tissue, and supported the growth of encapsulated human keratocytes *in vitro*. After 28 days of culturing the encapsulated keratocytes, printed and non-printed samples were implanted into rabbits to establish *in vivo* compatibility for a further 28 days. After this time, the structures demonstrated no signs of degradation and contained collagen fibrils that mimicked human corneal tissue. Isaacson *et al* from the University of Newcastle have fabricated corneal structures based on collagen and alginate inks using a pneumatic 3D extrusion method [225]. The printed structures were based on a patient-specific digital model where the corneas complex structure and topography was replicated. Composite constructs with various concentrations of collagen and alginate were printed, using inks loaded with human keratocytes. The printed structures were shown to closely match the corneas structure, and support a high viability of encapsulated keratocytes after 7 days. This work is an example of proof of concept of bio-printing corneal structures, however the printed constructs need to be further characterised for their transparency and mechanical properties. An alternative corneal substitute was developed by Ulag *et al* based on chitosan (CS) and polyvinyl-alcohol (PVA) [226]. This study utilised a Tribot 3D printing device to build up a corneal structure within a mould. The printed constructs were seen to closely match the corneas size, curvature and thickness and had handleable mechanical properties. In particular the 13 wt % PVA with 1,3

and 5 wt % CS variants all demonstrated cyto-compatibility with human adipose tissue-derived mesenchymal stem cells (hASCs). However, the percentage light transmittance of the PVA/CS constructs were in the range of 50-65%, which is much lower than the transparency of the cornea at 90 % [166]. These results suggest although this seems to be a viable method for producing tissue engineering constructs, the ink chemistry may need to be optimised further to achieve a more suitable transparency for a corneal application.

Various groups have manufactured corneal constructs using extrusion and laser-assisted printing, which have shown success in early *in vitro* and *in vivo* trials. Very little has been reported on the use of inkjet printing methods for the manufacture of corneal tissue engineering constructs, which may show advantages over other AM methods such as a high resolution and the ability to print cells throughout biological materials. 3D printed corneal constructs have yet to make it into clinical use, which has prompted researchers into investigating this further.

The purpose of this chapter was to evaluate the suitability of poly-ε-lysine based inks for different methods of additive manufacturing. The AM techniques trialled included extrusion 3D printing and reactive inkjet 3D printing. Different ink stability techniques were performed to analyse the rheological properties of the hydrogel inks, followed by preliminary trials of these printing methods. Due to the scalability, high resolution and ease of producing complex parts, this branch of techniques has previously been utilised for the production of medical devices and tissue engineering scaffolds. The printed scaffolds were designed for a corneal tissue engineering application, and the suitability of poly-ε-lysine for manufacturing printed scaffolds was compared against other hydrogel inks.

The hypothesis investigated in this chapter was that poly-ε-lysine could be tailored to be an ink suitable for printing via additive manufacturing, and would be capable of producing substrates for corneal tissue engineering.

The aims to evaluate this hypothesis were as follows:

1. Characterise pεk based inks prior to printing to assess suitability.

2. Optimise printed tracks – printing speed and step spacing.

3. Characterise printed substrates: optical and SEM imaging, transparency

The work in this section included the assessment of the suitability of poly-ε-lysine inks for additive manufacturing techniques, outlined in method section 2.3, and the optimisation and reactive inkjet printing of poly-ε-lysine with gellan gum, detailed in method section 2.4. This chapter concludes with a discussion of how suitable poly-ε-lysine is for production using additive manufacturing techniques.

4.2 Results

Poly-ε-lysine cross-linked with octanedioic acid for extrusion printing

4.2.1 Rheological properties of hydrogel during polymerisation

The rheological properties of a hydrogel based on poly-ε-lysine (pεK) cross-linked with octanedioic acid (ODA) was measured to establish how the hydrogel behaves during polymerisation. Understanding this behaviour allows us to determine the suitability of pεK based inks for extrusion printing. The rheological assessments in this section included a time sweep and a temperature sweep, to measure the viscosity of the hydrogel over time and increasing temperature.

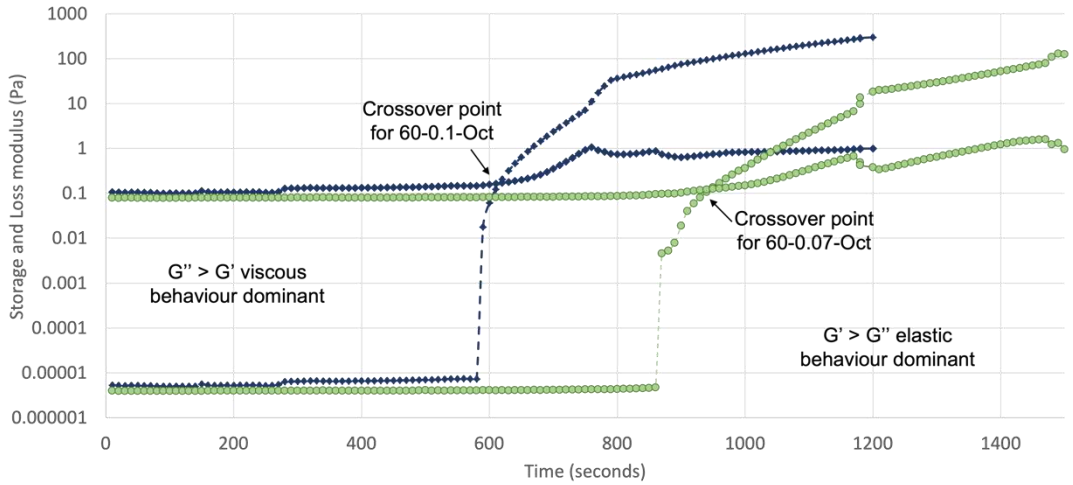

Figure 4.1: Storage and Loss modulus over time during polymerisation of poly-ε-lysine hydrogel variants. (n=3). **Key**: Navy blue line = 60-0.1-Oct, Light green line = 60-0.07-Oct, Dashed lines = Storage modulus (G'), Solid lines = Loss modulus (G'')

A time sweep was performed to demonstrate the increase in modulus over time of different pεK hydrogel variants, establishing a window of polymerisation for each variant. The time sweep demonstrates the increase in storage and loss modulus of the 60-0.1-Oct and 60-0.07-Oct hydrogel variants over time (**Figure 4.1)**. When the storage modulus overtakes the loss modulus, the material is changing from a liquid phase to a solid phase. The sweep in Figure 4.1 identifies the point at which the hydrogel sets, and a window of early polymerisation leading up to this point. The 60-0.1-Oct variant is seen to polymerises after approximately 10 minutes and the 60-0.07-Oct variant around 14 minutes. The data shows that increasing the polymer density of the hydrogel reduces the amount of time it takes to set, by at least 4 minutes, when repeated in triplicate. The window of polymerisation also appears to be smaller for the higher polymer density of the 60-0.1-Oct variant, as the storage modulus increase is steeper in comparison to the lower 0.07 g/ml density variant. From the initial increase in storage modulus, it takes 50 seconds for the storage modulus to overtake the loss modulus in the 60-0.1-Oct variant, whereas the 60-0.07-Oct variant takes 2 minutes to achieve a storage modulus greater than the loss modulus. These results show that the 60-0.1-Oct variant forms a solid hydrogel in a shorter time frame than the lower polymer density variant.

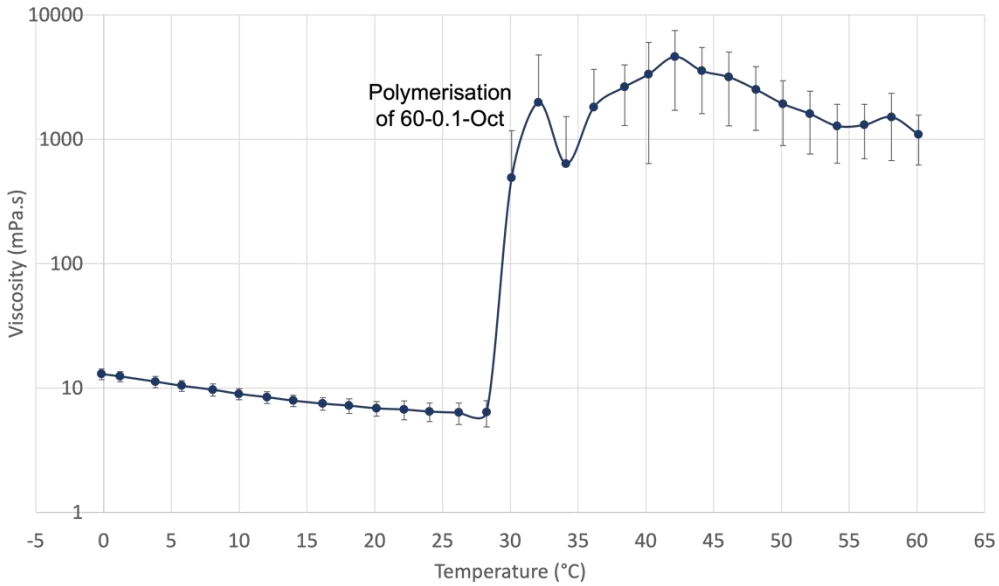

Figure 4.2: Viscosity over increasing temperature during polymerisation of poly-ε-lysine hydrogel variant 60-0.1-Oct. (n=3)

A sweep was performed to establish the effect of temperature on the time taken for the pεK hydrogel to set. Increasing the temperature of the rheometer from 0-70°C increased the viscosity of the 60-0.1-Oct hydrogel variant (**Figure 4.2**)**.** The data shows that at 28 °C the viscosity increases from 6 mPa.s to 2000 mPa.s at 32 °C. From this, it can be deduced that an optimum temperature to induce gelation in the hydrogel is in the range of 28-32 °C. Furthermore, the increased temperature has an effect on the time it took the hydrogel to set. The hydrogel polymerisation occurred after 7 minutes as opposed to 10 minutes at room temperature in Figure 4.1. These results were as expected, as when the components were heated up whilst in the stirrer device in the previous chapter the hydrogel polymerised faster. Figure 4.2 shows that increasing the temperature speeds up the rate of reaction of polymerisation.

Poly-ε-lysine cross-linked with octanedioic acid for inkjet printing

4.2.2 Rheological properties of individual components

The components of pεK cross-linked with ODA were separated and their rheological properties further evaluated for an inkjet printing technique. The components included pεK, ODA and activating agents N-Hydroxysuccinimide (NHS) and 1-Ethyl-3-(3-dimethylaminopropyl) carbodiimide (EDCI). The hypothesis for this work was

that when the components are combined during reactive inkjet printing, that they polymerise and can be built up into a solid hydrogel. To understand if these hydrogel components were suitable for inkjet printing, their rheological properties were assessed, including; viscosity sweeps and shear rate ramps.

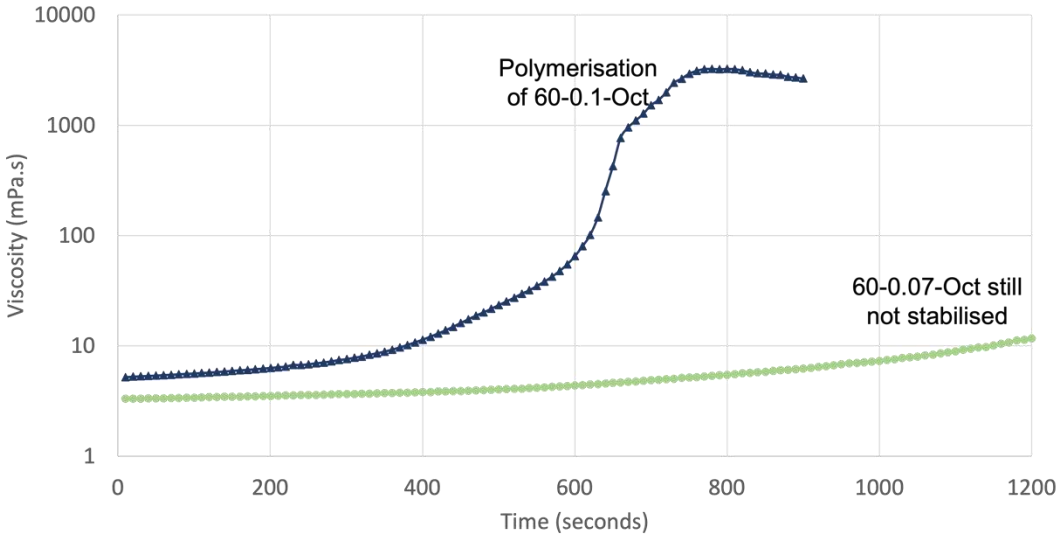

Figure 4.3: Viscosity over time during polymerisation of poly-ε-lysine hydrogel variants. (n=3) **Key**: Navy blue line = 60-0.1-Oct, Light green line = 60-0.07-Oct

The viscosity of two different hydrogel variants was measured over time to understand the polymerisation time of the hydrogel. A viscosity sweep demonstrates the increase in viscosity of the 60-0.1-Oct and 60-0.07-Oct hydrogel variants over time as shown in **Figure 4.3.** This measurement was performed to establish a setting time of the hydrogel variants to assess their suitability for reactive inkjet printing. The 60-0.1-Oct hydrogel begins to increase in viscosity after 6 minutes, and is polymerised after around 12 minutes. However, the lower polymer density of 0.07 g/ml begins to increase in viscosity after 10 minutes, but still hadn't stabilised after 20 minutes. Casting this hydrogel variant in a petri dish showed that polymerisation occurred after at least 30 minutes, which is too long for an inkjet printing application.

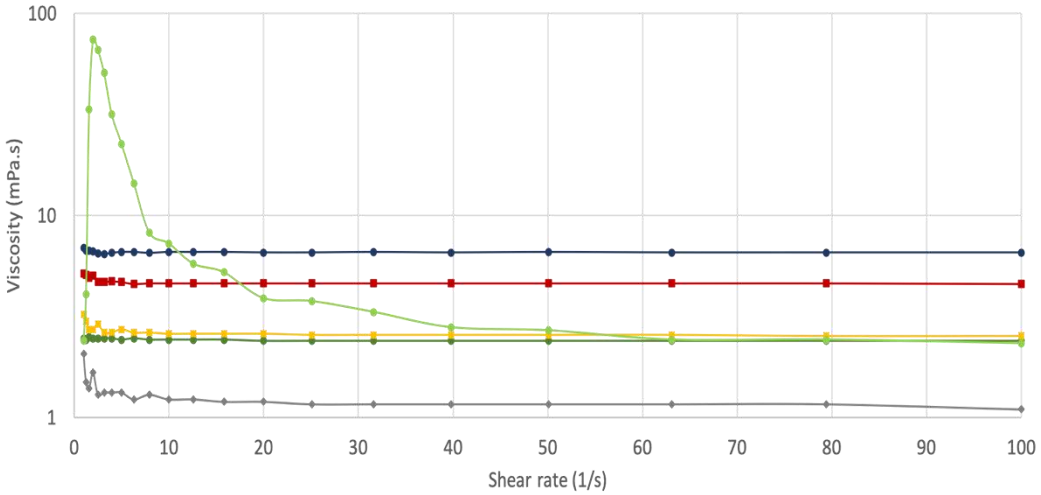

Figure 4.4: Shear rate ramp of components of 60-0.07-Oct. (n=3) **Key**: Navy blue = poly-ε-lysine, Dark green = ODA, Grey = NHS, Yellow = EDCI, Red = Ink 1, Light green = Ink 2. Ink 1 = pεK and ODA Ink 2 = NHS and EDCI

The individual components were separated and their viscosity measured to understand their suitability for inkjet printing. The shear rate ramp of the components of 60-0.07-Oct identified a viscosity value at 100 s^{-1} (**Figure 4.4**). For all components, the viscosity stabilises with increasing shear rate and plateaus, giving a final viscosity reading. Ink 1 is composed of Poly-ε-lysine with ODA. Ink 2 is composed of NHS dissolved with EDCI, which initiates an exothermic reaction when the two are combined. This reaction produces bubbles of CO_2 which causes the viscosity reading to peak at 74 mPa.s at a shear rate of 2 s^{-1}. Once the air bubbles have settled the viscosity reading stabilises, at around 50 s^{-1} and is similar to EDCI alone. At a shear rate of 100 s^{-1}, EDCI has a viscosity of 2.53 mPa.s and Ink 2 has a viscosity of 2.33 mPa.s. The viscosity values for this polymer density are in a suitable range for inkjet printing, all of which are less than 10 mPa.s.

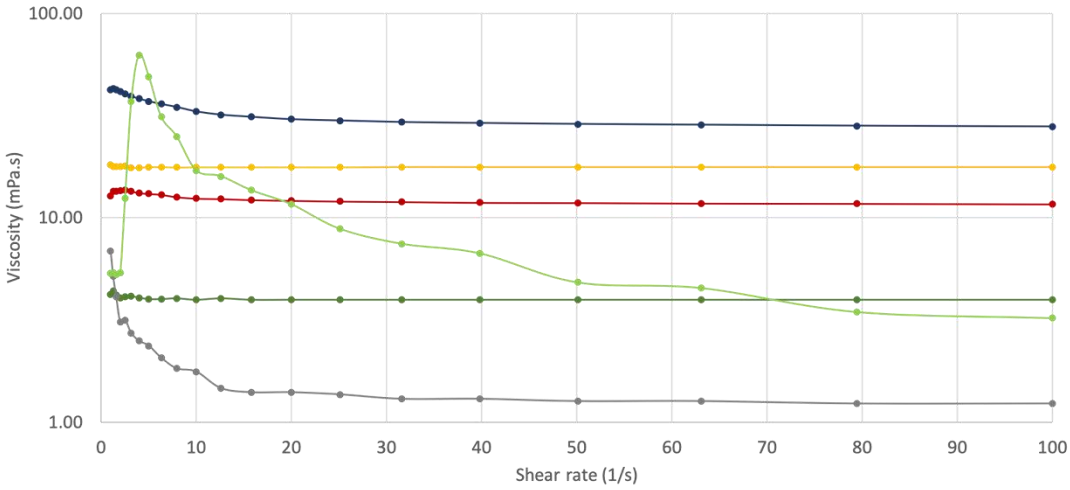

Figure 4.5: Shear rate ramp of components of 60-0.01-Oct. (n=3) **Key**: Navy blue = poly-ε-lysine, Dark green = octanedioic acid, Grey = NHS, Yellow = EDCI, Red = Ink 1, Light green = Ink 2. Ink 1 = pεK and octanedioic acid, Ink 2 = NHS and EDCI

A hydrogel chemistry with a higher pεK density was assessed for the viscosity of its individual components, as the higher density speeds up the polymerisation time, as seen in Figure 4.1. The shear rate ramp of the components of 60-0.1-Oct identified a viscosity value at 100 s^{-1} (**Figure 4.5**). These components are in the same ratio to one another as for the lower polymer density, with ODA dissolved with a 2:1 molar ratio to NHS. Again, for all components, the viscosity stabilises with increasing shear rate. A similar curve is seen for Ink 2 as in Figure 4.4, this is due to the same reaction between NHS/EDCI causing CO_2 bubbles to affect the viscosity reading. The viscosities are higher for poly-ε-lysine, EDCI and Ink 1 compared to Figure 4.4, as the density of pεK is increased. The higher pεK density therefore requires a higher quantity of EDCI to activate the carbodiimide cross-linking reaction. ODA showed a slight increase of viscosity when the hydrogel chemistries were varied between Figures 4.4 and 4.5. In the 60-0.07-Oct chemistry, ODA has a viscosity of 2.4 mPa.s, whereas for 60-0.1-Oct ODA has a higher viscosity of 3.9 mPa.s. The viscosity of NHS remained similar, with viscosities of 1.1 and 1.23 mPa.s for the 60-0.07-Oct and 60-0.1-Oct chemistries respectively.

4.2.3 Ink stability of components of poly- ε-lysine cross-linked with ODA

To further assess the suitability of the components of pεK hydrogels for inkjet printing, their ink stability was measured. These measurements included contact angle and surface tension studies to further understand how the inks might behave when they are jetted using an inkjet printer.

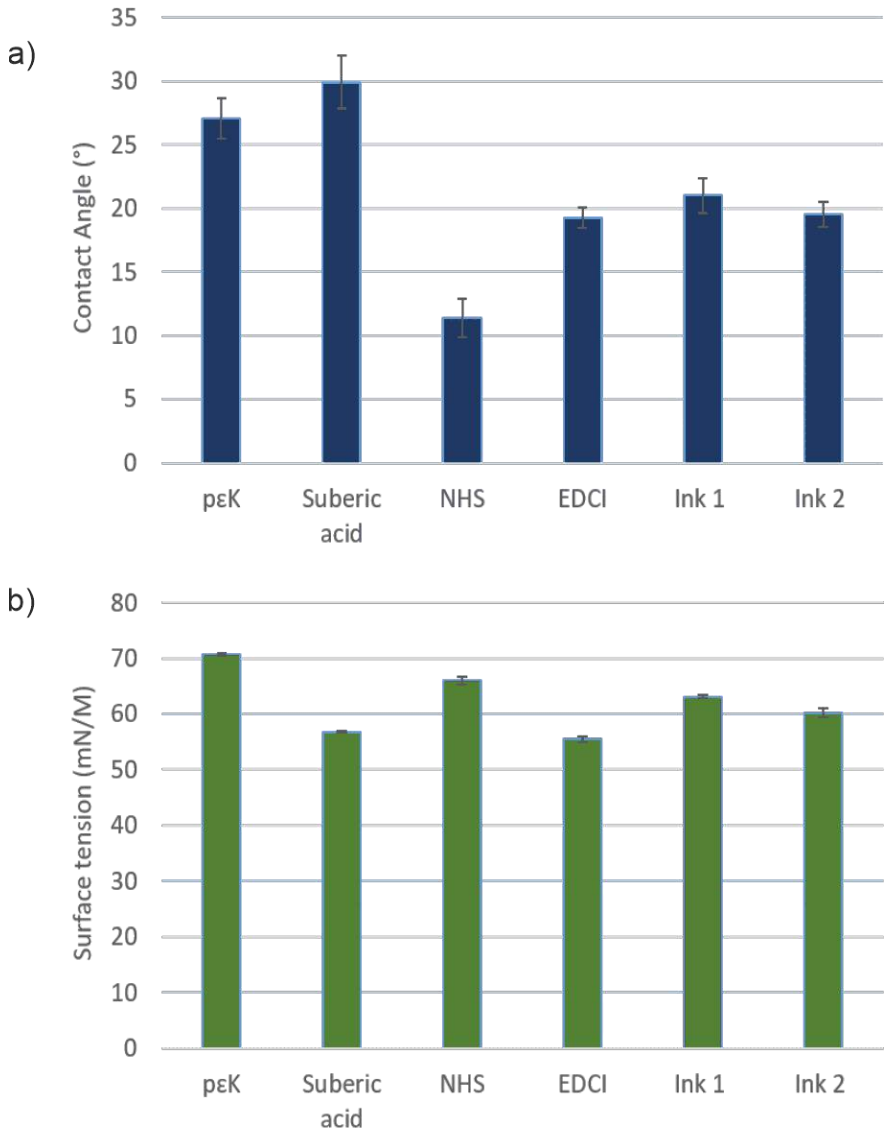

Figure 4.6: A) Contact angle **B)** Surface tension of components of 60-0.07-Oct poly-ε-lysine hydrogel variant. (n=1)

It is important to measure the contact angle of the inks to understand how they would behave when inkjet printed onto a glass substrate. Each of the components required to form the 60-0.07-Oct hydrogel have low contact angles in a the range of 11-30 ° (**Figure 4.6A**). In particular, the NHS activator spread across the surface to

the glass coverslip once deposited, with the lowest contact angle of 11 °. Octanedioic acid had the highest contact angle of 30 °, which demonstrates it would spread less than the other components.

Surface tension measurements were performed to further establish how printable the inks are when jetted, and how they would behave when jetted from the inkjet printer. The surface tension of all the ink components of 60-0.07-Oct were within the range of 55 – 70 mN/m (**Figure 4.7B**). The small range in surface tension is due to the components all being dissolved in the same carrier vehicle, dH_2O, which has a known surface tension of 72 mN/m.

4.2.4 Z number of components of poly- ε-lysine cross-linked with ODA

Table 4.2: Rheological properties and Z number of components of 60-0.07-Oct hydrogel. Ink 1 = pεK and ODA, Ink 2 = NHS and EDCI. Z number calculated for use with an 80 µm print head

	Contact Angle (°)	**Viscosity (kg/ms)**	**Density (kg/m^3)**	**Surface tension (N/m)**	**Ohnesorge number**	**Z number (1/Oh)**
pεK	27.1	0.0066	1051	0.071	0.085	12
ODA	29.9	0.0024	1023	0.057	0.035	28
NHS	11.4	0.0011	1031	0.066	0.015	67
EDCI	19.3	0.0025	1013	0.056	0.038	26
Ink 1	21.0	0.0046	1067	0.063	0.063	16
Ink 2	19.6	0.0023	1064	0.060	0.033	31

The rheological properties of the components of the 60-0.07-Oct hydrogel were combined to calculate a Z number as shown in **Table 4.1**. These values assist in evaluating the printability of the components for inkjet technology. The contact angles for all of the components are low, suggesting a hydrophilic substrate, which might introduce problems with the inks spreading during printing. The viscosities are all within a suitable range for inkjet printing, all between 0.0011 – 0.0066

kg/ms, with the highest viscosity being pεK. There are few differences seen between the densities of each of the components, as they are all dissolved in the same medium, water. The viscosity, density, surface tension and printhead diameter were used to calculate the Ohnesorge number, the inverse of which gives the Z number. The calculated Z numbers are within the range of 12-67. This is a large range and is affected by the varying viscosity values for each component.

Poly-ε-lysine cross-linked with Gellan gum

Further ink characterisation was performed with pεK hydrogels based on electrostatic interaction with gellan gum (GG). The rheological properties of pεK and GG inks in various concentrations were measured to establish the most appropriate inks to take forward for reactive inkjet printing. Rheological measurements included shear rate ramps and temperature sweeps.

4.2.5 Rheological properties of pεK and GG inks

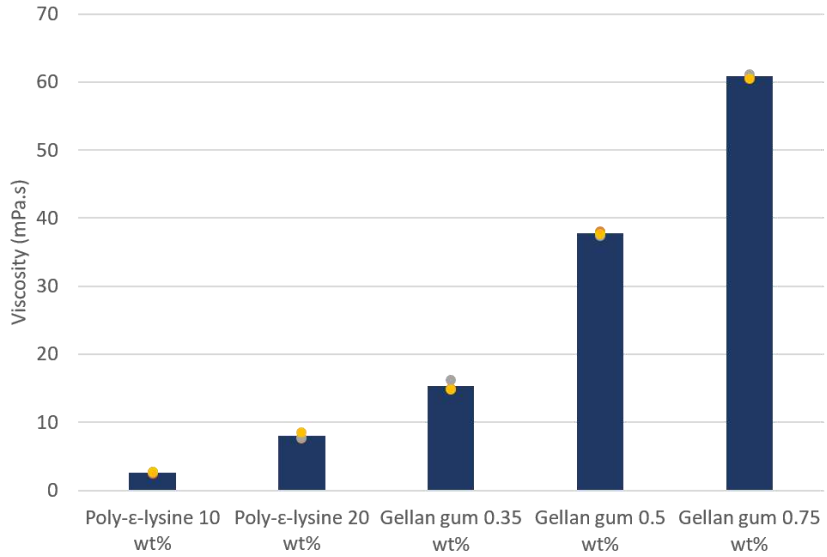

Figure 4.7: Viscosities of varying concentrations of poly-ε-lysine and gellan gum inks for printing. (n=3) Graph plots mean ± SD and individual data points.

A shear rate ramp was performed to establish the viscosity of varying concentrations of pεK and GG at room temperature. Increasing the concentration of both poly-ε-lysine and gellan gum was shown to increase the ink viscosity (**Figure 4.7**). As the concentration of the pεK ink increases from 10 wt % and 20 wt %, the

viscosity increases from 2.6 to 8 mPa.s. Increasing the concentration of the GG ink from 0.35 wt % to 0.75 wt % increases the viscosity from 15 mPa.s to 61 mPa.s, with the viscosity of the 0.5 wt % GG ink in the middle at 38 mPa.s. A suitable range for inkjet printing is 0-20 mPa.s, which suggests that at room temperature, some of the gellan gum inks are too viscous to print.

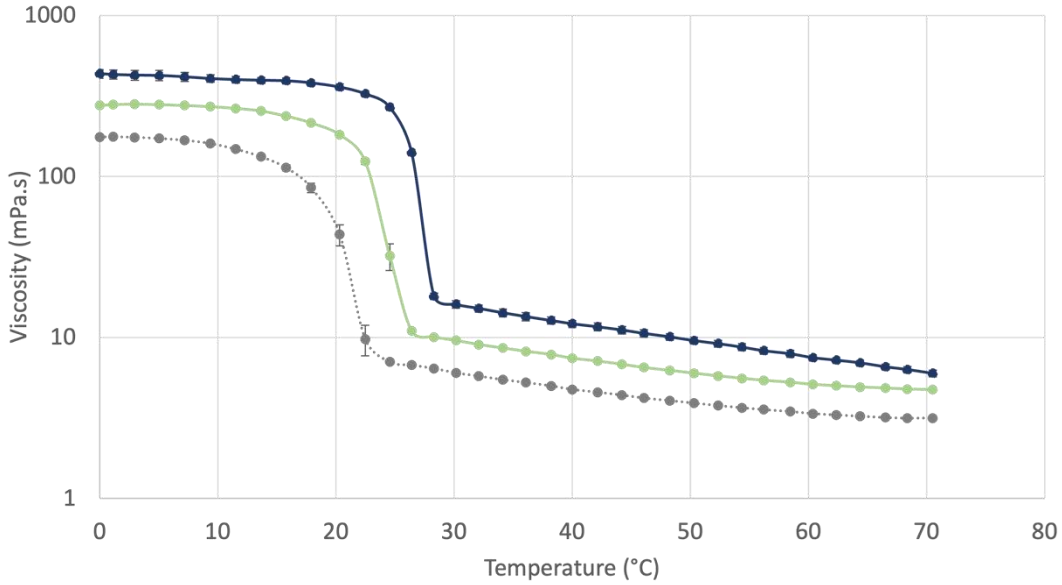

Figure 4.8: Temperature ramp of varying concentrations of gellan gum inks for printing. (n=3). **Key:** Navy blue line = 0.75 wt %, Light green line = 0.5 wt %, Grey line = 0.35 wt %

A sweep was performed to determine the effect of increasing temperature on the viscosity of gellan gum based inks. Temperature ramps for varying concentrations of gellan gum show that increasing the temperature reduces the viscosity (**Figure 4.8**). For all of the inks, increasing the temperature from 0 – 70 °C decreases the viscosity to around 3% of its original value. At a temperature of 0 °C, the GG inks had viscosities in the range of 176 – 430 mPa.s. The 0.35 wt % GG ink decreased in viscosity to 6 mPa.s at around 23 °C. A higher temperature of 26 °C is required to reduce the viscosity of 0.5 wt % GG to 9 mPa.s. Finally, the 0.75 wt % GG ink reduced in viscosity to 16 mPa.s at 30 °C. Figure 4.8 shows that increasing the temperature above room temperature reduces the viscosity of GG inks into a more printable range, which is between 0-20 mPa.s for a jetlab inkjet printer [227].

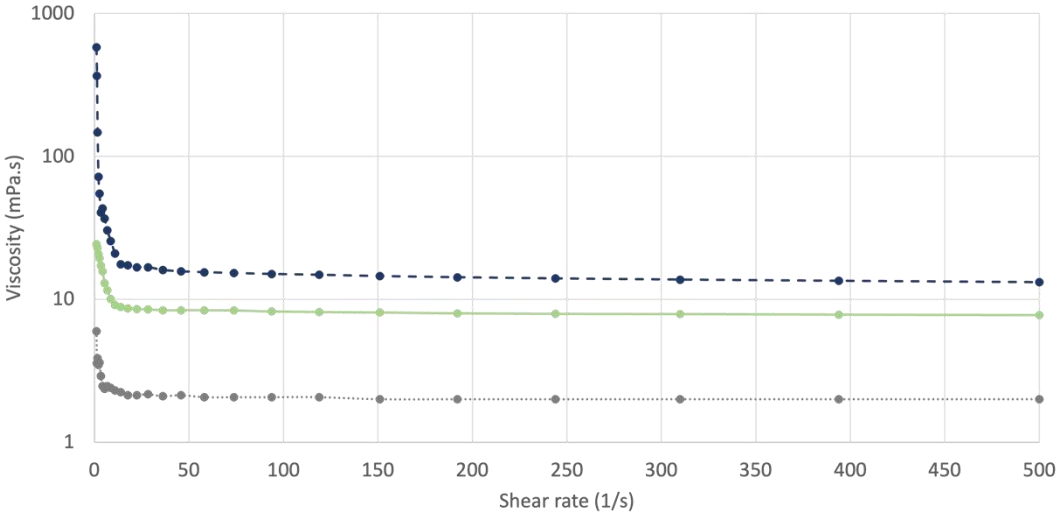

Figure 4.9: Shear rate ramp at 37 °C of varying concentrations of poly-ε-lysine and gellan gum inks for printing. (n=3). **Key:** Navy blue line = Gellan gum 0.75 wt%, Light green line = Gellan gum 0.5 wt%, Grey line = poly-ε-lysine 10 wt%

A shear rate ramp was performed at 37 °C demonstrating the viscosity of pεK and GG inks above room temperature (**Figure 4.9**). These rheology measurements were performed after experimental work indicated that gellan gum inks decrease in viscosity with increasing temperature. All inks were characterised at this temperature as in a Jetlab 4 printer, the printer heads cannot be heated individually. At 500 s^{-1}, all of the inks are in a suitable viscosity range for printed, 0-20 mPa.s. Whereas at room temperature, the higher concentration of gellan gum inks were outside of this range making them more difficult to print.

4.2.6 Ink stability of pεK and GG inks

To assess the suitability of the pεK and GG inks for reactive inkjet printing further ink stability experiments were performed. The measurements included contact angle and surface tension to understand how the inks might behave when they are jetted using an inkjet printer.

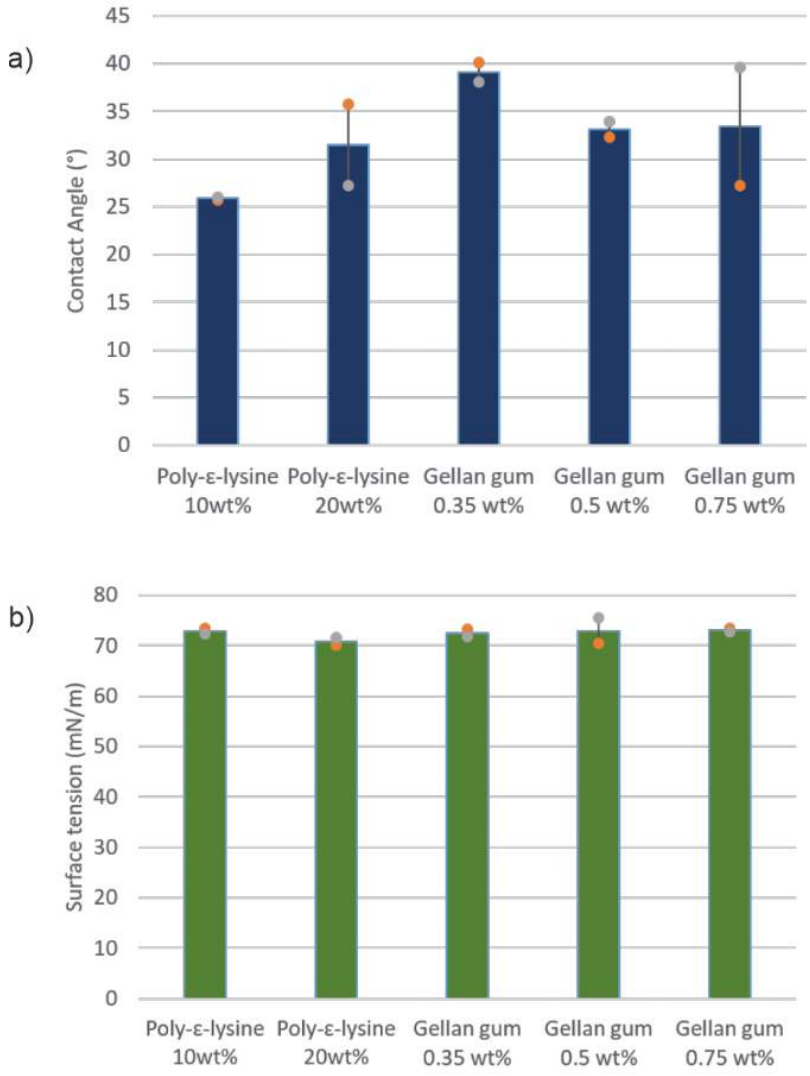

Figure 4.10: **A)** Contact angle **B)** Surface tension of varying concentrations of poly-ε-lysine and gellan gum inks for printing. (n=2) Graph plots mean ± SD and individual data points.

The contact angle of varying concentrations of both pεK and GG were within a range of 25-39 ° (**Figure 4.10A**). Poly-ε-lysine becomes more hydrophilic with increasing concentration, whereas the opposite trend was true for the increasing concentration of gellan gum. All of these contact angles are higher than the

activators used when poly-ε-lysine is cross-linked with octanedioic acid, which suggests this the pεK and GG inks for hydrogel manufacture will be easier to print, as they are less likely to spread across the glass substrate.

The surface tension of various concentrations of poly-ε-lysine and gellan gum are within the range of 70-73 mN/m (**4.10B**). This is a narrow window which is again due to the same DI water carrier vehicle being used to dissolve the polymers. All of the inks are outside of the printing (20-70 mN/m) range for the Jetlab 4 machine. As the surface tensions are only outside of this range by a maximum of 3 mN/m, the inks were trialled in the printer, as the waveforms could be optimised to induce the jetting of the inks.

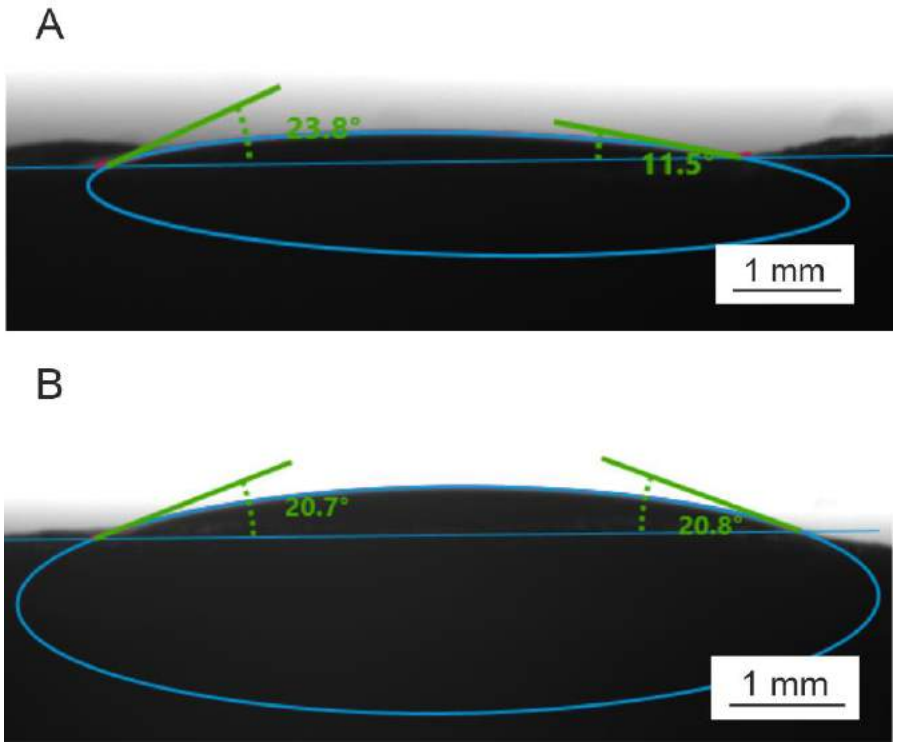

Figure 4.11: Contact angle of **A)** 20 wt % poly-ε-lysine and **B)** 0.35 wt % gellan gum inks on a cast hydrogel substrate. (n=3)

Table 4.2: Average contact angle of 20 wt % poly-ε-lysine and 0.35 wt % gellan gum inks on a cast hydrogel substrate (n=3)

Hydrogel ink	Contact Angle (°)
20 wt % pεK	20.4 ± 1.5
0.35 wt % GG	21.3 ± 2.5

Further contact angle measurements included the use of a cast pεK/GG as a substrate, to understand how much the inks will spread when each layer is printed as the hydrogel builds up. The contact angle of 20 wt % pεK and 0.35 wt % GG was measured on a cast hydrogel (**Figure 4.11** and **Table 4.2**). The average contact angles were 20.4 ° ± 1.5 for 20 wt % pεK and 21.3 ° ± 2.5 for 0.3 wt % GG. The 20 wt % pεK had a contact angle 10 ° lower on the hydrogel substrate than when analysed with a glass substrate. The 0.35 wt % GG was 18 ° lower on the hydrogel substrate, demonstrating that the cast pεK/GG hydrogel is more hydrophilic than a glass slide. The pεK and GG inks demonstrate similar contact angles on the hydrogel substrate, therefore they will have a similar spreading behaviour when the layers are printed on top of one another, which was confirmed when the inks were printed together.

4.2.7 Z number of pεK and GG inks

Table 4.3: Rheological properties of pεK and Gellan gum inks for printing. Z number calculated for use with an 80 µm print head

	Contact Angle (°)	**Viscosity (kg/ms)**	**Density (kg/m^3)**	**Surface tension (N/m)**	**Ohnesorge number**	**Z number (1/Oh)**
0.35 wt % GG	39	0.015	999	0.0725	0.20	5
0.5 wt % GG	33	0.032	967	0.0729	0.43	2.4
0.75 wt % GG	39	0.061	994	0.0731	0.80	1.3
10 wt % pεK	26	0.003	780	0.0733	0.044	23
20 wt % pεK	32	0.008	951	0.070	0.109	9

The variation in rheological properties for increasing concentrations of gellan gum and pεK inks for inkjet printing is shown in **Table 4.3**. As seen in the table, the contact angle for gellan gum is higher than both concentrations of pεK, which suggests it would spread less when jetted onto a glass substrate. The contact angles of pεK and GG inks suggest that gellan gum should be the first in the sequence to be jetted, followed by the pεK, to maintain as high resolution as possible. The viscosity of the 0.5 wt % and 0.75 wt % GG at room temperature is too high, but it can be brought down to a more suitable value by increasing the temperature of the print head. However, it was decided to take the 0.35 wt % GG ink forward to reduce the optimisation needed to print constructs, as the viscosity of this ink was within a printable range (0-20 kg/ms). The surface tensions of the pεK and GG inks are close to the suitable range for printing, and are similar to each other, as seen in Figure 4.10B. The inks with the lowest surface tension and therefore closest to the suitable range is the 20 wt % pεK and the 0.35 wt % GG. These surface tension values along with the viscosity, density and the printhead diameter were combined to calculate

an Ohnesorge number. This number can be inverted to provide the Z number, which determines the printability of inks for inkjet printing. The Z numbers of varying concentrations of pεK and GG are within the range of 1.3-23. The GG inks have a lower Z number than the pεK inks, as their high viscosity will dominate the Ohesorge calculation. Table 4.3 shows that increasing the concentration of GG increases the Z number, as 0.35 wt % GG has a Z number of 5, and 0.75 wt % GG has a Z number of 1.3. The opposite trend is shown for increasing the concentration of pεK, as the Z number for 10 wt % pεK at 23 reduces to 9 when the concentration is increased to 20 wt %.

At this stage, the 10 wt % pεK was discounted due to its high Z number, meaning it would likely form satellite droplets which reduces the quality of the print. Furthermore, the 0.5 wt % and 0.75 wt % GG inks were discounted due to their high viscosity, which was outside of the range of the inkjet printer and therefore would be difficult to jet through the printhead. Based on the combined ink stability data the 20 wt % pεK and 0.35 wt % GG were taken forward for track optimisation and inkjet printing of hydrogel constructs.

4.2.8 Inkjet Printing optimisation of pεK and GG inks

After the concentrations of the pεK and GG inks had been determined, further optimisation stages were required before hydrogel constructs could be printed. The inks needed to form a stable droplet, which required optimisation of the waveform within the jetlab software. Furthermore, track optimisation was performed to establish the appropriate parameters for printing uniform tracks of 20 wt % pεK and 0.35 wt % GG.

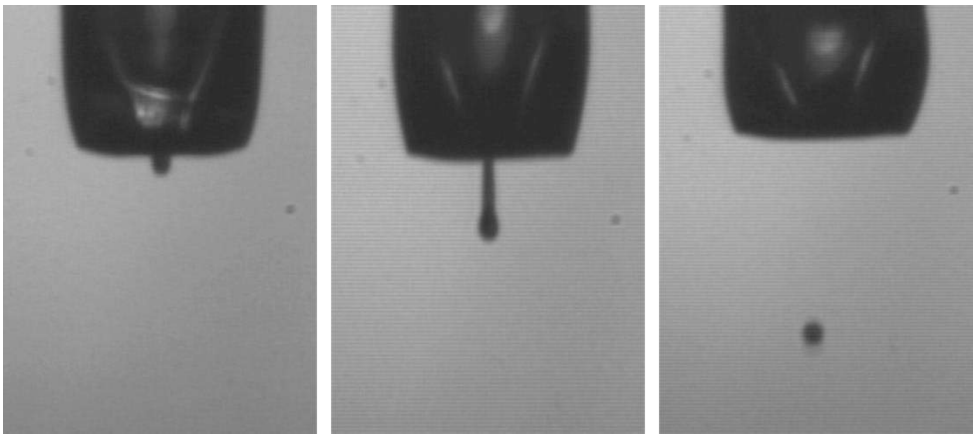

Figure 4.12: Stable droplet of 20 wt % pεK

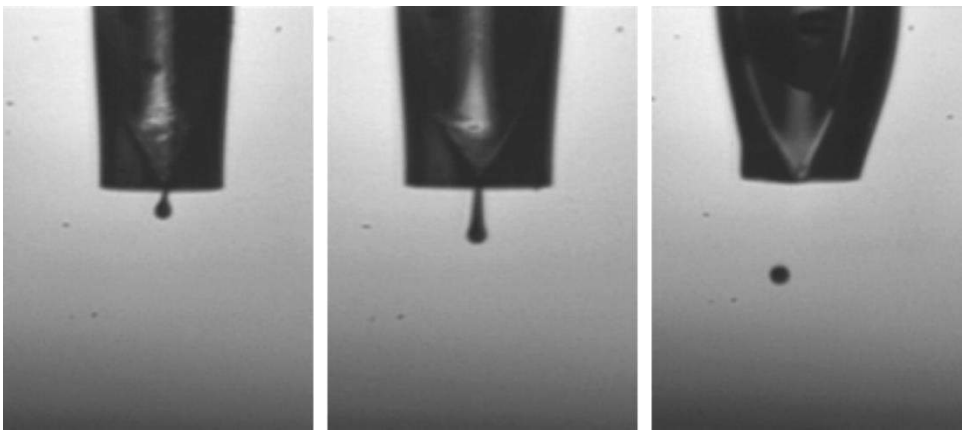

Figure 4.13: Stable droplet of 0.35 wt % GG

The formation of a stable droplet during printing is an important feature which will affect the resolution of the final printed construct. A stable droplet being jetted is dependent upon the rheological properties previously discussed. Images were captured of the stable droplets formed by a 20 wt % pεK ink and a 0.35 wt % GG ink as seen in **Figures 4.12-13.** It is shown that both pεK and GG form stable droplets based on the waveforms in Methods section 2.4.2. These images suggest that 20 wt % pεK and 0.35 wt % GG are suitable for inkjet printing.

Table 4.4: Average track thickness (µm) of 20 wt % poly-ε-lysine after 3 repeats of varying step spacings and speeds

	Step spacing (mm)			
Speed (mm/s)	0.05	0.1	0.15	0.2
5	890 ± 45	630 ± 128	596.7 ± 110	603.3 ± 83
10	954.3 ± 42	610 ± 51	626.7 ± 159	706.7 ± 26
15	836.7 ± 93	653.3 ± 53	733.3 ± 160	600 ± 41
20	826.7 ± 61	620 ± 37	660 ± 98	663.3 ± 31
25	800 ± 64	653.3 ± 78	620 ± 65	503.3 ± 17
30	756.7 ± 37	640.0 ± 88	633.3 ± 52	436.7 ± 39

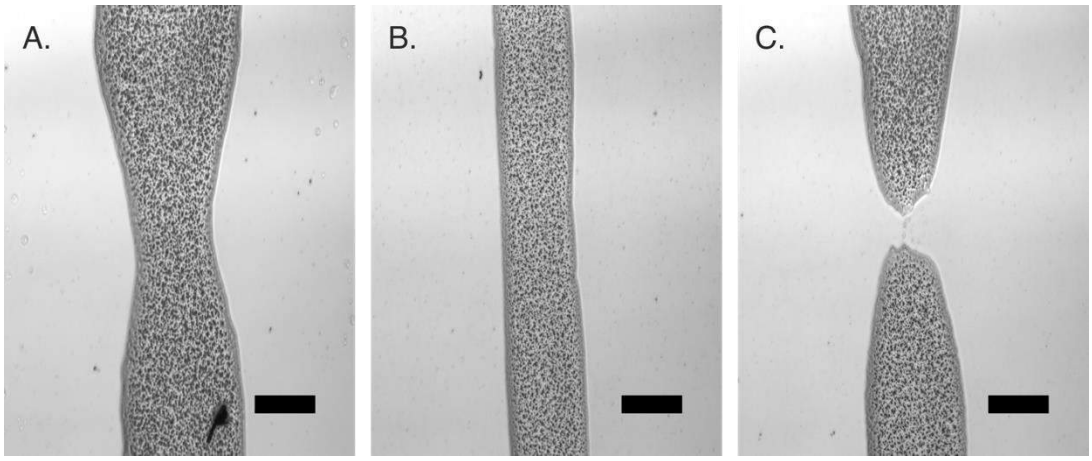

Figure 4.14: Tracks of 20 wt% poly-ε-lysine a) Speed too slow/spacing too close together b) Uniform tracks c) Speed too fast/spacing too far apart. Scale bar = 500 µm

A variety of speeds and step spacing's were trialled to find the optimum settings to print a uniform track of 20 wt % pεK (**Table 4.4 and Figure 4.14**). Printhead speeds were increased from 5 – 30 mm/s and step spacing's increased from 0.05 – 0.2 mm. Table 4.4 shows that on average, increasing the step spacing of the print reduces the track thickness. A step spacing of 0.05 mm generates tracks with an average thickness of 844 ± 63 µm whereas a higher step spacing of 0.2 mm shows an average track thickness of 585 ± 91 µm. At the lower step spacing's, the tracks are uneven as there are sections that are wider than others due to the ink spreading outwards, Image A Figure 4.14 (15 mm/s 0.05 mm). The variability in the tracks could account for the inconsistencies in the increasing speed reducing the track thickness. Several different parameter combinations formed uniform tracks, Image B Figure 4.14 (20 mm/s 0.15 mm), where the step spacing and printing speed were in a sensible range, Table 4.5.

Table 4.5: Parameter combinations which formed uniform tracks of 20 wt % pεK

Step spacing (mm)	Corresponding printhead speed (mm/s)
0.05	30
0.1	15,20,25,30
0.15	10,15,20,25
0.2	10,15

Increasing the step spacing and printhead speed reached a critical point, where after which, the tracks were no longer joined up and had a series of gaps

throughout them, like the tracks visible in Image C Figure 4.14 (25 mm/s 0.2mm). Increasing the step spacing seemed to have more of an influence on the track thickness than increasing the printing speed.

Table 4.6: Average track thickness (µm) of 0.35 wt % gellan gum after 3 repeats of varying step spacings and speeds

	Step spacing (mm)			
Speed (mm/s)	0.025	0.05	0.1	0.15
5	1380 ± 114	903 ± 126	770 ± 88	550 ± 35
10	1213 ± 62	823 ± 53	720 ± 96	546 ± 26
15	1290 ± 86	780 ± 86	603 ± 66	526 ± 40
20	1380 ± 216	680 ± 107	633 ± 114	473 ± 74
25	1280 ± 67	753 ± 161	683 ± 119	466 ± 46
30	1223 ± 82	847 ± 160	583 ± 24	490 ± 59

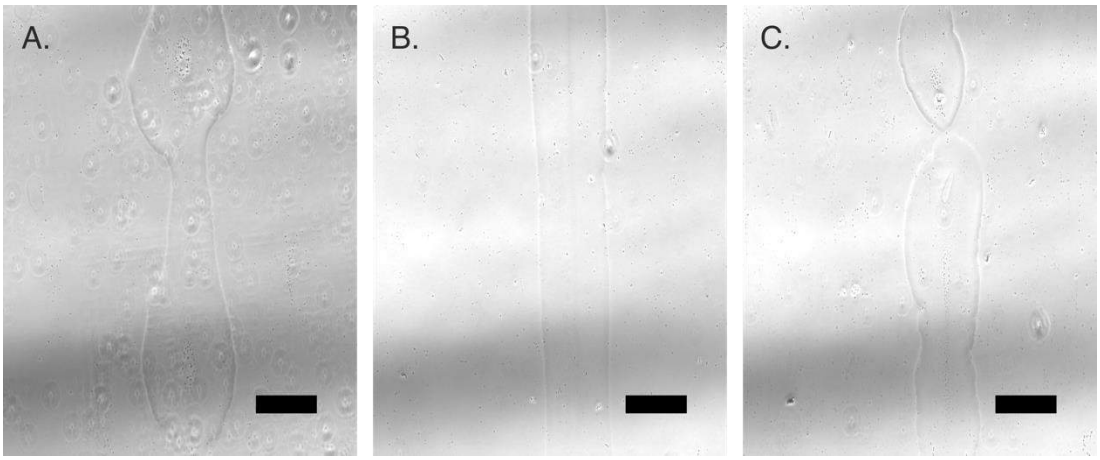

Figure 4.15: Tracks of 0.35 wt% Gellan gum a) Speed too slow/spacing too close together b) Uniform tracks c) Speed too fast/spacing too far apart. Scale bar = 500 µm

To find the optimum settings to print a uniform 0.35 wt % gellan gum track, printing speeds were altered from 5 – 30 mm/s and step spacing's from 0.025 – 0.15 mm. Brightfield images were taken of each track to measure the track thickness (**Table 4.6 and Figure 4.15**). Similar trends as those seen with 20 wt % pεK were established in that increasing the step spacing reduced the track thickness. A step

spacing of 0.025 mm generates tracks with an average thickness of 1294 ± 67 µm whereas a higher step spacing of 0.15 mm shows an average track thickness of 508 ± 934 µm Additionally, images of the tracks showed that the lower step spacing's and speeds produced non-uniform tracks with large bulges where the droplet was dispensed, image A Figure 4.15(10 mm/s 0.05 mm). Uniform tracks were produced in the intermediate speeds and step spacing's, Image B Figure 4.15 20 mm/s 0.1 mm). Finally, gaps occurred in the tracks when the speed and step spacing's were increased further, Image C Figure 4.15(30 mm/s 0.15 mm).

The parameters for pεK and GG inks were narrowed down to those that produced uniform tracks, and then the final parameters selected based on which produced similar track thicknesses so as to increase the resolution of the final print. For 20 wt % pεK, a speed of 15 mm/s and a step spacing of 0.1 mm was chosen. For 0.35 wt % gellan gum, a speed of 20 mm/s and a step spacing of 0.1 mm was chosen. These parameters were chosen due to the similar track thicknesses that they produce, which are 653.3 µm ± 53 pεK tracks and 633 µm ± 114 GG tracks.

4.2.9 Printed pεK/GG Hydrogel Characterisation

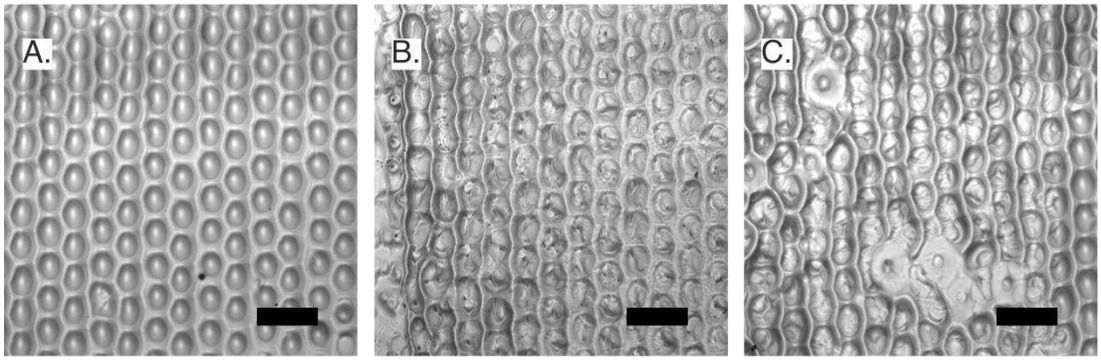

Figure 4.16: Optical micrographs of 75 mm^2 pεK/GG hydrogel print with a) 1 pass of each ink b) 3 passes of each ink c) 5 passes of each ink.

75 mm^2 square arrays were printed with 1,3, and 5 layers of each ink using the appropriate parameters identified during track optimisation. The gellan gum ink layer was printed first with the pεK layer printed directly on top. Each pass takes 80 seconds with a 3 second pause in between for the system to adjust the printing channel. These printed hydrogel arrays were then imaged using optical microscopy

as seen in **Figure 4.17**. The reaction between the two ink droplets as they are dispensed creates a crater which introduces a honeycomb-like topography across the whole printed surface. This topography becomes more pronounced as the number of passes of each ink increases from 1 to 3, shown from Figure 4.16A to Figure 4.16C.

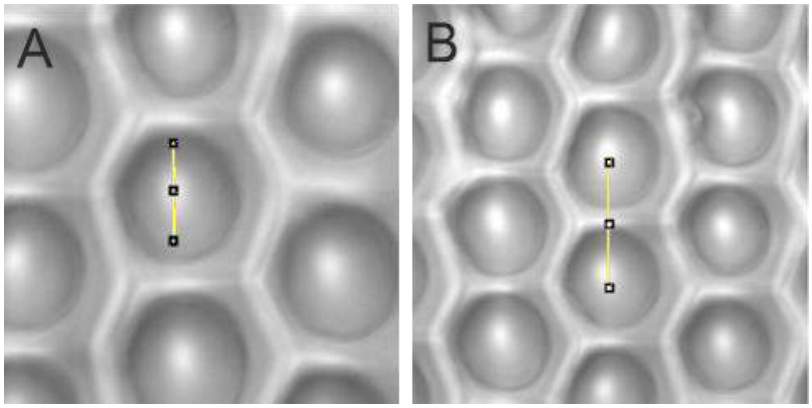

Figure 4.17: Image analysis using ImageJ to evaluate **A)** the diameter of the repeating units and **B)** the distance in between the units in the printed construct

Table 4.7: The diameter of the repeating units when the two inks are printed together and the distance in between the centre of each unit. An average was taken from at least three optical micrographs

Diameter of unit (mm)	Space in between units (mm)
0.148 ± 0.012	0.22 ± 0.018

The diameter of the repeating units identified in the SEM micrographs is 0.148 mm, and the space in between these units averaged at 0.22 mm (**Figure 4.17** and **Table 4.7**)**.** The SEM measurements were performed to further characterise and understand the honeycomb topography of the hydrogel constructs. The diameter of the unit averaged at 0.148 mm, and was in a range of 0.133-0.174 mm. The average space in between the repeating units was identified as 0.22 mm which is close to the chosen step spacing of 0.15 mm. The differences between these values may be indicative of the inks spreading on the glass substrate.

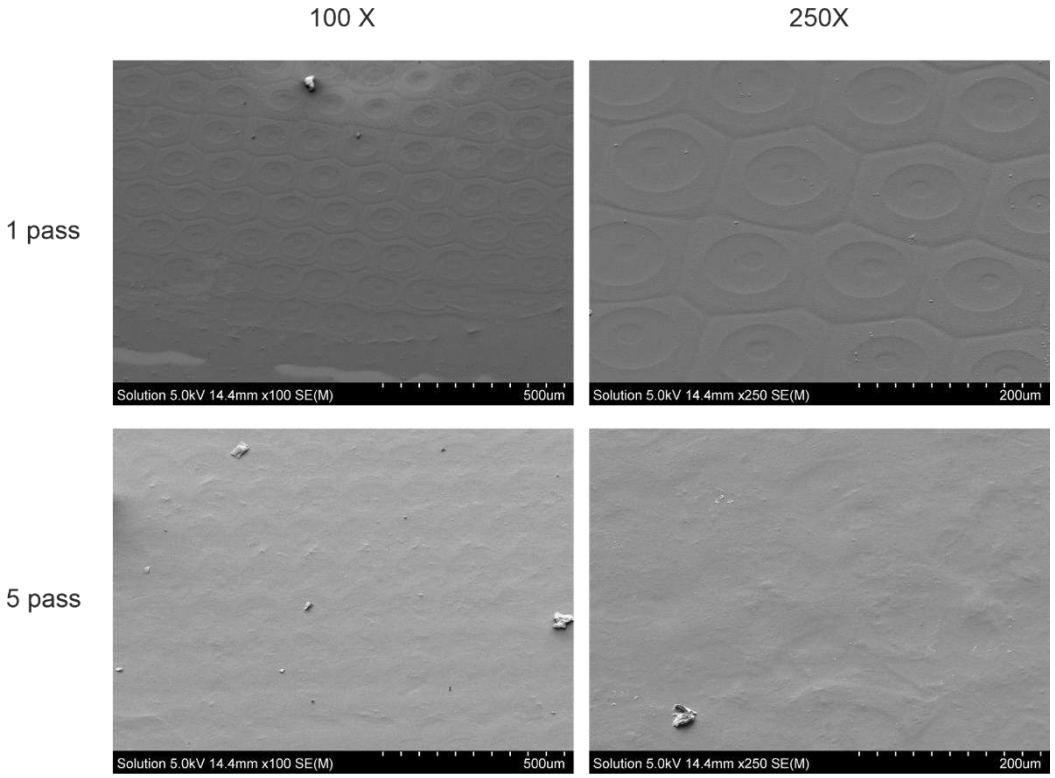

Figure 4.18: Representative SEM micrographs of 75 mm^2 pεK/GG hydrogel print with 1 and 5 passes of each ink. Images taken at a 45 ° angle to visualise the topography.

SEM analysis was performed to establish the topography of 1 and 5 passes of each ink at high magnification, of 100 and 250 X. 1 pass of each ink produces a surface with a clear honeycomb-like topography with repeating hexagonal units every 130 µm. 5 passes of each ink shows a repeating structure but the fine details of the structure isn't as clear as with a 1 pass per ink print.

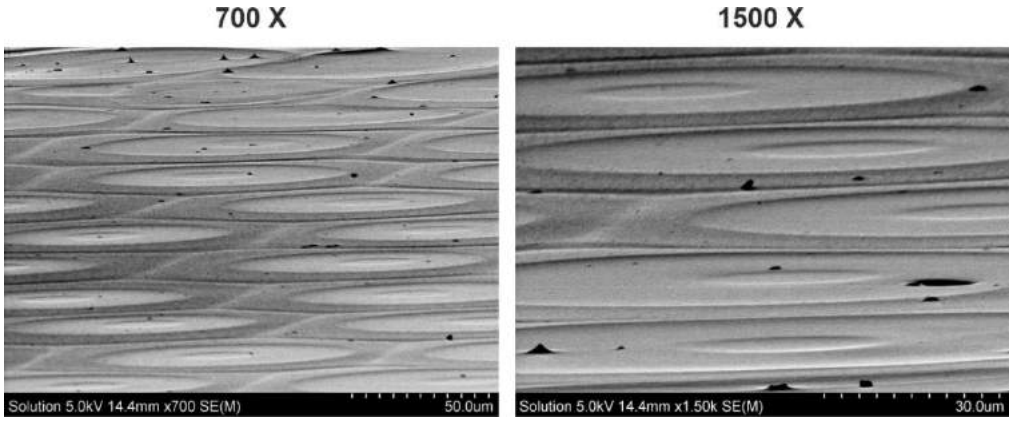

Figure 4.19: SEM micrographs of 75 mm^2 pεK/GG hydrogel print 1 pass of each ink. Images taken at a 90 ° angle to view the cross section of the printed hydrogel.

Cross sectional SEM images at 90 ° were also taken to further understand the topography of the printed hydrogels, and establish whether the repeating units were raised or troughs (**Figure 4.19**). Hydrogels with 1 pass of each ink were chosen for this analysis as they show the clearest repeating units in Figure 4.18. SEM analysis shows that each of the hexagonal structures seems to be a trough with a raised edge in between units.

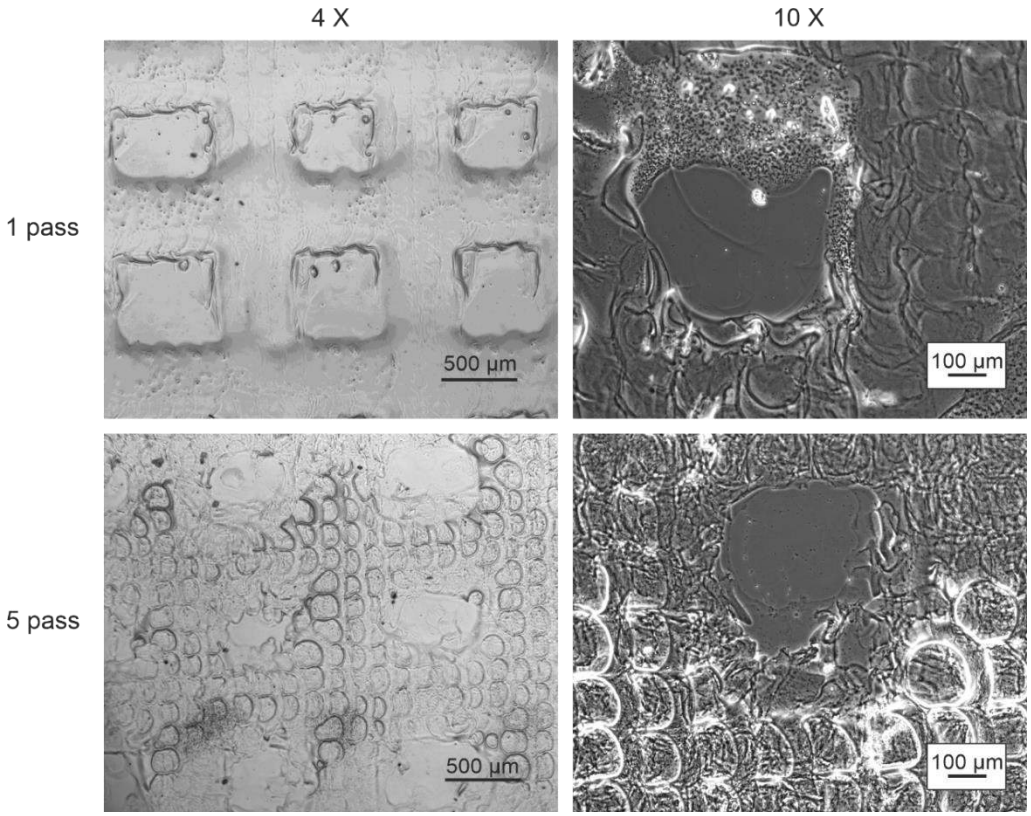

Figure 4.20: Optical micrographs of 1 and 5 passes of a 75 mm^2 porous pεK/GG hydrogel print

The printed arrays were modified to include pores throughout the structure, in order to replicate alternative tissue engineering hydrogels. Porous structures were printed using a bitmap entered into the jetlab script, as seen in Figure 2.8 in Methods section 2.4.4. These prints were based on a 75 mm ^{2} circular bitmap which included gaps throughout the print. These gaps can be seen at both 4 X and 10 X magnification and at both 1 and 5 passes (**Figure 4.20**). The pore sizes included in the bitmap were square with a width between 400 - 500 µm in size. When the optical micrographs were analysed, it was seen that at 1 pass per ink, the pores had an average width within this range, with an average of 470 µm ± 20, demonstrating

a high printing resolution at a low number of passes. When the print is increased to 5 passes per ink, the size of the pores reduce, with an average printed pore size of 380 µm ± 40. The repeating structure in the topography of the printed hydrogel seen in the arrays in Figures 4.15 and 4.17 is also present in the porous bitmaps.

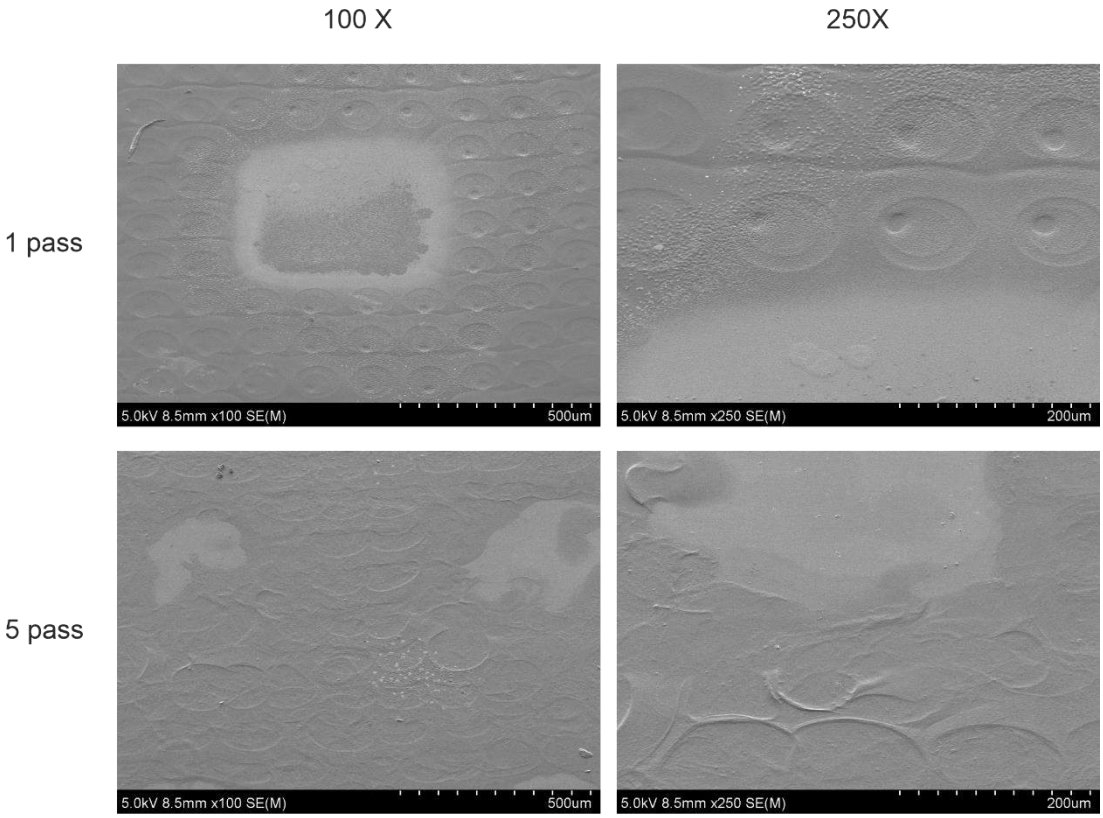

Figure 4.21: Representative SEM micrographs of 75 mm^2 porous pεK/GG hydrogel print with 1 and 5 passes of each ink. Images taken at a 45 ° angle to

SEM analysis was also performed on the printed porous samples to visualise the pores at a higher magnification, of 100 and 250 X (**Figure 4.21**). A similar pattern is seen with the optical imaging in that the shape of the pores lose resolution, and reduce in size, as the number of passes increases from 1 to 5. At 1 pass per ink, the pores averaged at 450 µm ± 33 in width, and when the passes were increased to 5 per ink, the pore width reduced to 320 µm ± 40. Again, in a print with 1 pass per ink, a clear repeating structure of hexagonal units can be seen as in the printed arrays in Figure 4.17. This pattern is still present in printed hydrogels with 5 passes per ink, however the clarity of the structure is reduced.

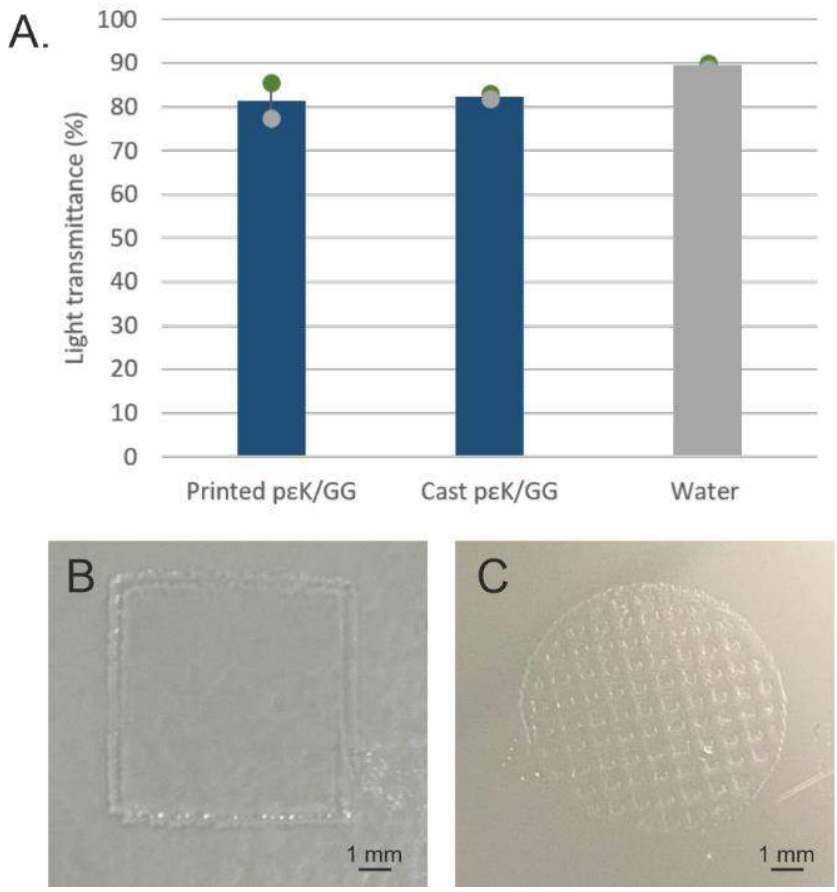

Figure 4.22: **A)** Percentage light transmittance of printed and cast hydrogels based on 20 wt % pεK and 0.35 wt % GG. Water positive control. (n=2) Graph plots mean ± SD and individual data points. **B and C)** Photographs of **B)** 75 mm^2 printed pεK/GG array **C)** 75 mm^2 printed pεK/GG porous bitmap. Scale bars = 1 mm

The transparency of the printed hydrogels was measured using percentage light transmittance. It is important to understand the transparency for a corneal tissue engineering application as a high transparency is required to replicate the human cornea. Percentage light transmittance demonstrated that printed and cast hydrogels made using 20 wt % pεK and 0.35 wt % GG showed a high transparency of 81-82 % (**Figure 4.22**). It is shown that both of the hydrogel variants have a lower percentage light transmittance than the DI water positive control, which has a transparency of 90 %. The printed pεK/GG hydrogel demonstrates a light transmittance of 81 %, while the cast hydrogel demonstrates 82 % transmittance. When an independent T-test was run there was no statistical significance seen between the two groups. The transparency data shows that the different manufacturing methods, and in particular the honeycomb topography of the printed pεK/GG hydrogels, have no significant effect on the substrate transparency.

The photographs in **Figures 4.22B** and **C** further demonstrate the high transparency of the hydrogel variants.

4.3 Discussion

The results in this chapter show that it is possible to manufacture hydrogels via a reactive inkjet 3D printing process using poly-ε-lysine based inks. The hydrogel is formed when a layer of positively charged pεK is printed directly on top of a negatively charged layer of gellan gum. These polymers of opposing charges form ionic bonds, and set to form a hydrogel with a unique honeycomb topography, as shown in Figure 1.7 in section 1.4.3. The versatility of inkjet printing also allows the modification of the shapes printed, which can be designed to meet design specifications.

Producing potential corneal constructs via additive manufacturing (AM) techniques has been investigated in literature, with constructs from multiple groups manufactured via extrusion printing methods. Previous research has shown that it is difficult to replicate the complex architecture of the human cornea, a limitation that may be overcome by 3D printing. Certain AM techniques can allow for precise control over the shape and dimensions of printed constructs, which can be tailored to meet specific design criteria [228]. The high resolution of AM techniques has potential to design constructs that could feature the layered structure of the cornea, where biopolymers could be used to mimic the lamellae within the stroma. In the case of the human cornea, its thickness, shape and curvature has a direct impact on its function, to refract light onto the retina. Therefore, in order to achieve a functional construct with a high likelihood of success, it is important to meet these design criteria. Furthermore, particular AM techniques such as inkjet 3D printing can allow for the deposition of cells at specific locations throughout a printed construct [229]. This is a feature that may be advantageous for building a cell-loaded corneal implant, as the different cell types can be deposited at their typical location in the native human cornea. Finally, corneal tissue has several design advantages over producing other tissues via additive manufacturing; as it is homogeneous, avascular and has a low metabolic demand [230]. For these reasons,

3D printing of a cornea substitute has become a priority for tissue engineering research in recent years.

Although artificial cornea substrates have made it through to Phase I clinical trials [231], there is still no tissue equivalent that is available for clinical use. This leaves the floor open to research groups to investigate alternative materials for 3D printing of an artificial cornea, with a handful making it through to *in vivo* trials. In order to be deemed suitable for a corneal tissue engineering construct, 3D printed constructs must be characterised for their transparency, mechanical properties, swelling and degradation properties, cyto-compatibility *in vitro*, and eventually their biocompatibility *in vivo* [232].

4.3.1 Extrusion printing of poly-ε-lysine cross-linked with octanedioic acid

Our group have previously reported the production of hydrogels for ocular applications based on the cross-linking of poly-ε-lysine with bi-carboxylic acids [233-236]. Additionally, the fragmented and macroporous pεK hydrogel variants in Chapter 3 were based on this same chemistry. Hence, the rheological properties of the components of these hydrogels were evaluated, to assess suitability for 3D printing.

Initially, the rheological properties of pεK were evaluated with the idea of extrusion 3D printing in mind. This would involve extruding the combined hydrogel components as they were polymerising, to deposit and build up a solid 3D structure. The rheological properties of the pεK hydrogels were measured with a 60-0.07-Oct and 60-0.1-Oct chemistry. These two hydrogel chemistries were chosen as they had been characterised previously by our group for a contact lens application [233], therefore the properties were understood. Rheology sweeps analysing the storage and loss modulus over time, allowed a close look at how the ink properties changed. Where the loss modulus is greater than the storage modulus, the viscous forces dominate the inks viscosity. Viscous behaviour occurs as a result of internal friction between molecules in a fluid, which in turn develops frictional heat within the fluid. The result is a transformation of deformation energy into heat energy which is absorbed by the sample. Loss modulus therefore characterises the deformation energy lost through friction. However, when the

storage modulus overtakes the loss modulus, the elastic forces dominate the viscosity, and after this point, the hydrogel becomes too difficult to extrude. Storage modulus characterises the stored deformation energy, which is based on the elastic deformation of internal structures without damaging the material. The point where G' > G'' represents the formation of physical links within the material, which in the 60-0.1-Oct and 60-0.07-Oct hydrogels, is where the amide bonds are formed between the pεK and ODA. The ideal printing window was identified as when the hydrogel had begun to set, up until just before the viscosity of the hydrogel was too high to extrude. For the 60-0.1-Oct chemistry, the printing window was identified as between 8-12 minutes after the components were added together. For the 60-0.07-Oct chemistry, the window was between 12-15 minutes. Before this window, the hydrogel inks are too low in viscosity, and spread across the substrate before setting. After this window, the hydrogel will polymerise, and become too viscous to extrude through the syringe. Additionally, after this point, the layers that would then be printed on top of the original layer would not bind together, as the polymerisation reaction had already taken place. The polymerisation timing of the pεK hydrogels cross-linked with ODA identified in these results limits the printing window to 3 minutes, which introduces issues for the additive manufacturing of complex parts. Due to the corneas high complexity and multiple layers with different structures, it is likely that printing times for substrates for corneal tissue engineering would take longer than this 3 minute window allows. This limitation could be overcome by the hydrogel components being combined at different stages throughout the printing process so that the part can be built up, however, this would increase the complexity of the process.

The 'ideal printing window' can be visualised in **Figure 4.23,** where the 60-0.1-Oct hydrogel was loaded into a Fab@Home extrusion printer in a trial, and printed after 8 minutes of letting the components polymerise. The first few lines that were printed were too low in viscosity, at ~20 mPa.s, and spread across the glass substrate. After around 9/10 minutes, polymerisation had occurred and a solid hydrogel was extruded. After around 12 minutes, the extrusion was more sporadic,

as the syringe struggled to eject the hydrogel due to its high viscosity of > 3000 mPa.s.

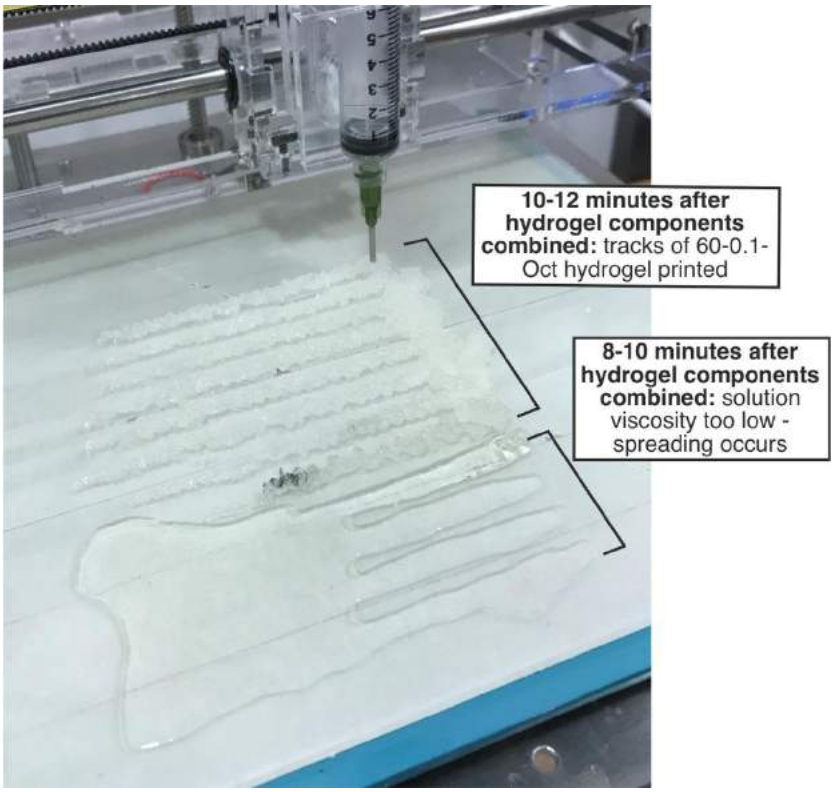

Figure 4.23: Extrusion of 60-0.1-Oct using a Fab@Home extrusion printer setup

A temperature sweep of the 60-0.1-Oct hydrogel was performed to see if the temperature influenced how the hydrogel polymerised. This was done to see if modifying the temperature of the base plate of the extrusion printer would adjust the printing window of the hydrogel. This temperature sweep showed a rapid increase in viscosity around 28 °C suggesting that is where the hydrogel had set. The increase in the temperature of the hydrogel sample would increase the kinetic energy throughout it, and therefore speed up the rate of reaction. The same trend of faster polymerisation was also observed when the fragmented hydrogels from Chapter 3 were manufactured above room temperature. Above 28 °C, there was little changes in the viscosity for the rest of the sweep up until 60 °C. Based on this finding, several printing trials were performed with the base plate heated to 30 °C. The increased temperature sped up the rate of reaction and the hydrogel polymerised sooner, however the printable window was still limited to around 3 minutes.

Due to the short time window where the hydrogel could be suitably extruded, and the limited modifications to the extrusion set up, a different additive manufacture method was explored. The limitations seen with the extrusion printing of poly-ε-lysine in this thesis could be overcome with an alternative printing setup which could allow for additional modifications such as further temperature controls or the addition of separate ink channels.

4.3.2 Reactive inkjet printing of poly-ε-lysine cross-linked with octanedioic acid

After proving difficult to print poly-ε-lysine cross-linked with ODA via extrusion printing, its properties were then analysed for inkjet 3D printing.

The viscosity over time of the hydrogels with the same two chemistries was measured to establish how long it would take for the hydrogel to set once the inks had been combined. Ideally for inkjet printing, the inks reacting together needs to set immediately, so that additional layers can be printed on top of the previous layer. This time sweep identified that 60-0.1-Oct hydrogel took around 12 minutes to fully set and the lower polymer density ink of 60-0.07-Oct still had not set after 20 minutes. As this time window was out of the suitable range for inkjet printing, the sweep was stopped running at 20 minutes. As identified in the temperature sweep in Figure 4.2, the reaction time could be sped up by increasing the temperature of the base plate within the inkjet printer, therefore further rheological assessments were performed on the 60-0.07-Oct variant.

The jetlab inkjet printer has a requirement that the ink viscosity must be in the range between 0-20 mPa.s [227]. For this reason, the hydrogel components needed to be separated and analysed individually for reactive inkjet printing. The four hydrogel components dissolved in water; pεK, suberic acid, NHS and EDCI were analysed, as well as combinations of the components. Ink 1 = pεK combined with suberic acid and Ink 2 = NHS and EDCI.

Shear rate ramps were performed to establish the viscosity of the individual components and Inks 1 and 2. For the 60-0.07-Oct chemistry, all of the measured components had a viscosity of less than 10 mPa.s, falling within the printable range of the jetlab printer. For the higher polymer density 60-0.1-Oct chemistry, the

viscosity of both the pεK and EDCI inks had increased, in turn increasing the viscosity of Inks 1 and 2. This increase put the viscosities of the inks to the higher end of this 0-20 mPa.s range which would make it more difficult to inkjet print hydrogels of this chemistry. In both chemistries, the sweep shows that the viscosity of Ink 2 increased before decreasing back into a suitable range for inkjet printing, 0-20 mPa.s. This increase then decrease in viscosity is thought to be due to the effervescent reaction between NHS and EDCI, causing the formation of bubbles within the ink which in turn affects the viscosity reading. This reaction can be seen in the photograph in **Figure 4.24A.** After the reaction has taken place, the bubbles settle down and the NHS/EDCI is usable to activate the cross-linking of pεK with suberic acid, however after around an hour, a precipitate of O-acylurea is formed, **Figure 4.24B.** The presence of a precipitate would prove difficult for inkjet printing of complex prints that take a long time, as the precipitate formed in the ink reservoir may block the print heads. For this reason, the components were analysed further separately, as up to four inks could be used at any one time for a print in the jetlab 4 setup.

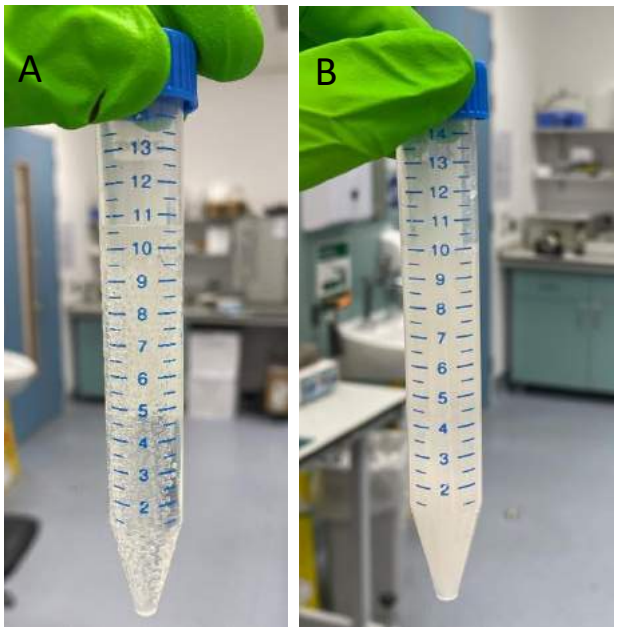

Figure 4.24: Photographs of **A)** Immediate reaction between NHS and EDCI causing the formation of bubbles and **B)** The cloudy precipitate formed after the NHS/EDCI reaction after 1 hour

As the 60-0.1-Oct hydrogel components had a higher viscosity, some of which were approaching the limits on the viscosity range, the 60-0.07-Oct was taken forward for further analysis. This included establishing the ink stability using contact angle and surface tension measurements, which were, in turn, used to calculate the Z number for inkjet printability.

The contact angle of the inks is important to establish how the ink will interact with the substrate once printed. It is of particular importance for reactive inkjet printing, as combining more than one ink together will cause the inks to spread across the surface of the substrate, due to the increased liquid volume. A high contact angle, > 90 °, indicates that the substrate is hydrophobic, and the ink will remain in a rounded ball on its surface. A low contact angle, < 90 °, indicates that the substrate is hydrophilic, allowing the ink to spread across the surface. Studies have shown that a contact angle around 56 ° has minimal spreading, creating monotonic tracks, whereas a contact angle of > 90 ° shows a recoil of the droplet [237]. The track diameter is controlled by the droplet diameter upon impact, which is a function of initial drop size and contact angle [155]. Therefore the resolution is controlled by this minimum diameter, which increases with a decreasing contact angle. Contact angle analysis showed the ink components all fall into a range between 11 - 30 °. The lowest contact angle of 11 ° was the NHS component, which shows that this ink would spread the most across the substrate surface when printed. The spreading behaviour of NHS was not assessed as the NHS and EDCI were combined into one print head channel, which was unable to form a stable droplet. Furthermore, the variation in the contact angles would cause differences in the thicknesses of the printed tracks, which could reduce the print resolution. Again, tracks of the components for pεK cross-linked with ODA were not printed as Ink 1 and Ink 2 were unable to form a stable droplet based on their complex rheological properties.

The surface tension of the inks allows further understanding of the droplet behaviour of the inks when they are jetted from a jetlab 4 inkjet printer. Additionally, it is required to calculate the Ohnesorge number, used to assess printability of inks. A low surface tension may result in the formation of satellite droplets, as it when a droplet is dispensed, it would likely form a longer ligament

which would break up into additional satellite droplets [238], shown in the schematic in **Figure 4.25.** A higher surface tension would more likely result in a stable droplet as the increased tension would cause the ligament to retract into the main drop during flight. Satellite droplets are caused by the forces the inks are subject to when they are dispensed from the inkjet head, therefore the ink properties will vary how the forces affect the stable droplet. The formation of satellites was observed when 10 wt % pεK was dispensed from the jetlab printer, which was likely due to the low viscosity dominating the fluid properties. However, a surface tension that is too high may result in difficulty dispensing a droplet at all, as the droplet energy cannot overcome the barrier formed by the fluid/air interface. For a 60-0.07-Oct chemistry, all of the components are within the 20-70 mN/m range [227] for the Jetlab 4 printer. This data suggests they will all be printable using inkjet methods, when the waveforms have been optimised.

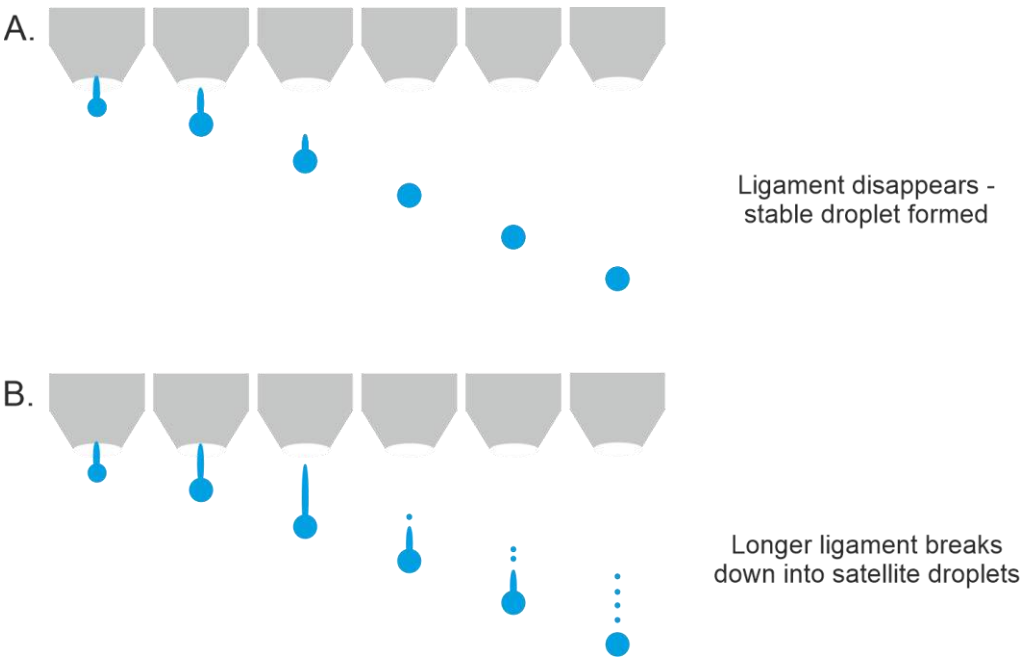

Figure 4.25: Schematic showing **A)** The formation of a stable droplet **B)** The formation of satellite droplets due to low surface tension. Figure made using CorelDraw.

The rheological properties were used to calculate the Ohnesorge number, which, in turn, was used to calculate the Z number. The Z number range which is deemed

printable for inkjet printing is 1-10 [144, 155]. Below this range, the high viscosity of the ink dominates the rheological properties, and it is too difficult to expel an ink droplet. Above a Z number of 10, inkjet printing would likely result in the formation of satellite droplets, due to either the low viscosity or low surface tension. This printing range is shown in more detail in **Figure 4.26.** When the Z numbers of the components of 60-0.07-Oct were calculated, all of the values were outside of the 1-10 range. This is influenced by both the low viscosity and the low surface tension of these components. Although outside of the theoretical printable range, some Z numbers are still printable. When trialled in the inkjet printer, the components were combined to make Ink 1 and Ink 2, which in turn were pεK + ODA and NHS + EDCI. The pεK + ODA channel formed stable droplets, however the NHS + EDCI was unable to jet due to the formation of the O-acylurea precipitate which blocked the 80 µm print head.

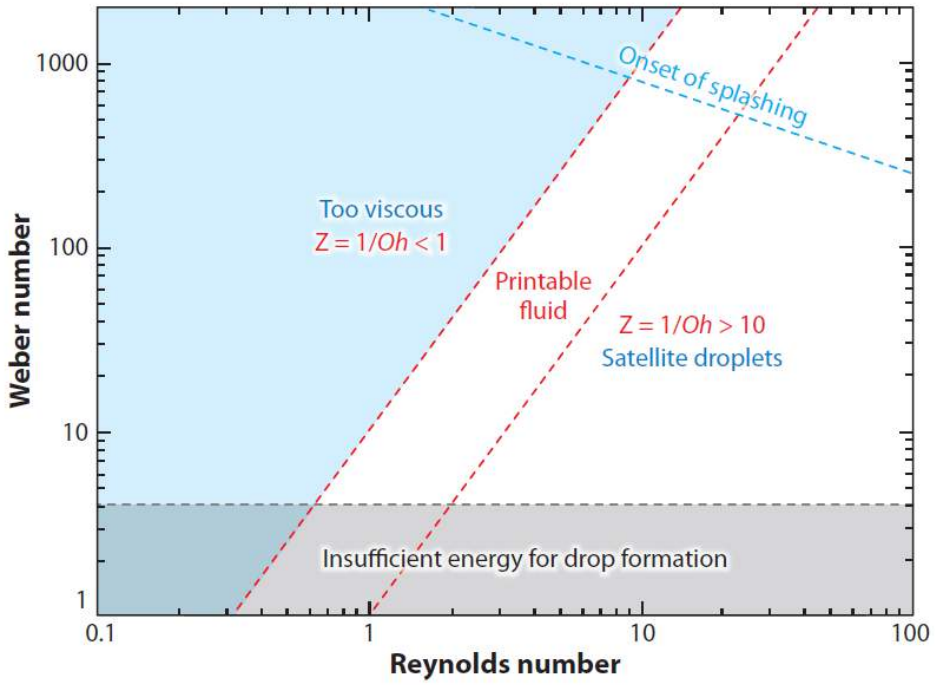

Figure 4.26: The effect of the Z number on the printability of an ink via inkjet printing – B. Derby et al [142]

Due to the rheological properties of the pεK components when cross-linked using ODA, and the long reaction time, it was concluded that this polymer chemistry was

unsuitable for reactive inkjet printing. Additionally, the requirement to keep the inks separate before printing increased the complexity of the printing process and using 3-4 different print channels at once would take lots of optimisation and add complexity to the manufacturing process.

4.3.3 Reactive inkjet printing of poly-ε-lysine cross-linked with Gellan Gum

As a result of the unsuitability of poly-ε-lysine cross-linked with ODA for reactive inkjet printing, different cross-linking chemistries were explored for their compatibility. As previously outlined, the inks needed to meet certain criteria to be deemed suitable for the jetlab 4 printer, such as; a viscosity between 0-20 mPa.s and a surface tension of 20-70 mN/m. Furthermore, for reactive inkjet printing, an additional requirement is that the printing inks react immediately to form a solid substrate before the subsequent layers are printed on top. Based on these criteria, a method was devised where the positive amine groups on the pεK backbone, shown in Figure 1.5 in section 1.4.3, were utilised to form a cross-linked hydrogel based on electrostatic interaction.

This discussion section focuses on results sections 4.2.5-4.2.9, the ink characterisation, optimisation and reactive inkjet printing of poly-ε-lysine and gellan gum to produce a hydrogel substrate.

Rheological assessments were performed on varying concentrations of pεK and GG inks, to evaluate which inks were in a suitable viscosity range for RIJ. Across all measured ink concentrations for both polymers, increasing the wt % of the polymer increased the viscosity of the ink. Both 10 and 20 wt % pεK had viscosities within the printable window, of 2.6 mPa.s and 8 mPa.s. Initially, 0.75 wt % GG was trialled for RIJ, however rheological evaluations showed that the viscosity of 61 mPa.s was too high to be printed using a jetlab 4 printer. When the GG concentration was reduced to 0.5 wt % and 0.35 wt %, the viscosities measured 38 mPa.s and 15 mPa.s. This data shows that only the 0.35 wt% GG has a viscosity that was printable in a jetlab 4 printer [227]. Furthermore, for a corneal tissue engineering application, a low viscosity ink has been identified to be more suitable for producing structures

with a high resolution [225]. The necessity of low viscosity inks is to preserve the form of the structure during extrusion and the building of the part, but also to minimise the shear stress inflicted on the extruded material, which is particularly important if cells are included in the printing ink.

As the jetlab 4 printer setup included components that could be heated, including a base plate and a printhead block, a temperature sweep was performed on the GG inks to establish how increasing the temperature affected the viscosity of the inks. For all of the GG inks, increasing the temperature decreased the viscosity to 3% of its original value, shows that increasing the temperature above room temperature reduces the viscosity of GG inks into a more printable range. The increasing temperature during the sweep will in turn increase the kinetic or thermal energy within the sample, which allows the molecules to be more mobile. The increased mobility reduces the attractive binding energy and as a result the viscosity of the sample will reduce. The high viscosity of gellan gum at low concentrations is likely due to its molecular structure. Gellan gum molecules form double helices, which at high concentrations change to thicker aggregates and form a gel [239]. When gellan gum is heated, the double helices relax and extend to form disordered coil states, which reduce the solutions viscosity [240]. Previous studies showing the rheological behaviour of gellan gum further support this data, where GG demonstrates thermo-reversible properties [241], where increasing the temperature reduces the viscosity, which then returns to normal upon cooling of the solution.

Although the temperature of certain components within the printer could be adjusted, the reservoirs where the inks were stored during printing were separate, and not able to be heated. This meant that the when the higher concentration GG inks were loaded into the reservoirs for printing, the ink viscosity was unaffected by the higher temperature, and were still too high to be expelled through the printhead.

Further ink stability measurements were performed to characterise the inks for RIJ. The contact angle of varying concentrations of both pεK and GG were performed to establish how the ink interacts with the substrate, a glass slide. Establishing the contact angle of printed inks is vital for defining the minimum possible printed track

thickness, and the extent of the inks spreading. In RIJ, the resolution of the printed construct is influenced by the spreading behaviour of the inks on the substrate. If the inks have a high degree of spreading, the resolution of the print will be reduced as the layers of hydrogel build up. A high resolution, in at least the micron range, is important to achieve a fine detail during manufacture, which is useful in particular for complex biomaterial parts. In particular for corneal tissue engineering, the resolution would need to be high, in the micron range, to achieve the complexity of individual corneal layers, for example the endothelial monolayer at a 5 µm thickness. A contact angle that is too low, typically less than 65 ° [242], will result in ink spreading across the substrate. Whereas, a contact angle that is too high will prevent the formation of a uniform layer, due to the lack of efficient ink spreading [243]. On a glass substrate, pεK inks were seen to become more hydrophilic with increasing concentration, whereas the opposite trend was true for the increasing concentration of GG inks. All of the contact angles were in the range 25-39 ° which shows that all the measured polymer inks have a high wettability on glass. When measured on a cast hydrogel substrate, the pεK and GG inks had similar contact angles of 20.4 ° and 21.3 ° respectively. The hydrophilic nature of the hydrogels may incur issues with printing fine detail parts with a high number of passes, as this data shows, the inks are more likely to spread when printed on top of one another as opposed to on a glass substrate.

As the GG ink had a higher contact angle on glass than the pεK, this was chosen to be printed first, to limit the ink spreading across the substrate in the initial layer. The two inks both had similar contact angles when measured on a cast hydrogel substrate, so the resolution as the print built up would be similar despite the order in which the inks were printed.

It is important to understand the surface tension of the inks as this affects how they will jet when loaded for RIJ. All of the pεK and GG inks measured had a surface tension in the range 70-73 mN/m. This shows that the differences in the polymer dissolved have little effect on the final surface tension. The similarities are likely due to the same carrier vehicle being used for all inks, DI water, which has a known surface tension of 72 mN/m.

The inks rheological properties were used to calculate the Z number, and, as described in section 4.2.3, the ideal range for the Z number is between 1-10 [144, 155]. The data describes that the only pεK variant to fall into this window is the 20 wt % concentration, with a Z number of 9. The lower concentration of 10 wt % has a Z number of 23, which suggests that it would produce satellite droplets when trialled in an inkjet printer. The satellite droplets are likely caused by the low viscosity of the 10 wt % pεK, and would result in unwanted features throughout the final print. For this reason, 10 wt % pεK was discounted, and 20 wt % pεK was taken forward for track optimisation. Although 0.5 wt % and 0.75 wt % have Z numbers within the suitable window, with values of 2 and 1 respectively, their viscosity is much too high to be printed using this particular method. For this reason, 0.35 wt % GG was taken forward for track optimisation for RIJ.

Track optimisation is an important step to take prior to inkjet printing of constructs, particularly when more than one ink is involved. This stage was performed to identify optimum printing parameters for printing uniform tracks of the chosen inks: 20 wt % pεK and 0.35 wt % GG. This stage involved varying the step spacing and the printing speed for the two inks and comparing the thickness and the quality of the tracks produced. The optimum parameters were established by analysing the uniformity and the thickness of the tracks. For each ink, there were several parameters that achieved uniform tracks in terms of quality, however the thicknesses varied across different speeds and step spacings. For this reason, the two sets of parameters were also chosen based on the thicknesses of the tracks produced, to closely match them for the pεK and GG inks. Both inks were printed using a step size of 0.1 mm, with pεK ink at a speed of 15 mms^{-1} and GG ink at 20 mms^{-1}. The pεK parameters produced tracks with a thickness of 653.3 µm ± 53 and the GG parameters produced tracks of 633 µm ± 114. The tracks produced by the two inks having only a small difference of 20 µm should improve the resolution of the printed hydrogel when the inks are deposited on top of one another. Once the ideal parameters were established for the two inks, printing of various hydrogel constructs could begin.

A variety of shapes with multiple different layers were printed via RIJ, using the parameters outline for the two polymer inks, which were loaded into separate channels in the jetlab printer. Furthermore, due to the variable temperature in the laboratory, the printhead block was set to a temperature of 25 °C and the base plate to a temperature of 30 °C. These temperatures were chosen based on the rheology data previously discussed, and the behaviour of the inks identified in optimisation stages. The hydrogels were printed into either 75 mm^2 square arrays, or 75 mm^2 circular bitmaps, and were analysed using optical and scanning electron microscopy to characterise their topography.

Optical micrographs show that the printed arrays form a honeycomb like structure in a repeating ordered pattern, visible throughout 1,3 and 5 passes of each ink. This repeating pattern is likely due to the immediate reaction between the two polymers, where the pεK causes a crater upon droplet impact with the dispensed GG layer. This suggestion is further supported by the spacing between two adjacent units, identified as 0.22 mm ± 0.018. This is close to the step spacing used for both inks at 0.1 mm. The difference between the space between adjacent droplets and the step spacing used may be accounted for by the ink spreading, due to the high wettability of pεK and GG when printed onto both a glass substrate, and the hydrogel itself. SEM analysis of the printed arrays shows a similar repeating structure when 1 and 5 passes of each ink are printed. The 100 and 250 X magnification used in SEM characterises the topography in more detail than optical imaging, which confirms that the honeycomb structure is likely caused by droplet impact. This is further supported when the printed samples are imaged at a 90 ° angle, showing that each unit is crater-like in its depth of structure. The hexagonal shape surrounding the individual units is likely formed as the droplets dispensed in RIJ provides the minimum surface area of shapes that fit together with no gaps. The images show that printed constructs with 1 layer of each ink have a clear repeating topography, whereas when 5 layers of each ink are printed, a repeating structure can be identified, however the clarity is lost.

The same imaging techniques were used to analyse pεK/GG bitmaps with 1 and 5 passes of each ink. These constructs were based on a 75 mm^2 circular bitmap

which contained spaces throughout the print. Again, the honeycomb topography is visible at both 1 and 5 passes of each ink, surrounding the porous gaps. These pores can also be seen using both optical and SEM imaging methods. The images reported in section 4.2.9 demonstrate a reduction in resolution and pore size of the printed samples when the number of passes of each ink is increased from 1 to 5. The pore sizes reduce from an average of 470 µm to 380 µm and appear more rounded in shape when 5 passes of each ink are printed. The 90 µm reduction in pore size and lower resolution may be due to a higher incidence of ink spreading, due to an increased ink volume in the higher number of passes. The resolution of these prints at higher passes may be able to be optimised by adjusting the temperature of the base plate within the printer, as this results in the ink layers drying faster, which reduces the likelihood of ink spreading.

The transparency of the printed hydrogels is important for a corneal tissue engineering application, as the aim of the substrate is to restore the transparency of the cornea following damage to one or more corneal layers. The two polymer inks used to make this hydrogel have previously been reported to produce transparent hydrogels when cross-linked, therefore it was hypothesised they would produce transparent constructs when combined. Percentage light transmittance data and photographs confirm the high transparency of the printed pεK/GG hydrogels. The printed hydrogels used in the percentage light transmittance measurements were printed with 10 passes of each ink, however were still thin sheets. An independent T-test found no significant difference between printed and cast pεK/GG hydrogel variants, which demonstrates that the manufacturing process does not significantly affect the optical properties of the hydrogel. This is a notable finding, as RIJ is a low-cost method that achieves high resolution, tuneable printed parts when compared to hydrogels made via static casting [155, 244]. Specifically, this data shows that the honeycomb topography has not significantly altered the light transmittance when compared to a cast pεK/GG hydrogel, demonstrating that the unique structure has not reduced the amount of light that can pass through the hydrogel. Both cast and printed variants had a percentage light transmittance of 81-82 %, approaching that of the human cornea at 90 % [166].

Although a variety of constructs for corneal tissue engineering being investigated via AM, very few have made it further than preliminary *in vitro* study. Furthermore, most reported techniques have utilised extrusion 3D printing, with little data published on the reactive inkjet 3D printing for corneal tissue engineering. RIJ has shown several advantages over other AM techniques, such as solution processability, low cost, and a high accuracy and resolution in the low micron range when depositing droplets [145, 244]. These features have seen RIJ investigated for multiple biomaterials applications. For example, RIJ of alginate with calcium has demonstrated manufacture of macroporous constructs based on printed beads of alginate demonstrating an average size of 48 µm [245], a scale relevant to cell culture and tissue engineering. Furthermore, RIJ has been used elsewhere to print complex cellular patterns designed for neural networks, with neuronal cells printed into the complex structure [246].

Despite reaching proof of concept with this manufacture process based on these two polymers, there were some limitations that hindered the work from progressing further. Due to the complex rheological behaviour of gellan gum, it was difficult to maintain a stable droplet during printing. In order to re-establish a stable droplet, the lines had to be purged after several passes of printing. This meant that it was difficult to achieve samples with a higher thickness, as the prints had to be stopped to purge the lines. Additionally, due to the specification of the printer, a 'purge' command wasn't able to be written into the code, so this had to be done manually, and then prints continued to run. If this project was to be taken further, it may benefit from a jetlab 4 printer with a perfusion setup, so that a purge command can be written into the print code, and a thick hydrogel sample can be developed with a high number of passes of each ink.

4.4 Conclusions

In conclusion, the technique described allows the flexibility to print hydrogel scaffolds that show potential to be tuned to meet different size and shape specifications. RIJ of pεK/GG has been shown to be capable of manufacturing thin constructs, based on a low number of passes. This finding is relevant for corneal tissue engineering, as a thin construct is suitable to replicate the structure of the

corneal epithelium and endothelium. The human corneal epithelium is around 50 µm and endothelium is approximately 5 µm in thickness [7], achievable by the resolution of the jetlab 4 printer in the micron range. The combination of these two materials to produce a hydrogel demonstrates a sustainable method for manufacturing potential tissue engineering constructs.

This chapter outlines multiple different trials for developing a repeatable method of 3D printing hydrogels based on poly-ε-lysine, including earlier trials for the extrusion and inkjet printing of pεK cross-linked with ODA. Although these trials were unsuccessful at printing hydrogel substrates, this may be due to limitations with the equipment available at the time of the data collection for this thesis, as opposed to the suitability of pεK for 3D printing.

The chapter concludes with a proof of concept for producing pεK/GG hydrogel substrates. This work has shown it is possible to print various hydrogel structures, both with and without pores, based on the reactive inkjet printing of poly-ε-lysine and gellan gum. The instantaneous reaction between the two polymer inks creates a unique honeycomb-like topography, visible under optical microscopy and SEM. Furthermore, printed hydrogels demonstrated a comparable high transparency with cast hydrogels of the same chemistry, closely mimicking that of the human cornea.

In the next chapter, I will demonstrate the interactions of different corneal cell types with the poly-ε-lysine hydrogel substrates introduced in this thesis so far. This includes the fragmented pεK hydrogels, macroporous pεK substrates and printed pεK/GG substrates. I then discuss how these results suggest hydrogels based poly-ε-lysine show potential for substrates for corneal tissue engineering applications.

Chapter 5: Corneal cell interaction with various peptide based hydrogels

5.1 Introduction

Substrates for corneal tissue engineering have been widely investigated, for both partial and full thickness replacements. In particular, hydrogels are common in this research area due to their desirable properties. Materials commonly investigated for partial thickness corneal substitutes to treat the epithelium and endothelium include collagen and silk based hydrogels.

Hydrogels based on various types of collagen have been widely investigated for corneal tissue engineering due to the abundance of collagen protein in native corneal tissue. Additionally, hydrogels based on tissue engineered recombinant collagen have shown good bio-compatibility, low immunogenicity and a biodegradability suitable for a corneal substrate [247]. These desirable properties for a corneal substrate have advanced research into *in vivo* and early clinical stages [248, 249]. In the clinical study, corneal re-epithelialisation occurred in all patients in which the collagen substrate was implanted. Based on these results, collagen presents a potential substrate for corneal tissue engineering, however, the poor mechanical properties and low transparency of collagen based materials could be improved [221, 250, 251]. Membranes based on fish scale collagen were evaluated for their suitability for an endothelial substrate *in vitro* and *in vivo*. These substrates demonstrated a high transparency and water content and supported the growth of cultivated endothelial cells *in vitro* [252]. Furthermore, when implanted into a rabbit, the fish scale collagen substrates seeded with endothelial cells showed good bio-compatibility and the mechanical strength of the substrates was appropriate for surgical handling. However, additional studies have found that fish scale collagen derived substrates may require further modifications in order to be suitable for an endothelial cell construct [253]. These may include surface polishing or coating the scaffolds with ECM proteins in order to encourage uniform endothelial cell attachment across the substrate surface.

A biomaterial that has improved upon the transparency and mechanical properties of collagen is silk fibroin. A study has shown that silk fibroin can be manufactured

into membranes, which support the culture of corneal epithelial cells *in vitro* [94]. However, corneal epithelial cell attachment was significantly less on silk fibroin constructs than on amniotic membrane, which suggests a lack of cell binding sites on silk based constructs [95]. Despite the improved optical and mechanical properties, the limitations in cell attachment limit silk fibroin progressing further as a construct for corneal epithelial tissue engineering.

Silk fibroin (SF) has also shown promise as a corneal endothelial substrate due to its high transparency and compatibility with human corneal cells [254]. Further *in vivo* studies also demonstrated that SF grafts fully integrated with corneal tissue and regained the corneal transparency after a 6 week follow up [255]. Despite the SF constructs being trialled in vivo and showing good compatibility with corneal endothelial cells, surgeons found the films difficult to use and fragile during the procedure [256].

The limitations with heavily researched biomaterials such as collagen and silk has prompted the development of alternative materials, such as peptide-based hydrogels. In particular, poly-ε-lysine hydrogels have demonstrated a less variable transparency and mechanical handleability [233, 257], have an abundance of cell binding sites for corneal cell types [235, 257], and finally come from a synthetic origin but are still capable of mimicking the natural ECM.

Several stages of *in vitro* and *in vivo* testing are required before biomaterials can reach pre-clinical trials. These involve assessing the compatibility of suggested materials with the appropriate cells and tissues. Cyto-compatibility testing includes establishing the adherence, viability and proliferation of cells using assays and immunostaining techniques. Any material that induces toxicity in cells will not be suitable for further assessment. Establishing the cyto-compatibility of materials is the first step in determining if it is suitable for clinical use further down the line after rigorous pre-clinical studies.

Multiple corneal cell types were seeded separately onto the hydrogel variants to establish cyto-compatibility. The corneal cells used were a human corneal epithelial transformed cell line (HCE-T), a human corneal endothelial cell line (HCEC-12) and

primary human corneal fibroblasts (hCF). These were chosen in order to determine the suitability of the different hydrogels for supporting the growth of cells from the three main layers of the cornea.

The hypothesis for this chapter was that human corneal epithelial and endothelial cells would form functioning monolayers across the different pεK hydrogel substrates, and stromal cells would integrate into the porous hydrogel structure, demonstrating pεK cytocompatibility. The objectives to evaluate this hypothesis include:

1. Seed corneal cells on to various poly-ε-lysine based hydrogels
2. Perform cytotoxicity assays and immunostaining to establish cell morphology and cyto-compatibility.
3. Compare pεK cyto-compatibility with GelMA hydrogels, which have been heavily investigated for tissue engineering applications.

The results in this chapter are based on the culture of corneal epithelial, endothelial and stromal cells, outlined in methods section 2.5, and the cyto-compatibility of these cells with various pεK based substrates. This chapter concludes with a discussion of how pεK substrates compare with other tissue engineering constructs outlined in literature.

5.2 Fragmented poly-ε-lysine hydrogels

5.2.1 Immunostaining of HCE-Ts and HCEC-12s

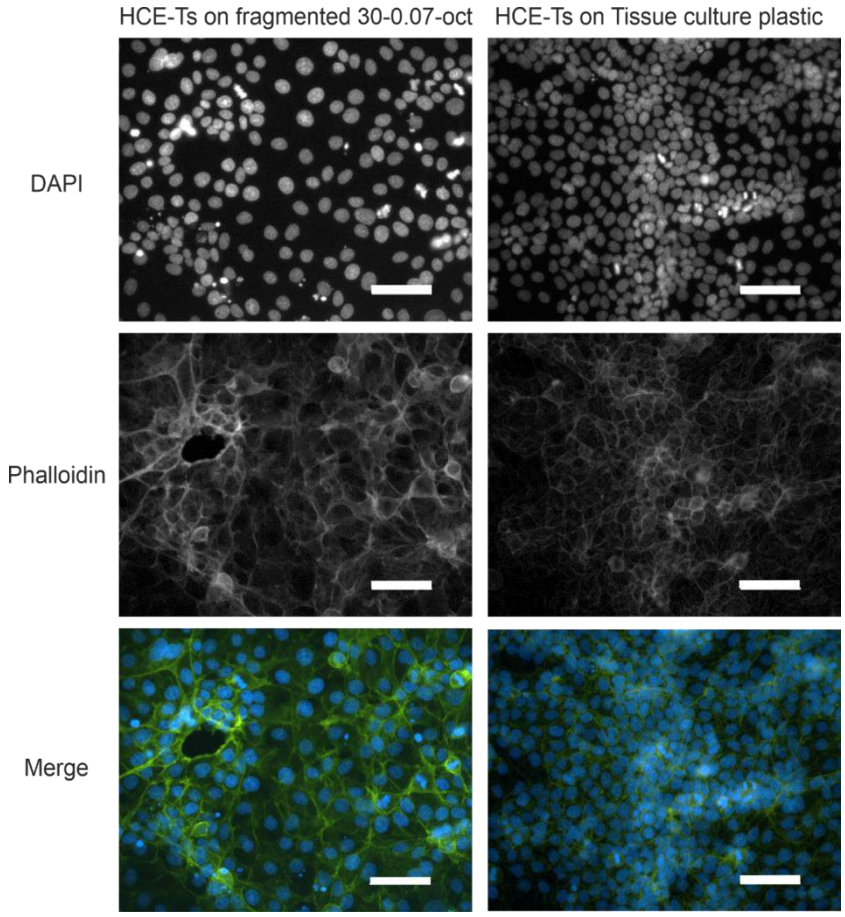

Figure 5.1: Representative images of DAPI and 488 Phalloidin staining of HCE-Ts seeded on fragmented 30-0.07-Oct hydrogel and tissue culture plastic (TCP). Scale bars equal 100 µm. Blue stain shows nuclei of cells and green stain shows cytoplasm.

HCE-T cells showed a similar morphology when cultured on fragmented 30-0.07-Oct and TCP for 3 weeks, when stained with DAPI and Phalloidin (**Figure 5.1**). On both substrates, the HCE-Ts have formed a monolayer, covering the surface of the substrate. These images demonstrate that the fragmented 30-0.07-Oct hydrogels are not cytotoxic to the HCE-T cell line, and support epithelial cell adhesion and growth on their surface.

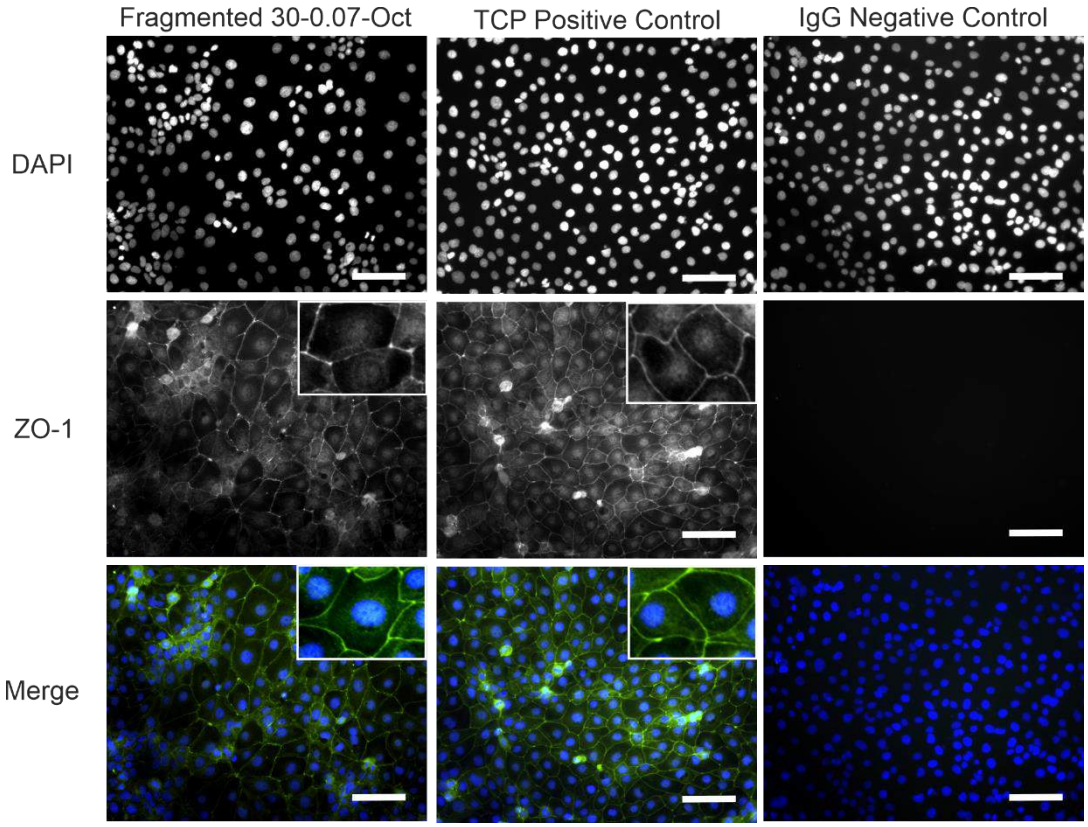

Figure 5.2: Representative images of DAPI and ZO-1 staining of HCE-Ts seeded on fragmented 30-0.07-oct hydrogel and tissue culture plastic (TCP) for 3 weeks of culture. Scale bars equal 100 µm. Blue stain shows nuclei of cells and green stain shows tight junctions in between epithelial cells.

When seeded onto 30-0.07-Oct fragmented hydrogels, HCE-Ts showed positive staining for ZO-1 (**Figure 5.2**). This demonstrates the formation of tight cell-cell junctions in the epithelial monolayer similar to that seen in the corneal epithelium. The cell monolayer seen on the hydrogel are comparable to the positive tissue cultute plastic control. The IgG negative control is included to demonstrate the absence of non-specific antibody staining, as these cells did not stain positive for ZO-1.

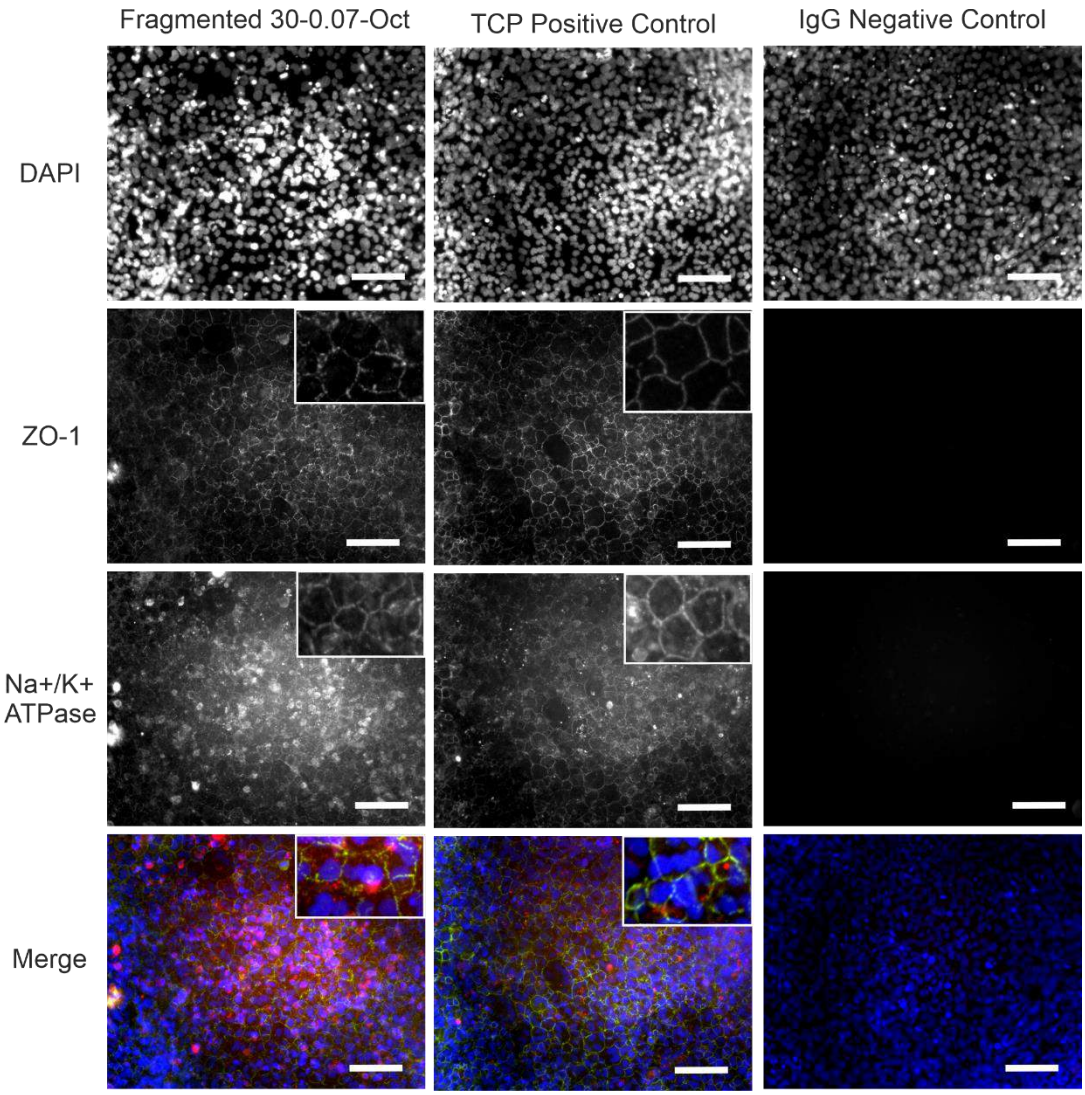

Figure 5.3: Representative images of DAPI, ZO-1 and Na^+/K^+ ATPase staining of HCEC-12s seeded on fragmented 30-0.07-Oct hydrogel and tissue culture plastic (TCP). Imaged using a Nikon Ti-E fluorescent microscope. 20X magnification. Scale bars equal 100 µm. Blue stain shows nuclei of cells, green stain shows tight junctions, red stain shows the presence of Na^+/K^+ ATPase pump.

ICC staining was performed on HCEC-12s cultured on fragmented 30-0.07-Oct hydrogels after 3 weeks in culture. Corneal endothelial cells exhibit a typical cobblestone morphology across the hydrogel surface, which stained positive for both ZO-1 and Na^+/K^+ ATPase antibodies (**Figure 5.3**). Positive ZO-1 staining gives confidence of the formation of a tight monolayer, as this identifies tight cell-cell junctions. Furthermore, the positive Na^+/K^+ ATPase staining suggests the presence of functional Na^+/K^+ ATPase pumps throughout the monolayer of the cells. The ICC staining of HCECs on the fragmented hydrogels is comparable with the cells seeded onto TCP. This result gives confidence of the cyto-compatibility of 30-0.07-Oct

fragmented hydrogels with HCEC-12s, and that they support the growth of a functioning monolayer after 3 weeks.

5.2.2 CCK-8 Assay

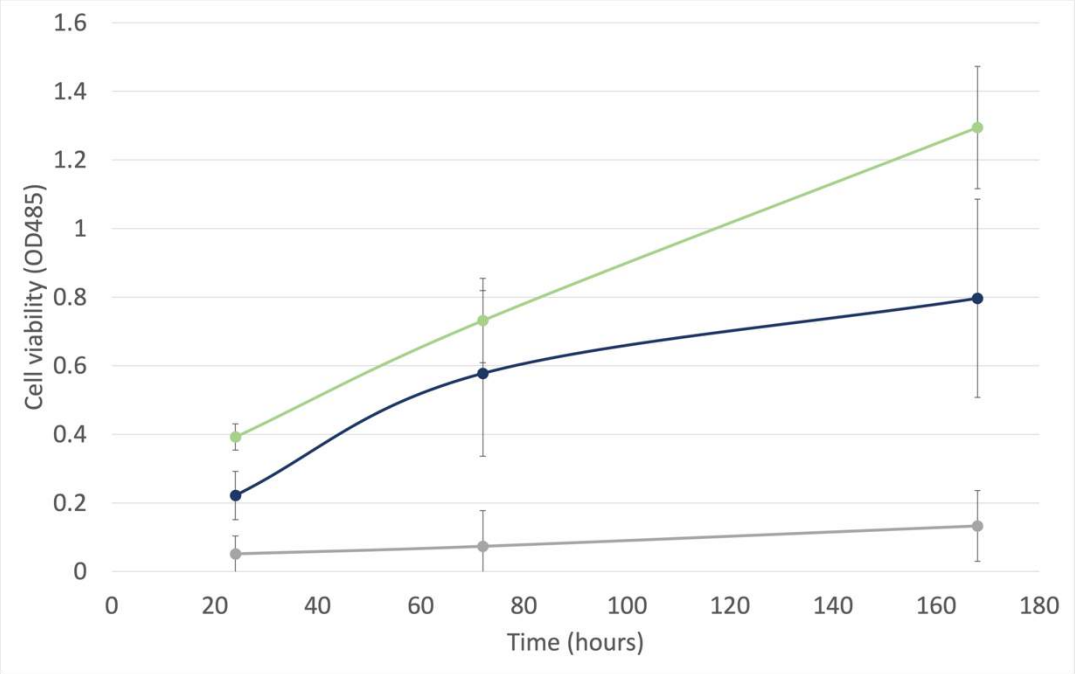

Figure 5.4: Cytotoxicity of the leachables from the 30-0.07-Oct fragmented hydrogel on the HCE-T cell line. 5 samples/run. (n=3) **Key:** Blue line = fragmented hydrogel, Green line = Tissue Culture Plastic (TCP) positive control, Grey line = hydrogel with bound phosphate groups negative control

HCE-Ts cultured in various media over 1,3 and 7 days showed variable cell viabilities (**Figure 5.4**). The media was left for 3 days prior to cell seeding in either tissue culture plastic, a regular 30-0.07-Oct fragmented hydrogel, or a hydrogel with bound phosphate groups. The CCK8 technique is an example of an indirect cytotoxicity study. The cell viability of the HCE-Ts with the TCP media showed the highest viability over all of the measured time points, which is as expected as the positive control. The negative control, showed a low cell viability close to zero for all 3 time points, indicating that this culture media was cyto-toxic to the HCE-T cell line. After 7 days, the cells seeded into the 30-0.07-Oct hydrogel media demonstrate a cell viability of 0.8, which when normalised, is a 67 % viability. This shows that nearly 70 % of the cells are still alive and metabolising over these time

points, and that the media cultured with the 30-0.07-Oct hydrogel is not cyto-toxic to HCE-Ts. This further supports the cyto-compatibility of the hydrogels when compared with immunostaining of HCE-Ts.

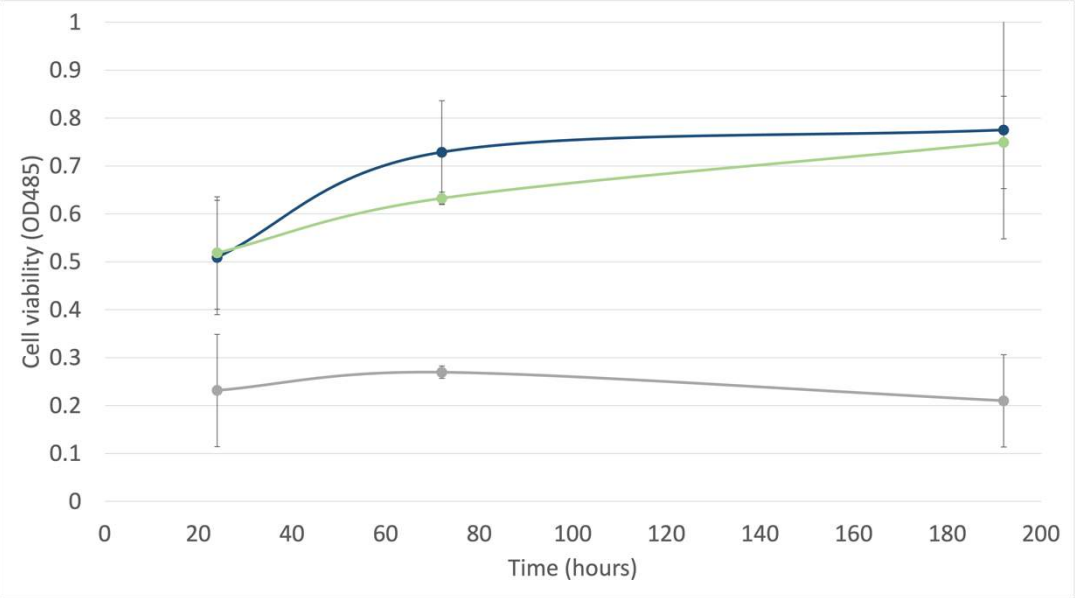

Figure 5.5: Cytotoxicity of the leachables from the 30-0.07-Oct fragmented hydrogel on the HCEC-12 cell line. 5 samples/run. (n=3) **Key:** Blue line = fragmented hydrogel, Green line = Tissue Culture Plastic (TCP) positive control, Grey line = hydrogel with bound phosphate groups negative control

HCEC-12s grown in various culture media over 1, 3 and 8 days showed variable cell viabilities (**Figure 5.5**). The same indirect CCK-8 method as the previous figure was applied in this experiment, with HCEC-12s seeded into either standard Medium 199: Hams F12 media or culture media in which the 30-0.07-Oct hydrogel had been incubated for 3 days. The figure shows the HCEC-12s in the fragmented 30-0.07-Oct hydrogel media had the highest cell viability over the three time points, and was comparable with the TCP positive control. The negative control, showed a low cell viability for all 3 time points, again indicating cyto-toxicity of the culture media as a result of leachables from the hydrogel with bound phosphate groups. The high cell viability after 8 days when cells are seeded into hydrogel soaked media further supports the immunostaining results which shows the gels support regular endothelial cell growth and function.

hCF Cell evaluations

5.2.3 GFP Stromal fibroblasts

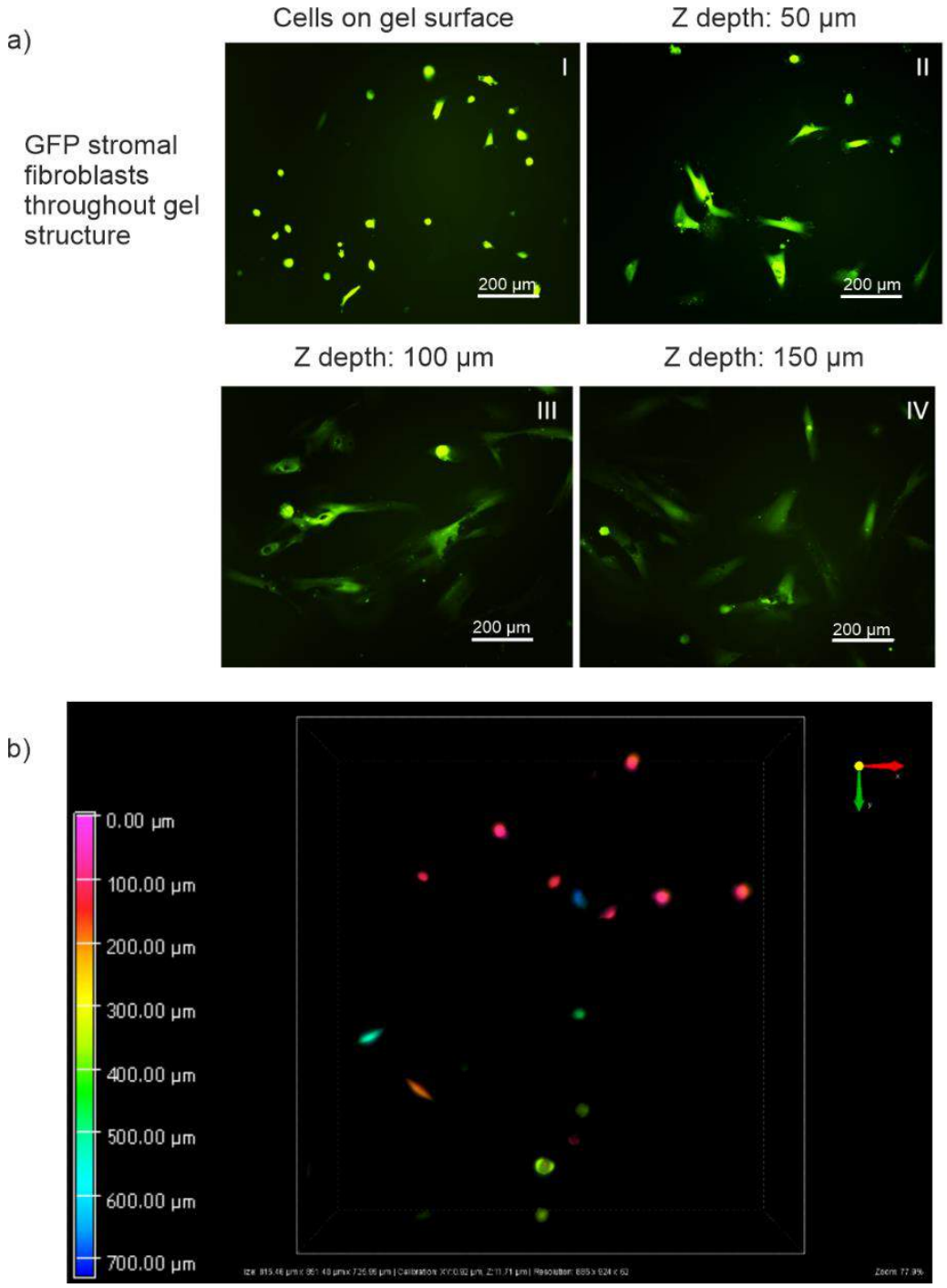

Figure 5.6 A) GFP Human stromal fibroblasts seeded on 30-0.07-Oct fragmented hydrogels. Cultured for 5 weeks, imaged here after 3 weeks. Imaged using a Nikon Ti-E fluorescent microscope. 10X magnification. Scale bars equal 200 µm. Images at different z heights shows the cells have migrated into the porous hydrogel structure. **B)** Volume plot of z stack images in xy- plane, colour scale represents z depth into the pεK porous construct.

Stromal fibroblasts seeded onto the surface of fragmented 30-0.07-Oct were seen to penetrate into the porous hydrogel structure (**Figure 5.6**). Stromal fibroblasts were imaged at different z depths within the structure of the porous pεK hydrogels, **5.6A**. The cells were initially seeded on top of the hydrogels, and over time migrated down into the porous gel network. The hCFs were left to culture within the hydrogels for 5 weeks, and these representative images were taken after 3 weeks of hCF culture. A volume plot of the cells at different z heights was produced which demonstrates the hCFs at different z depths using colour coding, which depicts the cells spread out through the structure of the hydrogel from 0 – 700 µm, **5.6B**. Both of these figures demonstrate that the 30-0.07-Oct hydrogels are not cytotoxic to human corneal stromal fibroblasts, and that they support cell growth and migration into its porous network. This finding prompted evaluations into how the presence of stromal fibroblasts throughout the hydrogel network influenced the mechanical and optical properties of the gel.

5.2.4 Compression over time

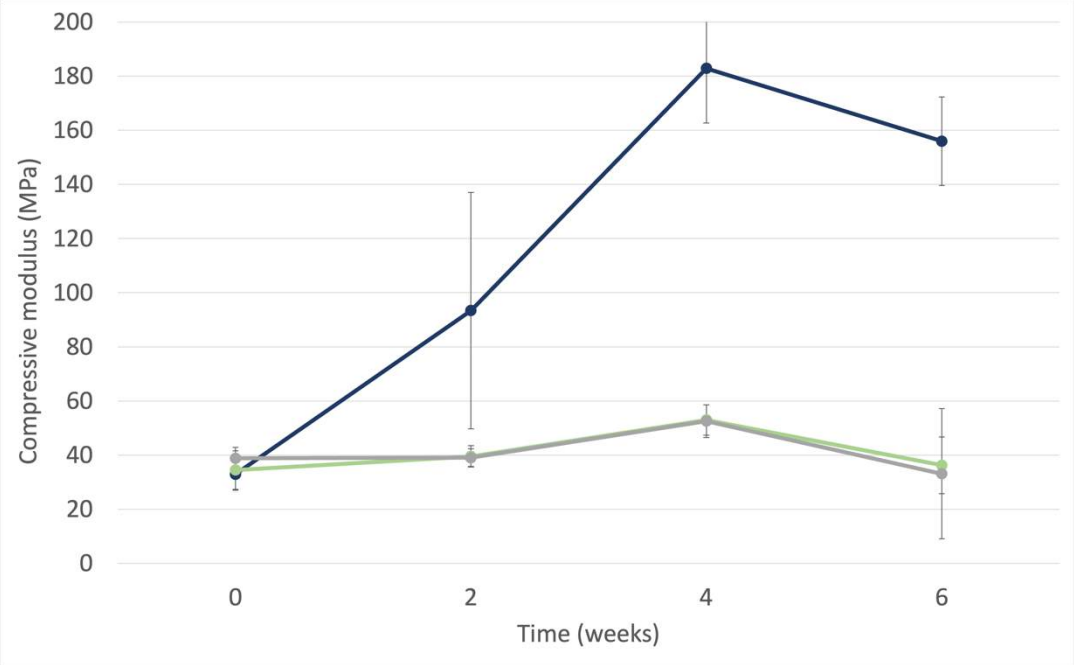

Figure 5.7: Compressive modulus of 30-0.07-Oct poly-ε-lysine hydrogels over 6 weeks with and without human corneal stromal fibroblasts (hCFs) seeded within structure. **Key:** Navy blue line = hCFs with A_2P media, Green line = hCFs with standard media, Grey line = hydrogels with no cells

Supplementing hCF culture media with A_2P was shown to increase the compressive moduli of fragmented 30-0.07-Oct hydrogels seeded with hCFs over 6 weeks (**Figure 5.7**). The cells were either fed with regular hCF media, supplemented as described in Chapter 2.5.2, or with an additional supplement of ascorbic acid (A_2P) to encourage the fibroblasts to deposit collagen into the hydrogel matrix. Finally, a control hydrogel was used with no cells seeded. All of the hydrogels used had the same 30-0.07-Oct chemistry. Hydrogels left in all 3 conditions were tested 24 hours after seeding cells and demonstrated similar compressive moduli at around 35 kPa. Over the 6 weeks, the gels in regular media and the gels with no cells exhibited very similar mechanical properties, which deviated very little from 35-50 kPa. However, the hydrogels containing hCFs with media supplemented with A_2P gradually increased in mechanical properties, which peaked with a modulus of 180 kPa after 4 weeks in culture. After 6 weeks, the hCFs cultured with A_2P showed a slight decrease in compressive moduli to around 160 kPa. These results suggest that the hCF cells are responding to the A_2P in the culture media and this is significantly increasing the hydrogel mechanical properties.

5.2.5 Transparency over time

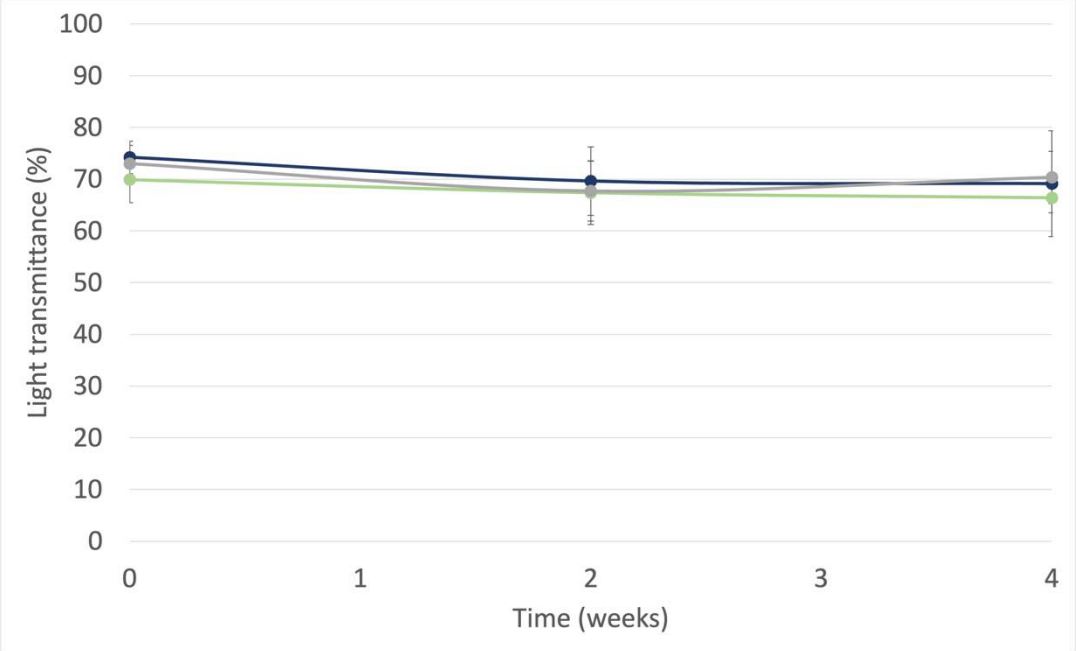

Figure 5.8: Percentage light transmittance of 30-0.07-Oct poly-ε-lysine hydrogels over 4 weeks with and without human corneal stromal fibroblasts (hCFs) seeded within structure. **Key:** Navy blue line = hCFs with A_2P media, Green line = hCFs with standard media, Grey line = hydrogels with no cells

The effect of the ingrowth of human corneal stromal fibroblasts was shown to have little effect on the transparency of fragmented 30-0.07-Oct hydrogels (**Figure 5.8**). The same controls were used as with Figure 5.7, with some gels in regular hCF media and some with no cells seeded. For all 3 groups, the hydrogels showed little differences in the percentage light transmittance results over 4 weeks of culture. When compared with the compressive modulus results, this shows that despite an increase in compressive modulus, the transparency of the hydrogel is not compromised.

5.2.6 Extracellular collagen immunostaining

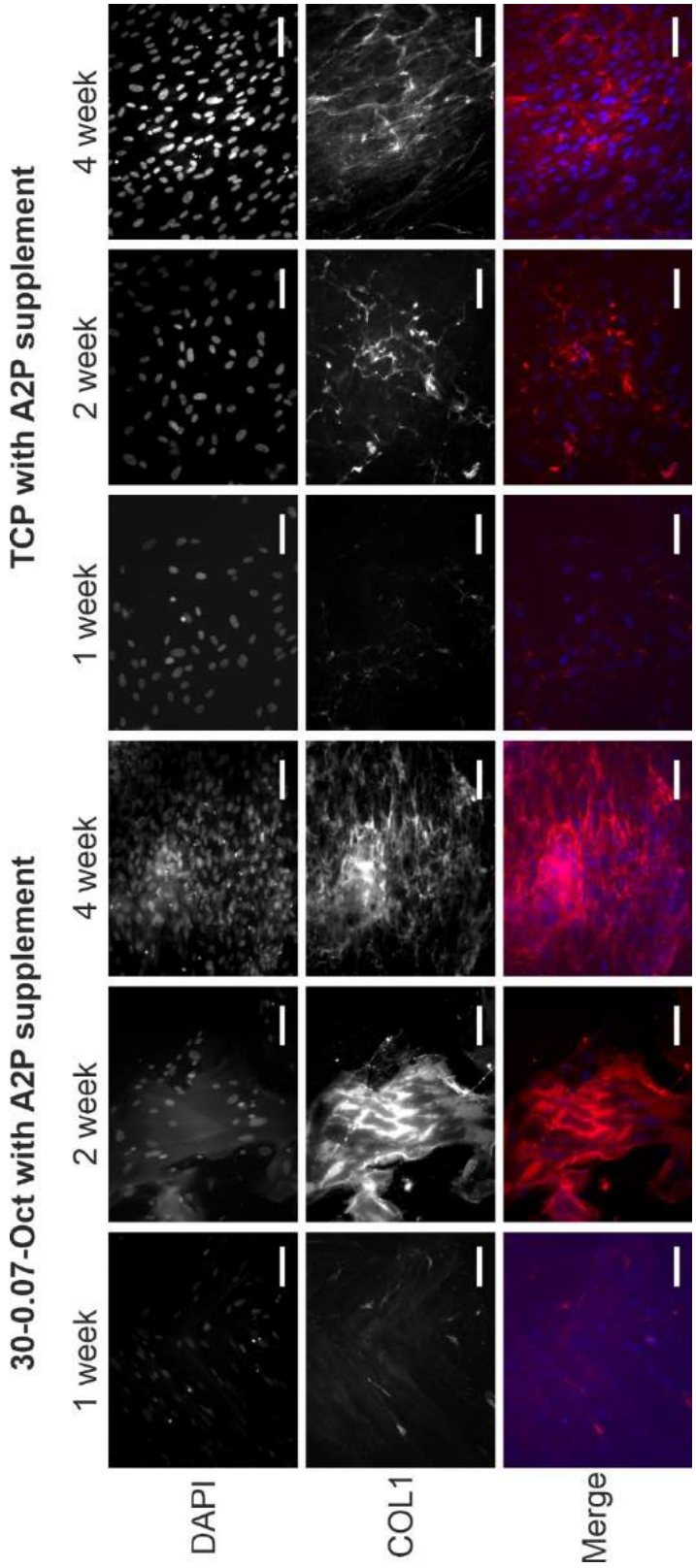

Figure 5.9: Representative images of Extracellular COL-1 staining of hCFs seeded on fragmented 30-0.07-Oct hydrogel and Tissue culture plastic (TCP). Cell culture used supplemented with A_2P. Scale bars equal 100 µm. Blue stain shows nuclei of cells and red stain shows extracellular COL-1.

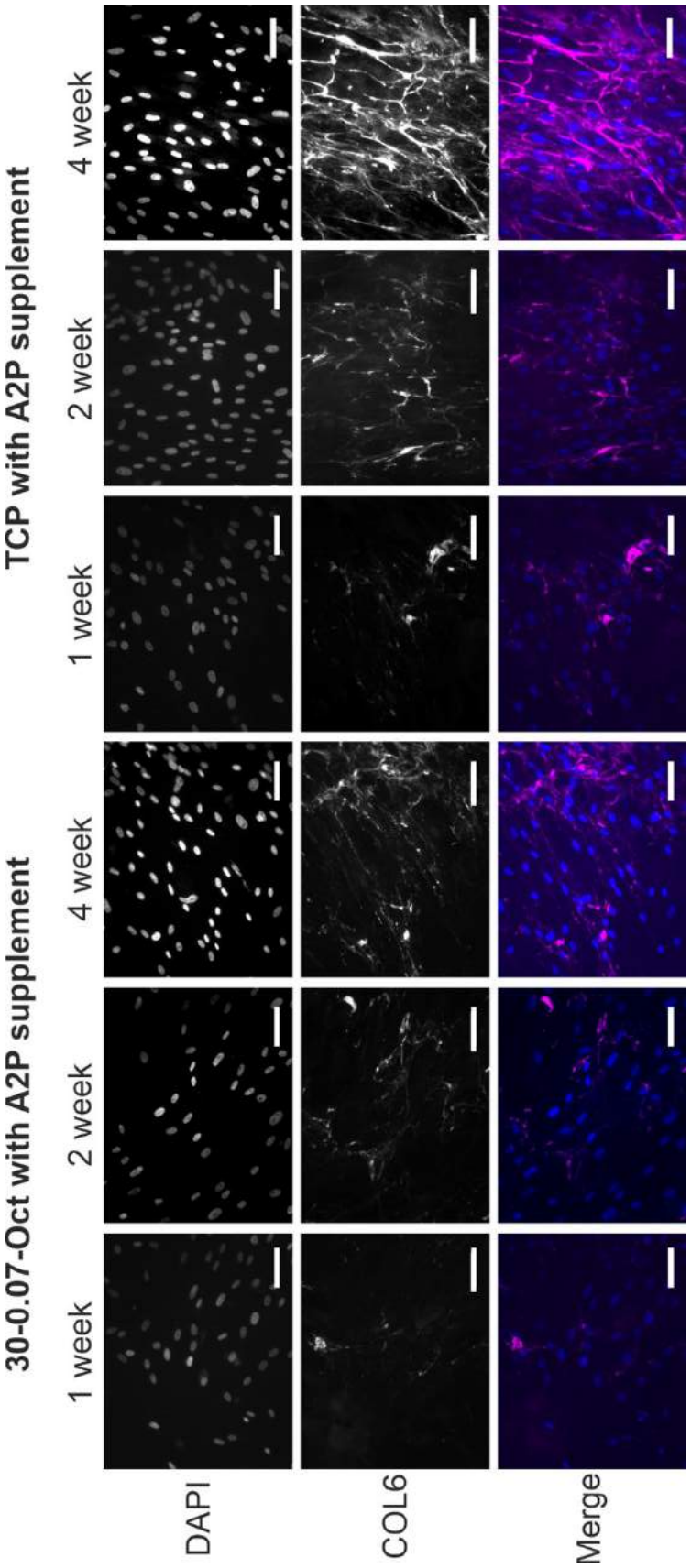

Figure 5.10: Representative images of Extracellular COL-6 staining of hCFs seeded on fragmented 30-0.07-Oct hydrogel and Tissue culture plastic (TCP). Cell culture used supplemented with A_2P. Scale bars equal 100 µm. Blue stain shows nuclei of cells and red stain shows extracellular COL-6.

hCFs cultured with A_2P supplemented media seeded onto both 30-0.07-Oct hydrogels and TCP were shown to stain positive for extracellular COL-1 and COL-6 (**Figures 5.9-10**). For extra-cellular staining, the same method was followed as that outlined in section 2.5.6, however the Triton-X100 step was skipped so that the cells were not permeabilised and no intra-cellular collagen was stained. After 1 week of culture, there is low levels of staining, showing that a small amount of collagen has been deposited by the cells, however after 2 and 4 weeks, this deposition increases. In Figure 5.9, it is clear that the COL-1 has been deposited throughout the hydrogel matrix, which appears to become more ordered over the 4 week time points. Furthermore, the hCFs show a similar adhesion on the fragmented hydrogels when compared with the positive TCP control. These results support the increase in mechanical properties of fragmented 30-0.07-Oct hydrogels seen in Figure 5.7, suggesting this is due to the increase in collagen deposition over time. A negative IgG control was also run which showed no positive staining for COL1 or COL6. This demonstrates the lack of nonspecific staining by these two antibodies.

5.3 Macroporous poly-ε-lysine hydrogels

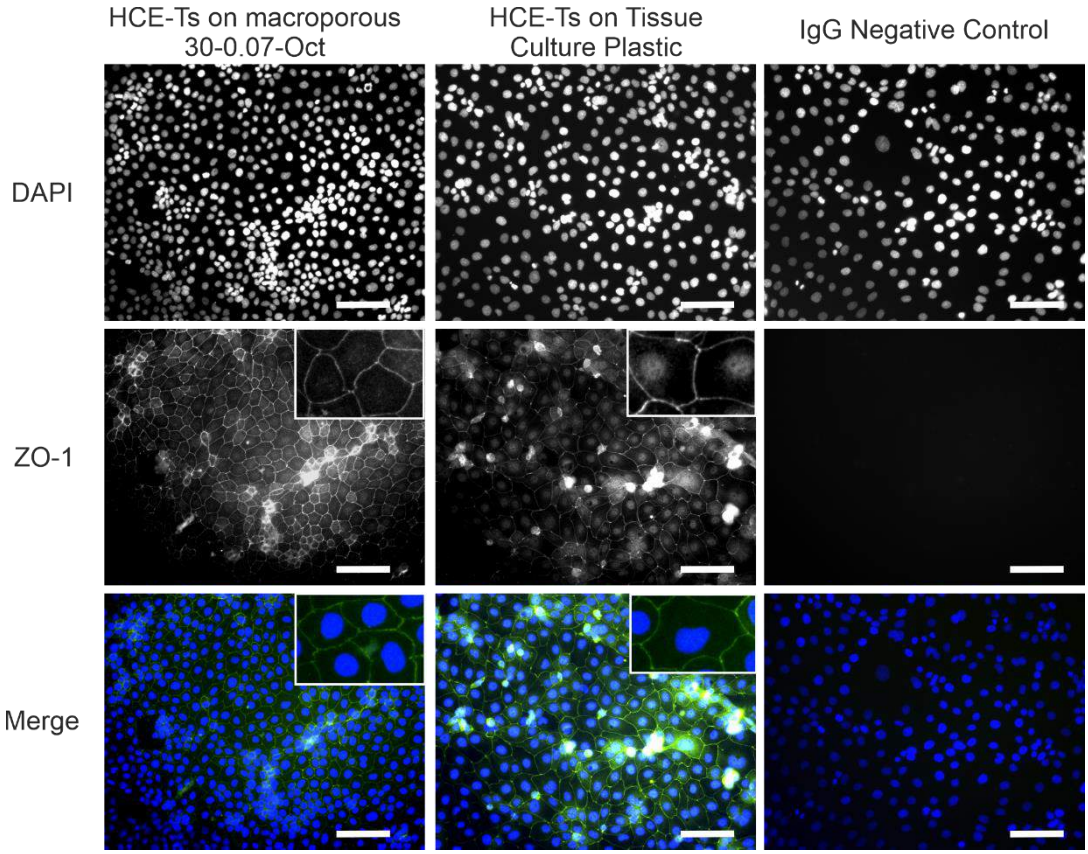

Figure 5.11: Representative images of DAPI and ZO-1 staining of HCE-Ts seeded on macroporous 30-0.07-oct hydrogel and Tissue culture plastic (TCP) for 3 weeks of culture. Imaged using a Nikon Ti-E fluorescent microscope. 20X magnification. Scale bars equal to 100 µm. Blue stain shows nuclei of cells and green stain shows tight junctions in between epithelial cells.

The percentage light transmittance of macroporous hydrogels was analysed in section 3.3.1 which showed that increasing the percentage cross-linking from 30 % to 60 % significantly reduced hydrogel transparency. Macroporous 30-0.07-Oct hydrogels were chosen for cell seeding with corneal epithelial cells due to their transparency, with the other variants discounted due to opacity. HCE-Ts were seen to form a monolayer across the surface of the hydrogels when left to culture for 3 weeks (**Figure 5.11**). This monolayer demonstrated positive staining for ZO-1 showing the formation of tight junctions, typical of the corneal epithelium. This monolayer is comparable with that formed when seeded onto tissue culture plastic.

5.4 Cast and 3D printed Poly-ε-lysine/Gellan gum

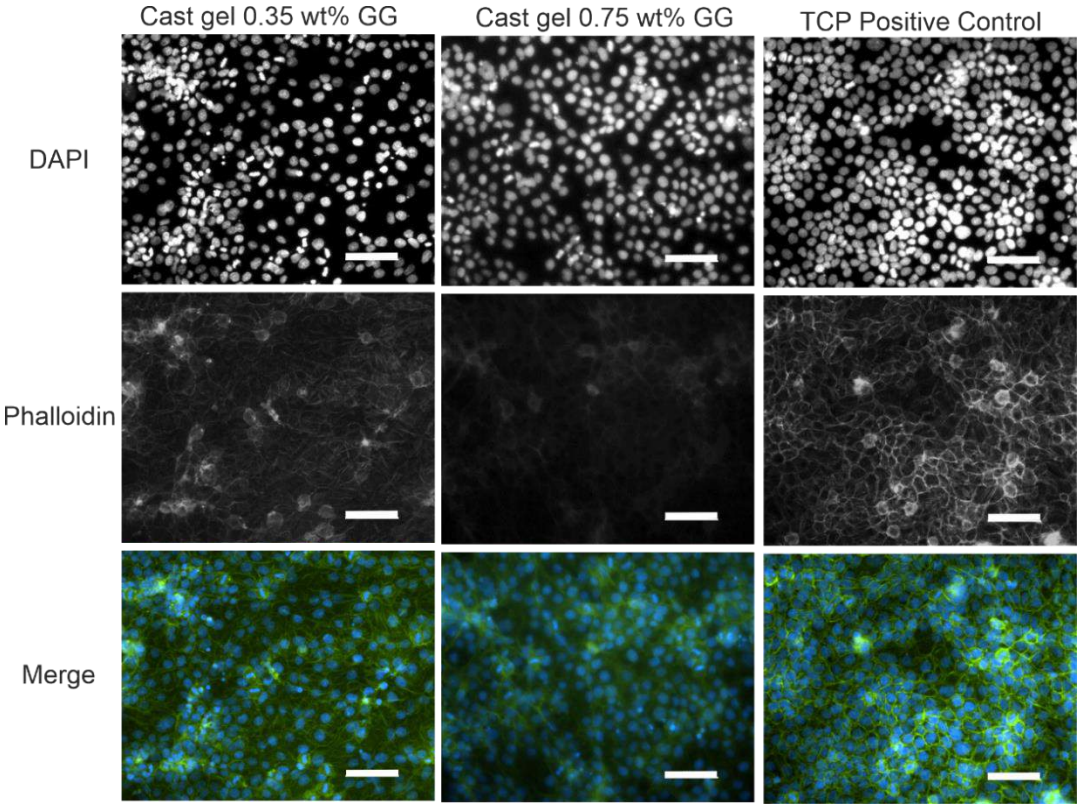

Figure 5.12: Representative images of DAPI and 488 Phalloidin staining of HCE-Ts seeded on cast hydrogels made with 20 wt % pεK and 0.35 wt % and 0.75 wt % Gellan gum. Compared with a positive control seeded on Tissue culture plastic (TCP). Scale bars equal 100 µm. Blue stain shows nuclei of cells and green stain shows cytoplasm.

Immunostaining was performed on epithelial cells seeded onto cast hydrogels made with pεK and either 0.35 wt % or 0.75 wt % gellan gum. DAPI and Phalloidin staining shows that HCE-Ts demonstrate a similar morphology on both variants and a TCP positive control (**Figure 5.12**). The morphology of the cells in all three cases is typical of epithelial cells in a monolayer, which demonstrates cyto-compatibility of these materials.

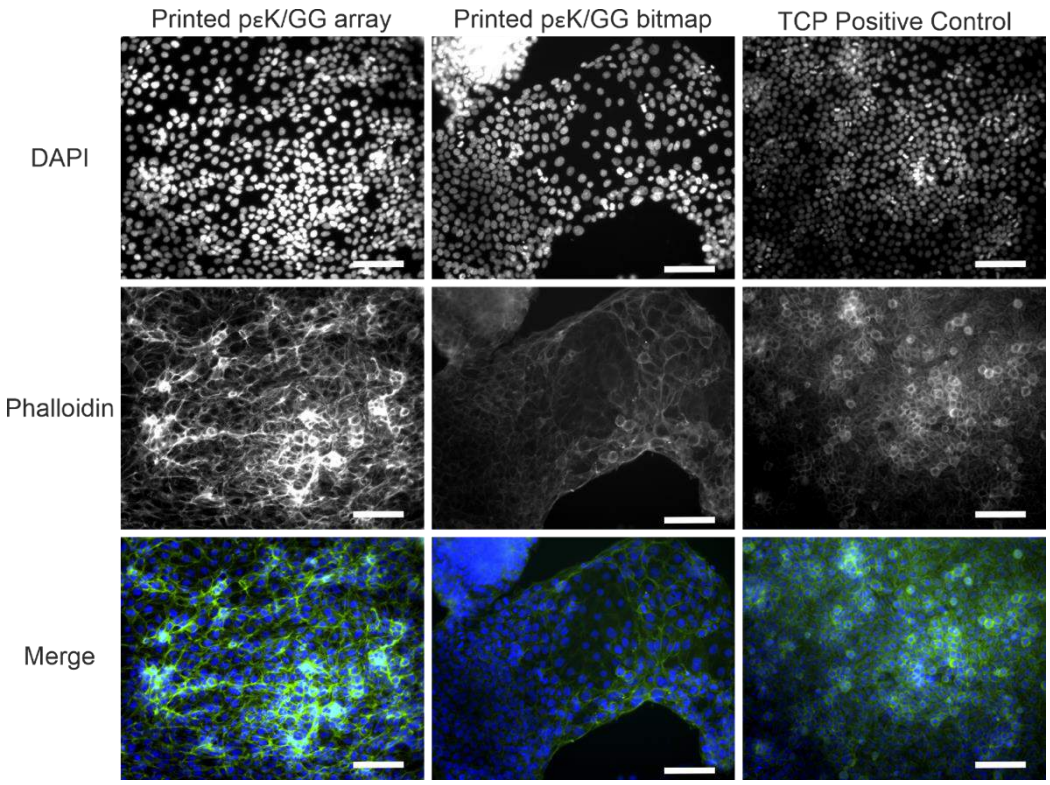

Figure 5.13: Representative images of DAPI and 488 Phalloidin staining of HCE-Ts seeded onto printed arrays and porous bitmaps of pεK/GG and TCP. Scale bars equal 100 µm. Blue stain shows nuclei of cells and green stain shows cytoplasm.

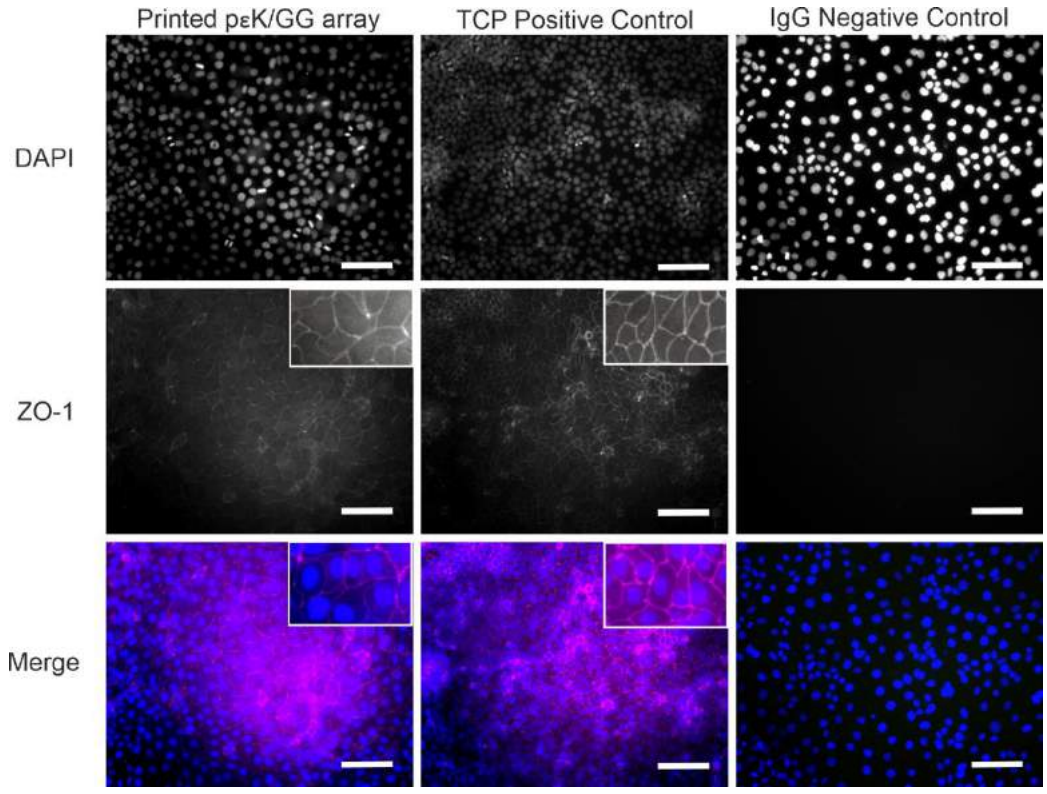

Figure 5.14: Representative images of DAPI and ZO-1 staining of HCE-Ts seeded on printed arrays of pεK/GG and TCP for 10 days of culture. Scale bars equal to 100 µm. Blue stain shows nuclei of cells and pink stain shows tight junctions in between epithelial cells.

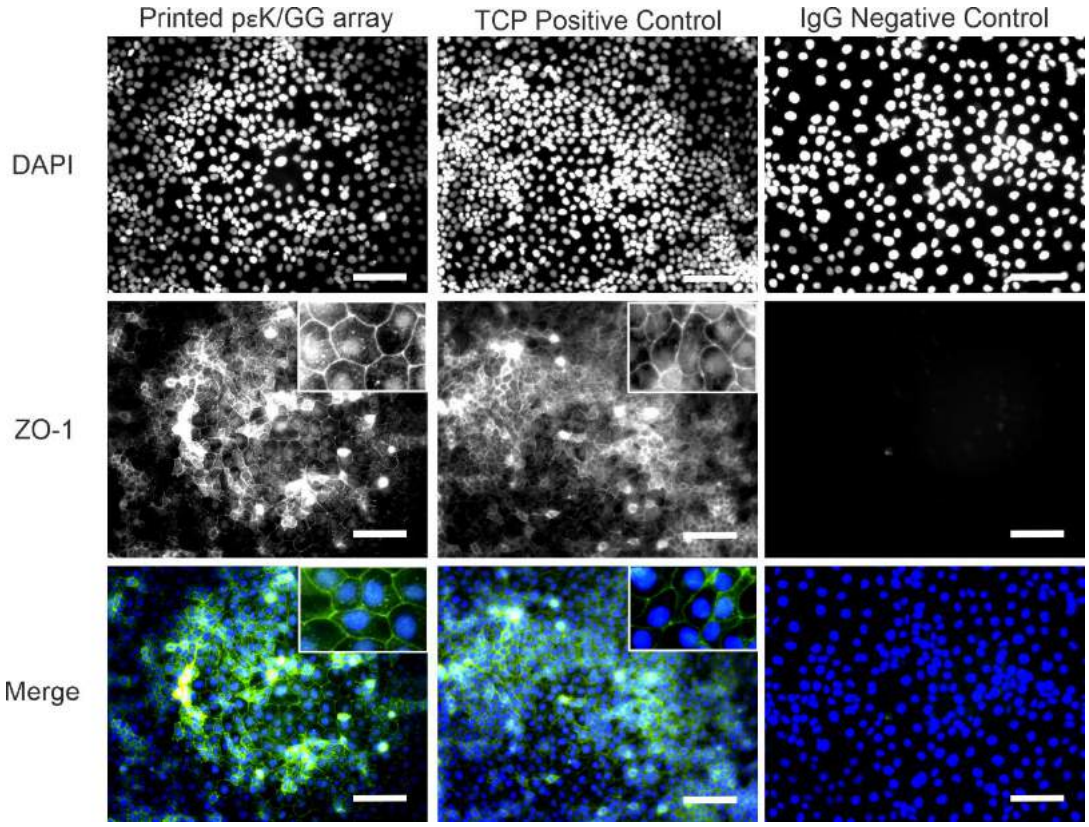

Figure 5.15: Representative images of DAPI and ZO-1 staining of HCE-Ts seeded on printed arrays of pεK/GG and Tissue culture plastic (TCP) for 3 weeks of culture Scale bars equal to 100 µm. Blue stain shows nuclei of cells and green stain shows tight junctions in between epithelial cells.

HCE-Ts seeded onto printed arrays and bitmaps of pεK/GG were shown to form a monolayer with a typical epithelial morphology (**Figure 5.13-15**). DAPI and phalloidin staining was performed on printed pεK/GG arrays and bitmaps after 10 days in culture. It is shown that there is a high proportion of HCE-Ts that have adhered to the surface of the printed pεK/GG array, and demonstrate an epithelial morphology comparable with the TCP positive control. These images show that the topography of the printed hydrogel surface has not affected cell attachment, and a layer of cells can grow uniformly across it. Printed bitmaps of pεK/GG also demonstrated attachment of HCE-T cells, however this was more patchy compared to the array. This is likely due to the detachment of the printed bitmap from the surface of the coverslip from repeated cell feeding and washing stages during immunostaining. However, the sections of hydrogel that remained were shown to support the attachment of HCE-Ts which demonstrated a similar morphology to the cells on printed pεK/GG arrays and TCP.

ZO-1 staining was also performed on HCE-Ts cells after 10 days and 3 weeks in culture, and demonstrates the formation of an epithelial monolayer across the pεK/GG array. The positive ZO-1 staining shows the presence of tight junctions in the HCE-T monolayer which is typical in the corneal epithelium. The data show that the HCE-Ts form a monolayer after 10 days and the pεK/GG array supports this monolayer for up to 3 weeks in culture.

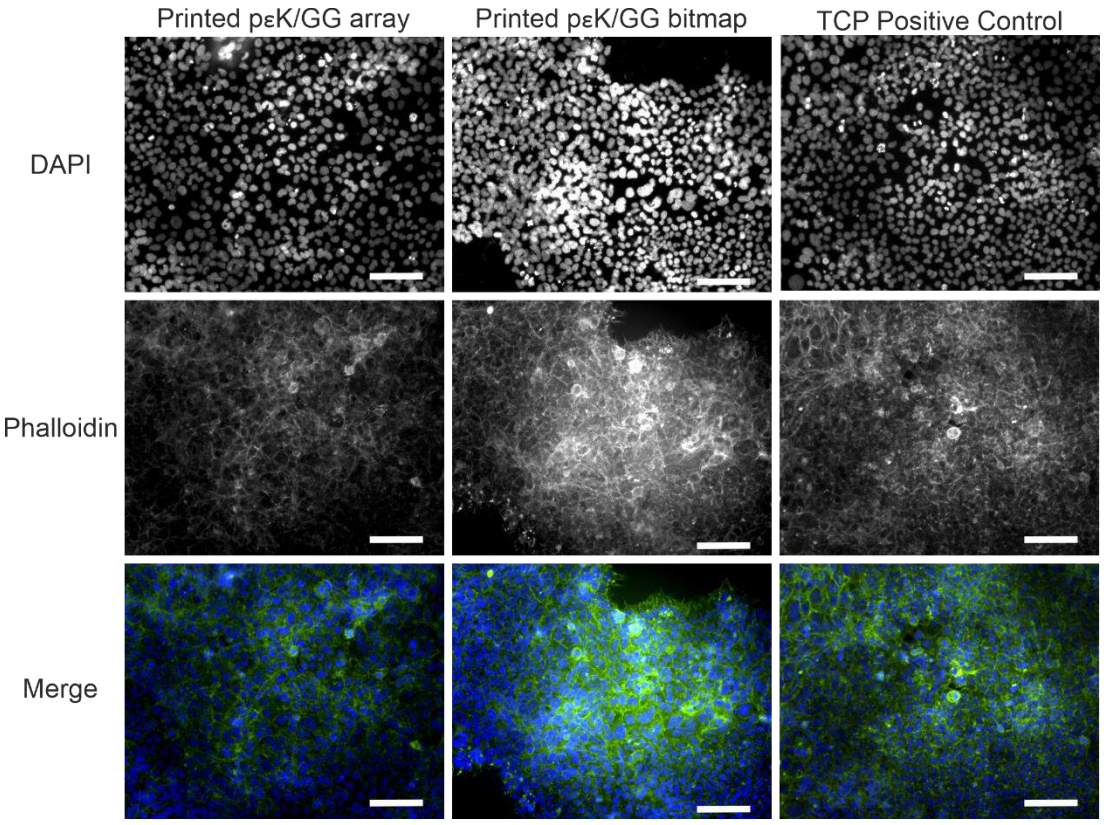

Figure 5.16: Representative images of DAPI and 488 Phalloidin staining of HCEC-12s seeded onto printed arrays and porous bitmaps of pεK/GG. Compared with a positive control seeded on Tissue culture plastic (TCP). Scale bars equal 100 µm. Blue stain shows nuclei of cells and green stain shows cytoplasm.

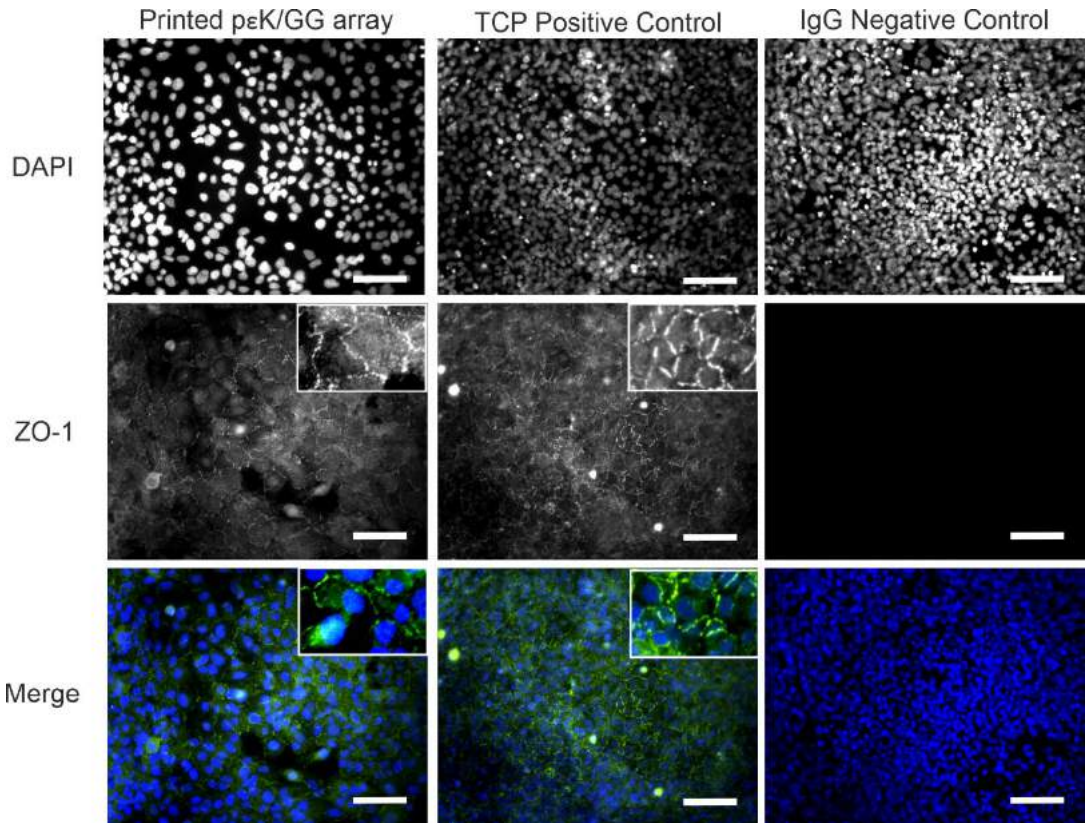

Figure 5.17: Representative images of DAPI and ZO-1 staining of HCEC-12s seeded on printed arrays of pεK/GG and Tissue culture plastic (TCP) for 3 weeks of culture. Scale bars equal to 100 µm. Blue stain shows nuclei of cells and green stain shows tight junctions in between epithelial cells.

Immunostaining of HCEC-12s on printed pεK/GG arrays and bitmaps shows a typical cobblestone morphology when cultured for 10 days and 3 weeks (**Figures 5.16-17**). DAPI and phalloidin staining highlights a comparable HCEC attachment and morphology on the pεK/GG arrays as on the TCP positive control. These data demonstrate that the honeycomb topography of these printed hydrogels does not affect the attachment of HCEC cells when compared with a flat surface. The printed pεK/GG bitmaps were seen to become detached in sections from the glass coverslip. This resulted in a patchy distribution of HCEC cells. However, the hydrogel that remained was shown to support the attachment of HCECs which demonstrated a similar morphology to the cells on printed pεK/GG arrays and TCP. ZO-1 staining was performed on HCEC-12s that were fixed on the pεK/GG array after 3 weeks of culture. Positive ZO-1 staining demonstrates the formation of a monolayer and the presence of tight junctions in between the cells. This suggests the cyto-compatibility of printed pεK/GG with the HCEC-12 cell line.

5.5 Cast and 3D printed Methacrylated poly-ε-lysine (pεKMA)

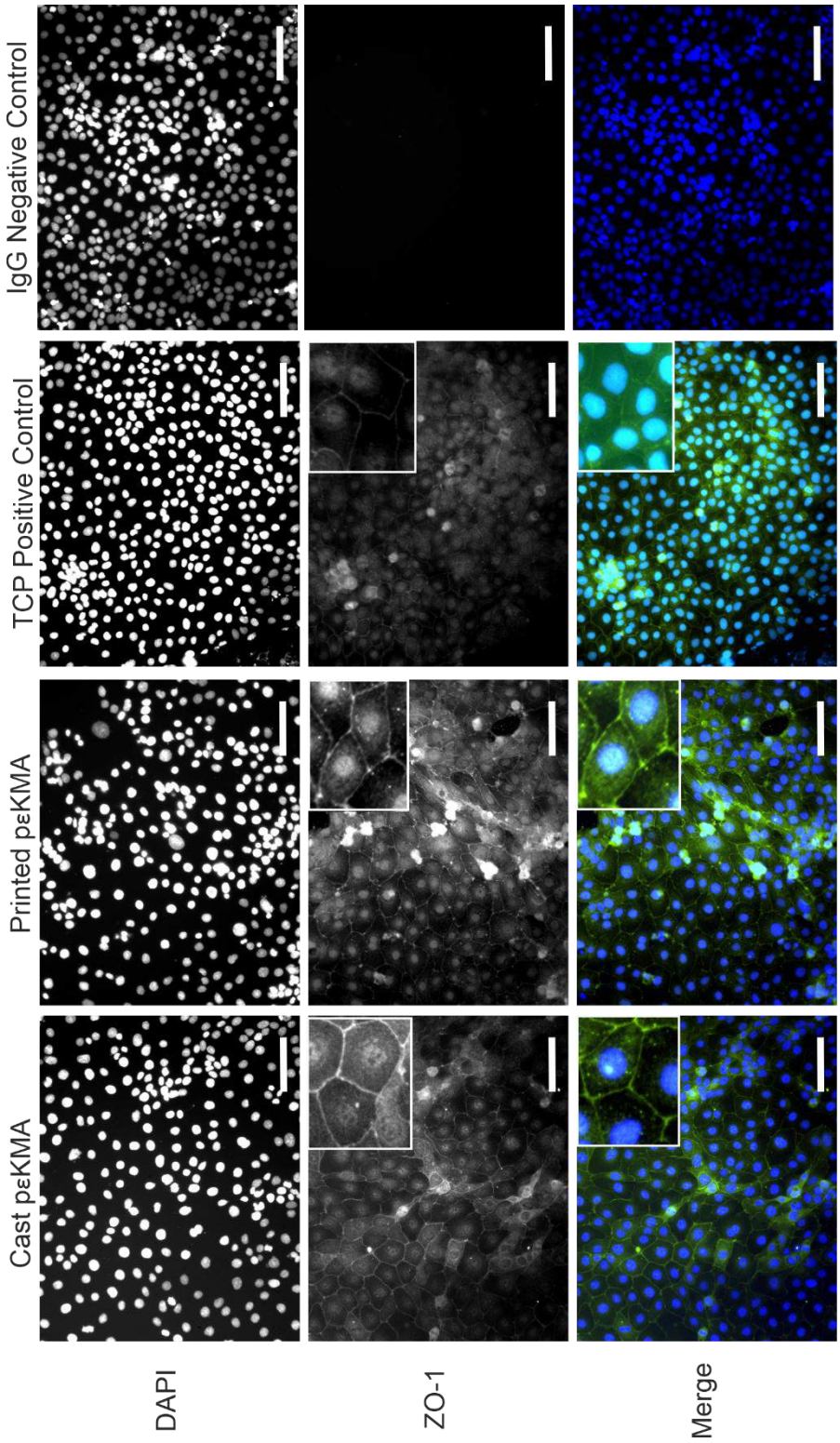

Figure 5.18: Representative images of DAPI and ZO-1 staining of HCE-Ts seeded on cast and 3D printed methacrylated pεK hydrogel and Tissue culture plastic (TCP) for 3 weeks of culture. Scale bars equal to 100 µm. Blue stain shows nuclei of cells and green stain shows tight junctions in between epithelial cells.

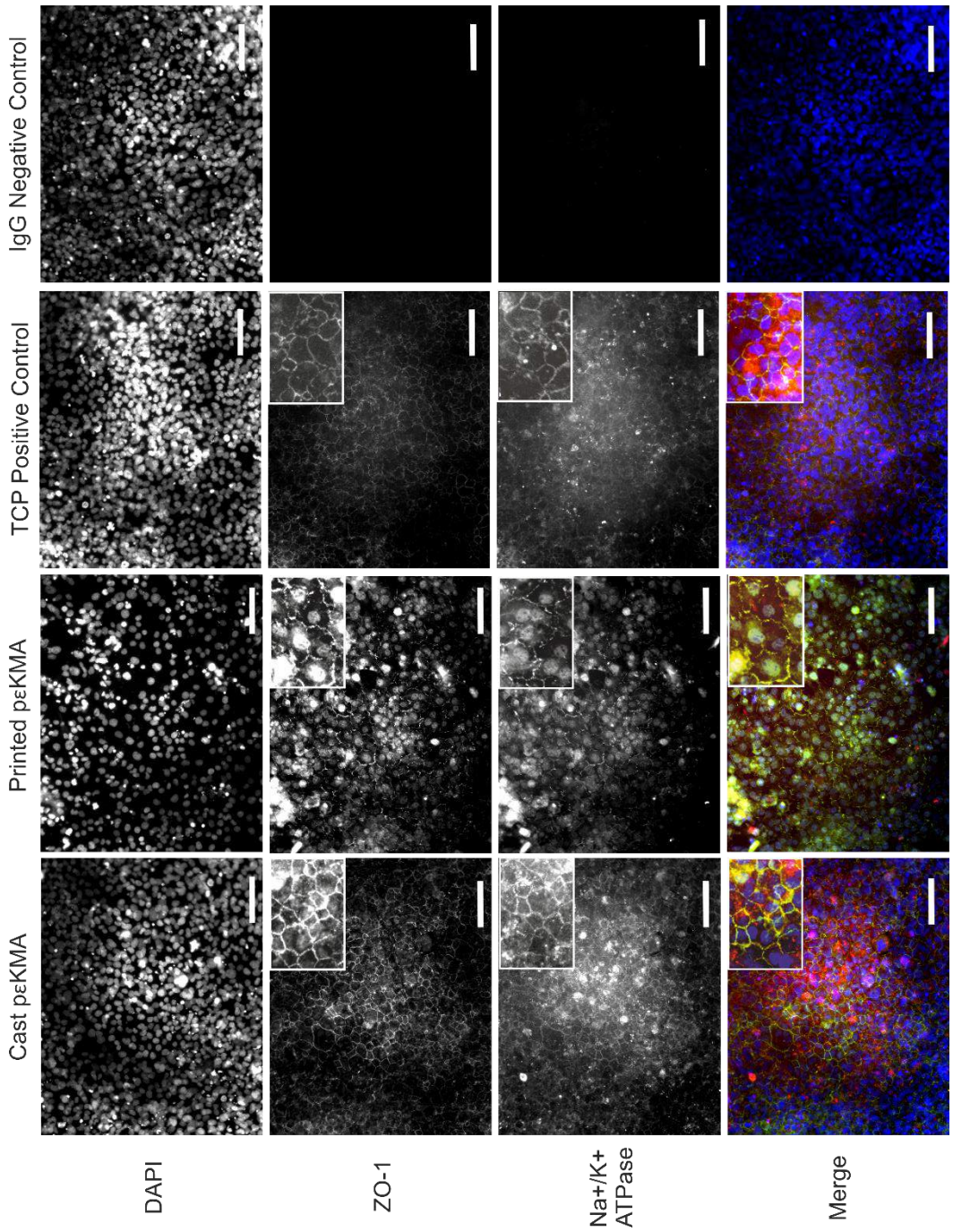

Figure 5.19: Representative images of DAPI, ZO-1 and Na^+/K^+/ATPase staining of HCEC-12s seeded on cast and 3D printed methacrylated pεK hydrogel and Tissue culture plastic (TCP) and cultured for 3 weeks. Scale bars equal 100 µm. Blue stain shows nuclei of cells, green stain shows ZO-1, red stain shows Na^+/K^+ ATPase.

HCE-Ts were cultured on pεKMA for 3 weeks and in this time formed a complete monolayer across both the cast and printed hydrogel surfaces (**Figure 5.18**). Positive ZO-1 staining demonstrates tight junction formation in between HCE-T cells on both cast and 3D printed pεKMA hydrogel, a typical characteristic of epithelial tissue. The cells look slightly less confluent on the hydrogels compared to TCP, however, the ZO-1 staining is comparable with the positive control. Immunostaining gives confidence of cyto-compatibility with a corneal epithelial cell line.

HCEC-12s seeded onto cast and 3D printed pεKMA showed positive staining for ZO-1 and Na^+/K^+/ATPase antibodies, **Figure 5.19**. The HCEC-12s were fixed on the pεKMA substrates after 3 weeks of culture. Positive ZO-1 staining demonstrates the formation of a monolayer after 3 weeks on both the cast and printed pεKMA, which is comparable with the TCP positive control. Further positive staining of Na^+/K^+/ATPase demonstrates the monolayer is functional due to the presence of Na^+/K^+/ATPase pumps in the plasma membrane of the endothelial cells. Again, the positive staining is similar across both cast and printed pεKMA and TCP. The HCEC-12s display a cobblestone morphology compared to the HCE-Ts, which is typical of human corneal endothelial cells. These findings suggest the cyto-compatibility of pεKMA with this cell line.

5.6 3D printed Methacrylated gelatin (GelMA)

7 mm diameter discs of GelMA were printed via a stereolithography technique, performed and provided by Jonathan Wojciechowski from Imperial College London.

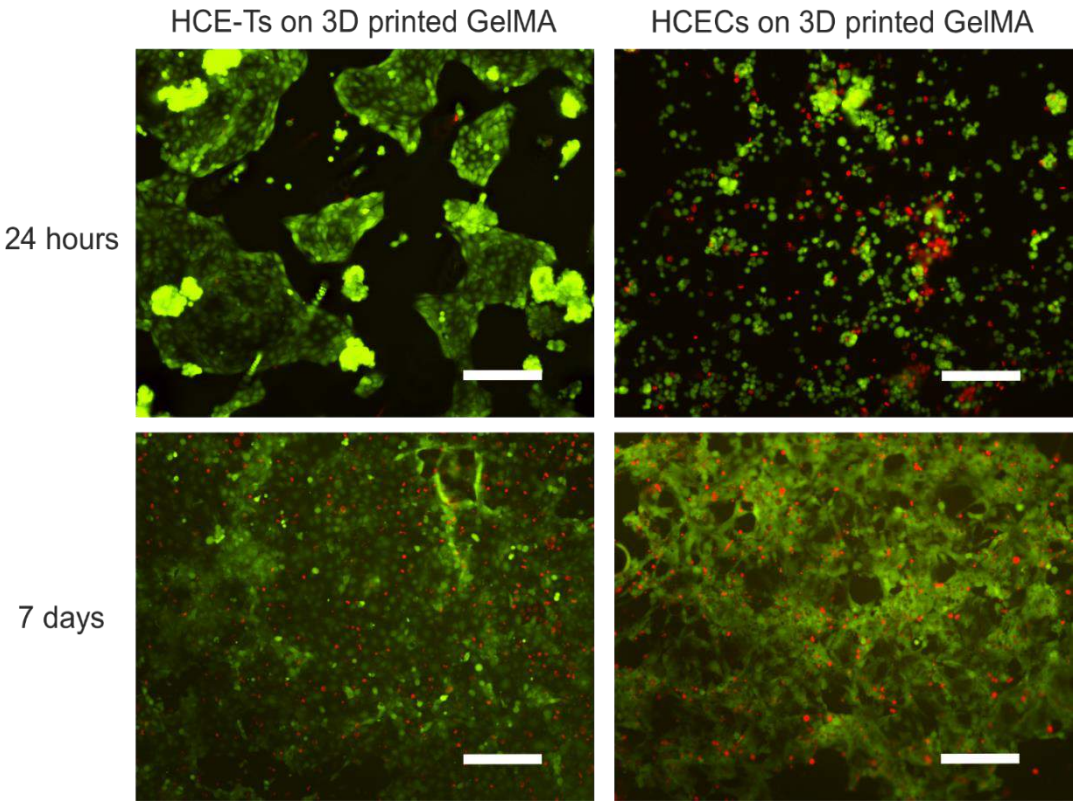

Figure 5.20: Representative images of Live/Dead staining of HCE-Ts and HCEC-12s seeded on methacrylated gelatin hydrogel for 24 hours and 7 days of culture. Scale bars equal to 100 µm. Green shows live cells and red shows dead cells.

A Live/Dead assay of HCE-Ts and HCEC-12s seeded onto GelMA shows a high cell viability after 24 hours and 7 days (**Figure 5.20**). Live/Dead staining demonstrates cell viability as it quantifies the proportion of alive vs dead cells in various environments. Fluorescent green calcein AM identifies intracellular activity and fluorescent red ethidium homodimer-1 indicates the breakdown of plasma membranes in cell death. It can be seen that 24 hours after cell seeding that both epithelial and endothelial cell types demonstrate a high cell viability, with a high proportion of green cells seen in both cases. After 7 days, the confluency of both cell types has increased and the high cell viability remains. Red cells can be identified after 7 days in both cell types however the low proportion compared to

live green cells gives confidence of the cyto-compatibility of GelMA with these two cell lines.

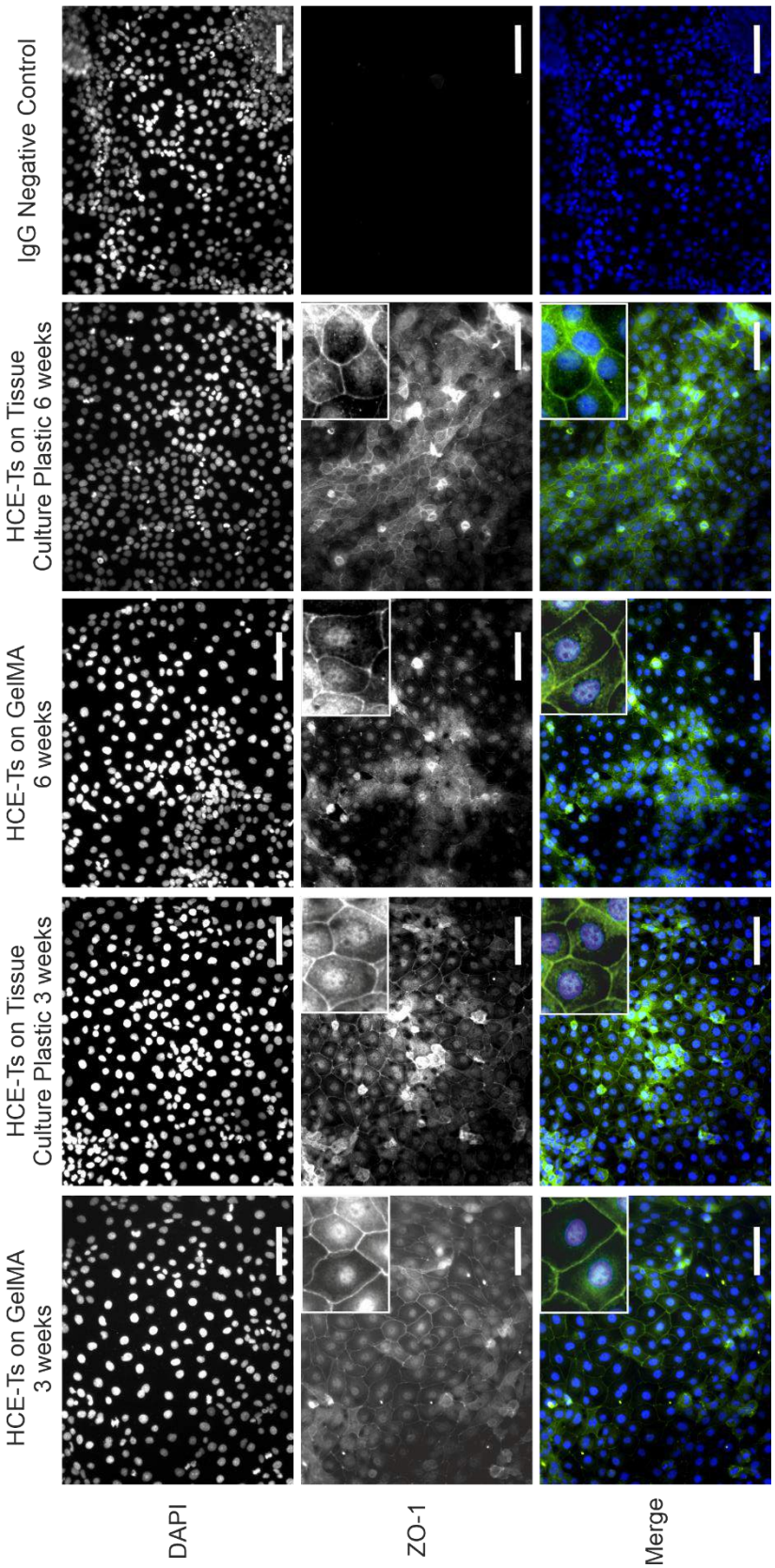

Figure 5.21: Representative images of DAPI and ZO-1 staining of HCE-Ts seeded on 3D printed GelMA hydrogel and Tissue culture plastic (TCP) for 3 and 6 weeks of culture. Scale bars equal to 100 µm. Blue stain shows nuclei of cells and green stain shows tight junctions in between epithelial cells.

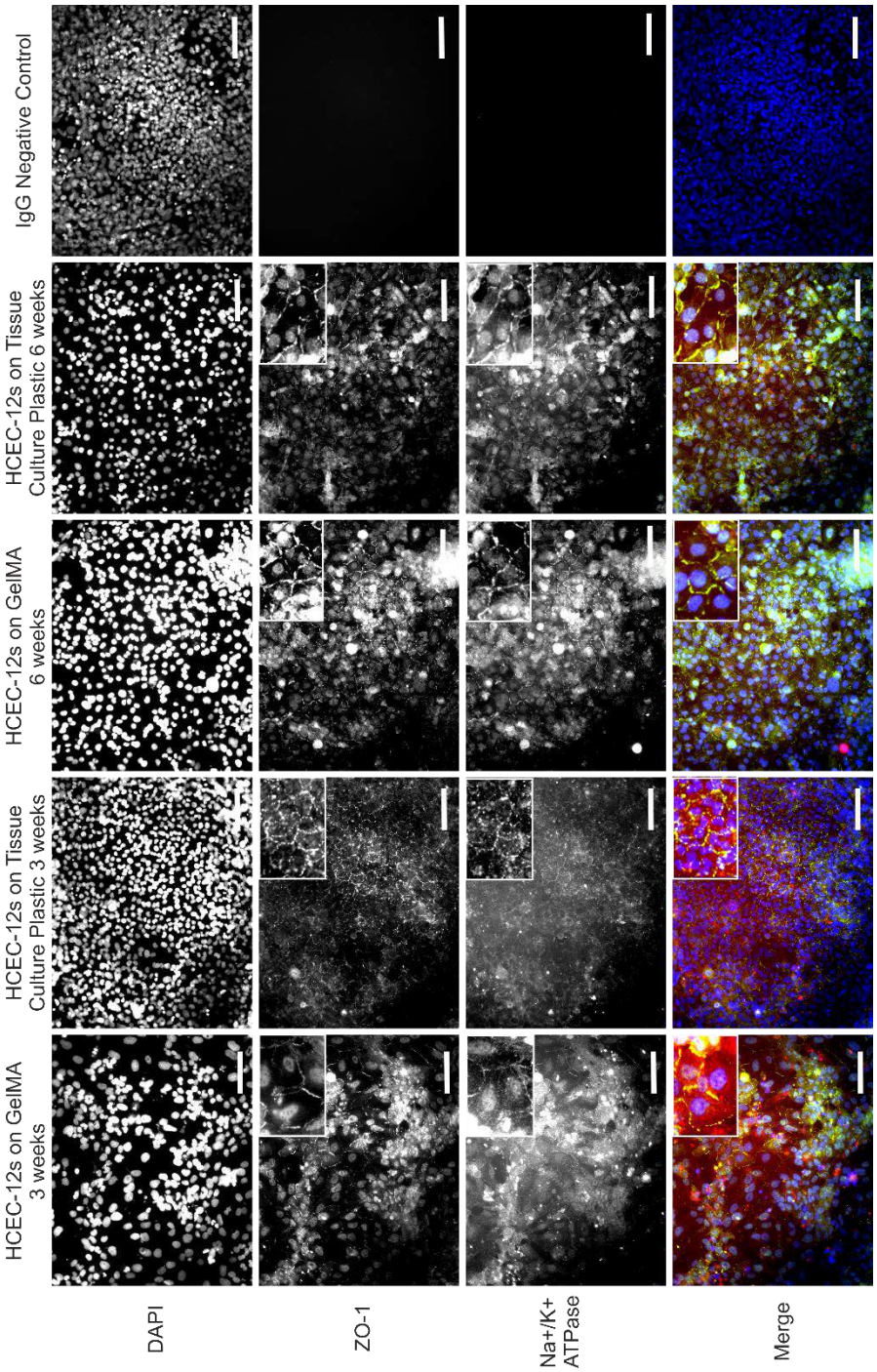

Figure 5.22: Representative images of DAPI and ZO-1 staining of HCEC-12s seeded on 3D printed GelMA hydrogel and Tissue culture plastic (TCP) for 3 and 6 weeks of culture. Scale bars equal to 100 µm. Blue stain shows nuclei of cells and green stain shows tight junctions in between epithelial cells.

HCE-T cells were seeded onto 3D printed GelMA and fixed at 3 and 6 week time points. At both time points, there was strong positive ZO-1 staining visible on cells seeded on the printed GelMA (**Figure 5.21**). The cells on the GelMA became more confluent between 3 and 6 weeks, and the ZO-1 staining remained similar. The monolayers formed across the GelMA is comparable with that formed on TCP, a positive control. This data shows that GelMA is compatible with HCE-T cells and supports cell growth for up to 6 weeks in culture. The IgG negative control was included to demonstrate the lack of nonspecific staining in this experiment.

Similar immunostaining experiments were performed with HCEC-12s seeded onto GelMA showing positive ZO-1 and Na^+/K^+/ATPase staining at 3 and 6 week time points (**Figure 5.22**). The ZO-1 staining after 3 weeks shows weak positive staining, which becomes stronger after the cells have been cultured and fixed at 6 weeks. The same trend is shown for the Na^+/K^+/ATPase staining, which is stronger after 6 weeks in culture. The positive staining of these two antibodies demonstrates that HCEC-12s form a functioning monolayer on the surface of GelMA. Furthermore, the morphology of the HCEC-12s is similar on the GelMA as it is on the TCP positive control, demonstrating a cobblestone morphology typical of endothelial cells. These results suggest the cyto-compatibility of GelMA with this human corneal endothelial cell line. An IgG negative control was included to demonstrate the lack of nonspecific staining in this experiment.

5.7 Discussion

Corneal tissue engineering is defined as the use of a combination of cells, materials and biochemical factors to replace or regenerate one or more layers of the damaged cornea. Various attempts have been made to produce either cell-based or materials-based tissue engineered scaffolds that act as either cell delivery vehicles for individual layers of the cornea, or a full thickness replacement in severe cases. Stimulating the body's natural repair mechanisms is considered the gold standard for the healing of damaged tissues and organs [258], which has prompted more recent attempts to design tissue engineered constructs so that they can degrade and be remodelled by human corneal cells. In this chapter we report the compatibility of pεK based hydrogels with cells from each main layer of the cornea,

and discuss how these materials may be suitable for different applications within corneal tissue engineering.

5.7.1 Corneal epithelial cell interactions with different hydrogel materials

HCE-Ts are a well characterised human-derived cell line, established in 1995 [259]. HCE-Ts have been used in corneal cell models for various applications, including a human cornea equivalent co-culture model with stromal cells used in drug absorption studies [260, 261]. Based on their extensive use in corneal research, and their morphological similarities to corneal epithelial cells, this cell line was chosen to represent the epithelial layer of the cornea and establish compatibility with the hydrogel materials.

Immunostaining of HCE-T cells seeded onto various substrates was performed. The substrates for cell seeding included: fragmented pεK hydrogels (pεK F), macroporous pεK hydrogels, cast and 3D printed methacrylated pεK (pεKMA), cast and 3D printed pεK/GG, and 3D printed GelMA. A variety of pεK based hydrogels were chosen to establish any differences in cell attachment and morphology between alternative cross-linking methods, and manufacture methods. HCE-T compatibility was also further compared with a GelMA substrate, which has been well characterised in literature due to its suitable biological properties and adjustable physical characteristics [262].

Immunostaining is described as the use of antibodies to target specific proteins, to understand expression and distribution at both a tissue and cellular level. The fluorescent stains used in this section included DAPI, phalloidin and a ZO-1 primary antibody alongside a secondary fluorescent conjugate. General cell morphology was established using DAPI and Phalloidin staining, targeting DNA in cell nuclei and the protein F-actin. The formation of tight junctions in an epithelial cell monolayer was characterised using ZO-1 staining.

4', 6-diamidino-2-phenylindole (DAPI) is a fluorescent dye that binds to adenine-thymine rich sections in DNA. This highlights the nuclei of cells and can be used for assessing cell morphology and quantifying cell number. Phalloidin is a peptide that

can be fluorescently labelled to highlight filamentous actin (F-actin). F-actin is essential for cell stability, and is one of the major proteins present in the cytoskeleton [263]. Targeting and fluorescently labelling F-actin allows the study of cellular morphology.

Zonal occludens- 1 (ZO-1), also known as tight junction protein-1, is a 220 kDa protein that is associated with the cytoplasmic surfaces of tight junctions in epithelial and endothelial cells (**Figure 5.23**). ZO-1 has been identified to interact with both occludins and F-actin, suggesting a role as a scaffold protein, linking and anchoring tight junctions to the actin cytoskeleton [264]. It has been demonstrated that ZO-1 is present in the human corneal epithelium when evaluated in vivo, and was most prominent in the apical and superficial epithelial layers [265].

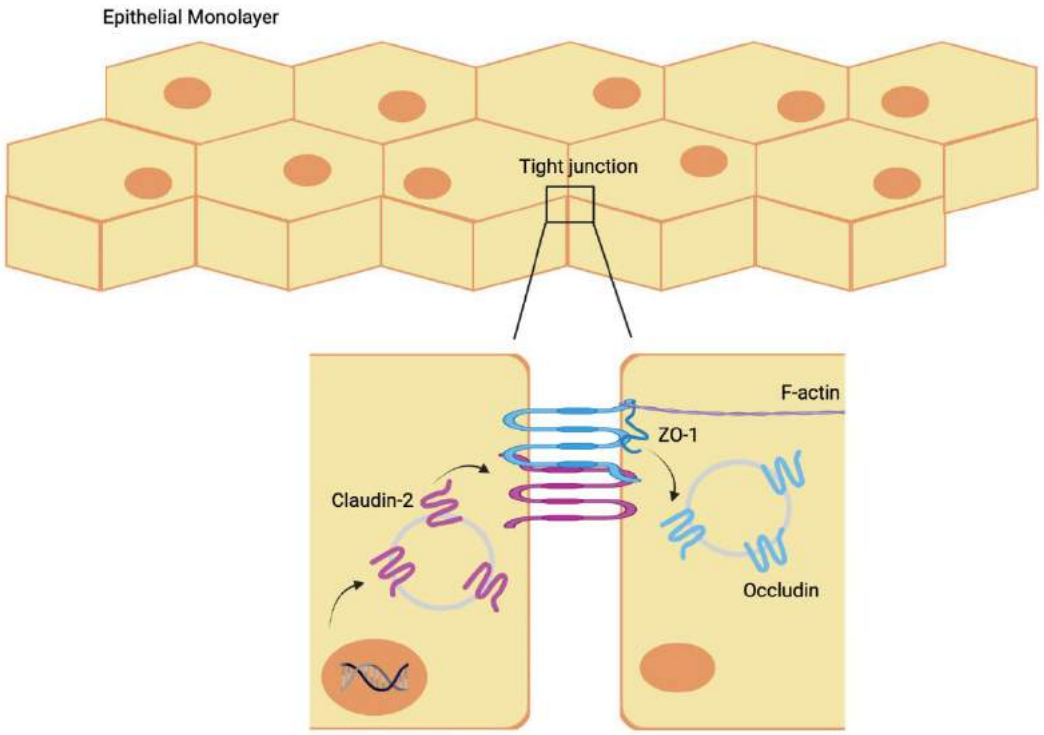

Figure 5.23: Schematic showing the presence of tight junctions in a corneal epithelial monolayer and the location of the ZO-1 protein within the tight junction. Created using BioRender.com

The immunostaining results showed that HCE-T cells had formed comparable monolayers across all substrates analysed, all boasting positive ZO-1 staining after 3

weeks in culture. Positive ZO-1 expression is typical of an epithelial monolayer, demonstrating the presence of tight junctions and the diffusion barrier mechanism [266]. The formation of a complete monolayer of epithelial cells is important for corneal function, as the epithelial layer is vital for protecting the cornea from infection and trauma. Staining for tight junction proteins in particular gives confidence of the presence of a complete monolayer and therefore epithelial barrier function. These results confirm the pεK based materials, manufactured using a variety of methods, support the formation and growth of a uniform monolayer of corneal epithelial cells. These results give confidence of the cyto-compatibility of these materials with the HCE-T corneal cell type.

The pεK based substrates were compared with GelMA, which had HCE-Ts seeded on the surface for up to 6 weeks. The HCE-Ts fixed on GelMA stained positive for ZO-1 at both 3 and 6 week time points. After 6 weeks on TCP, a positive control, the HCE-Ts began to grow on top of one another, due to limited space. Whereas the cell distribution was much more uniform across GelMA, with the HCE-Ts exhibiting a typical epithelial cell morphology. The compatibility of the GelMA substrates was similar to the pεK hydrogel variants, based on the amount of positive ZO-1 staining and the uniformity of the monolayers.

An additional indirect cyto-compatibility study was performed with the fragmented pεK hydrogels. A CCK8 assay was performed to establish if the leachables from the fragmented 30-0.07-Oct induced any toxicity in the HCE-T cell line when they were soaked in culture media for a period of 3 days prior to cell seeding. The results showed that the cells seeded into the hydrogel soaked culture media had a viability of 70 % when compared with a TCP positive control. This shows that after 7 days in culture, a high proportion of the HCE-Ts are alive and metabolising. These data further support the cyto-compatibility of fragmented pεK and their potential as a corneal epithelial substrate.

This work demonstrates that both poly-ε-lysine and gelatin based hydrogels show promise for corneal constructs including epithelial cells. Thin constructs based on either pεK or GelMA demonstrate potential for partial thickness constructs, which could be used as a substrate for tissue regeneration following damage to the

corneal epithelium. Treatments targeting the corneal epithelium are most commonly performed after limbal stem cell deficiency (LSCD). LSCD is characterised as a depletion of stem cells in the limbus, which are responsible for the re-population of the corneal epithelium. When a patient develops LSCD, their corneal epithelium is no longer able to regenerate itself and perform its primary function as a barrier to the tissues below. Two surgical procedures performed clinically to treat patients with LSCD include cultivated limbal epithelial transplantation (CLET) and cultivated oral mucosal epithelial transplantation (COMET) [267]. In both of these methods, human cells are cultured on the amniotic membrane (AM). Thus far, the AM has proved a viable substrate as an alternative to a corneal transplantation, due to its ability to support cell adhesion and migration, and its anti-inflammatory properties. However, the AM presents issues for corneal epithelial tissue engineering due to its opacity, poor mechanical handleability and the risk of disease transmission and rejection [221, 250]. The limitations with AM as a substrate has encouraged research into finding a suitable alternative scaffold for the re-epithelialisation of the cornea following damage.

Here we present that a variety of poly-ε-lysine based materials can support the growth of a monolayer of human corneal epithelial cells. These substrates show comparable cyto-compatibility with GelMA, a well characterised substrate for tissue engineering constructs. We have published that these pεK hydrogel variants demonstrate handleable mechanical properties and a high transparency [257], when compared with other polymer hydrogels for corneal tissue engineering applications, such as collagen and silk. Based on these early findings, we believe that poly-ε-lysine has properties that could be advantageous over the amniotic membrane for corneal re-epithelialisation following damage.

5.7.2 Corneal endothelial cell interactions with different hydrogel materials

HCEC-12s are an immortalised, transformed cell line, derived from human corneal endothelial cells. Based on immunostaining for typical endothelial markers, including ZO-1 and Na+/K+ ATPase, the HCEC-12 cell line demonstrated a typical cobblestone endothelial cell morphology and represented an ideal model for

differentiated HCECs in vivo [268, 269]. This cell line has been used previously in evaluating substrates for corneal endothelial cell expansion and transplantation [235, 256]. Based on the data obtained on this cell line in previous literature, it was chosen to represent the endothelial layer of the cornea and measure cyto-compatibility with various hydrogel constructs.

Similar immunostaining experiments were performed on human corneal endothelial cells, targeting ZO-1 and Na^+/K^+ ATPase. The human corneal endothelium is composed of a monolayer of hexagonal cells that is roughly 5 µm thick. Similar to the corneal epithelium, the cells within the endothelial monolayer are joined together by focal tight junctions, which contain the ZO-1 protein. One of the main functions of the endothelium is to maintain corneal transparency via a "pump-and-leak" mechanism. This mechanism moves water in and out of the cornea via osmosis, based on an ion gradient of sodium and potassium ions [19, 20]. This gradient is established by the Na^+/K^+ ATPase pump which is an enzyme located in the plasma membrane of endothelial cells (**Figure 5.24**). This pump uses energy to maintain a low concentration of Na^+ and a high concentration of K^+ inside the cornea. This balance maintains stromal deturgescence and corneal thickness and is essential for the function of a healthy cornea. Human corneal endothelial cells have been shown to express α1 and α3 isoforms of Na^+/K^+ ATPase [270]. These proteins can be targeted in immunocytochemistry to demonstrate that the endothelial cell monolayer is functioning.

The immunostaining results demonstrated that the corneal endothelial cells expressed similar attachment to all of the hydrogel substrates evaluated, on both pεK and GelMA.

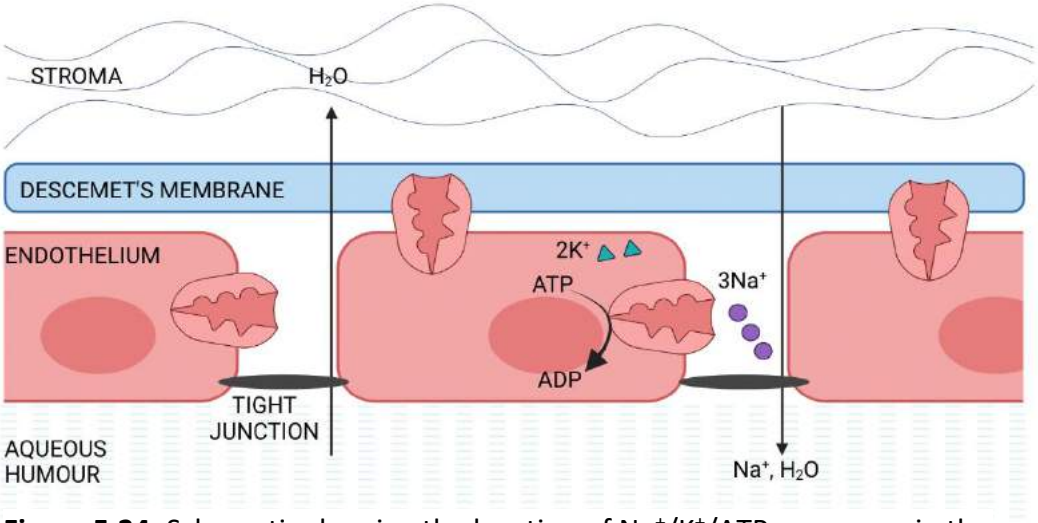

Figure 5.24: Schematic showing the location of Na^+/K^+/ATPase pumps in the plasma membrane of endothelial cells in the cornea. Created using BioRender.com

The immunostaining results confirm that pεK based hydrogels, manufactured via casting, fragmenting and 3D printing, support the culture of a functioning monolayer of corneal endothelial cells. All of the HCEC-12s on pεK substrates were fixed after 3 weeks, and immuno-stained for ZO-1 and Na^+/K^+ ATPase. Positive ZO-1 staining demonstrates the formation of tight junctions between the cells and therefore the formation of a complete monolayer. Positive Na^+/K^+ ATPase staining demonstrates that the monolayer is functioning and can actively transport Na^+ and K^+ ions across the monolayer. The images confirm the presence of both targeted proteins and therefore that pεK substrates support the formation of an endothelial monolayer after 3 weeks in culture.

HCEC-12s were also cultured on GelMA hydrogels and fixed at 3 and 6 week time points. At both time points the HCEC-12s exhibit positive ZO-1 and Na^+/K^+ ATPase staining. This staining becomes stronger after the HCEC-12s have been cultured on the GelMA for 6 weeks. These results show that the HCEC-12s have formed a functional monolayer across the GelMA after 3 weeks, however, after 6 weeks there is a stronger Na^+/K^+ ATPase stain throughout the monolayer, suggesting a higher functioning monolayer. These results give confidence of the compatibility of these hydrogels with the HCEC-12 cell line.

This section demonstrates that various constructs based on poly-ε-lysine and GelMA show promise for corneal endothelial tissue engineering substrates. These could be utilised as a substrate for the culture and expansion of primary corneal cells, or as a scaffold for transplantation alongside endothelial cells. Using a hydrogel scaffold to transplant an endothelial monolayer would mimic the current clinical procedure of a partial transplant for repairing the endothelium following damage. A common disease that affects the corneal endothelium and results in blindness is Fuchs' Endothelial Corneal Dystrophy (FECD). FECD is characterised by a loss of endothelial cells and as a result, the disruption of the ion pump function. The lack of an ion gradient causes water to travel into the cornea, resulting in stromal oedema. To regain corneal transparency, the damaged endothelium needs to be replaced with a functioning endothelium, which is currently achieved using endothelial keratoplasty surgery. This procedure is largely successful, however has several limitations. These include the limited availability of donor tissue, graft rejection and infection [256]. To overcome the limitations of the current clinical method for treating FECD, various research groups are developing material constructs on which healthy endothelial cells can be cultured and expanded for implantation. This procedure would still use endothelial cells taken from cadaveric donor tissue, however these cells could be expanded in order to increase the number of implants that can be developed from one tissue donor. This process is describe using a schematic in **Figure 5.25**. In order to be suitable for this application, the biomaterial must be capable of supporting the growth and culture of corneal endothelial cells, and must be mechanically strong for surgical manipulation.

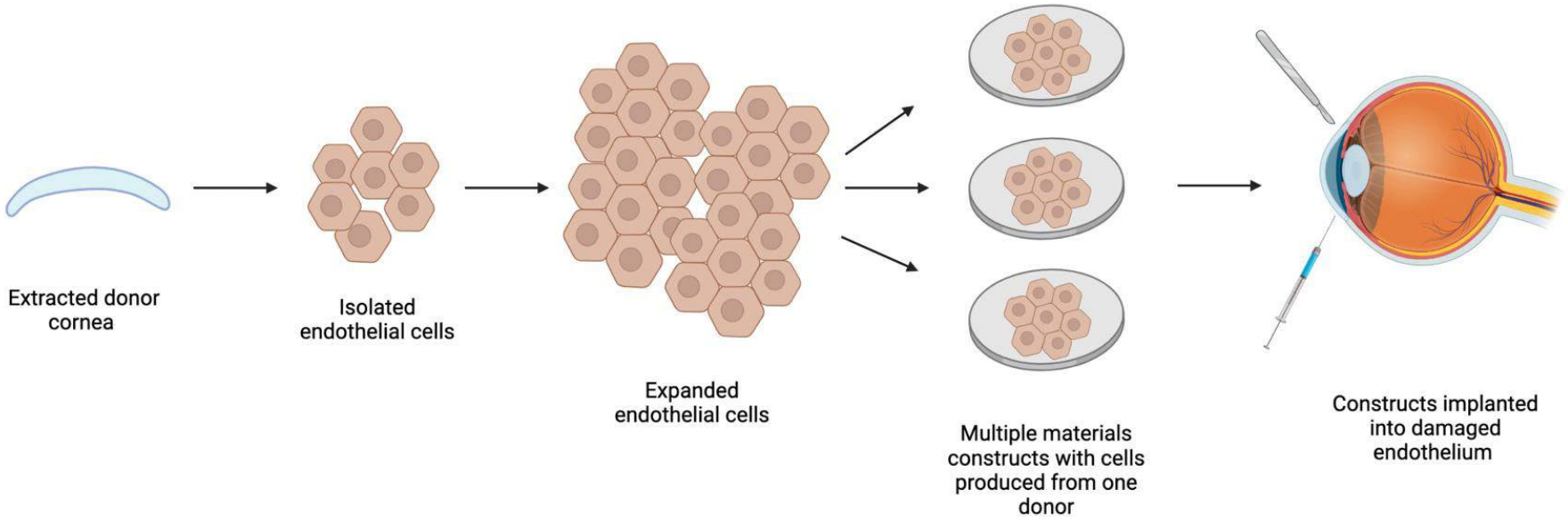

Figure 5.25: Schematic showing culture and expansion of human corneal endothelial cells on biomaterial constructs for transplantation into a damaged cornea**.** Created with BioRender.com

Our group has previously published data on the use of cast pεK substrates for the culture and expansion of an endothelial cell line (HCEC-12s) and primary porcine endothelial cells (pCECs) [235]. The pεK substrates were functionalised to encourage cell attachment and were shown to support the growth of a functioning monolayer of pCECs, confirmed by the expression of ZO-1 and Na^+/K^+ ATPase. Further *in vivo* study has shown that rabbit corneas responded well to the pεK substrates after implantation, showing no signs of inflammation or rejection. Modifying the chemistry or manufacture method of the pεK based substrates, such as that done in this thesis, may encourage endothelial cell attachment and eradicate the need for additional functionalisation.

GelMA substrates have also been trialled as substrates for cell transplantation due to their bio-compatibility and mechanical strength [271]. In particular for a corneal application, gelatin-based substrates have shown a superior transparency when compared to collagen due to the different cross-linking mechanisms used [251]. Literature has shown that primary HCEC monolayers can be cultured on GelMA *in vitro* [272], in the same study, GelMA without HCECs was implanted into the anterior chamber of rabbits to evaluate biodegradability and biocompatibility *in vivo*. The results showed that all of the rabbit corneas remained transparent and showed no signs of inflammation after 4 months. These results demonstrate promise for GelMA as a tissue engineering cell-carrier construct.

Here we demonstrate that various poly-ε-lysine and gelatin-based materials can support the culture of a functioning monolayer of human corneal endothelial cells. Based on these early findings, as well as on-going study within our research group, we believe that poly-ε-lysine substrates show promise as a suitable alternative to donor tissue for HCEC delivery to the damaged corneal endothelium.

5.7.3 Corneal stromal cell interactions with fragmented pεK hydrogel

Primary human corneal fibroblasts (hCFs) can be extracted from corneal tissue via collagenase extraction, and expanded for use in cyto-compatibility studies. Previous studies have shown that these primary cells can form stable 3D cell cultures and can deposit various corneal proteoglycans [273]. Based on their stromal phenotype, hCFs have been cultured on a variety of biomaterial substrates, including patterned

silk constructs to establish their suitability for reconstructing corneal stromal tissue [274]. Furthermore, these cells can be stimulated using ascorbic acid to deposit extracellular matrix (ECM) [275], which in turn will develop a construct that more closely mimics the human corneal stroma. For this reason, hCFs were chosen for seeding onto the fragmented poly-ε-lysine hydrogels to establish their suitability for the formation of a corneal stromal construct.

Initial investigations with hCFs included a live cell migration study over 5 weeks to establish the migration of the fibroblasts into the porous hydrogel network. The results shows stromal fibroblasts at different z depths within the structure of the porous pεK hydrogels. The cells were initially seeded on top of the porous gels, and had a more circular morphology, however over time, the cells migrated down into the network and demonstrated a fibroblastic phenotype. The ingrowth of cells into the porous hydrogel is important for the success of the scaffold for a tissue engineering application. Without space to migrate through the hydrogel, cells would become entrapped and not function at their optimal level. Cell migration and interaction facilitates important cell functions such as proliferation, cell division and ECM production [276]. The migration of the stromal fibroblasts through the porous pεK hydrogel suggests the cells are able to proliferate and function as normal, further demonstrating the cyto-compatibility of the fragmented pεK hydrogels. The success of this initial study prompted experiments into how the presence of the fibroblasts throughout the porous network would affect the mechanical and optical properties of the implant.

The compressive moduli of fragmented pεK hydrogels was measured over 6 weeks, and the percentage light transmittance measured over 4 weeks with the ingrowth of corneal stromal fibroblasts into the hydrogel network. An increase in compressive moduli of the hydrogels containing hCFs cultured with ascorbic acid suggested that the fibroblasts were depositing ECM material, therefore enhancing the hydrogel mechanical properties. However, at the same time, the percentage light transmittance of these hydrogels remained similar, suggesting that although ECM material is being laid down, the transparency is unaffected. The compressive

moduli of the pεK hydrogels after 24 hours of hCF culture was between 33-39 kPa, and for hydrogel variants with regular hCF media or no cells, the moduli remained within a range of 35-50 kPa over the 6 weeks of measurements. The pεK hydrogels containing hCFs cultured with A_2P reached a peak compressive moduli of 182 kPa. Literature places the compressive modulus of the human cornea somewhere between 0.1-57 MPa [216-218]. Originally, the pεK hydrogels are slightly outside of this range, however, the ingrowth of hCFs and ECM deposition within these hydrogels improves the mechanical properties pushing the constructs within the range of the human cornea. This suggests that pεK hydrogels containing hCFs are more handleable, and have mechanical properties that more closely resemble those of the human cornea. Throughout this thesis it has been discussed that the fragmented pεK hydrogels can be tailored, as adjusting the hydrogel chemistry, i.e. the percentage cross-linking and polymer density, has a direct effect on the hydrogels transparency and mechanical properties. The transparency of the fragmented pεK hydrogels containing hCFs remained around 70 %, which is slightly lower than that of the native human cornea at 90 % [167]. However, if the deposited ECM was shown to improve the mechanical properties of the fragmented pεK hydrogels, then the hydrogel chemistry could be further optimised to improve the original transparency, so that is more closely resembles the human cornea.

Various studies have demonstrated the use of ascorbic acid (vitamin C) to influence corneal stromal fibroblasts to deposit extracellular matrix material. Guo *et al* reported that ascorbic acid influenced human corneal stromal keratocytes to deposit ordered parallel ECM material which contained both collagen type V and VI [275]. A more recent study by Hasenzahl *et al* has shown that when human corneal fibroblasts were cultured with various different supplements, that TGF-β1 and insulin both with the addition of vitamin C significantly increased the deposition of ECM [277]. hCF cell sheets cultured with these additional supplements were shown to deposit COL-1 and COL-5 and demonstrated handleable mechanical properties when evaluated for their tensile strength. The cell sheets also demonstrated a high transparency, in particular, when supplemented with vitamin C alone, hCFs demonstrated a light transmittance of 82-94 %, which was significantly higher when

compared to an amniotic membrane control. The results of this study support the findings within this chapter, where the culture of hCFs with ascorbic acid results in an increase in mechanical properties, while maintaining a high material transparency.

Further studies have demonstrated that the culture of stromal fibroblasts with ascorbic acid has encouraged a keratocyte phenotype and the upregulation of typical keratocyte markers such as keratocan, ALDH3A1, COL1 and CD34 [278]. In particular, culture with L-Ascorbic acid 2-phosphate (A_2P), a phosphate derivate of ascorbic acid shown to have a more prolonged vitamin C activity when compared to ascorbic acid, enhanced the proliferation of rabbit keratocytes [279]. These studies suggest additional benefits to culturing corneal stromal cells with ascorbic acid, as well as the influence of collagen deposition.

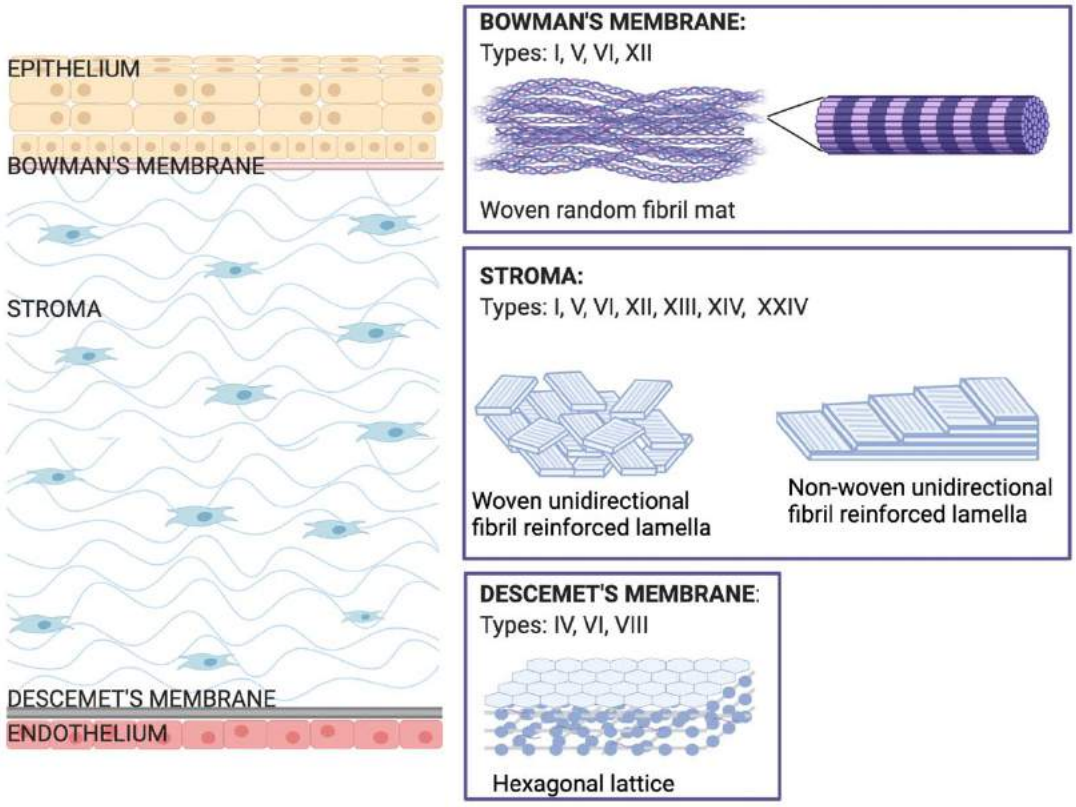

Figure 5.26: Schematic showing the types of collagen present in the human cornea. Created using BioRender.com

The deposition of collagen throughout the fragmented pεK hydrogels was characterised by the immunostaining of COL-1 and COL-6. These collagen types were chosen as they have been shown to be present in the human cornea, and have a key role in the structure of the stromal fibrils. The most abundant collagen type in the human cornea is type I, with smaller quantities of collagen V, VI, XII, XIII, XIV and XXIV also present [280] (**Figure 5.26**).

Collagen type I has been shown to be distributed evenly throughout striated corneal stromal fibrils [281], whereas type VI forms beaded filaments randomly deposited throughout the stroma [280]. Although randomly deposited, COL-6 is thought to be involved in the spacing of COL-1 fibrils, and therefore important for maintaining the ordered structure of the corneal stroma.

hCFs supplemented with ascorbic acid cultured either within fragmented pεK hydrogels or on a tissue culture plastic positive control were shown to stain positive for COL-1 and COL-6. The immunostaining protocol was modified to remove the step where the hCF cells were permeabilised, therefore all of the positive collagen staining would be extra-cellular. The images show that there seems to be a higher quantity of COL-1 deposited than COL-6 over the 4 week period. Furthermore, the deposited collagen seems to increase in its order over time, with the 4 week time points displaying aligned collagen fibres. Ascorbic acid influences cells to deposit collagen as it is involved in the hydroxylation of proline to hydroxyproline, a step which is required for collagen helix formation and the subsequent ECM secretion [282-284]. This suggests why the hCFs cultured with A_2P stained positive for these collagen types, and further confirms why the mechanical properties of the fragmented pεK hydrogels increased when compared to hCFs cultured with regular media.

The results showed that the hCFs have migrated into the porous structure of the fragmented pεK hydrogels, therefore, the ECM that they secrete will be distributed throughout the hydrogel matrix, resulting in a three dimensional material. The compatibility of a biomaterial with corneal stromal cells is very important for a full thickness replacement, as the stroma makes up 90 % of the corneas structure.

Damage to the stroma may be as a result of ocular trauma affecting all three corneal layers, which would require either a full or partial thickness donor cornea to treat the trauma. A biomaterial alternative may be more suitable than PK or DALK surgeries, due to limitations with graft rejection, tissue availability and delayed corneal epithelial wound healing. Although PK surgeries are common, they are being overtaken by partial keratoplasties as there is a higher rejection risk associated with the implantation of a higher quantity of foreign tissue.

Tissue engineered corneal equivalents (TECEs) have been discussed in literature, and are composed of the combination of a natural polymer/biological component and corneal cells, to mimic corneal tissue and encourage integration into the host [285]. A method of producing a tissue engineered corneal equivalent is the integration of corneal cells into a substrate, and allowing them to secrete their own extracellular matrix to build up a scaffold (**Figure 5.27**). Utilising a polymer substrate as a scaffold in which the corneal cells lay down ECM would likely produce a more handleable three dimensional construct compared to ECM deposited from a hCF cell sheet. Proulx *et al* reported on the self-assembly of a human cornea entirely based on the ECM deposited by stromal and dermal fibroblasts [209]. When seeded with epithelial and endothelial cells, they were shown to express typical markers and resembled the native human cornea. However, the authors reported that the constructs were between 35-50 µm, which is much thinner than the human cornea, which is approximately 500 µm. Improving on the thickness of the construct would be important for a full thickness corneal replacement.

Scaffolds used for TECEs have often been based on collagen, due to the high collagen content of the cornea, with some reaching clinical trials [217, 231]. However, no TECE or biomaterial replacement has overtaken the use of donor corneal tissue in the clinic, which is still the current gold standard. Poly-ε-lysine based hydrogels may be advantageous for TECE substrates over collagen and other commonly used materials such as the amniotic membrane as they are from a synthetic source, and have tuneable transparency, mechanical properties and degradability.

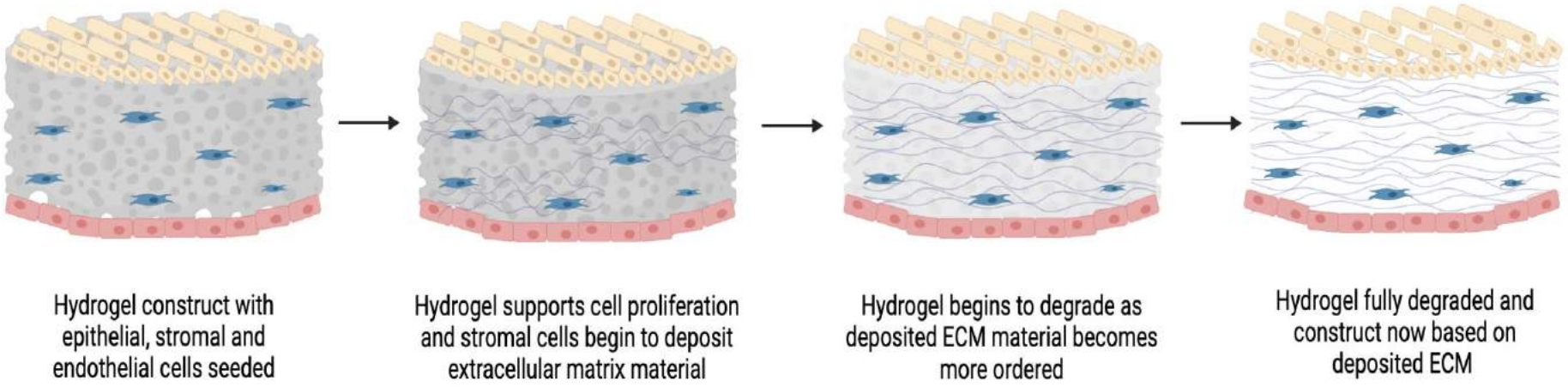

Figure 5.27: Full thickness corneal tissue engineering. Schematic showing the deposition of ECM by corneal cells within a hydrogel carrier vehicle, which degrades to leave a construct of corneal cells and deposited collagen. Created using BioRender.com.

5.8 Conclusions

To conclude, this chapter has demonstrated the cyto-compatibility of pεK based hydrogels manufactured via casting, fragmentation and additive manufacturing techniques. Furthermore, these hydrogels have shown a comparable compatibility with GelMA, a heavily research material for tissue engineering applications. The results showed that both epithelial and endothelial cells adhered to pεK and GelMA hydrogels and displayed markers that demonstrated the formation of a functioning monolayer. Further investigations with fragmented pεK hydrogels involved the seeding of primary corneal stromal fibroblasts. The results from this chapter showed that the fragmented hydrogels were shown to support the migration of hCFs into the porous matrix, where they were shown to deposit ECM material including COL1 and COL6. The deposition of ECM was shown to increase the mechanical properties of the fragmented hydrogels but did not alter the transparency. We propose that the materials discussed in this chapter have several advantages over materials currently used in the clinic, such as donor corneal tissue, amniotic membrane and collagen. Due to the versatility of manufacture of poly-ε-lysine, its transparency, handleability and cyto-compatibility with corneal cells, we suggest that these hydrogels show early promise for a various corneal regeneration applications, such as cell carrier devices or tissue engineering corneal equivalents.

Chapter 6: Discussion

The overarching hypothesis when this work was commenced was that porous poly-ε-lysine hydrogels could be manufactured, and could demonstrate properties suitable for substrates for corneal tissue engineering.

- It was hypothesised that porous poly-ε-lysine hydrogels could be manufactured via fragmentation techniques and reactive inkjet printing
- The hydrogels produced would show comparable properties to other hydrogels for corneal tissue engineering applications
- The final hypothesis was that the various pεK substates would support the growth and adhesion of functioning corneal cells

6.1 Management of diseased and damaged corneal tissue

The type of management for corneal opacities depends on the cause, extent and location of the damage. For instance, minor damage to the corneal epithelium as a result of trauma may be successfully treated with eye drops, however extensive damage to the corneal stroma, or multiple layers of the cornea may require surgical intervention.

There are various different surgical procedures performed within the clinic to regain transparency of the cornea following opacity. These procedures are all based on the transplantation of donor tissue, in various keratoplasty surgeries, or using an amniotic membrane substrate to transplant limbal epithelial cells in LSCD patients.

Keratoplasty is the most common transplantation procedure performed worldwide, which is largely due to the ease of transportation and storage of corneal tissue. However, a major limitation with all keratoplasty procedures is the limited availability of donor tissue for transplantation. Partial keratoplasties such as DSEK, DMEK and DALK surgeries have advantages over full PK, in that a smaller amount of tissue is transplanted, and therefore a large surgical wound is avoided, and the likelihood of rejection is reduced [63]. Furthermore, due to the size and thickness of the tissue used in PK surgeries, graft failure and rejection is common [58], which may result in the need for a second surgery later on in the patient's life.

Patients diagnosed with LSCD may require a cultivated limbal epithelial transplantation (CLET) to restore the population of limbal stem cells in the damaged cornea. This surgery uses a human amniotic membrane as a substrate for delivering LSCs to the patient's cornea. This is a highly successful procedure, with success rates of approximately 76 % [66], however there are still issues surrounding the use of donor tissue as the cell carrier. Furthermore, studies have shown that HAM has a variable transparency and poor mechanical properties [76-78], which further limits the success of the implant.

The limitations with current surgical procedures has encouraged researchers to investigate a suitable material alternative for regaining the transparency of the cornea following damage and injury.

6.2 Poly-ε-lysine hydrogels produced in this thesis

The research reported in this thesis produced various novel porous hydrogel variants based on poly-ε-lysine, using different manufacturing methods, and characterised the final constructs.

Porous poly-ε-lysine hydrogels were made using a unique novel fragmentation method which utilised a stirrer device to introduce gaps into the final hydrogel structure. These hydrogels were based on the cross-linking of poly-ε-lysine with a bi-carboxylic acid, using an NHS/EDCI mediated reaction. The four components were added together in the stirrer device, which was left to run for around 20 minutes when the hydrogel began to set, and the fragmented hydrogel was removed and cast between two glass plates. Pressing the hydrogel to cast in this way allowed for the control of the thickness of the hydrogel sheet, which was tailored to match the thickness of the human cornea. Multiple hydrogel chemistries were produced using this method, by varying the percentage cross-linking and the polymer density to establish a construct that most closely met the requirements discussed above. Based on the results, a hydrogel was manufactured based on 30 % cross-linking with octanedioic acid using a 0.07 g/ml pεK density. These 30-0.07-Oct hydrogels had a high transparency, water content, interconnected porosity, handleable mechanical properties and supported the culture of corneal epithelial,

stromal and endothelial cells. This was the first time this technique was used to produce hydrogels based on poly-ε-lysine for a corneal tissue engineering application.

Macroporous poly-ε-lysine hydrogels were developed by introducing a porogen into the typical casting method. These hydrogels were produced using the same cross-linking chemistry, with a bi-carboxylic acid and activated by NHS/EDCI. Again, the hydrogel chemistry was altered to establish a particular composition that most closely met the criteria. In this case, the bi-carboxylic acid and the percentage cross-linking was varied to determine the effect on the hydrogel properties. The hydrogel variants showed a variable transparency, high water content, high swelling ratio and handleable mechanical properties.

Increasing the percentage cross-linking from 30 % to 60 % significantly reduced the transparency, therefore the 30-0.07-Oct chemistry was taken forward for corneal cell seeding, and was demonstrated to support the growth of a monolayer of corneal epithelial cells.

Hydrogel constructs were also manufactured by reactive inkjet 3D printing using poly-ε-lysine and gellan gum as the reacting inks. These constructs were based on a different cross-linking chemistry after the bi-carboxylic acid components were found to be unsuitable for inkjet printing. The positive amine groups on the poly-ε-lysine chains were utilised for cross-linking via electrostatic interaction, and formed ionic bonds with the negative carboxylate groups on the gellan gum chain. These inks reacted immediately when combined, which ensured they were suitable for producing constructs via reactive inkjet printing. After ink stability measurements were performed, 20 wt % pεK and 0.35 wt % GG was taken forward for printing. This combination was printable using the jetlab4 printer, and produced printed arrays and porous shapes which featured a unique honeycomb topography. The printed arrays were shown to have a high transparency of 81 % and supported the growth of monolayers of both corneal epithelial and endothelial cells. This was the first time that poly-ε-lysine and gellan gum have been reported to manufacture hydrogels via reactive inkjet printing, and showed early promise for substrates for corneal tissue engineering.

6.3 Comparison of Manufacture Methods

The hydrogels investigated were manufactured by a variety of routes including; fragmentation, casting with a porogen, reactive inkjet 3D printing and stereolithography. These techniques introduced pores into the hydrogel structures in different ways and they each have their own advantages and disadvantages.

Poly-ε-lysine hydrogels were produced via a fragmentation method developed within our research group. This method deployed a simple stirrer device which introduced pores into the hydrogel structure upon polymerisation, and the resulting material was cast in between two glass plates. The fragmentation method successfully produced hydrogel sheets with an interconnected porosity, and could manufacture ≈10x10 cm sheets in under 30 minutes. However, this method offered little control over the porosity and pore size throughout the hydrogels which limits the substrate for particular applications where the porosity needs to be tuned. Furthermore, the process would have to be modified to allow for the scaling up of the fragmentation of hydrogels, as the time restraints with removing the hydrogel from the stirrer upon setting makes it difficult to scale up. For instance, a continuous process could be designed whereby there is an inlet to load the hydrogel components, and a separate outlet where the set hydrogel is removed from due to the change in material density as polymerisation takes place. The fragments could be extruded out of this outlet and cast into a petri dish with a similar glass plate setup.

Hydrogel casting with the inclusion of a porogen has been heavily investigated for the production of tissue engineering scaffolds. This method is based on the dissolution of a porogen into the hydrogel components before gelling, which when combined and cast, results in the solidification of the polymer phase around dispersed particles. The porogen is subsequently leached after hydrogel casting, often by immersing the material in a solvent which dissolves the particulates and leaves behind a porous structure. Use of a porogen allows for control over the pore size and average porosity as the porogen concentration and molecular weight can be adjusted [286]. Additionally, casting of hydrogels is a simple and low-cost technique, which is ideal for producing large quantities of material. However, there

is little control over the orientation of the particulates and the interconnectivity of the pores in the final construct. Finally, the leaching solvents are often cyto-toxic, which results in multiple washing and processing stages, and the constructs must be thin to allow the solvents to penetrate the structure to ensure all of the porogen is removed [287].

Reactive inkjet 3D printing (RIJ) is based on the combination of inks in a piezoelectric inkjet printing system which react to form a solid printed structure. Research has shown that DOD RIJ can be used to produce constructs with a high resolution (≈50 µm), and is a low cost high efficiency technique [288]. Furthermore, inkjet printing methods can be used to deposit cells throughout printed constructs, and has shown a high cell viability of 70-95 % post-printing [289]. However, there are strict requirements for materials that can be printed using RIJ, such as a low viscosity and immediate reaction between inks, which limits the manufacture to a smaller range of materials.

Methacrylated poly-ε-lysine and gelatin substrates were manufactured via stereolithography as substrates for corneal cell culture. Stereolithography (SLA) involves the curing of specific sections of a tank of resin to form a 3D solid part, based on a CAD model. Materials such as poly-caprolactone (PCL), poly(ethylene glycol) (PEG), and poly-lactic acid have been manufactured using SLA techniques and investigated for their suitability for tissue engineering scaffolds [290]. SLA techniques have been shown to produce parts with a high resolution, and can be tailored to alter the porosity and interconnectivity of constructs. However, it has limitations for the materials suitable for curing as they need to be photo-polymerisable and it requires large quantities of material to fill the resin tank which may be costly to produce [291]. A way to overcome the limitations of SLA printing techniques may be to use two-photon-polymerisation. This is an additive manufacturing technique which utilises the combined energy of two photons to initiate photo-polymerisation and is able to manufacture parts from a small quantity of ink with a high resolution [292].

6.4 Alternative applications of manufactured poly-ε-lysine materials

The poly-ε-lysine hydrogels manufactured for this thesis have met some of the suitability criteria for an artificial cornea application, but may also be suitable for other applications within the field of tissue engineering and beyond.

Poly-ε-lysine hydrogels manufactured via fragmentation methods based on a 30-0.07-Oct chemistry have demonstrated a high transparency, high water content, interconnected porosity and handleable mechanical properties. Furthermore, they were shown to support the growth of monolayers of corneal endothelial and epithelial cells, and the migration of corneal stromal cells into the porous network. These different cell types could be combined within the fragmented hydrogel substrate to produce a fully synthetic tissue engineered cornea which could prove suitable for 3D *in vitro* corneal disease models. This alternative application could advance the understanding of the interactions between the different cell types within the cornea, and their roles in corneal disease and damage, and could also reduce the need for animal testing for a pharmaceutical purpose [293]. Alternatively, porous hydrogel scaffolds have been investigated for various applications within the body, such as the regeneration of nerve tissue, bone scaffolds, and vascular and cardiac tissue engineering [294]. For these alternative applications where transparency is not required, the chemistry of fragmented pεK hydrogels could be altered, by either increasing the percentage cross-linking or the polymer density, to increase the mechanical integrity of the substrate for a high strength application.

Macroporous pεK hydrogels cast with a porogen demonstrated tuneable transparency and mechanical properties, a high water content and a high swelling ratio. The 60 % cross-linked variants had a low transparency, but a high stiffness, in the range of 900 kPa – 1700 kPa, which may be more suitable for an alternative application such as cartilage tissue engineering. Scaffolds for this application would require a high strength to withstand the high impact environment, as human articular cartilage has an elastic compressive modulus in the range of 240–1000 kPa [295]. However for cartilage, transparency is not an essential criterion. The implantation of a scaffold for cartilage regeneration may combat some of the

disadvantages with current clinical techniques, such as a long healing period of 9-12 months and tissue hypertrophy resulting in secondary operations [296]. On the other hand, the 30 % cross-linked macroporous scaffolds demonstrated a lower stiffness and a high swelling ratio. This feature, as well as the natural antimicrobial behaviour of poly-ε-lysine suggests a potential application for a wound healing bandage. In order to be suitable for a wound healing application, a material must have a suitable viscosity and mechanical properties [198], and also have a propensity for absorbing large quantities of fluid while minimising the risk of infection.

PεK/GG substrates have demonstrated proof of concept for a reactive inkjet printing method to produce hydrogel constructs. These hydrogels have a high transparency, a unique honeycomb topography and can be printed to include pores into the structure. The capability of inkjet printing to produce complex structures, with the option of including human cells, presents pεK/GG substrates as potential scaffolds for tissue engineering. Gellan gum boasts a high melting point, bio-compatibility, high transparency and a strong gelling ability [133, 134], properties which have seen this material heavily researched in tissue engineering applications. However, the mechanical properties of gellan gum are an order of magnitude below the properties of cartilage and other hard human tissues [297], therefore printed pεK/GG scaffolds would be more suitable for soft tissue applications.

The work in this thesis was based on exploring different methods to manufacture a poly-ε-lysine hydrogel construct. The methods trialled included a fragmentation technique, casting with a porogen, and 3D reactive inkjet printing. These techniques produced a library of hydrogels, based on various chemistries of poly-ε-lysine, which resulted in different optical, physical and mechanical properties. Furthermore, the different manufacture methods affected the porosity of the final construct, with the fragmented hydrogels having the most defined and controlled porosity. These hydrogels were designed for corneal tissue engineering, with two constructs in particular showing potential for the regeneration of different layers of

the cornea. The fragmented hydrogels were transparent and mechanically handleable, with a high water content and an interconnected porosity. These variants showed cyto-compatibility with corneal epithelial, endothelial and stromal cells and demonstrated potential for a full thickness construct or an *in vitro* corneal model. The 3D inkjet printed pεK/GG hydrogels were thin and highly transparent, and boasted a unique honeycomb topography. Due to their cyto-compatibility, these hydrogel variants showed promise for corneal epithelial and endothelial applications which requires thinner constructs to act as a cell delivery device. The preliminary characterisation of these hydrogels demonstrated comparable properties with other hydrogels and materials for corneal tissue engineering applications. Further investigation would be required to confirm *in vivo* compatibility.

Chapter 7: Conclusions

This study has suggested the potential of poly-ε-lysine based hydrogels for corneal tissue engineering applications. Hydrogels based on poly-ε-lysine were manufactured by fragmentation, casting with a porogen and inkjet 3D printing. These different techniques were shown to have different effects on the hydrogel transparency, porosity and mechanical properties. In particular, fragmented hydrogels showed comparable properties with other common hydrogels for corneal tissue engineering applications such as collagen and alginate. These hydrogels showed cyto-compatibility with corneal epithelial, endothelial and stromal cells.

Physical and Mechanical characterisation of the cast hydrogels:

- A range of porous hydrogels could be manufactured based on poly-ε-lysine that were either fragmented or cast with a porogen
- These hydrogel variants were made with varying chemistry by altering the di-acid cross-linker, percentage cross-linking and polymer density
- Fragmented hydrogels were shown to have a high transparency, high water content, interconnected porosity and handleable mechanical properties
- 30 % cross-linked macroporous hydrogels demonstrated a high transparency, high water content and degree of swelling, but had minimal porosity and weak mechanical properties
- 60 % cross-linked macroporous hydrogels demonstrated a high water content, high stiffness and a defined porosity, however had a low transparency
- A fragmented hydrogel variant (30-0.07-Oct) was shown to have comparable properties with other common hydrogels for corneal tissue engineering

3D printing of poly-ε-lysine:

- Poly-ε-lysine cross-linked with ODA was found to be unsuitable for extrusion 3D printing based on the polymerisation time of the hydrogel and the equipment we had available at the University
- Poly-ε-lysine cross-linked with ODA was found to be unsuitable for inkjet 3D printing based on the polymerisation time of the hydrogel and the NHS/EDCI combination forming a precipitate blocking the 80 µm printhead
- Poly-ε-lysine reacted with gellan gum was found to be printable using inkjet methods based on contact angle, surface tension, density and Z number calculations (20 wt % pεK and 0.35 wt % GG)
- Hydrogels were 3D printed based on 20 wt % pεK and 0.35 wt % GG and were shown to have a high transparency and a unique honeycomb topography and were printed with and without pores in the structure

Hydrogel cyto-compatibility:

- Fragmented 30-0.07-Oct demonstrated cyto-compatibility with and supported the growth of a monolayer of HCE-T and HCEC-12 cell lines
- Fragmented 30-0.07-Oct demonstrated cyto-compatibility with hCFs as they migrated into the porous pεK structure and deposited COL1 and COL6, which increased the hydrogels compressive moduli but did not alter transparency
- Macroporous 30-0.07-Oct supported the growth of a HCE-T monolayer across the surface which immunostained positive for ZO-1
- Inkjet printed pεK/GG supported the growth of HCE-T and HCEC-12 monolayers and stained positive for ZO-1
- Cast and 3D printed pεKMA supported the growth of HCE-T and HCEC-12 monolayers and stained positive for ZO-1 and Na^+/K^+/ATPase
- 3D printed GelMA supported the growth of HCE-T and HCEC-12 monolayers and stained positive for ZO-1 and Na^+/K^+/ATPase

Chapter 8: Future Direction

In this thesis, two different cast porous poly-ε-lysine hydrogels have been developed and well characterised for their physical and mechanical properties. Furthermore, a reactive inkjet printing technique has been developed whereby pεK can be printed with gellan gum to produce unique hydrogel constructs.

The fragmented pεK hydrogel variant 30-0.07-Oct have been characterised and discussed in this thesis for its potential applications in corneal tissue engineering. This hydrogel showed a high transparency, high water content and porosity handleable mechanical properties and cyto-compatibility with corneal epithelial, endothelial and stromal cells. It has been discussed that this material has shown potential to be superior over other common materials for corneal TE, such as collagen based substrates. However, further investigation into the material *ex vivo* and *in vivo* is required before it can be taken further. In particular, the fragmented pεK hydrogels degradation properties need to be further assessed, and the performance of the hydrogel when all three corneal cell types are included into the construct.

Macroporous pεK hydrogels demonstrated a library of materials with a tuneable transparency, porosity, swelling and mechanical properties. Although the 30 % cross-linked variants showed a suitable transparency for a corneal TE application, they demonstrated weak mechanical properties and an unstable swelling behaviour. These materials may be more suitable for a wound healing application, therefore the necessary investigation would be required for the macroporous pεK to go down this route.

Reactive inkjet printing of pεK/GG constructs reached proof of concept, however further printing optimisation and hydrogel characterisation is required for this construct to be taken further. Modifications to the inkjet printer may be useful in further fine-tuning the process so that a thicker hydrogel construct can be printed using a higher number of passes. Furthermore, the hydrogel construct needs to be characterised for other important properties for corneal TE, such as water content, degradation behaviour and mechanical properties before it can be taken further. A printed pεK/GG substrate with increased thickness and structural complexity could

allow for the production of a hydrogel construct that could more closely mimic the human cornea. Once an ideal structure has been established, cell-loaded inks could be utilised to deposit corneal epithelial, stromal and endothelial cells throughout the construct, to build up a bioengineered cornea suitable for transplantation.

Finally, several studies were performed establishing cyto-compatibility of the three main corneal cell types with different pεK based materials. Future work to build on the results of this chapter could include further *in vitro* studies with human primary epithelial and endothelial cell types. This would more accurately determine the suitability of these hydrogels for tissue engineering using these cell types. Further investigation into the deposition of ECM by the stromal cells would be important to quantify the amount of material being laid down in the fragmented pεK hydrogels, this would help us to understand the capability of hCFs for building an ECM based construct within the hydrogel network. Finally, a co-culture model with all three corneal cell types would characterise how these cells behave with the material and how their growth and attachment is influenced by the presence of one another. These results would be important for advancing the work in this thesis and establishing the suitability of pεK based hydrogels for corneal tissue engineering.

Chapter 9: Appendices

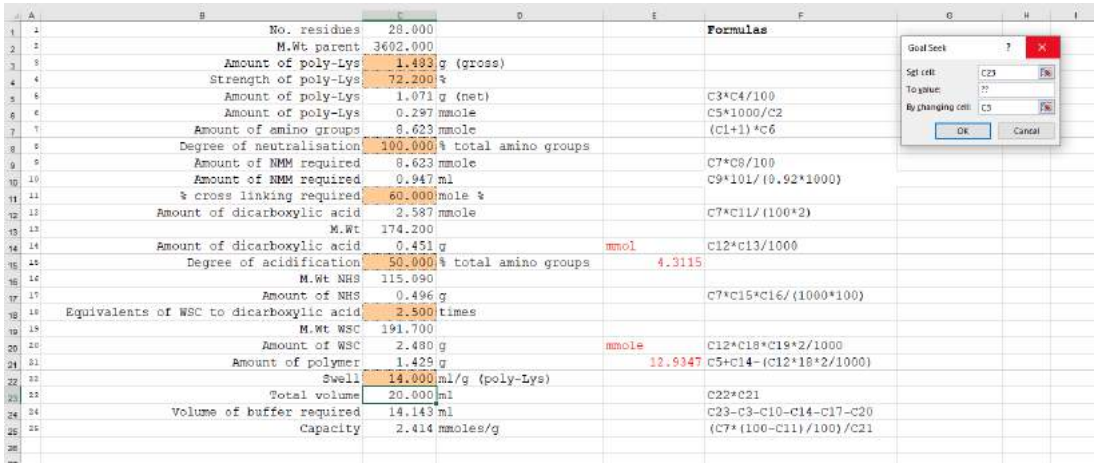

	No. residues	28.000			Formulas	
	M.Wt parent	3602.000				
	Amount of poly-Lys	1.483	g (gross)			
	Strength of poly-Lys	72.200	%			
	Amount of poly-Lys	1.071	g (net)		C3*C4/100	
	Amount of poly-Lys	0.297	mmole		C5*1000/C2	
	Amount of amino groups	8.623	mmole		(C1+1)*C6	
	Degree of neutralisation	100.000	% total amino groups			
	Amount of NMM required	8.623	mmole		C7*C8/100	
	Amount of NMM required	0.947	ml		C9*101/(0.92*1000)	
	% cross linking required	60.000	mole %			
	Amount of dicarboxylic acid	2.587	mmole		C7*C11/(100*2)	
	M.Wt	174.200				
	Amount of dicarboxylic acid	0.451	g	mmol	C12*C13/1000	
	Degree of acidification	50.000	% total amino groups	4.3115		
	M.Wt NHS	115.090				
	Amount of NHS	0.496	g		C7*C15*C16/(1000*100)	
	Equivalents of WSC to dicarboxylic acid	2.500	times			
	M.Wt WSC	191.700				
	Amount of WSC	2.480	g	mmole	C12*C18*C19*2/1000	
	Amount of polymer	1.429	g	12.9347	C5+C14-(C12*18*2/1000)	
	Swell	14.000	ml/g (poly-Lys)			
	Total volume	20.000	ml		C22*C21	
	Volume of buffer required	14.143	ml		C23-C3-C10-C14-C17-C20	
	Capacity	2.414	mmoles/g		(C7*(100-C11)/100)/C21	

Figure 9.1: Excel spreadsheet for determining hydrogel composition

An excel spreadsheet was designed and optimised by Dean Simpkin and Andrew Gallagher from SpheriTech Ltd. This spreadsheet was used to calculate the polymer composition of each variant required to make a desired quantity of the pεK hydrogel, **Figure 9.1**. The orange highlighted boxes are the parameters that can be adjusted to determine the desired polymer chemistry. For example, a 30-0.07-Oct chemistry would require a 30 % cross-linking and a 14 ml/g swell to be added into the appropriate cells. A goal seek is run whereby the desired total volume of solution is entered, and the analysis is based on cell C3, which is the gross amount of pεK in grams. When the goal seek analysis is complete, the required amounts of pεK, ODA, NHS, NMM and EDCI will be displayed in the table.

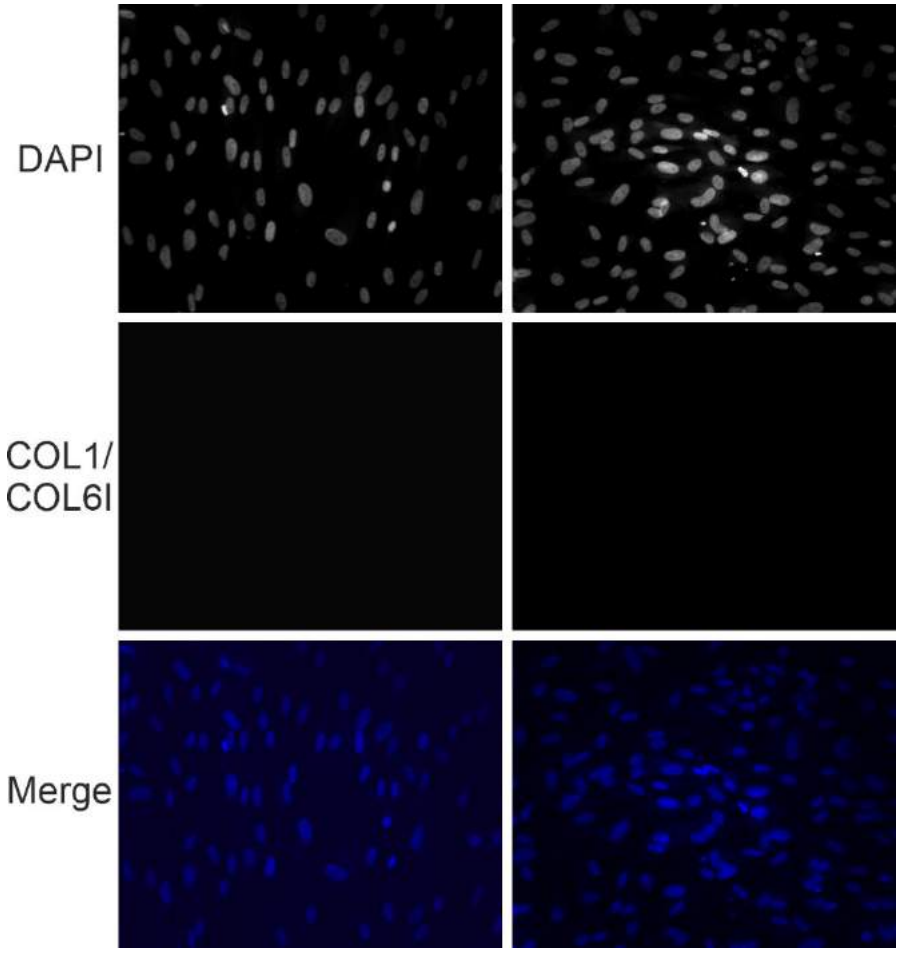

Figure 9.2: IgG Negative controls for COL1 and COL6 immunostaining

To eliminate the chance of non-specific staining of COL1 and COL6, a negative Go-Ra IgG control was included. The absence of positive staining in the COL1/COL6 channel demonstrated that no non-specific staining was present, and the positive COL1/COL6 staining in section 5.2.6 can be trusted to be accurate.

References

[1] B. D. Kels, A. Grzybowski, and J. M. Grant-Kels, "Human ocular anatomy," *Clin Dermatol,* vol. 33, no. 2, pp. 140-6, Mar-Apr 2015, doi: 10.1016/j.clindermatol.2014.10.006.

[2] H. Kolb, "Gross Anatomy of the Eye " in *The Organization of the Retina and Visual System*, H. Kolb, E. Fernandez, and R. Nelson Eds. Salk Lake City, UT: University of Utah Health Sciences Centre 2005, pp. 3-9.

[3] N. R. Galloway, W. M. K. Amoaku, P. H. Galloway, and A. C. Browning, "Basic Anatomy and Physiology of the Eye " in *Common Eye Diseases and their Management* London: Springer 2006, pp. 7-15.

[4] K. Irsch and D. L. Guyton, "Anatomy of Eyes," in *Encyclopedia of Biometrics*, S. Z. Li and A. Jain Eds. Boston, MA: Springer, 2009, pp. 11-16.

[5] J. V. Forrester, A. D. Dick, P. G. McMenamin, F. Roberts, and E. Pearlman, "Anatomy of the Eye and Orbit " in *The Eye: Basic Sciences in Practice* J. V. Forrester, A. D. Dick, P. G. McMenamin, F. Roberts, and E. Pearlman Eds., Fourth ed.: W. B. Saunders 2016, pp. 1-102.

[6] I. Grierson, *The eye book : eyes and eye problems explained*. Liverpool: Liverpool University Press, 2000.

[7] D. W. DelMonte and T. Kim, "Anatomy and physiology of the cornea," *Journal of Cataract and Refractive Surgery,* vol. 37, pp. 588-598, 2011.

[8] C. H. Dohlman, "The function of the corneal epithelium in health and disease. The Jonas S. Friedenwald Memorial Lecture," *Invest Ophthalmol,* vol. 10, no. 6, pp. 383-407, Jun 1971.

[9] S. Gandhi and S. Jain, "The anatomy and physiology of cornea," in *Keratoprostheses and Artificial Corneas: Fundamentals and Surgical Applications* M. S. Cortina and J. d. l. Cruz Eds. Berlin: Springer-Verlag, 2015, pp. 19-25.

[10] W. J. Dupps, Jr. and S. E. Wilson, "Biomechanics and wound healing in the cornea," *Exp Eye Res,* vol. 83, no. 4, pp. 709-20, Oct 2006, doi: 10.1016/j.exer.2006.03.015.

[11] Keith M. Meek and C. Knupp, "Corneal structure and transparency," *Progress in Retinal and Eye Research,* vol. 49, pp. 1-16, 2015.

[12] Y. M. Michelacci, "Collagens and proteoglycans of the corneal extracellular matrix," *Braz J Med Biol Res,* vol. 36, no. 8, pp. 1037-46, Aug 2003, doi: 10.1590/s0100-879x2003000800009.

[13] J. H. Stern *et al.*, "Regenerating Eye Tissues to Preserve and Restore Vision," (in eng), *Cell Stem Cell,* vol. 23, no. 3, p. 453, Sep 2018, doi: 10.1016/j.stem.2018.08.014.

[14] S. V. Patel, J. W. McLaren, D. O. Hodge, and W. M. Bourne, "Normal Human Keratocyte Density and Corneal Thickness Measurement by Using Confocal Microscopy In Vivo," *Investigative Ophthalmology and Visual Science,* vol. 42, pp. 333-339, 2001.

[15] M.Pavelka and J. Roth, "Descemet's Membrane," in *Functional Ultrastructure* Vienna: Springer-Verlag, 2010, pp. 184-185.

[16] S. Jacob and P. Naveen, "Anatomy of the Cornea," in *Mastering Endothelial Keratoplasty*, vol. 1, S. Jacob Ed. India: Springer, 2016, ch. 1, pp. 7-10.
[17] S. J. Tuft and D. J. Coster, "The corneal endothelium," *Eye (Lond),* vol. 4 (Pt 3), pp. 389-424, 1990, doi: 10.1038/eye.1990.53.
[18] N. C. Joyce, "Proliferative capacity of the corneal endothelium," *Prog Retin Eye Res,* vol. 22, no. 3, pp. 359-89, May 2003, doi: 10.1016/s1350-9462(02)00065-4.
[19] W. M. Bourne, "Biology of the corneal endothelium in health and disease," *Eye (Lond),* vol. 17, no. 8, pp. 912-8, Nov 2003, doi: 10.1038/sj.eye.6700559.
[20] J. A. Bonanno, "Molecular mechanisms underlying the corneal endothelial pump," *Exp Eye Res,* vol. 95, no. 1, pp. 2-7, Feb 2012, doi: 10.1016/j.exer.2011.06.004.
[21] M. S. Sridhar, "Anatomy of cornea and ocular surface," *Indian Journal of Opthamology,* vol. 66, pp. 190-194, 2018.
[22] E. M. Van Buskirk, "The anatomy of the limbus," *Eye (Lond),* vol. 3 (Pt 2), pp. 101-8, 1989, doi: 10.1038/eye.1989.16.
[23] N. Polisetti, M. Zenkel, J. Menzel-Severing, F. E. Kruse, and U. Schlotzer-Schrehardt, "Cell Adhesion Molecules and Stem Cell-Niche-Interactions in the Limbal Stem Cell Niche," *Stem Cells,* vol. 34, no. 1, pp. 203-19, Jan 2016, doi: 10.1002/stem.2191.
[24] K. Grieve *et al.*, "Three-dimensional structure of the mammalian limbal stem cell niche," *Exp Eye Res,* vol. 140, pp. 75-84, Nov 2015, doi: 10.1016/j.exer.2015.08.003.
[25] M. A. Dziasko and J. T. Daniels, "Anatomical Features and Cell-Cell Interactions in the Human Limbal Epithelial Stem Cell Niche," *The Ocular Surface,* vol. 14, no. 3, pp. 322-330, 2016.
[26] D. A. Dartt and M. D. Willcox, "Complexity of the tear film: importance in homeostasis and dysfunction during disease," *Exp Eye Res,* vol. 117, pp. 1-3, Dec 2013, doi: 10.1016/j.exer.2013.10.008.
[27] A. J. Bron, J. M. Tiffany, S. M. Gouveia, N. Yokoi, and L. W. Voon, "Functional aspects of the tear film lipid layer," *Exp Eye Res,* vol. 78, no. 3, pp. 347-60, Mar 2004, doi: 10.1016/j.exer.2003.09.019.
[28] L. Cwiklik, "Tear film lipid layer: A molecular level view," *Biochim Biophys Acta,* vol. 1858, no. 10, pp. 2421-2430, Oct 2016, doi: 10.1016/j.bbamem.2016.02.020.
[29] V. Paranjpe, L. Phung, and A. Galor, "The Tear film: Anatomy and Physiology," in *Ocular Fluid Dynamics*: Birkhäuser, Cham, 2019, pp. 329-345.
[30] Y. Hori, "Secreted Mucins on the Ocular Surface," *Invest Ophthalmol Vis Sci,* vol. 59, no. 14, pp. DES151-DES156, Nov 1 2018, doi: 10.1167/iovs.17-23623.
[31] R. R. Hodges and D. A. Dartt, "Tear film mucins: front line defenders of the ocular surface; comparison with airway and gastrointestinal tract mucins," *Exp Eye Res,* vol. 117, pp. 62-78, Dec 2013, doi: 10.1016/j.exer.2013.07.027.
[32] D. Xia *et al.*, "The Ultrastructures and Mechanical Properties of the Descement's Membrane in Fuchs Endothelial Corneal Dystrophy," *Sci Rep,* vol. 6, p. 23096, Mar 16 2016, doi: 10.1038/srep23096.

[33] A. O. Eghrari and J. D. Gottsch, "Fuchs' corneal dystrophy," *Expert Rev Ophthalmol,* vol. 5, no. 2, pp. 147-159, Apr 2010, doi: 10.1586/eop.10.8.
[34] G. G. Nanda and D. P. Alone, "REVIEW: Current understanding of the pathogenesis of Fuchs' endothelial corneal dystrophy," *Mol Vis,* vol. 25, pp. 295-310, 2019.
[35] A. M. Eltony, F. Clouser, P. Shao, R. Pineda, 2nd, and S. H. Yun, "Brillouin Microscopy Visualizes Centralized Corneal Edema in Fuchs Endothelial Dystrophy," *Cornea,* vol. 39, no. 2, pp. 168-171, Feb 2020, doi: 10.1097/ICO.0000000000002191.
[36] P. Gain *et al.*, "Global Survey of Corneal Transplantation and Eye Banking," *JAMA Ophthalmol,* vol. 134, no. 2, pp. 167-73, Feb 2016, doi: 10.1001/jamaophthalmol.2015.4776.
[37] R. Singh, N. Gupta, M. Vanathi, and R. Tandon, "Corneal transplantation in the modern era," *Indian J Med Res,* vol. 150, no. 1, pp. 7-22, Jul 2019, doi: 10.4103/ijmr.IJMR_141_19.
[38] Q. Le, J. Xu, and S. X. Deng, "Review. The diagnosis of limbal stem cell deficiency," *Ocular Surface,* vol. 16, pp. 58-69, 2018.
[39] K. Sejpal, P. Bakhtiari, and S. X. Deng, "Presentation, diagnosis and management of limbal stem cell deficiency," *Middle East Afr J Ophthalmol,* vol. 20, no. 1, pp. 5-10, Jan-Mar 2013, doi: 10.4103/0974-9233.106381.
[40] H. S. Dua and A. Azuara-Blanco, "Limbal stem cells of the corneal epithelium," *Surv Ophthalmol,* vol. 44, no. 5, pp. 415-25, Mar-Apr 2000, doi: 10.1016/s0039-6257(00)00109-0.
[41] B. Y. Kim *et al.*, "Medically reversible limbal stem cell disease: clinical features and management strategies," *Ophthalmology,* vol. 121, no. 10, pp. 2053-8, Oct 2014, doi: 10.1016/j.ophtha.2014.04.025.
[42] S. X. Deng *et al.*, "Global Consensus on Definition, Classification, Diagnosis, and Staging of Limbal Stem Cell Deficiency," *Cornea,* vol. 38, no. 3, pp. 364-375, Mar 2019, doi: 10.1097/ICO.0000000000001820.
[43] A. E. Ghareeb, M. Lako, and F. C. Figueiredo, "Recent Advances in Stem Cell Therapy for Limbal Stem Cell Deficiency: A Narrative Review," *Ophthalmol Ther,* vol. 9, no. 4, pp. 809-831, Dec 2020, doi: 10.1007/s40123-020-00305-2.
[44] R. Alnabulsi, M. Showail, Ni.Sorkin, A. Einan-Lifshitz, and D. Rootman, "Fuchs' endothelial dystrophy masquerading as keratoconus," *Canadian Journal of Ophthalmology,* vol. 54, pp. 176-180, 2019.
[45] R. Sharif, S. Bak-Nielsen, J. Hjortdal, and D. Karamichos, "Pathogenesis of Keratoconus: The intriguing therapeutic potential of Prolactin-inducible protein," *Prog Retin Eye Res,* vol. 67, pp. 150-167, Nov 2018, doi: 10.1016/j.preteyeres.2018.05.002.
[46] T. Sherwin and N. H. Brookes, "Morphological changes in keratoconus: pathology or pathogenesis," *Clin Exp Ophthalmol,* vol. 32, no. 2, pp. 211-7, Apr 2004, doi: 10.1111/j.1442-9071.2004.00805.x.
[47] M. L. Khaled, I. Helwa, M. Drewry, M. Seremwe, A. Estes, and Y. Liu, "Molecular and Histopathological Changes Associated with Keratoconus," *Biomed Res Int,* vol. 2017, p. 7803029, 2017, doi: 10.1155/2017/7803029.

[48] A. E. Davidson, S. Hayes, A. J. Hardcastle, and S. J. Tuft, "The pathogenesis of keratoconus," *Eye (Lond),* vol. 28, no. 2, pp. 189-95, Feb 2014, doi: 10.1038/eye.2013.278.
[49] D. M. Gore, A. J. Shortt, and B. D. Allan, "New clinical pathways for keratoconus," *Eye (Lond),* vol. 27, no. 3, pp. 329-39, Mar 2013, doi: 10.1038/eye.2012.257.
[50] K. Omer, "Epidemiology of Keratoconus Worldwide," *The Open Ophthalmology Journal,* vol. 12, pp. 289-299, 2018.
[51] T. Georgiou, C. L. Funnell, A. Cassels-Brown, and R. O'Conor, "Influence of ethnic origin on the incidence of keratoconus and associated atopic disease in Asians and white patients," *Eye (Lond),* vol. 18, no. 4, pp. 379-83, Apr 2004, doi: 10.1038/sj.eye.6700652.
[52] D. Aghadoost, "Ocular trauma: an overview," *Arch Trauma Res,* vol. 3, no. 2, p. e21639, Jun 2014, doi: 10.5812/atr.21639.
[53] A. Fujikawa *et al.*, "Visual outcomes and prognostic factors in open-globe injuries," *BMC Ophthalmol,* vol. 18, no. 1, p. 138, Jun 8 2018, doi: 10.1186/s12886-018-0804-4.
[54] A. A. Ayanniyi and M. K. Fasasi, "Uniocular Blindness Following Thermal Injury," *Malaysian Journal of Medical Sciences,* vol. 20, pp. 88-91, 2013.
[55] M. Eslani, A. Baradaran-Rafii, A. Movahedan, and A. R. Djalilian, "The ocular surface chemical burns," *J Ophthalmol,* vol. 2014, p. 196827, 2014, doi: 10.1155/2014/196827.
[56] K. Mashige, "Chemical and thermal ocular burns: a review of causes, clinical features and management protocol," *South African Family Practice,* vol. 58, pp. 1-4, 2016.
[57] S. Ahmad, J. Klawe, C. A. Utine, D. Srikumaran, J. Jimenez, and E. Akpek, "Survival of penetrating keratoplasty: a claims-based longitudinal analysis," *Can J Ophthalmol,* vol. 56, no. 1, pp. 12-16, Feb 2021, doi: 10.1016/j.jcjo.2020.07.019.
[58] K. Krysik, E. Wroblewska-Czajka, A. Lyssek-Boron, E. A. Wylegala, and D. Dobrowolski, "Total Penetrating Keratoplasty: Indications, Therapeutic Approach, and Long-Term Follow-Up," *J Ophthalmol,* vol. 2018, p. 9580292, 2018, doi: 10.1155/2018/9580292.
[59] M. Kawashima, T. Kawakita, S. Den, S. Shimmura, K. Tsubota, and J. Shimazaki, "Comparison of deep lamellar keratoplasty and penetrating keratoplasty for lattice and macular corneal dystrophies," *Am J Ophthalmol,* vol. 142, no. 2, pp. 304-9, Aug 2006, doi: 10.1016/j.ajo.2006.03.057.
[60] S. W. S. Chan, Y. Yucel, and N. Gupta, "New trends in corneal transplants at the University of Toronto," *Canadian Journal of Ophthalmology,* vol. 53, pp. 580-587, 2018.
[61] F. Palma-Carvajal *et al.*, "Trends in corneal transplantation in a single center in Barcelona, Spain. Transitioning to DMEK," *J Fr Ophtalmol,* vol. 43, no. 1, pp. 1-6, Jan 2020, doi: 10.1016/j.jfo.2019.06.026.
[62] M. A. P. Fajgenbaum, N. Kopsachilis, and E. J. Hollick, "Descemet's membrane endothelial keratoplasty: surgical outcomes and endothelial cell count modelling from a UK centre," *Eye (Lond),* vol. 32, no. 10, pp. 1629-1635, Oct 2018, doi: 10.1038/s41433-018-0152-x.

[63] J. van Rooij, E. H. Lucas, A. J. Geerards, L. Remeijer, and R. Wubbels, "Corneal transplantation for Fuchs endothelial dystrophy: A comparison of three surgical techniques concerning 10 year graft survival and visual function," *PLoS One,* vol. 13, no. 10, p. e0203993, 2018, doi: 10.1371/journal.pone.0203993.

[64] A. Anshu, M. O. Price, D. T. Tan, and F. W. Price, Jr., "Endothelial keratoplasty: a revolution in evolution," *Surv Ophthalmol,* vol. 57, no. 3, pp. 236-52, May-Jun 2012, doi: 10.1016/j.survophthal.2011.10.005.

[65] P. Rama, G. Ferrari, and G. Pellegrini, "Cultivated limbal epithelial transplantation," *Curr Opin Ophthalmol,* vol. 28, no. 4, pp. 387-389, Jul 2017, doi: 10.1097/ICU.0000000000000382.

[66] M. Haagdorens *et al.*, "Limbal Stem Cell Deficiency: Current Treatment Options and Emerging Therapies," *Stem Cells Int,* vol. 2016, p. 9798374, 2016, doi: 10.1155/2016/9798374.

[67] V. M. Borderie *et al.*, "Long-Term Results of Cultured Limbal Stem Cell Versus Limbal Tissue Transplantation in Stage III Limbal Deficiency," *Stem Cells Transl Med,* vol. 8, no. 12, pp. 1230-1241, Dec 2019, doi: 10.1002/sctm.19-0021.

[68] V. S. Sangwan, S. Basu, S. MacNeil, and D. Balasubramanian, "Simple limbal epithelial transplantation (SLET): a novel surgical technique for the treatment of unilateral limbal stem cell deficiency," *Br J Ophthalmol,* vol. 96, no. 7, pp. 931-4, Jul 2012, doi: 10.1136/bjophthalmol-2011-301164.

[69] S. Basu, S. P. Sureka, S. S. Shanbhag, A. R. Kethiri, V. Singh, and V. S. Sangwan, "Simple Limbal Epithelial Transplantation: Long-Term Clinical Outcomes in 125 Cases of Unilateral Chronic Ocular Surface Burns," *Ophthalmology,* vol. 123, no. 5, pp. 1000-10, May 2016, doi: 10.1016/j.ophtha.2015.12.042.

[70] B. Salvador-Culla and P. E. Kolovou, "Keratoprosthesis: A Review of Recent Advances in the Field," *J Funct Biomater,* vol. 7, no. 2, May 19 2016, doi: 10.3390/jfb7020013.

[71] C. R. Hicks *et al.*, "AlphaCor: Clinical outcomes," *Cornea,* vol. 25, no. 9, pp. 1034-42, Oct 2006, doi: 10.1097/01.ico.0000229982.23334.6b.

[72] K. V. Chalam, A. Chokshi, S. Agarwal, and D. P. Edward, "Complications of AlphaCor Keratoprosthesis: A Clinicopathologic Report," *Cornea,* vol. 26, pp. 1258-1260, 2007.

[73] J. L. Alio, A. A. Abdelghany, S. K. Abu-Mustafa, and G. Zein, "A new epidescemetic keratoprosthesis: pilot investigation and proof of concept of a new alternative solution for corneal blindness," *Br J Ophthalmol,* vol. 99, no. 11, pp. 1483-7, Nov 2015, doi: 10.1136/bjophthalmol-2014-306264.

[74] P. Studeny, D. Krizova, and P. Kuchynka, "Use of PocketMaker Microkeratome for Creation of Corneal Pocket for Foldable Keratoprosthesis KeraKlear Implantation – Case Series," *The Open Ophthalmology Journal,* vol. 9, pp. 126-130, 2015.

[75] E. J. Hollick, S. L. Watson, J. K. Dart, P. J. Luthert, and B. D. Allan, "Legeais BioKpro III keratoprosthesis implantation: long term results in seven patients," *Br J Ophthalmol,* vol. 90, no. 9, pp. 1146-51, Sep 2006, doi: 10.1136/bjo.2006.092510.

[76] I. Massie, A. K. Kureshi, S. Schrader, A. J. Shortt, and J. T. Daniels, "Optimization of optical and mechanical properties of real architecture for 3-dimensional tissue equivalents: Towards treatment of limbal epithelial stem cell deficiency," *Acta Biomaterialia,* vol. 24, pp. 241-250, 2015.
[77] H. Niknejad, H. Peirovi, M. Jorjani, A. Ahmadiani, J. Ghanavi, and A. M. Seifalian, "Properties of the amniotic membrane for potential use in tissue engineering," (in English), *Eur Cells Mater,* vol. 15, pp. 88-99, Jan-Jun 2008.
[78] C. J. Connon *et al.*, "The variation in transparency of amniotic membrane used in ocular surface regeneration," (in English), *Brit J Ophthalmol,* vol. 94, no. 8, pp. 1057-1061, Aug 2010, doi: 10.1136/bjo.2008.153064.
[79] L. Zhang *et al.*, "An Ultra-thin Amniotic Membrane as Carrier in Corneal Epithelium Tissue-Engineering," *Scientific Reports,* vol. 6, p. 21021, 2016.
[80] N. Koizumi, T. Inatomi, A. J. Quantock, N. J. Fullwood, A. Dota, and S. Kinoshita, "Amniotic Membrane as a Substrate for Cultivating Limbal Corneal Epithelial Cells for Autologous Transplantation in Rabbits," *Cornea,* vol. 19, pp. 65-71, 2000.
[81] B. Sikora, M. Rafat, and M. J. Łos, "Examples of Successful Biomaterial-Based Artificial Tissues—Artificial Corneas," in *Stem Cells and Biomaterials for Regenerative Medicine*, M. J. Łos, A. Hudecki, and E. Wiecheć Eds.: Academic Press, 2019, pp. 191-202.
[82] N. Arrighi, "Stem Cells at the Core of Cell Therapy," in *Stem Cells*, N. Arrighi Ed.: Elsevier, 2018, ch. 3, pp. 73-100.
[83] F. Li *et al.*, "Cellular and nerve regeneration within a biosynthetic extracellular matrix for corneal transplantation," *Proc Natl Acad Sci U S A,* vol. 100, pp. 15346–15351, 2003.
[84] C. R. McLaughlin *et al.*, "Regeneration of functional nerves within full thickness collagen–phosphorylcholine corneal substitute implants in guinea pigs," *Biomaterials,* vol. 31, pp. 2770–2778, 2010.
[85] P. Fagerholm, N. S. Lagali, D. J. Carlsson, K. Merrett, and M. Griffith, "Corneal regeneration following implantation of a biomimetic tissue-engineered substitute," *Clin Transl Sci,* vol. 2, no. 2, pp. 162-4, Apr 2009, doi: 10.1111/j.1752-8062.2008.00083.x.
[86] Per Fagerholm *et al.*, "A Biosynthetic Alternative to Human Donor Tissue for Inducing Corneal Regeneration: 24-Month Follow-Up of a Phase 1 Clinical Study," *Science Translational Medicine,* vol. 2, pp. 46-61, 2010.
[87] H. J. Levis, A. K. Kureshi, I. Massie, L. Morgan, A. J. Vernon, and J. T. Daniels, "Tissue Engineering the Cornea: The Evolution of RAFT," *J Funct Biomater,* vol. 6, no. 1, pp. 50-65, Jan 22 2015, doi: 10.3390/jfb6010050.
[88] H. J. Levis, R. A. Brown, and J. T. Daniels, "Plastic compressed collagen as a biomimetic substrate for human limbal epithelial cell culture," *Biomaterials,* vol. 31, pp. 7726-7737, 2010.
[89] H. J. Levis *et al.*, "Plastic Compressed Collagen as a Novel Carrier for Expanded Human Corneal Endothelial Cells for Transplantation," (in English), *Plos One,* vol. 7, no. 11, Nov 30 2012, doi: ARTN e50993 10.1371/journal.pone.0050993.

[90] J. B. Rose *et al.*, "Gelatin-Based Materials in Ocular Tissue Engineering," *Materials (Basel),* vol. 7, no. 4, pp. 3106-3135, Apr 17 2014, doi: 10.3390/ma7043106.
[91] E. Prina *et al.*, "Bioinspired Precision Engineering of Three-Dimensional Epithelial Stem Cell Microniches," *Adv Biosyst,* vol. 4, no. 6, p. e2000016, Jun 2020, doi: 10.1002/adbi.202000016.
[92] M. Rizwan *et al.*, "Sequentially-crosslinked bioactive hydrogels as nano-patterned substrates with customizable stiffness and degradation for corneal tissue engineering applications," (in eng), *Biomaterials,* vol. 120, pp. 139-154, 03 2017, doi: 10.1016/j.biomaterials.2016.12.026.
[93] C. E. Ghezzi, B. Marelli, F. G. Omenetto, J. L. Funderburgh, and D. L. Kaplan, "3D Functional Corneal Stromal Tissue Equivalent Based on Corneal Stromal Stem Cells and Multi-Layered Silk Film Architecture," *PLoS One,* vol. 12, no. 1, p. e0169504, 2017, doi: 10.1371/journal.pone.0169504.
[94] L. J. Bray, K. A. George, S. L. Ainscough, D. W. Hutmacher, T. V. Chirila, and D. G. Harkin, "Human corneal epithelial equivalents constructed on Bombyx mori silk fibroin membranes," (in English), *Biomaterials,* vol. 32, no. 22, pp. 5086-5091, Aug 2011, doi: 10.1016/j.biomaterials.2011.03.068.
[95] C. Vepari and D. L. Kaplan, "Silk as a biomaterial," (in English), *Prog Polym Sci,* vol. 32, no. 8-9, pp. 991-1007, Aug-Sep 2007, doi: 10.1016/j.progpolymsci.2007.05.013.
[96] J. Xiao *et al.*, "Construction of the recellularized corneal stroma using porous acellular corneal scaffold," *Biomaterials,* vol. 32, pp. 6962-6971, 2011.
[97] K. Zhang, X.-X. Ren, P. Li, K.-P. Pang, and H. Wang, "Construction of a full-thickness human corneal substitute from anterior acellular porcine corneal matrix and human corneal cells," *International Journal of Ophthalmology* vol. 12, pp. 351-362, 2018.
[98] P. Deshpande *et al.*, "Using poly(lactide-co-glycolide) electrospun scaffolds to deliver cultured epithelial cells to the cornea," *Regenerative Medicine,* vol. 5, no. 3, pp. 395-401, 2010.
[99] P. Deshpande, C. Ramachandran, V. S. Sangwan, and S. MacNeil, "Corneal Regenerative Medicine: Methods and Protocols," in *Methods in Molecular Biology*, vol. 1014, B. Wright and C. J. Connon Eds. New York: Springer Science 2013.
[100] F. Sefat *et al.*, "Production, Sterilisation and Storage of Biodegradable Electrospun PLGA Membranes for Delivery of Limbal Stem Cells to the Cornea," *Procedia Engineering,* vol. 00, pp. 000-000, 2013.
[101] C. Ramachandran *et al.*, "Proof-of-concept study of electrospun PLGA membrane in the treatment of limbal stem cell deficiency," *BMJ Open Ophthalmology,* vol. 6, p. e000762, 2021.
[102] J. Zhu, "Bioactive modification of poly(ethylene glycol) hydrogels for tissue engineering," *Biomaterials,* vol. 31, no. 17, pp. 4639-56, Jun 2010, doi: 10.1016/j.biomaterials.2010.02.044.
[103] B. Ozcelik *et al.*, "Biodegradable and biocompatible poly(ethylene glycol)-based hydrogel films for the regeneration of corneal endothelium," *Adv Healthc Mater,* vol. 3, no. 9, pp. 1496-507, Sep 2014, doi: 10.1002/adhm.201400045.

[104] I. Ortega, P. Deshpande, A. A. Gill, S. MacNeil, and F. Claeyssens, "Development of a microfabricated artificial limbus with micropockets for cell delivery to the cornea," *Biofabrication,* vol. 5, no. 2, p. 025008, Jun 2013, doi: 10.1088/1758-5082/5/2/025008.
[105] T. N. Abraham, V. Raj, T. Prasad, P. R. A. Kumar, K. Sreenivasan, and T. V. Kumary, "A Novel Thermoresponsive Graft Copolymer Containing Phosphorylated HEMA for Generating Detachable Cell Layers," *Journal of Applied Polymer Science,* vol. 115, pp. 52-62, 2009.
[106] K. Nishida *et al.*, "Functional bioengineered corneal epithelial sheet grafts from corneal stem cells expanded ex vivo on a temperature-responsive cell culture surface," *Transplantation,* vol. 77, no. 3, pp. 379-85, Feb 15 2004, doi: 10.1097/01.TP.0000110320.45678.30.
[107] B. K. Madathil, Pallickaveedu RajanAsari Anil Kumar, and T. V. Kumary, "N-Isopropylacrylamide-co-glycidylmethacrylate as a Thermoresponsive Substrate for Corneal Endothelial Cell Sheet Engineering," *Biomed Res Int,* vol. 2014, p. 450672, 2014.
[108] R. Parke-Houben *et al.*, "Interpenetrating polymer network hydrogel scaffolds for artificial cornea periphery," *J Mater Sci: Mater Med,* vol. 26, 2015.
[109] X. W. Tan *et al.*, "In vivo biocompatibility of two PEG/PAA interpenetrating polymer networks as corneal inlays following deep stromal pocket implantation," *Journal of Materials Science: Materials in Medicine,* vol. 24, pp. 967-977, 2013.
[110] L. Hartmann *et al.*, "Toward the development of an artificial cornea: improved stability of interpenetrating polymer networks," *J Biomed Mater Res B Appl Biomater,* vol. 98, no. 1, pp. 8-17, Jul 2011, doi: 10.1002/jbm.b.31806.
[111] H. Bakhshandeh *et al.*, "Poly (ε-caprolactone) nanofibrous ring surrounding a polyvinyl alcohol hydrogel for the development of a biocompatible two-part artificial cornea," *International Journal of Nanomedicine,* vol. 6, pp. 1509-1515, 2011.
[112] J. Maitra and V. K. Shukla, "Cross-linking in Hydrogels - A Review," *American Journal of Polymer Science,* vol. 4, pp. 25-31, 2014.
[113] C. Fan and D. Wang, "Macroporous Hydrogel Scaffolds for Three-Dimensional Cell Culture and Tissue Engineering," *Tissue Engineering: Part B,* vol. 23, pp. 451-461, 2017.
[114] K. Y. Lee and D. J. Mooney, "Alginate: properties and biomedical applications," *Prog Polym Sci,* vol. 37, no. 1, pp. 106-126, Jan 2012, doi: 10.1016/j.progpolymsci.2011.06.003.
[115] T. Zhu *et al.*, "Recent Progress of Polysaccharide-Based Hydrogel Interfaces for Wound Healing and Tissue Engineering," *Advanced Material Interfaces,* vol. 6, p. 1900761, 2019.
[116] A. Bosaka *et al.*, "Capillary alginate gel (Capgel™) for the treatment of full-thickness dermal wounds in a hypoxic mouse model," *International Journal of Polymeric Materials and Polymeric Biomaterials,* vol. 68, pp. 1108-1117, 2019.

[117] S. Grijalvo, M. Nieto-Díaz, R. M. Maza, R. Eritja, and D. D. Díaz, "Alginate Hydrogels as Scaffolds and Delivery Systems toRepair the Damaged Spinal Cord," *Biotechnology Journal* vol. 14, p. 1900275, 2019.
[118] M. M. Perez-Madrigal, J. E. Shaw, M. C. Arno, J. A. Hoyland, S. M. Richardson, and A. P. Dove, "Robust alginate/hyaluronic acid thiol-yne click-hydrogel scaffolds with superior mechanical performance and stability for load-bearing soft tissue engineering," *Biomater Sci,* vol. 8, no. 1, pp. 405-412, Jan 1 2020, doi: 10.1039/c9bm01494b.
[119] S. Atzet, S.Curtin, P. Trinh, S. Bryant, and B. Ratner, "Degradable poly(2-hydroxyethyl methacrylate)-copolycaprolactone Hydrogels for Tissue Engineering Scaffolds," *Biomacromolecules* pp. 3370–3377, 2008.
[120] D. Cetin, A. S. Kahraman, and M. Gumusderelioglu, "Novel Scaffolds Based on Poly(2-hydroxyethyl methacrylate) Superporous Hydrogels for Bone Tissue Engineering," *Journal of Biomaterials Science-Polymer Edition,* vol. 22, no. 9, pp. 1157-1178, 2011, doi: 10.1163/092050610x501704.
[121] J. Y. Lai, T. P. Wang, Y. T. Li, and I. H. Tu, "Synthesis, characterization and ocular biocompatibility of potential keratoprosthetic hydrogels based on photopolymerized poly(2-hydroxyethyl methacrylate)-co-poly(acrylic acid)," *Journal of Materials Chemistry,* vol. 22, no. 5, pp. 1812-1823, 2012, doi: 10.1039/c1jm14211a.
[122] J. Kopecek, "Hydrogels from soft contact lenses and implants to self-assembled nanomaterials," *Journal of Polymer Science A: Polymer Chemistry,* vol. 47, pp. 5929-5946, 2009.
[123] M. K. Ashtiani, M. Zandi, P. Shokrollahi, M. Ehsani, and H. Baharvand, "Surface modification of poly(2-hydroxyethyl methacrylate) hydrogel for contact lens application," (in English), *Polym. Adv. Technol.,* Article vol. 29, no. 4, pp. 1227-1233, Apr 2018, doi: 10.1002/pat.4233.
[124] M. Griffith and D. G. Harkin, "Recent advances in the design of artificial corneas," *Curr Opin Ophthalmol,* vol. 25, no. 3, pp. 240-7, May 2014, doi: 10.1097/ICU.0000000000000049.
[125] Y. Wang *et al.*, "Recent advances in the fabrication, functionalization, and bioapplications of peptide hydrogels," *Soft Matter,* vol. 16, no. 44, pp. 10029-10045, Nov 18 2020, doi: 10.1039/d0sm00966k.
[126] F. Gelain, Z. Luo, M. Rioult, and S. Zhang, "Self-assembling peptide scaffolds in the clinic," *NPJ Regen Med,* vol. 6, no. 1, p. 9, Feb 17 2021, doi: 10.1038/s41536-020-00116-w.
[127] A. Jain, L. Sailaja Duvvuri, S. Farah, N. Beyth, A. J. Domb, and W. Khan, "Antimicrobial Polymers," *Advanced Healthcare Materials,* vol. 3, pp. 1969-1985, 2014.
[128] D. A. Wellings and A. Gallagher, "Three-Dimensional Scaffolds for Tissue Culture and Regenerative Medicine," *International Pharmaceutical Industry,* vol. 4, pp. 44-46, 2012.
[129] A. G. Gallagher, J. A. Alorabi, D. A. Wellings, R. Lace, M. J. Horsburgh, and R. L. Williams, "A Novel Peptide Hydrogel for an Antimicrobial Bandage Contact Lens," *Advanced Healthcare Materials,* 2016.
[130] A. G. Gallagher, K. McLean, R. M. K. Stewart, D. A. Wellings, H. E. Allison, and R. L. Williams, "Development of a Poly-e-Lysine Contact Lens as a Drug

Delivery Device for the Treatment of Fungal Keratitis," *Investigative Opthalmology and Visual Science,* vol. 58, pp. 4499-4505, 2017.
[131] S. Kennedy *et al.*, "Poly-ε-lysine based hydrogels as synthetic substrates for the expansion of corneal endothelial cells for transplantation," *Journal of Materials Science: Materials in Medicine,* vol. 30, 2019.
[132] M. Q. Guo, X. Hu, C. Wang, and L. Ai, "Polysaccharides: Structure and Solubility," in *Structure of Polysaccharides* Z. Xu Ed. South China University of Technology, China: IntechOpen, 2017.
[133] N. P. Dave and A. Gor, "Natural Polysaccharide-Based Hydrogels and Nanomaterials: Recent Trends and Their Applications," in *Handbook of Nanomaterials for Industrial Applications*: Micro and Nano Technologies, 2018, pp. 36-66.
[134] Z. Zhang, O. Ortiz, R. Goyal, and J. Kohn, "Biodegradable Polymers," in *Handbook of Polymer Applications in Medicine and Medical Devices*, K. Modjarrad and S. Ebnesajjad Eds.: William Andrew Publishing 2014, pp. 303-335.
[135] Z. Xu, Z. Li, S. Jiang, and K. Bratlie, "Chemically Modified Gellan Gum Hydrogels with Tunable Properties for Use as Tissue Engineering Scaffolds," *ACS Omega* vol. 3, pp. 6998-7007, 2018
[136] C. Ferris, K. J. Gilmore, G. G. Wallace, and M. in het Panhuis, "Modified gellan gum hydrogels for tissue engineering applications," *Soft Matter* vol. 9, p. 3705, 2013.
[137] J. T. Oliveira *et al.*, "Gellan gum injectable hydrogels for cartilage tissue engineering applications: in vitro studies and preliminary in vivo evaluation," *Tissue Eng Part A,* vol. 16, no. 1, pp. 343-53, Jan 2010, doi: 10.1089/ten.TEA.2009.0117.
[138] J. Shah, B. Snider, T. Clarke, S. Kozutsky, M. Lacki, and A. Hosseini, "Large-scale 3D printers for additive manufacturing: design considerations and challenges," *International Journal of Advanced Manufacturing Technology,* vol. 104, no. 9-12, pp. 3679-3693, Oct 2019, doi: 10.1007/s00170-019-04074-6.
[139] J. Herzberger, J. M. Sirrine, C. B. Williams, and T. E. Long, "Polymer Design for 3D Printing Elastomers: Recent Advances in Structure, Properties, and Printing," *Progress in Polymer Science,* vol. 97, Oct 2019, Art no. Unsp 101144, doi: 10.1016/j.progpolymsci.2019.101144.
[140] J. K. Placone and A. J. Engler, "Recent Advances in Extrusion-Based 3D Printing for Biomedical Applications," *Adv Healthc Mater,* vol. 7, no. 8, p. e1701161, Apr 2018, doi: 10.1002/adhm.201701161.
[141] A. Ghilan, A. P. Chiriac, L. E. Nita, A. G. Rusu, I. Neamtu, and V. M. Chiriac, "Trends in 3D Printing Processes for Biomedical Field: Opportunities and Challenges," *Journal of Polymers and the Environment,* vol. 28, no. 5, pp. 1345-1367, May 2020, doi: 10.1007/s10924-020-01722-x.
[142] H. Gojzewski *et al.*, "Layer-by-Layer Printing of Photopolymers in 3D: How Weak is the Interface?," *Acs Applied Materials & Interfaces,* vol. 12, no. 7, pp. 8908-8914, Feb 2020, doi: 10.1021/acsami.9b22272.
[143] D. Jang, D. Kim, and J. Moon, "Influence of Fluid Physical Properties on Ink-Jet Printability," *Langmuir,* vol. 25, pp. 2629-2635, 2009.

[144] B. Derby, "Inkjet printing ceramics: From drops to solid," *Journal of the European Ceramic Society,* vol. 31, pp. 2543–2550, 2011.
[145] M. Y. Teo, L. Stuart, K. C. Aw, J. Stringer, and Ieee, "Micro-reactive inkjet printer for 2D and 3D hydrogel structures," in *2018 Ieee/Asme International Conference on Advanced Intelligent Mechatronics*, (IEEE ASME International Conference on Advanced Intelligent Mechatronics, 2018, pp. 569-573.
[146] A. Negro, T. Cherbuin, and M. P. Lutolf, "3D Inkjet Printing of Complex, Cell-Laden Hydrogel Structures," *Scientific Reports,* vol. 8, Nov 2018, Art no. 17099, doi: 10.1038/s41598-018-35504-2.
[147] S.Kyle, Z. M. Jessop, A. Al-Sabah, and I. S. Whitaker, "'Printability' of Candidate Biomaterials for Extrusion Based 3D Printing: State-of-the-Art," *Adv Healthc Mater,* vol. 6, p. 170064, 2017.
[148] A. Wibowo *et al.*, "3D Printing of Polycaprolactone-Polyaniline Electroactive Scaffolds for Bone Tissue Engineering," *Materials,* vol. 13, no. 3, Feb 2020, Art no. 512, doi: 10.3390/ma13030512.
[149] H. Qu, "Additive Manufacturing for bone tissue engineering scaffolds " *Materials Today Communications* vol. 24, p. 101024, 2020.
[150] G. Chen, N. Chen, and Q. Wang, "Fabrication and properties of poly(vinyl alcohol)/β-tricalcium phosphate composite scaffolds via fused deposition modeling for bone tissue engineering," *Composites Science and Technology,* vol. 172, pp. 17-28, 2019.
[151] K. Yue, G. T.-d. Santiago, M. M. Alvarez, A. Tamayol, N. Annabi, and A. Khademhosseini, "Synthesis, properties, and biomedical applications of gelatinmethacryloyl (GelMA) hydrogels," *Biomaterials* vol. 73, pp. 254-271, 2015.
[152] L.Elomaa, E. Keshib, I. M. Sauerb, and M. Weinhart, "Development of GelMA/PCL and dECM/PCL resins for 3D printing ofacellular in vitro tissue scaffolds by stereolithography," *Materials Science and Engineering C,* vol. 112, p. 110958, 2020.
[153] W. Ye *et al.*, "3D printing of gelatin methacrylate-based nerve guidance conduits with multiple channels," *Materials and Design,* vol. 192, p. 108757, 2020.
[154] P. Rider, Z. P. Kacarevic, S. Alkildani, S. Retnasingh, and M. Barbeck, "Bioprinting of tissue engineering scaffolds," *Journal of Tissue Engineering,* vol. 9, Oct 2018, Art no. 2041731418802090, doi: 10.1177/2041731418802090.
[155] B. Derby, "Inkjet Printing of Functional and Structural Materials: Fluid Property Requirements, Feature Stability, and Resolution," *Annual Review of Materials Research,* vol. 40, pp. 395–414, 2010.
[156] P. M. Rider, I. M. Brook, P. J. Smith, and C. A. Miller, "Reactive Inkjet Printing of Regenerated Silk Fibroin Films for Use as Dental Barrier Membranes," *Micromachines,* vol. 9, no. 2, Feb 2018, Art no. 46, doi: 10.3390/mi9020046.
[157] J. D. Kim, J. S. Choi, B. S. Kim, Y. C. Choi, and Y. W. Cho, "Piezoelectric inkjet printing of polymers: Stem cell patterning on polymer substrates," *Polymer,* vol. 51, no. 10, pp. 2147-2154, May 2010, doi: 10.1016/j.polymer.2010.03.038.

[158] M. Mobaraki, M. Ghaffari, A. Yazdanpanah, Y. Luo, and D. K. Mills, "Bioinks and Bioprinting: A focused review " *Bioprinting,* vol. 18, p. e00080, 2020.
[159] V. Mironov, N. Reis, and B. Derby, "Review: bioprinting: a beginning," *Tissue Eng,* vol. 12, no. 4, pp. 631-4, Apr 2006, doi: 10.1089/ten.2006.12.631.
[160] D. M. Kirchmajer, R. Gorkin, and M. I. H. Panhuis, "An overview of the suitability of hydrogel-forming polymers for extrusion-based 3D-printing," *Journal of Materials Chemistry B,* vol. 3, no. 20, pp. 4105-4117, 2015, doi: 10.1039/c5tb00393h.
[161] S. Hong *et al.*, "3D Printing: 3D Printing of Highly Stretchable and Tough Hydrogels into Complex, Cellularized Structures," (in eng), *Adv Mater,* vol. 27, no. 27, p. 4034, Jul 2015, doi: 10.1002/adma.201570182.
[162] S. R. Moxon *et al.*, "Suspended Manufacture of Biological Structures," (in eng), *Adv Mater,* vol. 29, no. 13, Apr 2017, doi: 10.1002/adma.201605594.
[163] T. Lam *et al.*, "Photopolymerizable gelatin and hyaluronic acid for stereolithographic 3D bioprinting of tissue-engineered cartilage," *J Biomed Mater Res B Appl Biomater,* vol. 107, no. 8, pp. 2649-2657, Nov 2019, doi: 10.1002/jbm.b.34354.
[164] L. Magalhaes *et al.*, "Printing 3D Hydrogel Structures Employing Low-Cost Stereolithography Technology," *J Funct Biomater,* vol. 11, no. 1, Feb 22 2020, doi: 10.3390/jfb11010012.
[165] K. Christensen, A. Compaan, W. Chai, G. Xia, and Y. Huang, "In Situ Printing-then-Mixing for Biological Structure Fabrication Using Intersecting Jets," *ACS Biomaterials Science and Engineering,* vol. 3, p. 3687−3694, 2017.
[166] E. M. Beems and J. A. Van Best, "Light transmission of the cornea in whole human eyes," *Experimental Eye Research,* vol. 50, no. 4, pp. 393-395, 1990.
[167] K. M. Meek and C. Knupp, "Corneal structure and transparency," *Prog Retin Eye Res,* vol. 49, pp. 1-16, Nov 2015, doi: 10.1016/j.preteyeres.2015.07.001.
[168] S. Patel and L. Tutchenko, "The refractive index of the human cornea: A review," *Cont Lens Anterior Eye,* vol. 42, no. 5, pp. 575-580, Oct 2019, doi: 10.1016/j.clae.2019.04.018.
[169] S. Patel, J. Marshall, and F. W. Fitzke, 3rd, "Refractive index of the human corneal epithelium and stroma," *J Refract Surg,* vol. 11, no. 2, pp. 100-5, Mar-Apr 1995.
[170] M. Griffith, W. B. Jackson, N. Lagali, K. Merrett, F. Li, and P. Fagerholm, "Artificial corneas: a regenerative medicine approach," (in eng), *Eye (Lond),* vol. 23, no. 10, pp. 1985-9, Oct 2009, doi: 10.1038/eye.2008.409.
[171] D. Myung, P.-E. Duhamel, J. R. Cochran, J. Noolandi, C. N. Ta, and C. W. Frank, "Development of Hydrogel-Based Kerato-prostheses: A Materials Perspective," *Biotechnology Progress,* vol. 24, pp. 735-741, 2008.
[172] H. Goodarzi, K. Jadidi, S. Pourmotabed, E. Sharifi, and H. Aghamollaei, "Preparation and in vitro characterization of cross-linked collagen–gelatin hydrogel using EDC/NHS for corneal tissue engineering applications," *International Journal of Biological Macromolecules,* vol. 126, no. 620-632, 2019.
[173] N. K. Pengfei Duan, Jiajun Wang, Jinju Chen, "Rheological Characterization of Alginate Based Hydrogels for Tissue Engineering," *Biomaterials and Soft Materials,* vol. 2, no. 24, pp. 1309-1314, 2017.

[174] J. Hilbig, K. Hartlieb, M. Gibis, K. Herrmann, and J. Weiss, "Rheological and mechanical properties of alginate gels and films containing different chelators," *Food Hydrocolloids,* vol. 101, p. 105487, 2020.
[175] I. F. Farres, R. J. A. Moakes, and I. T. Norton, "Designing biopolymer fluid gels: A microstructural approach," (in English), *Food Hydrocolloid,* vol. 42, pp. 362-372, Dec 15 2014, doi: 10.1016/j.foodhyd.2014.03.014.
[176] I. F. Farres, M. Douaire, and I. T. Norton, "Rheology and tribological properties of Ca-alginate fluid gels produced by diffusion-controlled method," (in English), *Food Hydrocolloid,* vol. 32, no. 1, pp. 115-122, Jul 2013, doi: 10.1016/j.foodhyd.2012.12.009.
[177] K. M. Meek and C. Knupp, "Corneal structure and transparency," *Progress in Retinal and Eye Research,* vol. 49, pp. 1-16, 2015.
[178] S. Gupta, S. Goswami, and A. Sinha, "A combined effect of freeze--thaw cycles and polymer concentration on the structure and mechanical properties of transparent PVA gels," *Biomed Mater,* vol. 7, no. 1, p. 015006, Feb 2012, doi: 10.1088/1748-6041/7/1/015006.
[179] S. Patachia, C. Florea, C. Friedrich, and Y. Thomann, "Tailoring of poly(vinyl alcohol) cryogels properties by salts addition," (in English), *Express Polym Lett,* vol. 3, no. 5, pp. 320-331, May 2009, doi: 10.3144/expresspolymlett.2009.40.
[180] R. N. Palchesko, S. D. Carrasquilla, and A. W. Feinberg, "Natural Biomaterials for Corneal Tissue Engineering, Repair, and Regeneration," *Advanced Healthcare Materials,* vol. 7, no. 16, p. 1701434, 2018, doi: 10.1002/adhm.201701434.
[181] R. Williams, R. Lace, S. Kennedy, K. Doherty, and H. Levis, "Biomaterials for Regenerative Medicine Approaches for the Anterior Segment of the Eye," *Advanced Healthcare Materials,* vol. 7, no. 10, p. 1701328, 2018, doi: 10.1002/adhm.201701328.
[182] A. O. M. Salehi, S. H. Keshel, F. Sefat, and L. Tayebi, "Use of polycaprolactone in corneal tissue engineering: A review," *Materials Today Communications,* vol. 27, 2021.
[183] C. Kayal, R. J. Shipley, and J. B. Phillips, "Physical and mechanical properties of RAFT-stabilised collagen gels for tissue engineering applications," *J Mech Behav Biomed Mater,* vol. 99, pp. 216-224, Nov 2019, doi: 10.1016/j.jmbbm.2019.07.011.
[184] C. Ramachandran, P. Gupta, S. Hazra, and B. B. Mandal, "In Vitro Culture of Human Corneal Endothelium on Non-Mulberry Silk Fibroin Films for Tissue Regeneration," *Transl Vis Sci Technol,* vol. 9, no. 4, p. 12, Mar 2020, doi: 10.1167/tvst.9.4.12.
[185] S. Sharma, S. Mohanty, D. Gupta, M. Jassal, A. K. Agrawal, and R. Tandon, "Cellular response of limbal epithelial cells on electrospun poly-ε-caprolactone nanofibrous scaffolds for ocular surface bioengineering: a preliminary in vitro study," *Molecular Vision,* vol. 17, pp. 2898-2910, 2011.
[186] B. Ozcelik *et al.*, "Biodegradable and Biocompatible Poly(Ethylene Glycol)-based Hydrogel Films for the Regeneration of Corneal Endothelium," (in English), *Advanced Healthcare Materials,* vol. 3, no. 9, pp. 1496-1507, Sep 2014, doi: 10.1002/adhm.201400045.

[187] R. Parke-Houben *et al.*, "Interpenetrating polymer network hydrogel scaffolds for artificial cornea periphery," *Journal of Materials Science: Materials in Medicine* vol. 26, 2015.
[188] T. A. Arica, M. Guzelgulgen, A. A. Yildiz, and M. M. Demir, "Electrospun GelMA fibers and p(HEMA) matrix composite for corneal tissue engineering," (in English), *Mat Sci Eng C-Mater,* vol. 120, Jan 2021, doi: ARTN 111720
10.1016/j.msec.2020.111720.
[189] A. O. M. Salehi, M. S. Nourbakhsh, M. Rafienia, A. Baradaran-Rafii, and S. H. Keshe, "Corneal stromal regeneration by hybrid oriented poly (ε-caprolactone)/lyophilized silkfibroin electrospun scaffold," *International Journal of Biological Macromolecules,* vol. 161, pp. 377-388, 2020.
[190] P. Gupta, K. Vermani, and S. Garg, "Hydrogels: from controlled release to pH-responsive drug delivery," *Drug Discovery Today,* vol. 7, pp. 569-579, 2002.
[191] C. S. A. Musgrave and F. Fang, "Contact Lens Materials: A Materials Science Perspective," (in eng), *Materials (Basel),* vol. 12, no. 2, p. 261, 2019, doi: 10.3390/ma12020261.
[192] L. Santos *et al.*, "Degradation Studies and Biological Behavior on an Artificial Cornea Material," vol. 51, pp. 4274-4281, 2011.
[193] N. Polisetti, M. M. Islam, and M. Griffith, "The Artificial Cornea," in *Corneal Regenerative Medicine: Methods and Protocols*, B. Wright and C. J. Connon Eds. Totowa, NJ: Humana Press, 2013, pp. 45-52.
[194] Q. L. Loh and C. Choong, "Three-Dimensional Scaffolds for Tissue Engineering Applications: Role of Porosity and Pore Size," *Tissue Engineering: Part B,* vol. 19, no. 6, pp. 485-502, 2013.
[195] A. Sannino, M. Madaghiele, and L. Ambrosio, "Biocompatibility and other properties of hydrogels in regenerative medicine," in *Cellular Response to Biomaterials*, L. D. Silvio Ed.: Woodhead Publishing 2009, ch. 5, pp. 114-135.
[196] J. L. Drury and D. J. Mooney, "Hydrogels for tissue engineering: scaffold design variables and applications," *Biomaterials,* vol. 24, no. 24, pp. 4337-51, Nov 2003, doi: 10.1016/s0142-9612(03)00340-5.
[197] K. E. Swindle-Reilly and N. Ravi, "Designing hydrogels as vitreous substitutes in ophthalmic surgery," in *Biomaterials and Regenerative Medicine in Ophthalmology*, T. V. Chirila Ed.: Woodhead Publishing 2010, ch. 13, pp. 339-373.
[198] J. Xiang, L. Shen, and Y. Hong, "Status and future scope of hydrogels in wound healing: Synthesis, materials and evaluation," *European Polymer Journal,* vol. 130, p. 109609, 2020.
[199] T. L. Kelly, K. A. Williams, D. J. Coster, and R. Australian Corneal Graft, "Corneal transplantation for keratoconus: a registry study," *Arch Ophthalmol,* vol. 129, no. 6, pp. 691-7, Jun 2011, doi: 10.1001/archophthalmol.2011.7.
[200] C. Liu *et al.*, "The osteo-odonto-keratoprosthesis (OOKP)," *Semin Ophthalmol,* vol. 20, no. 2, pp. 113-28, Apr-Jun 2005, doi: 10.1080/08820530590931386.

[201] M. Zarei-Ghanavati and C. Liu, "Keratoprosthesis: Current Choices and Future Development," (in English), *Asia-Pac J Ophthalmo,* vol. 8, no. 6, pp. 429-431, Nov-Dec 2019, doi: 10.1097/Apo.0000000000000268.
[202] Z. Li *et al.*, "A sintered graphene/titania material as a synthetic keratoprosthesis skirt for end-stage corneal disorders," (in English), *Acta Biomaterialia,* vol. 94, pp. 585-596, Aug 2019, doi: 10.1016/j.actbio.2019.05.053.
[203] J. Kaur, "Osteo-odonto keratoprosthesis: Innovative dental and ophthalmic blending," *The Journal of Indian Prosthodontic Society* vol. 18, pp. 89-95, 2018.
[204] R. Viitala, V. Franklin, D. Green, C. Liu, A. Lloyd, and B. Tighe, "Towards a synthetic osteo-odonto-keratoprosthesis," (in English), *Acta Biomaterialia,* vol. 5, no. 1, pp. 438-452, Jan 2009, doi: 10.1016/j.actbio.2008.07.008.
[205] M. Gonzalez-Andrades *et al.*, "A study protocol for a multicentre randomised clinical trial evaluating the safety and feasibility of a bioengineered human allogeneic nanostructured anterior cornea in patients with advanced corneal trophic ulcers refractory to conventional treatment," *BMJ Open,* vol. 7, no. 9, p. e016487, Sep 24 2017, doi: 10.1136/bmjopen-2017-016487.
[206] L. Rico-Sanchez *et al.*, "Successful development and clinical translation of a novel anterior lamellar artificial cornea," *J Tissue Eng Regen Med,* vol. 13, no. 12, pp. 2142-2154, Dec 2019, doi: 10.1002/term.2951.
[207] N. Lagali, "Corneal Stromal Regeneration: Current Status and Future Therapeutic Potential," *Curr Eye Res,* vol. 45, no. 3, pp. 278-290, Mar 2020, doi: 10.1080/02713683.2019.1663874.
[208] R. M. Gouveia *et al.*, "Controlling the 3D architecture of Self-Lifting Auto-generated Tissue Equivalents (SLATEs) for optimized corneal graft composition and stability," *Biomaterials,* vol. 121, pp. 205-219, Mar 2017, doi: 10.1016/j.biomaterials.2016.12.023.
[209] S. Proulx *et al.*, "Reconstruction of a human cornea by the self-assembly approach of tissue engineering using the three native cell types," *Molecular Vision,* vol. 16, pp. 2192-2201, 2010.
[210] E. Taghiabadi, S. Nasri, S. Shafieyan, S. Jalili Firoozinezhad, and N. Aghdami, "Fabrication and characterization of spongy denuded amniotic membrane based scaffold for tissue engineering," *Cell J,* vol. 16, no. 4, pp. 476-87, Winter 2015, doi: 10.22074/cellj.2015.493.
[211] S. Leal-Marin *et al.*, "Human Amniotic Membrane: A review on tissue engineering, application, and storage," *J Biomed Mater Res B Appl Biomater,* vol. 109, no. 8, pp. 1198-1215, Aug 2021, doi: 10.1002/jbm.b.34782.
[212] A. M. Grillet, N. B. Wyatt, and L. M. Gloe, "Polymer Gel Rheology and Adhesion," in *Rheology*: Intech, 2012.
[213] V. S. Kulkarni and C. Shaw, "Rheological Studies," in *Essential Chemistry for Formulators of Semisolid and Liquid Dosages*: Academic Press, 2016, ch. 9, pp. 145-182.
[214] E. R. Morris, K. Nishinari, and M. Rinaudo, "Gelation of gellan – A review," *Food Hydrocolloids,* vol. 28, pp. 373-411, 2012.

[215] H. Hatami-Marbini, "Viscoelastic shear properties of the corneal stroma," *Journal of Biomechanics,* vol. 47, no. 3, pp. 723-728, 2014/02/07/ 2014, doi: https://doi.org/10.1016/j.jbiomech.2013.11.019.
[216] D. A. Hoeltzel, P. Altman, K. Buzar, and K. Choe, "Strip Extensiometry for Comparison of the Mechanical Response of Bovine, Rabbit, and Human Corneas," *J Biomech Eng,* vol. 114, pp. 202-215, 1992.
[217] K. Merrett *et al.*, "Tissue-Engineered Recombinant Human Collagen-Based Corneal Substitutes for Implantation: Performance of Type I versus Type III Collagen," *Investigative Ophthalmology and Visual Science,* vol. 49, pp. 3887-3894, 2008.
[218] N. Garcia-Porta, P. Fernandes, A. Queiros, J. Salgado-Borges, M. Parafita-Mato, and J. M. González-Méijome, "Corneal Biomechanical Properties in Different Ocular Conditions and New Measurement Techniques," *ISRN Ophthalmology,* vol. 2014, p. 724546, 2014.
[219] Y. Zeng, J. Yang, K. Huang, and X. Lee, "A comparison of biomechanical properties between human and porcine cornea," *Journal of Biomechanics* vol. 34, pp. 533-537, 2001.
[220] G. H. Altman *et al.*, "Silk-based biomaterials," *Biomaterials,* vol. 24, no. 3, pp. 401-16, Feb 2003, doi: 10.1016/s0142-9612(02)00353-8.
[221] R. Lace, C. Murray-Dunning, and R. Williams, "Biomaterials for ocular reconstruction," *Journal of Materials Science,* vol. 50, no. 4, pp. 1523-1534, 2015/02/01 2015, doi: 10.1007/s10853-014-8707-0.
[222] W. Z. Sun, D. A. Gregory, M. A. Tomeh, and X. B. Zhao, "Silk Fibroin as a Functional Biomaterial for Tissue Engineering," (in English), *Int J Mol Sci,* vol. 22, no. 3, Feb 2021, doi: ARTN 1499
10.3390/ijms22031499.
[223] D. C. Pye, "A clinical method for estimating the modulus of elasticity of the human cornea in vivo," *PLoS ONE,* Article vol. 15, no. 1, pp. 1-19, 2020, doi: 10.1371/journal.pone.0224824.
[224] H. Kim *et al.*, "Shear-induced alignment of collagen fibrils using 3D cell printing for corneal stroma tissue engineering," *Biofabrication,* vol. 11, 2019.
[225] A. Isaacson, S. Swioklo, and C. J. Connon, "3D bioprinting of a corneal stroma equivalent," *Exp Eye Res,* vol. 173, pp. 188-193, Aug 2018, doi: 10.1016/j.exer.2018.05.010.
[226] S. Ulaga *et al.*, "3D printed artificial cornea for corneal stromal transplantation," *European Polymer Journal,* vol. 133, 2020.
[227] M. Technologies. "Dispensing Devices - Low Temperature Devices " http://www.microfab.com/dispensing-devices (accessed 24/03/21.
[228] B. Zhang *et al.*, "3D bioprinting for artificial cornea: Challenges and perspectives," *Med Eng Phys,* vol. 71, pp. 68-78, Sep 2019, doi: 10.1016/j.medengphy.2019.05.002.
[229] E. L. Gill, X. Li, M. A. Birch, and Y. Y. S. Huang, "Multi-length scale bioprinting towards simulating microenvironmental cues," *Biodes Manuf,* vol. 1, no. 2, pp. 77-88, 2018, doi: 10.1007/s42242-018-0014-1.
[230] R. Gibney, S. Matthyssen, J. Patterson, E. Ferraris, and N. Zakaria, "The human cornea as a model tissue for additive biomanufacturing: a review," *Procedia CIRP,* vol. 65, pp. 56-63, 2017.

[231] P. Fagerholm *et al.*, "A biosynthetic alternative to human donor tissue for inducing corneal regeneration: 24-month follow-up of a phase 1 clinical study," *Sci Transl Med,* vol. 2, no. 46, p. 46ra61, Aug 25 2010, doi: 10.1126/scitranslmed.3001022.
[232] S. Ulaga *et al.*, "Recent developments and characterization techniques in 3D printing of corneal stroma tissue," *Polymer Advanced Technologies,* vol. 2021, pp. 1-10, 2021.
[233] A. G. Gallagher, J. A. Alorabi, D. A. Wellings, R. Lace, M. J. Horsburgh, and R. L. Williams, "A Novel Peptide Hydrogel for an Antimicrobial Bandage Contact Lens," *Advanced Healthcare Materials,* vol. 5, no. 16, pp. 2013-2018, 2016, doi: 10.1002/adhm.201600258.
[234] A. G. Gallagher, K. McLean, R. M. K. Stewart, D. A. Wellings, H. E. Allison, and R. L. Williams, "Development of a Poly-ε-Lysine Contact Lens as a Drug Delivery Device for the Treatment of Fungal Keratitis," *Investigative Ophthalmology & Visual Science,* vol. 58, no. 11, pp. 4499-4505, 2017, doi: 10.1167/iovs.17-22301.
[235] S. Kennedy *et al.*, "Poly-ε-lysine based hydrogels as synthetic substrates for the expansion of corneal endothelial cells for transplantation," (in eng), *J Mater Sci Mater Med,* vol. 30, no. 9, pp. 102-102, 2019, doi: 10.1007/s10856-019-6303-1.
[236] S. M. Kennedy *et al.*, "Antimicrobial Activity of Poly-epsilon-lysine Peptide Hydrogels Against Pseudomonas aeruginosa," *Investigative Ophthalmology & Visual Science,* vol. 61, no. 10, pp. 18-18, 2020, doi: 10.1167/iovs.61.10.18.
[237] C. Ukiwe, A. Mansouri, and D. Y. Kwok, "The dynamics of impacting water droplets on alkanethiol self-assembledmonolayers with co-adsorbed CH3and CO2H terminal groups," *Journal of Colloid and Interface Science* vol. 285, pp. 760-768, 2005.
[238] B. He, S. Yang, Z. Qin, B. Wen, and C. Zhang, "The roles of wettability and surface tension in droplet formation during inkjet printing," *Scientific Reports,* vol. 7, 2017.
[239] T. Khan, J. K. Park, and J. H. Kwon, "Functional biopolymers produced by biochemical technology considering applications in food engineering," *Korean Journal of Chemical Engineering,* vol. 24, no. 5, pp. 816-826, 2007.
[240] F. Freitas, V. D. Alves, and M. A. M. Reis, "Advances in bacterial exopolysaccharides: from production to biotechnological applications," *Trends in Biotechnology,* vol. 29, pp. 388-398, 2011.
[241] C. H. Gao, "Unique rheology of high acyl gellan gum and its potential applications in enhancement of petroleum production," *Journal of Petroleum Exploration and Production* vol. 6, pp. 743-747, 2016.
[242] A. Pietriková *et al.*, "Surface analysis of polymeric substrates used for inkjet printing technology," *Circuit World,* vol. 42, pp. 9-16, 2016.
[243] M. Bale. "Single Pass Inkjet – The Tension Between Jetting and Wetting." https://inkjetinsight.com/knowledge-base/single-pass-inkjet-the-tension-between-jetting-and-wetting/ (accessed 20/04/2021.

[244] P. M. Rider, I. M. Brook, P. J. Smith, and C. A. Miller, "Reactive Inkjet Printing of Regenerated Silk Fibroin Films for Use as Dental Barrier Membranes," *Micromachines,* vol. 9, p. 46, 2018.
[245] J. T. Delaney, A. R. Liberski, J. Perelaer, and U. S. Schubert, "Reactive inkjet printing of calcium alginate hydrogel porogens—a new strategy to open-pore structured matrices with controlled geometry," *Soft Matter,* vol. 6, pp. 866-869, 2010.
[246] T. Xu *et al.*, "Viability and electrophysiology of neural cell structures generated by the inkjet printing method," *Biomaterials,* vol. 27, pp. 3580-3588, 2006.
[247] B. Pourjabbar *et al.*, "Bio-polymeric hydrogels for regeneration of corneal epithelial tissue," *International Journal of Polymeric Materials and Polymeric Biomaterials,* 2021, doi: 10.1080/00914037.2021.1909586.
[248] K. Merrett *et al.*, "Tissue-Engineered Recombinant Human Collagen-Based Corneal Substitutes for Implantation: Performance of Type I versus Type III Collagen," *Investigative Ophthalmology & Visual Science,* vol. 49, pp. 3887-3894, 2008.
[249] P. Fagerholm *et al.*, "A Biosynthetic Alternative to Human Donor Tissue for Inducing Corneal Regeneration: 24-Month Follow-Up of a Phase 1 Clinical Study," *Science Translational Medicine,* vol. 2, pp. 46-61, 2010.
[250] R. Williams, R. Lace, S. Kennedy, K. Doherty, and H. Levis, "Biomaterials for Regenerative Medicine Approaches for the Anterior Segment of the Eye," *Adv Healthc Mater,* vol. 7, no. 10, p. e1701328, May 2018, doi: 10.1002/adhm.201701328.
[251] C. Romo-Valera, P. Guerrero, J. Arluzea, J. Etxebarria, K. de la Caba, and N. Andollo, "Cytocompatibility and Suitability of Protein-Based Biomaterials as Potential Candidates for Corneal Tissue Engineering," *International Journal of Molecular Science* vol. 22, 2021.
[252] K.-Y. Li *et al.*, "Fish-Scale Collagen Membrane Seeded with Corneal Endothelial Cells as Alternative Graft for Endothelial Keratoplasty Transplantation," *ACS Biomaterials Science and Engineering* vol. 6, pp. 2570-2577, 2020.
[253] M. Parekh, B. Van den Bogerd, N. Zakaria, D. Ponzin, and S. Ferrari, "Fish Scale-Derived Scaffolds for Culturing Human Corneal Endothelial Cells," *Stem Cells International,* vol. 2018, 2018.
[254] v. Madden, J. N. X. Lai, K. A. George, T. Giovenco, D. G. Harkin, and T. V. Chirila, "Human corneal endothelial cell growth on a silk fibroin membrane," *Biomaterials,* vol. 32, pp. 4076-4084, 2011.
[255] N. Vazquez *et al.*, "Silk Fibroin Films for Corneal Endothelial Regeneration: Transplant in a Rabbit Descemet Membrane Endothelial Keratoplasty," *Investigative Ophthalmology & Visual Science,* vol. 58, pp. 3357-3365, 2017.
[256] M. Parekh *et al.*, "Biomaterials for corneal endothelial cell culture and tissue engineering," *J Tissue Eng,* vol. 12, p. 2041731421990536, Jan-Dec 2021, doi: 10.1177/2041731421990536.
[257] R. Lace, G. L. Duffy, K. G. Doherty, O. Maklad, D. A. Wellings, and R. Williams, "Characterization of Tunable Poly-ε-Lysine-Based Hydrogels for Corneal

Tissue Engineering," *Macromolecular Bioscience* 2021, doi: 10.1002/mabi.202100036
[258] M. Mobaraki, R. Abbasi, S. Omidian Vandchali, M. Ghaffari, F. Moztarzadeh, and M. Mozafari, "Corneal Repair and Regeneration: Current Concepts and Future Directions," *Front Bioeng Biotechnol,* vol. 7, p. 135, 2019, doi: 10.3389/fbioe.2019.00135.
[259] K. Araki-Sasaki *et al.*, "An SV40-immortalized human corneal epithelial cell line and its characterization," *Invest Ophthalmol Vis Sci,* vol. 36, no. 3, pp. 614-21, Mar 1995.
[260] M. Hahne *et al.*, "Prevalidation of a Human Cornea Construct as an Alternative to Animal Corneas for In Vitro Drug Absorption Studies," *Journal of Pharmaceutical Sciences,* vol. 101, pp. 2976-2988, 2012.
[261] N. Beissner, M. Zorn-Kruppa, and S. Reichl, "Parameter study of shipping conditions for the ready-to-use application of a 3D human hemicornea construct in drug absorption studies," *Int J Pharm,* vol. 536, no. 1, pp. 377-387, Jan 30 2018, doi: 10.1016/j.ijpharm.2017.11.057.
[262] K. Yue, G. Trujillo-de Santiago, M. M. Alvarez, A. Tamayol, N. Annabi, and A. Khademhosseini, "Synthesis, properties, and biomedical applications of gelatinmethacryloyl (GelMA) hydrogels," vol. 73, pp. 254-271, 2015.
[263] R. Dominguez and K. C. Holmes, "Actin structure and function," *Annu Rev Biophys,* vol. 40, pp. 169-86, 2011, doi: 10.1146/annurev-biophys-042910-155359.
[264] A. S. Fanning, B. J. Jameson, L. A. Jesaitis, and J. M. Anderson, "The Tight Junction Protein ZO-1 Establishes a Link between the Transmembrane Protein Occludin and the Actin Cytoskeleton," *The Journal of Biological Chemistry* vol. 273, pp. 29745-29753, 1998.
[265] Y. Ban *et al.*, "Tight junction-related protein expression and distribution in human corneal epithelium," *Exp Eye Res,* vol. 76, no. 6, pp. 663-9, Jun 2003, doi: 10.1016/s0014-4835(03)00054-x.
[266] J. M. Anderson, M. S. Balda, and A. S. Fanning, "The structure and regulation of tight junctions," *Curr Opin Cell Biol,* vol. 5, no. 5, pp. 772-8, Oct 1993, doi: 10.1016/0955-0674(93)90024-k.
[267] M. Eslani, A. Baradaran-Rafii, and S. Ahmad, "Cultivated Limbal and Oral Mucosal Epithelial Transplantation," *Seminars in Ophthalmology,* vol. 27, pp. 80-93, 2012.
[268] M. Valtink, R. Gruschwitz, R. H. W. Funk, and K. Engelmann, "Two Clonal Cell Lines of Immortalized Human Corneal Endothelial Cells Show either Differentiated or Precursor Cell Characteristics," *Cells Tissues Organs,* vol. 187, pp. 286-294, 2008.
[269] T. Gotze *et al.*, "Cultivation of an immortalized human corneal endothelial cell population and two distinct clonal subpopulations on thermo-responsive carriers," *Graefes Arch Clin Exp Ophthalmol,* vol. 246, no. 11, pp. 1575-83, Nov 2008, doi: 10.1007/s00417-008-0904-6.
[270] B. Huang, G. Blanco, R. W. Mercer, T. Fleming, and J. S. Pepose, "Human Corneal Endothelial Cell Expression of Na+, K+–Adenosine Triphosphatase Isoforms," *Archives of Ophthalmology* vol. 121, pp. 840-845, 2003.

[271] S. Xiao *et al.*, "Gelatin Methacrylate (GelMA)-Based Hydrogels for Cell Transplantation: an Effective Strategy for Tissue Engineering," *Stem Cell Reviews and Reports,* vol. 15, pp. 664-679, 2019.
[272] M. Rizwan *et al.*, "Sequentially-crosslinked bioactive hydrogels as nano-patternedsubstrates with customizable stiffness and degradation for cornealtissue engineering applications," *Biomaterials,* vol. 120, pp. 139-154, 2017.
[273] R. Ren *et al.*, "Human primary corneal fibroblasts synthesize and deposit proteoglycans in long-term 3-D cultures," *Dev Dyn,* vol. 237, no. 10, pp. 2705-15, Oct 2008, doi: 10.1002/dvdy.21606.
[274] E. S. Gil, S. H. Park, J. Marchant, F. Omenetto, and D. L. Kaplan, "Response of human corneal fibroblasts on silk film surface patterns," *Macromol Biosci,* vol. 10, no. 6, pp. 664-73, Jun 11 2010, doi: 10.1002/mabi.200900452.
[275] X. Guo, A. E. Hutcheon, S. A. Melotti, J. D. Zieske, V. Trinkaus-Randall, and J. W. Ruberti, "Morphologic characterization of organized extracellular matrix deposition by ascorbic acid-stimulated human corneal fibroblasts," *Invest Ophthalmol Vis Sci,* vol. 48, no. 9, pp. 4050-60, Sep 2007, doi: 10.1167/iovs.06-1216.
[276] C. Fan and D. A. Wang, "Macroporous Hydrogel Scaffolds for Three-Dimensional Cell Culture and Tissue Engineering," *Tissue Eng Part B Rev,* vol. 23, no. 5, pp. 451-461, Oct 2017, doi: 10.1089/ten.TEB.2016.0465.
[277] M. Hasenzahl, M. Musken, S. Mertsch, S. Schrader, and S. Reichl, "Cell sheet technology: Influence of culture conditions on in vitro-cultivated corneal stromal tissue for regenerative therapies of the ocular surface," *J Biomed Mater Res B Appl Biomater,* vol. 109, no. 10, pp. 1488-1504, Oct 2021, doi: 10.1002/jbm.b.34808.
[278] J. Fernandez-Perez and M. Ahearne, "Influence of Biochemical Cues in Human Corneal Stromal Cell Phenotype," *Curr Eye Res,* vol. 44, no. 2, pp. 135-146, Feb 2019, doi: 10.1080/02713683.2018.1536216.
[279] S. Saika, R. Kanagawa, K. Uenoyama, K. Hiroi, and J. Hiraoka, "L-ascorbic acid 2-phosphate, a phosphate derivative of L-ascorbic acid, enhances the growth of cultured rabbit keratocytes," *Graefes Arch Clin Exp Ophthalmol,* vol. 229, no. 1, pp. 79-83, 1991, doi: 10.1007/BF00172267.
[280] K. M. Meek, "Corneal collagen-its role in maintaining corneal shape and transparency," *Biophys Rev,* vol. 1, no. 2, pp. 83-93, Jul 2009, doi: 10.1007/s12551-009-0011-x.
[281] F. Ruggiero, C. Burillon, and R. Garrone, "Human corneal fibrillogenesis. Collagen V structural analysis and fibrillar assembly by stromal fibroblasts in culture," *Invest Ophthalmol Vis Sci,* vol. 37, no. 9, pp. 1749-60, Aug 1996.
[282] N. Stone and A. Meister, "Function of ascorbic acid in the conversion of proline to collagen hydroxyproline," *Nature,* vol. 194, pp. 555-7, May 12 1962, doi: 10.1038/194555a0.
[283] S. Tajima and S. R. Pinnell, "Regulation of collagen synthesis by ascorbic acid. Ascorbic acid increases type I procollagen mRNA," *Biochem Biophys Res Commun,* vol. 106, no. 2, pp. 632-7, May 31 1982, doi: 10.1016/0006-291x(82)91157-3.

[284] S. Saika, "Ultrastructural effect of L-ascorbic acid 2-phosphate on cultured keratocytes," *Cornea,* vol. 11, no. 5, pp. 439-45, Sep 1992, doi: 10.1097/00003226-199209000-00014.
[285] M. A. Princz, H. Sheardown, and M. Griffith, "Corneal tissue engineering versus synthetic artificial corneas," in *Biomaterials and Regenerative Medicine in Ophthalmology*, T. V. Chirila Ed.: Woodhead Publishing 2010, pp. 134-149.
[286] P. Zorlutuna *et al.*, "Microfabricated biomaterials for engineering 3D tissues," *Adv Mater,* vol. 24, no. 14, pp. 1782-804, Apr 10 2012, doi: 10.1002/adma.201104631.
[287] N. Annabi *et al.*, "Controlling the porosity and microarchitecture of hydrogels for tissue engineering," *Tissue Eng Part B Rev,* vol. 16, no. 4, pp. 371-83, Aug 2010, doi: 10.1089/ten.TEB.2009.0639.
[288] X. Li *et al.*, "Inkjet Bioprinting of Biomaterials," *Chem Rev,* vol. 120, no. 19, pp. 10793-10833, Oct 14 2020, doi: 10.1021/acs.chemrev.0c00008.
[289] H. Gudapati, M. Dey, and I. Ozbolat, "A comprehensive review on droplet-based bioprinting: Past, present and future," (in English), *Biomaterials,* vol. 102, pp. 20-42, Sep 2016, doi: 10.1016/j.biomaterials.2016.06.012.
[290] T. M. Shick, A. Z. A. Kadir, N. H. A. Ngadiman, and A. Ma'aram, "A review of biomaterials scaffold fabrication in additive manufacturing for tissue engineering," (in English), *J Bioact Compat Pol,* vol. 34, no. 6, pp. 415-435, Nov 2019, doi: Artn 0883911519877426
10.1177/0883911519877426.
[291] A. Eltom, G. Y. Zhong, and A. Muhammad, "Scaffold Techniques and Designs in Tissue Engineering Functions and Purposes: A Review," (in English), *Adv Mater Sci Eng,* vol. 2019, 2019, doi: Artn 3429527
10.1155/2019/3429527.
[292] G. Weisgrab *et al.*, "3D Printing of large-scale and highly porous biodegradable tissue engineering scaffolds from poly(trimethylene-carbonate) using two-photonpolymerization," *Biofabrication,* vol. 12, p. 045036, 2020.
[293] R. Sharif, S. Priyadarsini, T. G. Rowsey, J. X. Ma, and D. Karamichos, "Corneal Tissue Engineering: An In Vitro Model of the Stromal-nerve Interactions of the Human Cornea," *J Vis Exp,* no. 131, Jan 24 2018, doi: 10.3791/56308.
[294] I. M. El-Sherbiny and M. H. Yacoub, "Hydrogel scaffolds for tissue engineering: Progress and challenges," *Glob Cardiol Sci Pract,* vol. 2013, no. 3, pp. 316-42, 2013, doi: 10.5339/gcsp.2013.38.
[295] E. C. Beck, M. Barragan, M. H. Tadros, S. H. Gehrke, and M. S. Detamore, "Approaching the compressive modulus of articular cartilage with a decellularized cartilage-based hydrogel," *Acta Biomater,* vol. 38, pp. 94-105, Jul 1 2016, doi: 10.1016/j.actbio.2016.04.019.
[296] J. Iwasa, L. Engebretsen, Y. Shima, and M. Ochi, "Clinical application of scaffolds for cartilage tissue engineering," *Knee Surg Sports Traumatol Arthrosc,* vol. 17, no. 6, pp. 561-77, Jun 2009, doi: 10.1007/s00167-008-0663-2.

[297] C. Ferris, K. J. Gilmore, G. G. Wallace, and M. in het Panhuis, "Modified gellan gum hydrogels for tissue engineering applications," *Soft Matter,* vol. 9, 2013.